Modelling and Large Eddy Simulation of Large-scale Hydrogen-air Deflagration and Deflagration-to-Detonation Transition

Mohamed Sakr

BSc and MSc

Research conducted within the:
Faculty of Computing, Engineering and the Built Environment,
Hydrogen Safety Engineering and Research Centre
Ulster University

Thesis
Submitted for the degree of
DOCTOR OF PHILOSOPHY
November 2020

I confirm that the word count for this thesis is less than 100,000 words

DEDICATION

Dedicated to my Father, my Mother, my Two Brothers, and my Sister

TABLE OF CONTENTS

ACKNOWLEDGEMENTS

First and foremost, I thank my family for their love, support, and encourage. Thank you.

I would like to thank Dr. Dmitriy Makarov from Ulster University for discussion and for the technical support. I would like also to thank Dr. Andre Gaathaug from University of Southern Norway, Dr. Vincent Robin from University of Poitiers - France, and Dr. Arief Dahoe from TOP BV - Netherlands for their discussion.

I would like to thank Dr. Jacqueline Reilly and Kate McMorris from the Doctoral College for their support.

I acknowledge the funding from Ulster University.

Images used courtesy of ANSYS, Inc.

ABSTRACT

A release of hydrogen in industry could form a highly reactive mixture. Ignition of this mixture and acceleration of the flame due to turbulence and confinement could go for a transition to detonation through a mechanism called deflagration-to-detonation transition (DDT). Detonation produces high overpressure in the order of tens of bar, which produces risk for lives and damage to the buildings.

It would be required to numerically study the possibility of explosion and transition to detonation for a safety purpose. The prediction of the flame propagation velocity and overpressure of the explosion does not require resolving flame details. Therefore, flame wrinkling models are suitable candidates for studying industrial scales.

Hence, the aim of the current study is to develop a reliable flame wrinkling model to predict flame deflagration and detonation in the framework of the large eddy simulation. Two main mechanisms responsible for flame acceleration are considered in the current study, which are flame intrinsic instabilities and turbulence. The instabilities mechanism, including the interaction of turbulence, and the turbulence mechanism are separately modelled using the fractal description. A proposed model for the inner cut-off length scale of turbulence is developed, which is suitable for the corrugated flamelets and the thin reaction zones regimes. The effect of excessive stretching to quench the flame is included. For a complete closure of the turbulence modelling, the effect of the flame to generate turbulence is included.

The model is tested against three experiments: DDT in a channel, large-scale deflagration in an open atmosphere, and vented explosion. The DDT simulation predicts good flame propagation velocity compared with the shock propagation velocity of the experiment. The open atmosphere simulation qualitatively predicts flame propagation and overpressure comparable with the experiment and the state-of-the-art (SOTA). The vented explosion simulation qualitatively predicts flame propagation and overpressure in the order of the experiment and the SOTA. Despite, the predicted overpressure is not converged based on the resolutions of the tested meshes.

The overall performance of the model is qualitatively acceptable for simulating deflagration and DDT.

NOMENCLATURE

Latin

p	Static pressure
T	Static temperature
E	Total energy
q	Heat flux
K	Thermal conductivity
Le	Lewis number of the deficient reactant
Ka_{Δ}	Karlovitz number
Ka_{δ}	Karlovitz number based on the inner flame thickness
Pr	Prandtl number
Q	Energy released from combustion per unit mass
R	Flame propagation radius
Y	Species mass fraction
erf	The error function
l	Integral length scale
t	Time
h	Species enthalpy
x	Spatial coordinate
D	Molecular diffusion coefficient
H	Enthalpy
X	Mole fraction
C_k	Turbulent viscosity constant, calculated using dynamic procedure
C_{ε}	Dissipation rate constant, calculated using dynamic procedure

u_{CJ}	Chapman-Jouguet detonation velocity
u_{sp}	Spontaneous flame velocity
L	Length
u_{Δ}	Sub-grid scale turbulent velocity
U_{tr}	Transition turbulent intensity
C_1	Hydrodynamic function for the spherical flame
C_2	Hydrodynamic function for the spherical flame
C_3	Hydrodynamic function for the spherical flame
C_4	Hydrodynamic function for the spherical flame
D_{eff}	Effective diffusivity
D_s	Species s molecular diffusivity
D_L	Diffusivity of the limiting reactant
E_a	Activation energy
A	Area
$K\|_{eff}$	Effective thermal conductivity
Le_{eff}	Effective Lewis number
Pe	Peclet number
Re_{Δ}	Turbulent Reynolds number
S_E	Energy equation source term (Kg/ms^3)
S_{Y_s}	Source term for mass fraction equation of specie s (Kg/m^3s)
S_{u0}	Laminar burning velocity at the reference condition
S_u	Laminar burning velocity
S_{tur}	Turbulent burning velocity
FD	Fractal dimensional
Sc_{tur}	Turbulent Schmidt number

S_f	Flame propagation velocity with respect to the burned gas velocity
T_u	Unburned temperature
T_b	Adiabatic flame temperature
X_{H_2}	Mole fraction of the hydrogen
k_Δ	Sub-grid scale turbulent kinetic energy
k	Turbulent kinetic energy
Cp	Specific heat
D_c	Diffusivity of the progress variable
D_{tur}	Turbulent diffusion coefficient
u	Velocity
u_i	Velocity component
Pc	Pope criterion
S	Segregation factor
$\check{R}$	Universal gas constant
f	Wave number
f_{max}	Maximum perturbation wave number
f_{min}	Minimum perturbation wave number
B_1	Planar flame coefficient
B_2	Planar flame coefficient
B_3	Planar flame coefficient
G	Stretch (quenching) factor
Hc	Heat of chemical reaction ($J/Kg\ of\ burned\ gas$)
g_{cr}	Critical flow velocity gradient for quenching ($1/s$)
hrl	Half reaction length
$\mathbb{F}$	Orientation parameter

V_c	Volume of the computational cell

Greek

Ξ	Wrinkling factor
ρ	Density
μ_{tur}	Turbulent viscosity
μ_u	Unburned viscosity
τ_{ij}	Shear stress tensor
$\tau_{ij}\big\vert_{eff}$	Effective shear stresses
σ	Thermal expansion coefficient based on density ratio
σ_1	Thermal expansion coefficient based on temperature ratio
β	Zel'dovich number
γ	Specific heat ratio
ε	Dissipation rate of turbulent kinetic energy (m^2/s^3)
ε_{cr}	Critical dissipation rate (m^2/s^3)
$\mathfrak{s}$	Standard deviation of the log-normal distribution of ε
μ	Dynamic viscosity
χ	Thermal diffusivity coefficient
ϕ	Equivalence ratio
ϕ_1	Air/fuel equivalence ratio
Δ	LES filter width or grid size
β_1	Temperature exponent for laminar burning velocity
β_2	Pressure exponent for laminar burning velocity
δ_{th}	Thermal laminar flame thickness

I_{ij}	Kronecker delta function
δ_z	Zel'dovich laminar flame thickness
η	Inner cut-off length scale
$\in$	Pressure exponent for laminar burning velocity under adiabatic compression
ω	Dispersion relation growth rate for planar flame
ω_1	Dispersion relation growth rate for spherical flame
λ_{min}	Instability inner cut-off wavelength
λ_{eff}	Turbulence-induced effective instabilities inner cut-off length scale
λ_{max}	Instability outer cut-off wavelength
α	Stretch rate

Subscripts

CJ	Chapman-Jouguet
$ign, initial$	Ignition time
Δ	Sub-grid scale
cr	Critical
E	Energy
GI	Gibson length scale
KO	Kolmogorov scale
f	Flame
Cf	Coherent fine scale eddy diameter
N	Neumann state after an inner shock
ij	Indices with values of 1, 2, and 3
i	Index with values of 1, 2, and 3
j	Index with values of 1, 2, and 3

s	Species index with values of 1, 2, and 3
n	Species index with values of 1, 2, and 3
ign	Induction time
sp	Spontaneous
eff	Effective
tur	Turbulent
ins	Instability
FU	Fureby
HA	Hawkes
CK	Chakraborty
CH	Charlette
MU	Muppala
AN	Angelberger
WE	Weller
CO	Colin
PI	Pitsch
KA	Katragadda
SH	Inner cut-off length scale of Shim
NO	North & Santavicca
Mb	Markstein length defined with respect to the burned gas side
a	Activation
u	Unburned
b	Burned
ref	Reference
res	Resolved

0	Reference to initial condition
z	Zel'dovich
L	Limiting component
H_2	Hydrogen
O_2	Oxygen
$initial$	Initial condition
c	Control volume cell

Superscripts

$\sim$	Favre filtering
$\bar{}$	Reynolds filtering
$''$	Fluctuation
$\hat{}$	Normalized

List of Abbreviations

DDT	Deflagration-to-detonation transition
CFD	Computational fluid dynamics
LES	Large eddy simulation
RANS	Reynolds average Navier-Stokes equations
DNS	Direct numerical simulation
SGS	Sub-grid scale
CEA	The French alternative energies and atomic energy commission
FzK	Today part of Karlsruhe Institute of Technology
Gexcon	Fire and explosion consultants
NH	Norsk Hydro is a Norwegian aluminium and renewable energy company

JRC	Joint research centre at the European Commission
TNO	Netherlands organisation for applied scientific research
UU	Ulster University
CFL	Courant–Friedrichs–Lewy number
Air Liquide	Industrial gases company
APSYS	Risk engineering company
Fluidyn	Consultant company
ODZ	Consultant company
BML	Bray–Moss–Libby combustion model
CPU	Central processing unit
SOTA	State-of-the-art
DL	Darrieus-Landau instability
TD	Thermo-diffusive instability
rms	Root mean square
CJ	Chapman–Jouget
CLEM-LES	Compressible linear eddy model for large eddy simulation
Hexa	Hexahedral
Tetra	Tetrahedral
AUSM	Advection upstream splitting method
RT	Rayleigh-Taylor instability
RM	Richtmyer-Meshkov instability
AMR	Adaptive mesh refinement

LIST OF TABLES

LIST OF FIGURES

CHAPTER 1. INTRODUCTION

1.1 Introduction

Hydrogen is a green energy carrier, which has a wide range of flammability. It is an alternative candidate to replace the fossil fuel. It could be used directly as in the fuel cells or it could be blended with another fuel and use inside the internal combustion engines. Due to high diffusivity of the hydrogen, there is a risk of its release during any stage from its production, passing through its transport, and finally during its fuelling and usage. The release of hydrogen and mixing with the surrounding air produces highly reactive mixture. This reactive mixture could be ignited by a small energy source like a spark. This ignition produces deflagration wave, which could be propagated in a velocity in the order of one m/s to tens of m/s due to flame acceleration and the increase of the flame surface area with propagation. The deflagration wave pushes the quiescent flow in front of the flame. Hence, if the flow passes through obstacles, turbulence is generated, and the propagation velocity of the reactive wave increases farther to be in the order of hundreds of m/s. If the flame accelerated farther, there could be a probability of the transition to detonation though a mechanism called deflagration-to-detonation transition (DDT). Detonation wave is propagated in much higher velocity in the order of 2000 m/s, for a stoichiometric hydrogen-air mixture at the atmospheric pressure and temperature of 293 K. This propagation wave produces high overpressure in the order of tens of bar, which produces risk for lives and damage to the buildings.

1.2 Motivation

Different numerical studies were performed for deflagration and DDT. A Brief review of the numerical techniques of the state-of-the-art (SOTA) of deflagration and DDT are shown in the literature review chapter. Most of the mentioned studies that simulated DDT and detonation propagation were 2D. The main difference between the mentioned models is in the chosen method to model the species and the heat release rate. The simulations that have used chemistry, thickened flame approach, and linear eddy model have used fine grid sizes to resolve the flame thickness, which would require high computational resources. They have great ability to disclose detailed physics of the

initiation of DDT and the propagation of detonation. On the other hand, most of the models that were based on modelling the chemical reaction rate, weather using the flame wrinkling factor or the turbulent burning velocity closure, have used larger grid sizes. Their grid size could be larger than the flame thickness for some cases. Therefore, modelling DDT and detonation propagation based on using the flame wrinkling factor is a promising approach for large-scale geometries. This makes it more suitable for the industry scales.

DDT study in (Karanam, Sharma and Ganju, 2018) has shown that different flame wrinkling factors predicted closer flame propagation velocities in the deflagration regime. In the detonation regime, there was a slight difference in predicting the position of the initiation of the detonation and the peak velocity. At the same time, the vented deflagration study in (Di Sarli, Di Benedetto and Russo, 2010) has shown that different sub-grid scale (SGS) turbulent wrinkling models have provided different pressure prediction for the same configuration. Hence, the parameters of the tested models had be tuned for better prediction. The vented deflagration study in (Vermorel, Quillatre and Poinsot, 2017) was based on the thickened flame approach, which has incorporated two algebraic turbulent wrinkling models. It has also shown that, rescale the configuration would require tuning the wrinkling models' parameters for better prediction.

Therefore, there is a need to develop a reliable flame wrinkling model to predict flame deflagration and detonation without the need to tune the model parameters with the scale or the configuration. The model should use large grid sizes to be suitable for simulating industrial scales. It should predict the global flame parameters like flame propagation velocity and the overpressure in a reasonable running time.

1.3 Rationale in developing the proposed numerical model

Initiation of detonation through DDT involves different flame acceleration mechanisms. The flame surface cracks due to hydrodynamic & thermo-diffusive instabilities and cellular structure appears on the hydrogen flame surface, starting from an early propagation with the increase of the flame size. It leads to an increase in the flame burning rate due to the increase in the flame surface area. The interaction of the flame with turbulence leads to farther increase in the burning rate. The corrugation due to turbulence could be at scales different from the instabilities. There is another probability

of decreasing the burning rate due to excessive stretching of the flame, which could lead to local or global flame quenching. The formation of compression waves and shocks changes the unburned properties, which changes the burning rate. The interaction of the compression waves and the shocks with the flame add another change to the burning rate. Hence, for a better modelling of the burning rate the effect of these mechanisms or the dominant ones and their interactions should be considered.

1.4 Aims and objectives

The current study aims to develop a closure for the heat release rate of the hydrogen-air deflagration and detonation using flame wrinkling modelling concept in the framework of large eddy simulation (LES). It should use large grid sizes, so that it would be suitable in the future to be used for large industrial cases. In addition to that, a modelling for flame-generated turbulence closure should be included.

The objectives of the current study are as follows:

1- Developing a flame wrinkling model for the cellular flame propagation due to the hydrodynamic & thermo-diffusive instabilities.

2- Developing a flame wrinkling model due to flame-turbulence interaction valid for the corrugated flamelets and the thin reaction zones regimes in the combustion diagram.

3- Developing a model for the turbulence-hydrodynamic & thermo-diffusive instabilities interaction.

4- Implementing a flame quenching factor under excessive stretching of the flame that could decrease the heat release rate.

5- Implementing an algebraic closure for the generated turbulence due to heat release.

1.5 Thesis structure

The thesis is structured as follows:

Chapter 1 includes the project background, the motivation, the rationale of developing the proposed numerical model, and the aims and objectives of the current study.

Chapter 2 includes different topics from the literature related to the SOTA in modelling deflagration and DDT, deflagration and detonation waves, propagation velocity of the deflagration wave, the acceleration mechanisms, propagation of the turbulent deflagration wave, the interaction between turbulence and flame instabilities, propagation of the detonation wave, and flame-generated turbulence modelling.

Chapter 3 includes the reactive governing equations and the proposed models for flame wrinkling factor, turbulent burning velocity, and heat release rate.

Chapter 4 includes numerical simulation of DDT experiment in a channel using the proposed model.

Chapter 5 includes numerical simulation of large-scale deflagration experiment in an open atmosphere using the proposed model.

Chapter 6 includes numerical simulation of vented explosion experiment using the proposed model.

Chapter 7 includes the thesis conclusions and future recommendations.

CHAPTER 2. LITERATURE REVIEW

2.1 Introduction

This chapter presents a brief review of the SOTA in modelling deflagration and DDT. The rest of the chapter describes the basic elements and definitions required to understand the physics involved in deflagration and detonation propagation. The focus is toward developing flame wrinkling model therefore, the necessary elements are reviewed. These elements include the laminar burning velocity, the effects of initial pressure and temperature, the acceleration mechanisms due to intrinsic instabilities, the flame-turbulence interaction, the turbulence-instabilities interaction, the definition of the turbulent burning velocity, and the heat release rate. At the end, a brief review of another topic related to flame-generated turbulence is presented.

2.2 A brief review of the SOTA in modelling deflagration and DDT

Numerical simulation of deflagration and DDT would require solving the flame front over a computational grid. Owing to the small thickness of the flame front, a large computational cost would be required to resolve the species mass fraction equations for large scale geometries, even with the use of a single step chemistry. Therefore, different numerical techniques have been used to tackle this problem in the LES for the filtered mass fraction equations, as for example the filtered progress variable equation, the thickened flame approach, and the linear eddy model.

The progress variable is a scalar that represents flame front with a value equals to zero in the unburned gas and a value equals to one in the burned gas. It could be represented in terms of a selected species mass fraction. The chemical reaction rate of the filtered progress variable equation could be presented using different approaches as for example a flame wrinkling factor, a related flame surface density, a turbulent burning velocity closure, and an eddy dissipation model. The thickened flame approach (Colin *et al.*, 2000; Charlette, Meneveau and Veynante, 2002) is based on increasing the laminar flame thickness by increasing the diffusion coefficient of the mass fraction equation. Hence, the flame could be resolved over a coarser computational grid compared to the original flame thickness. At the same time, the chemical reaction rate is decreased by the

same order so that, the laminar burning velocity does not change. Thickening the flame would decrease the flame wrinkling. Therefore, an efficiency function that includes a wrinkling factor is used to cure this effect. The linear eddy model approach is based on using two coupled grids, super-grid for solving the flow and 1D sub-grid for solving the reaction (Menon, 2015a). Based on these numerical techniques, different studies were performed to study deflagration and DDT.

2.2.1 A brief review of the simulations of deflagration

Different numerical techniques have used to simulate deflagration problems. A brief review of these techniques is as follows and a summary of the key features of some of these studies is presented in Table 2.1:

1- Di Sarli et al. (Di Sarli, Di Benedetto and Russo, 2010) have used different SGS turbulent wrinkling models to close the filtered chemical reaction rate of the filtered progress variable equation for simulating vented deflagration chamber. They found that not all the models were able to correctly produce the deflagration pressure. Therefore, the model's coefficients needed to be tuned. Hence, they could produce comparable prediction with the experiment.

2- Bauwens et al. (Bauwens, Chaffee and Dorofeev, 2011) have used SGS wrinkling factors, which included the effects of Darrieus-Landau instability, turbulence, and Rayleight-Taylor instability. These wrinkling factors were used to close the filtered chemical reaction rate of the filtered regress variable equation, a complementary of the progress variable equation, for simulating vented deflagration chamber.

3- Wen et al. (Wen *et al.*, 2012) have compared the usage of SGS turbulent wrinkling factor, turbulent burning velocity closure, and an eddy dissipation model to close the filtered chemical reaction rate of the filtered progress variable equation. They simulated vented deflagration chamber. In their comparison, the chosen turbulent wrinkling factor predicted better matching with the experiment.

4- Gubba et al. (Gubba *et al.*, 2009) have used an algebraic flame surface density model based on the fractal concept to close the filtered chemical reaction rate of the filtered progress variable equation. They have simulated vented deflagration chamber by this model.

5- A LES model was developed at Ulster University for the filtered chemical reaction rate of the filtered progress variable equation based on the turbulent burning velocity closure (Molkov, 2012). The model contains five sub-models: 1- the effect of the pressure and temperature of the unburned gas on the laminar burning velocity 2- the effect of the approaching turbulence 3- the effect of the flame-generated turbulence 4- the effect of the preferential diffusion that was modelled using the leading point concept 5- fractal increase of the flame surface area.

6- Vermorel et al. (Vermorel, Quillatre and Poinsot, 2017) have used the thickened flame approach with two alternative algebraic turbulent wrinkling models to study deflagration in different scales of vented chambers. They found that the parameters of the algebraic turbulent wrinkling models were required to be tuned with the change in the chamber size.

Table 2.1: Summary of the key features of some of the simulations of deflagration.

Reference	Numerical technique	Configuration	Mesh topology
(Di Sarli, Di Benedetto and Russo, 2010)	LES – SGS turbulent wrinkling models	Vented chamber with a total volume of 0.01125 m^3 – contained internal obstacles	The mesh minimum cell size was 2 mm close to the walls
(Bauwens, Chaffee and Dorofeev, 2011)	LES – SGS wrinkling factors for Darrieus-Landau instability, turbulence, and Rayleight-Taylor instability	Vented chamber with a total volume of 63.48 m^3 – with no internal obstacles	3D – total mesh was 1 M cells including the external volume – minimum cell size was 5 cm inside the chamber

Continuation of Table 2.1.

(Wen *et al.*, 2012)	LES – alternative use of 1- SGS turbulent wrinkling model 2- turbulent burning velocity closure 3- eddy dissipation model	Vented chamber with a total volume of 0.01125 m^3 – contained internal obstacles	3D mesh – total mesh was 880 k cells including the external volume – minimum cell size was 2.5 mm – hexahedral elements inside the chamber and tetrahedral elements outside the chamber
(Gubba *et al.*, 2009)	LES – algebraic flame surface density based on fractal concept – CFL $=$ 0.5 – time step is less than 0.3 ms	Vented chamber with a total volume of 0.000625 m^3 – contained internal obstacles	3D mesh including an external volume
(Vermorel, Quillatre and Poinsot, 2017)	LES – thickened flame approach – $CFL = 0.7$	Vented chamber with three total volumes: 1- 0.000625 m^3 2- 0.135 m^3 3- 9.07924 m^3 – contained internal obstacles	Minimum cell size was from 0.5 to 12.2 mm, based on the configuration, i.e. 5 points were used inside the flame for some configuration – total mesh was 20 M tetrahedral elements including a plenum

2.2.2 A brief review of the simulations of DDT and detonation propagation

Different numerical techniques have used to simulate DDT and detonation propagation. A brief review of these techniques is as follows and a summary of the key features of these studies is presented in Table 2.2:

1- A single step Arrhenius model was used to close the chemical reaction rate in (Gamezo, Ogawa and Oran, 2007; C. J. Wang and Wen, 2017).

2- Khodadadi Azadboni et al. (Khodadadi Azadboni, Heidari and Wen, 2018; Khodadadi Azadboni *et al.*, 2019) have used monotone-integrated LES turbulence closure with detailed reaction mechanism for closing the chemical reaction rates.

3- Dounia et al. (Dounia *et al.*, 2019) have used alternatively single step Arrhenius model and multistep chemistry. They have found that DDT were initialized at different positions using the two closures. Using the single step model, DDT was initialized by the gradient mechanism in the unburned gas. Using the multistep chemistry, it was initialized in the flame brush due to pressure pulse amplification by the shock which crossed the flame.

4- Khodadadi Azadboni et al. (Azadboni *et al.*, 2017) have used LES turbulence closure with flame wrinkling combustion model of Weller for closing the chemical reaction rate.

5- Ettner et al. (Ettner, Vollmer and Sattelmayer, 2014) have used simultaneously two chemical reaction rates for the progress variable equation in the Reynolds average Navier-Stokes (RANS) formulation. The first was modelled using a transport equation for the flame wrinkling factor and a quenching factor. The second was activated if the solution of a transport equation for the delay time, based on the shock auto-ignition concept, was equated to unity.

6- Malik et al. (Malik *et al.*, 2016) have used simultaneously two chemical reaction rates for the progress variable equation in LES formulation. The first was modelled using a flame wrinkling factor and a quenching factor. The second was activated based on the shock auto-ignition concept incorporating the delay time.

7- Karanam et al. (Karanam, Sharma and Ganju, 2018) have used simultaneously two chemical reaction rates for the progress variable equation in RANS formulation. The first was modelled using a transport equation for the flame wrinkling factor and a quenching factor. The second was activated if the solution of a transport equation for the normalized induction delay time was equated to unity.

8- Gaathaug et al. (Gaathaug, Vaagsaether and Bjerketvedt, 2012) have used Euler equations to study DDT. They have modelled the chemical reaction rate of the regress variable equation as the maximum between two chemical reaction rates: the first was based on turbulent burning velocity closure and the second was based on two-step chemical kinetics.

9- Emami et al. (Emami *et al.*, 2015) have used full tabulated chemistry for the chemical reaction rates with the thickened flame approach in LES formulation.

10- Maxwell et al. (Maxwell *et al.*, 2015) have used the compressible linear eddy model for large eddy simulation (CLEM-LES) to simulate the propagation of 2D detonation wave at low pressure.

Table 2.2: Summary of the key features of the simulations of DDT and detonation propagation.

Reference	Numerical technique	Configuration	Mesh topology
(Gamezo, Ogawa and Oran, 2007)	Navier-Stokes – single step Arrhenius model	Baffled channel	2D: from mesh independence study, the finer mesh had a minimum grid size of 19.53125 μm, approximately 10 points per hrl 3D: minimum gird size of 78.125 μm, approximately 2.5 points per hrl

Continuation of Table 2.2.

(C.J. Wang and Wen, 2017)	Navier-Stokes – single step Arrhenius model	Rectangular channel with baffled part and smooth part	Minimum resolution was close to 1/32 of hrl
(Khodadadi Azadboni, Heidari and Wen, 2018; Khodadadi Azadboni *et al.*, 2019)	Monotone-integrated LES – detailed reaction mechanism	Rectangular channel with baffled part and smooth part	Minimum resolution based on adaptive mesh refinement (AMR): 30 points per hrl i.e. about 10 μm
(Dounia *et al.*, 2019)	Navier-Stokes – single step Arrhenius model or multistep chemistry	Rectangular channel with baffled part and smooth part	2D – multiple meshes with a resolution of 20 μm inside the flame and in the surrounding region & 120 μm else
(Azadboni *et al.*, 2017)	LES – flame wrinkling combustion model based on the Weller's formulation	Rectangular channel with baffled part and smooth part	2D – minimum resolution based on AMR: 30 points per hrl i.e. about 10 μm

Continuation of Table 2.2.

(Ettner, Vollmer and Sattelmayer, 2014)	RANS – transport equation for the flame wrinkling factor – Quenching factor – shock auto-ignition using a transport equation for the delay time	Rectangular channel with baffled part and smooth part	2D – uniform and rectangular mesh with a grid size of 2 mm
(Malik *et al.*, 2016)	LES with SGS of turbulent kinetic energy – flame wrinkling factor – Quenching factor – shock auto-ignition incorporating the delay time	Pipe with a turbulence generator part for initiation of detonation	2D – hexahedral mesh – a grid size of 2 mm and a total mesh size of 382500 cells
(Karanam, Sharma and Ganju, 2018)	RANS $(k-Omega)$ SST – transport equation for the flame wrinkling factor – Quenching factor – a transport equation for the normalized induction delay time – $CFL < 0.5$	Rectangular channel with baffled part and smooth part	2D – uniform mesh with hexahedral elements with a size of 4 mm

Continuation of Table 2.2.

(Gaathaug, Vaagsaether and Bjerketvedt, 2012)	Euler equations – chemical reaction rate was the maximum between two chemical reaction rates, which were based on turbulent burning velocity and two-step chemical kinetics	Square channel with one obstacle	2D mesh with a grid size of 0.5 mm and a total mesh size of 1.2 M cells
(Emami *et al.*, 2015)	LES – thickened flame approach – full tabulated chemistry	Baffled channel	2D uniform mesh – from mesh independence study, the finer mesh had a grid size of 62.5 μm i.e. 5-6 points inside the flame thickness
(Maxwell *et al.*, 2015)	CLEM-LES – single step Arrhenius law	Unobstructed narrow channel	2D mesh – super-grid size was 1/32 of hrl i.e. 0.3025 mm – sub-grid had 24 nodes for every super-grid cell i.e. 0.012604 mm

hrl is the half reaction length, which is defined as the distance between the shock and the progress variable with the value of 0.5 (Matalon, 2017).

2.3 Propagation of combustion wave

Deflagration and detonation are governed by conservation laws of mass, momentum, and energy in addition to the equation of state. Therefore, the solution of a stationary one-dimensional combustion wave as shown in Fig. 2.1 (Ciccarelli and Dorofeev, 2008) could be used to understand the basic features of deflagration and detonation. State (1) in the Fig. 2.1 is far before the combustion wave and state (2) is far after the combustion wave. The solution of the mass and momentum equations provides a thermodynamic relation, which is called the Rayleigh line or (Michelson line), while the solution of the mass and energy equations provides a thermodynamic relation, which is called the Hugoniot curve.

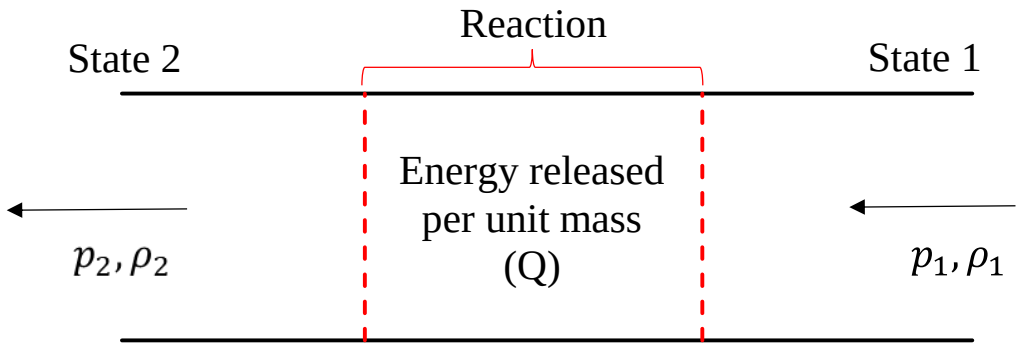

Figure 2.1: Schematic of a stationary one-dimensional combustion wave (Ciccarelli and Dorofeev, 2008).

p and ρ are pressure and density, respectively.

State (2) is obtained as the intersection of the Rayleigh line and the Hugoniot curve, as shown in Fig. 2.2 (Ciccarelli and Dorofeev, 2008; Matalon, 2017). The Rayleigh line has two branches, which produces two possible solutions of the combustion wave at state (2): deflagration or detonation. The intersections just below point (P) to point (C) represent the deflagration solutions, while the interactions between points (J) and (S) represent the detonation solutions for the case of a leading shock ignites the unburned mixture. The solution between points (V) and (P) is physically impossible. Points (C) and (J) represent the tangent to the Hugoniot curve, which are called the Chapman–Jouget (CJ) states. The only determined velocities at state (2) from the conservation equations are the CJ states, which have the minimum detonation velocity (u_{CJ}) at point (J) and the maximum deflagration velocity at point (C). Chapman-Jouget detonation velocity is

defined in terms of the energy released per unit mass (Q) and the specific heat ratio of burned gas (γ_b), as shown in Eq. (2.1) (Ciccarelli and Dorofeev, 2008) for a high energy release.

$$u_{CJ} \cong \sqrt{2\,Q\,(\gamma_b + 1)} \tag{2.1}$$

Deflagration solution is not physically possible at point (P) and for the points to the right of point (C). The first possible solution is the point just to the right of point (P), which has a small velocity. Velocity of state (2) increases along the branch (P)–(C) until it reaches its maximum possible value at point (C), which is a sonic velocity.

On the detonation branch, the solution at point (S) is called strong detonation (overdriven detonation). Velocity of state (2) at point (S) is subsonic while it increases along the branch (S)–(J) to reach a sonic velocity at point (J).

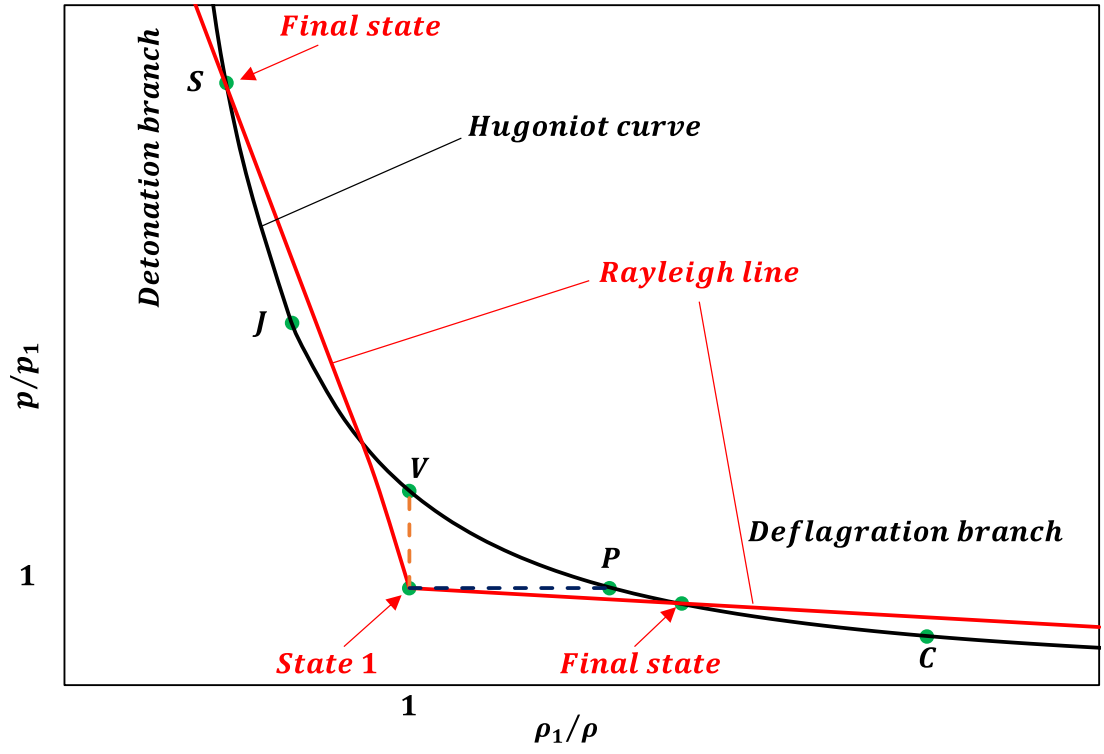

Figure 2.2: Schematic of the Rayleigh line and the Hugoniot curve of combustion wave (Ciccarelli and Dorofeev, 2008; Matalon, 2017).

The main differences between state (2) of the deflagration and the detonation waves are as follows: state (2) of the deflagration is expanded with an increase in the

velocity compared to state (1), while state (2) of the detonation is compressed with a drop in the velocity compared to state (1).

2.4 Propagation of deflagration wave

Deflagration wave is defined as a subsonic front that releases energy and propagates under the effect of thermal conduction (Modestov *et al.*, 2008), where compressibility effects could be neglected due to the small velocities in both the unburned and burned gases. If there is no initial turbulence in the unburned mixture, the weak ignition initiates laminar flame.

2.4.1 Planar laminar flame structure

A laminar flame could be defined as a permeable surface separating two gases with different properties, which are the unburned and burned gases. The continuation of diffusing the unburned gas across the flame to the burned side, sustains the generation of heat and provides flame propagation.

A schematic of stationary laminar flame is shown in Fig. 2.3 (Ciccarelli and Dorofeev, 2008). Laminar flame is constructed of two zones: the preheated zone with large thickness and the reaction zone with tiny thickness in the order of one tenth of the preheated zone thickness (Peters, 1997). In the preheated zone, the unburned gas temperature (T_u) increases due to thermal diffusivity while mass fraction (Y) of the reactants does not change. In the reaction zone the reactants are consumed, and chemical reaction occurs starting from a temperature that is in the order of the adiabatic flame temperature (T_b). Pressure across the laminar flame is nearly constant.

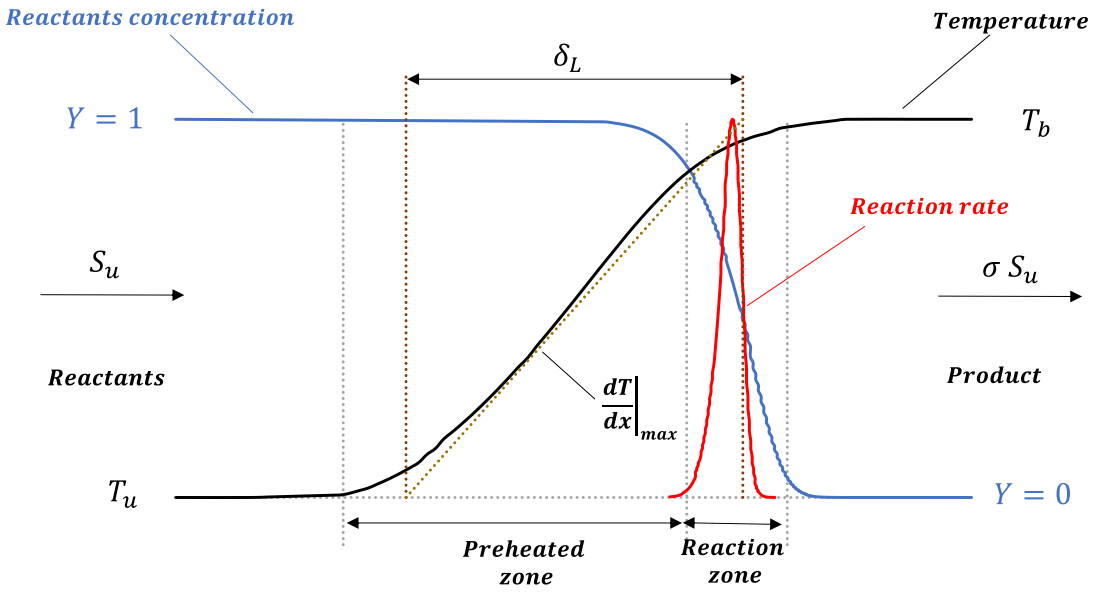

Figure 2.3: A schematic of stationary planar laminar flame (Ciccarelli and Dorofeev, 2008).

The velocity of the incoming reactants with respect to the stationary laminar flame is called the laminar burning velocity (S_u). It is a characterized velocity of the unburned mixture, which depends on the composition and the initial temperature and pressure. The burned gas exits the reaction zone with a velocity equal to ($\sigma\ S_u$). σ is the thermal expansion coefficient that is defined as the ratio between the unburned density (ρ_u) to the burned density (ρ_b) as shown in Eq. (2.2) (Matalon, 2009).

$$\sigma = \frac{\rho_u}{\rho_b} \tag{2.2}$$

The total flame thickness is in the order of preheated zone thickness. Therefore, some references relate the estimated flame thickness to the preheated zone thickness, while other references related it to the total flame thickness. There are different ways to estimate the flame thickness. An estimate of the preheated zone thickness could be done using the thermal flame thickness (δ_{th}), which is based on the maximum of the temperature gradient as shown in Eq. (2.3) (Kim *et al.*, 2015) and in Fig. 2.3.

$$\delta_{th} = \frac{T_b - T_u}{\left.\frac{dT}{dx}\right|_{max}} \tag{2.3}$$

$dT/dx|_{max}$ is the maximum gradient of the temperature (T). x is a spatial coordinate. Another estimate to the preheated zone thickness is based on the Zel'dovich flame thickness (δ_z) that is defined as the ratio between the unburned mixture thermal diffusivity (χ_u) and the laminar burning velocity as shown in Eq. (2.4) (Addabbo, Bechtold and Matalon, 2002). δ_z could be an order of magnitude smaller than the actual preheated zone thickness (Modestov *et al.*, 2008). Despite of that, it is extensively used as a representative length in the modelling. The reaction zone thickness is estimated as the preheated zone thickness divided by the Zel'dovich number (β). β is defined in Eq. (2.6) (Matalon, 2009), which could be in the order of 10 for some mixtures.

$$\delta_z = \frac{\chi_u}{S_u} = \frac{K_u}{\rho_u \, Cp_u \, S_u} \tag{2.4}$$

The unburned mixture thermal diffusivity is defined in Eq. (2.5) (Kim *et al.*, 2015), presented using the unburned properties.

$$\chi_u = \frac{K_u}{\rho_u \, Cp_u} \tag{2.5}$$

K_u is the unburned thermal conductivity and Cp_u is the unburned specific heat.

$$\beta = E_a \frac{T_b - T_u}{\check{R} T_b^2} \tag{2.6}$$

$\check{R}$ and E_a are the universal gas constant and the activation energy, respectively.

2.4.2 Unstretched laminar burning velocity at the reference condition (S_{u0})

Laminar burning velocity depends on the concentration, pressure, and temperature. Therefore, a reference value is defined at a standard pressure (p_0) and temperature (T_0) for a free stretch condition (S_{u0}). Usually the standard pressure is taken as the atmospheric pressure and the standard temperature is taken as 298 K, the concept

of stretch will be discussed later. S_{u0} is obtained either using experiments or through chemical kinetics. There are different measurements and modelling in the literature. Figure 2.4 provides the unstretched laminar burning velocity of the hydrogen-air mixture from experiments and chemical kinetics close to the standard atmospheric pressure and temperature of 298 K, from the collection in (Alekseev, Christensen and Konnov, 2015). S_{u0} follows a parabolic change with the hydrogen concentration. The maximum burning velocity is in the rich mixture. All the experiments and the chemical kinetics models correctly predict the same trend, but there is scatter in the data. Aung and Kwon reported their experimental uncertainties, which were less than 12% and 10% respectively.

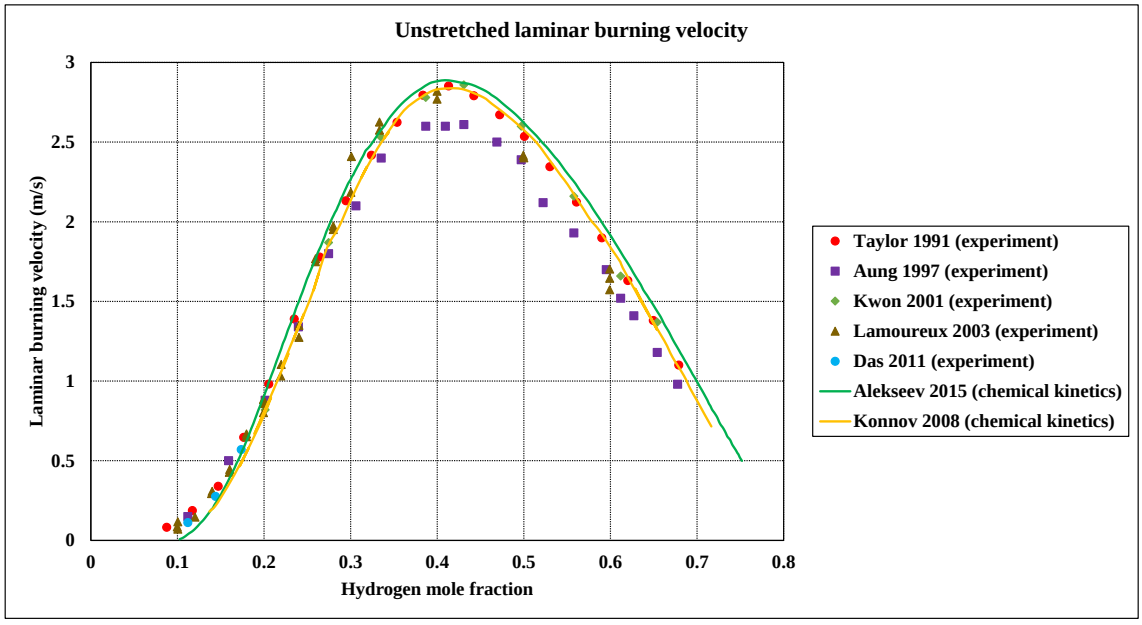

Figure 2.4: Unstretched laminar burning velocity of hydrogen-air mixture against hydrogen mole fraction close to the standard atmospheric pressure and temperature of 298 K (Taylor, 1991; Aung, Hassan and Faeth, 1997; Kwon and Faeth, 2001; Lamoureux, Djebaïli-Chaumeix and Paillard, 2003; Konnov, 2008; Das, Kumar and Sung, 2011; Alekseev, Christensen and Konnov, 2015).

2.4.3 Effects of the pressure and temperature of the unburned gas on the laminar burning velocity (S_u)

The change in the initial pressure and temperature of the unburned gas would change the laminar burning velocity from S_{u0}. The dependence of the burning velocity on the initial pressure and temperature of the unburned gas is characterized using experiments and chemical kinetics simulations. One of the common forms to describe this dependence is by using a power law relation, as shown in Eq. (2.7) (Dahoe, 2005; Jordan,

2007; Hu *et al.*, 2009; Molkov, 2012; Ettner, Vollmer and Sattelmayer, 2014). This relation provides S_u due to independent changes in the pressure and temperature.

$$S_u = S_{u0}(T_0 , p_0)\left(\frac{T}{T_0}\right)^{\beta_1}\left(\frac{p}{p_0}\right)^{\beta_2} \tag{2.7}$$

β_1 and β_2 are temperature and pressure exponents, respectively.

The pressure and temperature of the unburned gas could be changed according to an adiabatic relation, as shown in Eq. (2.8) (Dahoe, 2005; Molkov, 2012), if it assumed that the unburned gas is subject to an adiabatic compression and the combustion is adiabatic, which could occur for a spherical flame in a closed vessel (Jordan, 2007). This assumption provides a method to calculate the change in the temperature of the unburned gas with flame propagation.

$$\left(\frac{T}{T_0}\right) = \left(\frac{p}{p_0}\right)^{\frac{\gamma_u - 1}{\gamma_u}} \tag{2.8}$$

γ_u is the unburned gas specific heat ratio.

By replacing the temperature in Eq. (2.7) by the corresponding value from the adiabatic relation in Eq. (2.8), S_u could be defined in terms of the pressure only under an adiabatic compression of the burned gas, as shown in Eq. (2.9) (Dahoe, 2005; Jordan, 2007; Molkov, 2012).

$$S_u = S_{u0}(T_0 , p_0)\left(\frac{p}{p_0}\right)^{\beta_2 + \frac{\gamma_u - 1}{\gamma_u}\beta_1} = S_{u0}(T_0 , p_0)\left(\frac{p}{p_0}\right)^{\in} \tag{2.9}$$

$\in$ is a pressure exponent under adiabatic compression, which is defined in Eq. (2.10) (Dahoe, 2005; Jordan, 2007; Molkov, 2012).

$$\in = \beta_2 + \frac{\gamma_u - 1}{\gamma_u}\beta_1 \tag{2.10}$$

Equation (2.9) represents an adiabatic compression of the unburned mixture starting from the reference values p_0 and T_0. In case, the initial temperature ($T_{initial}$) is

different from the reference value, a correction to S_{u0} was used at Ulster University's deflagration UDF before applying the adiabatic compression as shown in Eq. (2.11).

$$S_u = S_{u0}(T_0, p_0) \left(\frac{T_{initial}}{T_0}\right)^{\beta_1} \left(\frac{p}{p_0}\right)^{\in} \quad (2.11)$$

It is difficult to conduct experiments to measure the unstretched laminar burning velocity at high pressure due to instabilities of the hydrogen (Verhelst *et al.*, 2011; Ravi and Petersen, 2012), which will be clarified in the next section. There are different models in the literature for the temperature and pressure exponents, which are either based on experiments or chemical kinetics, a summary of these models is as follows:

1- Dahoe (Dahoe, 2005) proposed constant values of 1.4 and 0.194 for β_1 and β_2 respectively, under the atmospheric pressure and temperature of 291 K, for the stoichiometric hydrogen-air mixture. The exponents values were provided from an analysis of a previous experimental data. The range of applicability was not stated explicitly but from Fig. 5 in the cited paper, it is approximately for the pressure ranged from 0.5 bar to 5.5 bar and the temperature ranged from 287.5 K to 362.5 K.

2- Ettner et al. (Ettner, Vollmer and Sattelmayer, 2014) used for their DDT simulations constant values for β_1 and β_2 of 1.75 and -0.2 respectively.

3- Jordan and Molkov (Jordan, 2007; Molkov, 2012) provided values for β_1 and β_2 from previous experimental work for various concentrations, as shown in Table 2.3. β_2 was obtained under the pressure range from 0.25 atm to 1 atm. There is a week correlation between β_2 and the hydrogen concentration, which was previously mentioned in (Dahoe, 2005).

Table 2.3: β_1 and β_2 for the laminar burning velocity (Jordan, 2007; Molkov, 2012).

X_{H_2}	0.15	0.2	0.25	0.295	0.35	0.4	0.43	0.45	0.5	0.55	0.6	0.65	0.7
β_1	2.6[1]	2.2[1]	1.9[1]	1.7	1.5[1]	1.45[1]	1.4	1.4[1]	1.45[1]	1.5[1]	1.7	1.9[1]	2.2[1]
β_2	-0.05	0.01	0.05	0.09	0.1	0.1	0.1	0.1	0.1	0.08	0.06	0.03	0

[1] β_1 are interpolated or extrapolated.

4- Hu et al. (Hu *et al.*, 2009) provided a correlation for the laminar burning velocity for the stoichiometric hydrogen-air mixture, by fitting chemical kinetics

simulations data, as shown in Eq. (2.12). The temperature exponent β_1 was found to have a linear increase with the temperature under the range from 303 K to 950 K, as shown in Eq. (2.13) (Hu *et al.*, 2009). β_2 was found to have a descending correlation with the pressure under the range from 1 atm to 80 atm, as shown in Eq. (2.14) (Hu *et al.*, 2009). The correlation has discrepancies with the chemical kinetics data at high temperature.

$$S_u = 2.406 \left(\frac{T}{303}\right)^{\beta_1} \left(\frac{p}{0.1}\right)^{\beta_2} \qquad (m/s), \quad T(K), \quad p\ (M\ Pa) \tag{2.12}$$

$$\beta_1 = 1.319 + (8.019 \times 10^{-4})\ T \qquad , \quad 303\ K \leq T \leq 950\ K \tag{2.13}$$

$$\beta_2 = -0.406 + 0.374\ e^{\left(\frac{-p}{1.451}\right)} \qquad , \quad 0.1\ MPa\ \leq p \leq 8.0\ MPa \tag{2.14}$$

5- Milton and Keck (Milton and Keck, 1984) measured laminar burning velocity of the hydrogen-air mixture using combustion pump. They used the expression shown in Eq. (2.15) for fitting five individual experimental data with a tolerance of $\pm 5\%$ under the pressure range from 1 atm to close to 7 atm and the corresponding temperature rage due to isentropic compression, which was from 298 K to close to 515 K.

$$log(S_u) = log(217) + 1.26 \times\ log\left(\frac{T}{298}\right) + 0.26 \times\ log(p)$$
$$1\ atm \leq p \leq 7\ atm \quad , \quad 298\ K \leq T \leq close\ to\ 515\ K \quad , \quad S_u(cm/s) \tag{2.15}$$

6- Ravi and Petersen (Ravi and Petersen, 2012) proposed correlations for the laminar burning velocity, as shown in Eq. (2.16), which was constructed from chemical kinetics data under the pressure, temperature, and equivalence ratio (ϕ) ranges from 1 atm to 30 atm, 270 K to 620 K, and 0.5 to 5 respectively. The discrepancies between most of the predicted data from the correlation and the original chemical kinetics data were between $\pm$ 15%.

$$S_u = S_{u0}(\phi) \left(\frac{T}{500}\right)^{\beta_1} \left(\frac{p}{10}\right)^{\beta_2} \qquad (cm/s), \quad T(K), \quad p\ (atm) \tag{2.16}$$

$S_{u0}(\phi)$ is calculated from Eq. (2.17) (Ravi and Petersen, 2012), β_1 and β_2 are calculated from Eqs. (2.18) and (2.19) (Ravi and Petersen, 2012) respectively.

$$S_{u0}(\phi) = [168.3 - 1100.1 \times \phi + 2466 \times \phi^2 - 1449.2 \times \phi^3 + 267.6 \times \phi^4]$$
$$0.5 \leq \phi \leq 2$$
$$S_{u0}(\phi) = [856.7 - 158.8 \times \phi - 1.94 \times \phi^2 + 1.33 \times \phi^3]$$
$$2 \leq \phi \leq 5 \quad (2.17)$$

$$\beta_1 = 5.61 - 7.75 \times \phi + 5.54 \times \phi^2 - 1.61 \times \phi^3 + 0.151 \times \phi^4$$
$$0.5 \leq \phi \leq 2$$
$$\beta_1 = 1.3 + 0.275 \times \phi$$
$$2 \leq \phi \leq 5 \quad (2.18)$$

$$\beta_2 = -0.71 + 0.8 \times \phi - 0.25 \times \phi^2$$
$$0.5 \leq \phi \leq 2$$
$$\beta_2 = 0.075 - 0.072 \times \phi$$
$$2 \leq \phi \leq 5 \quad (2.19)$$

7- Verhelst et al. (Verhelst *et al.*, 2011) proposed a correlation in the form of Eq. (2.20) for the laminar burning velocity, based on detailed chemical kinetics. It covers the air/fuel equivalence ratio (ϕ_1), temperature, and pressure ranges from 0.2 to 3, 500 K to 900 K, and 5 bar to 45 bar respectively. The correlation predicted most of the original data within $\pm 20\%$, for the entire ranges.

$$S_u = S_{u0}(\phi_1, p) \left(\frac{T}{300}\right)^{\beta_1(\phi_1, p)} \quad (2.20)$$
$$0.2 \leq \phi_1 \leq 3\,, \quad 500\ K \leq T \leq 900\ K \quad , \quad p\ (bar) \quad , \quad S_u(cm/s)$$

$S_{u0}(\phi_1, p)$ and $\beta_1(\phi_1, p)$ are calculated from Eqs. (2.21) and (2.22) (Verhelst *et al.*, 2011) respectively.

$$S_{u0}(\phi_1, p) = exp\Big[7.505661 - 1.903711 \times \phi_1 + 0.0538084 \times p - 0.03936929 \times p \times \phi_1 + 0.01896873 \times \phi_1^2 + 0.000596468 \times p^2 - 0.03010525 \times \phi_1^2 \times p - 0.0003431092 \times \phi_1 \times p^2 + 0.0009023031 \times \phi_1^3 \times p - 0.00001556492 \times \phi_1 \times p^3 + 0.0008452404 \times \phi_1^2 \times p^2 - \frac{0.478534}{\phi_1} - \frac{0.03105883 \times p}{\phi_1}\Big] \quad (2.21)$$

$$\beta_1(\phi_1, p) = 0.584069 + 1.09788 \times \phi_1 - 0.03683272 \times p + 0.02454259 \times p \times \phi_1 + 0.104381 \times \phi_1^2 - 0.000411935 \times p^2 + 0.007621143 \times \phi_1^2 \times p + 0.000762759 \times \phi_1 \times p^2 - 0.000449838 \times \phi_1^2 \times p^2 + \frac{0.331465}{\phi_1} + \frac{0.02165434 \times p}{\phi_1} \quad (2.22)$$

8- Gerke et al. (Gerke *et al.*, 2010) proposed a correlation for the quasi laminar burning velocity which included the effects of stretch and hydrodynamic & thermo-diffusive instabilities as shown in Eq. (2.23). It was based on single-cylinder compression machine measurements for the equivalence ratio, temperature, and pressure ranges from 0.4 to 2.5, 350 K to 700 K, and 10 bar to 45 bar respectively. The partial balance of the instabilities, which could occur at turbulent flow, was not considered in the correlation.

$$S_u = S_{u0}(\phi) \left(\frac{T}{600}\right)^{\beta_1} \left(\frac{p}{20}\right)^{\beta_2} \qquad (m/s), \quad T(K), \quad p\ (bar) \qquad (2.23)$$

$S_{u0}(\phi)$ is calculated from Eq. (2.24) (Gerke *et al.*, 2010), β_1 and β_2 are calculated from Eqs. (2.25) and (2.26) (Gerke *et al.*, 2010) respectively.

$$S_{u0}(\phi) = 0.25 \times \phi^6 - 3.4774 \times \phi^5 + 18.498 \times \phi^4 - 46.525 \times \phi^3 + 52.317 \times \phi^2 - 13.976 \times \phi + 1.2994$$

$$0.4 \leq \phi \leq 2.5 \qquad (2.24)$$

$$S_{u0}(\phi) = S_{u0}(\phi = 2.5) + [7.23 - S_{u0}(\phi = 2.5)]\frac{\phi - 2.5}{2.5} \quad , \quad \phi > 2.5$$

$$\beta_1 = \frac{0.0163}{\phi} + 2.2937 \tag{2.25}$$

$$\beta_2 = \frac{0.2037}{\phi} - 0.575 \tag{2.26}$$

They have also provided another correlation for unstretched and stable burning velocity, based on chemical kinetics, as shown in Eq. (2.27) (Gerke *et al.*, 2010). The correlation was valid for the equivalence ratio, temperature, and pressure ranges from 0.4 to 3.75, 300 K to 900 K, and 1 bar to 80 bar respectivily.

$$S_u = S_{u0}(\phi)\ \left(\frac{T}{500}\right)^{\beta_1} \left(\frac{p}{20}\right)^{\beta_2} \qquad (m/s), \qquad T(K), \qquad p\ (bar) \tag{2.27}$$

$S_{u0}(\phi)$ is calculated from Eq. (2.28) (Gerke *et al.*, 2010), β_1 and β_2 are calculated from Eqs. (2.29) and (2.30) (Gerke *et al.*, 2010) respectively.

$$\begin{gathered} S_{u0}(\phi) = -4.239 \times \phi^6 + 30.521 \times \phi^5 - 84.173 \times \phi^4 + 108.95 \times \phi^3 \\ - 65.998\ \times \phi^2 + 20.818 \times \phi - 2.813 \\ \phi \leq 2.0 \\ S_{u0}(\phi) = 0.172 \times \phi^3 - 1.603\ \times \phi^2 + 3.593 \times \phi + 2.94 \qquad , \qquad \phi > 2.0 \end{gathered} \tag{2.28}$$

$$\begin{gathered} \beta_1 = -54.278 \times \phi^3 + 116.3\ \times \phi^2 - 85.633 \times \phi\ + 24.877 \\ \phi \leq 0.5 \\ \beta_1 = -0.0685 \times \phi^5 + 0.9066\ \times \phi^4 - 4.7032 \times \phi^3\ + 12.019 \times \phi^2 \\ - 14.929\ \times \phi + 9.37 \\ \phi > 0.5 \end{gathered} \tag{2.29}$$

$$\begin{gathered} \beta_2 = -0.2426 \times \phi^2 + 0.8\ \times \phi - 1.1522 \\ \phi \leq 1.75 \\ \beta_2 = 0.0075 \times \phi^3 - 0.0994 \times \phi^2 + 0.243\ \times \phi - 0.6638 \\ \phi > 1.75 \end{gathered} \tag{2.30}$$

2.5 Propagation velocity for weakly stretched flame (S_f)

There is no unique definition of the flame propagation velocity, as it could be either defined with respect to the unburned gas velocity or to the burned gas velocity. It is defined in the current study as the time rate of change of the flame position with respect to the burned gas velocity, as shown in Eq. (2.31) (Hu *et al.*, 2009) in terms of the flame radius (R).

$$S_f = \frac{dR}{dt} \tag{2.31}$$

By this sense, the propagation velocity of the planar flame, which is shown in Fig. 2.3 is equal to $\sigma\, S_u$. If the flame is stretched, the propagation velocity changes from $\sigma\, S_u$. Stretch deviates the planar structure of the flame, as diffusion of the reactants takes place not only in the longitudinal direction as in the planar flame, but also in the transverse direction (Giannakopoulos *et al.*, 2015). Flame could be stretched due to the change of its curvature or due to the hydrodynamic strain. The change of the flame curvature could occur during flame propagation, while the hydrodynamic strain is resulted from the non-uniformities in the flow and is applied to the flame surface.

Stretch rate (α) is a measure for flame stretch, which is defined as the time (t) rate of the change of an elemental area (A) of the flame surface as shown in Eq. (2.32) (Ciccarelli and Dorofeev, 2008).

$$\alpha = \frac{1}{A}\,\frac{dA}{dt} \tag{2.32}$$

The area of a spherical flame is $4\pi R^2$. Therefore, the stretch rate of a spherical flame is related to the flame propagation velocity as shown in Eq.(2.33) (Bauwens, Bergthorson and Dorofeev, 2017).

$$\alpha = \frac{1}{A}\,\frac{dA}{dt} = \frac{1}{4\pi R^2}\,\frac{d(4\pi R^2)}{dt} = \frac{2}{R}\,\frac{dR}{dt} = \frac{2}{R}\,S_f \tag{2.33}$$

Flame propagation velocity could be obtained from experiments. Figure 2.5 (Bauwens, Bergthorson and Dorofeev, 2017) shows flame propagation velocity for a

spherical flame of a lean hydrogen-air mixture with propagation against the stretch rate. The experiment was under the atmospheric pressure and temperature of 300 K. Stretch rate decreases with flame propagation. The figure clearly classified two propagation regimes: the first is for the weakly stretched flame and the second is for the unstable and cellular flame.

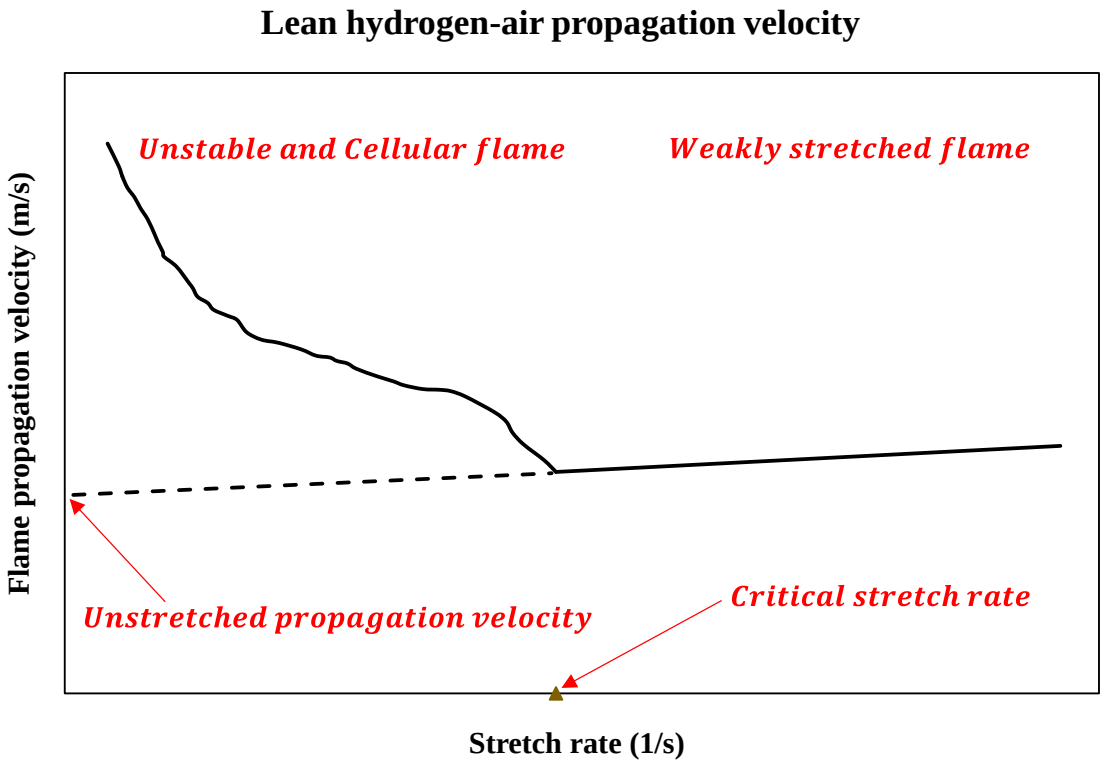

Figure 2.5: Flame propagation velocity against the stretch rate for a spherical flame of a lean hydrogen-air mixture (Bauwens, Bergthorson and Dorofeev, 2017).

S_f is linearly proportional to the stretch rate, in the weakly stretched regime, until the stretch rate reaches a critical value. The relation is defined in Eq. (2.34) (Giannakopoulos *et al.*, 2015) in terms of the Markstein length (L_{Mb}), which is defined with respect to the burned gas side.

$$S_f = \sigma\,(S_u - L_{Mb}\,\alpha) \tag{2.34}$$

L_{Mb} could be calculated either from experiments as the slope of the linear regime in Fig. 2.5 or based on the hydrodynamic theory, which provides a formula for L_{Mb}, as shown in Eq. (2.35) (Giannakopoulos *et al.*, 2015).

$$L_{Mb} = \left[\frac{1}{(\sigma - 1)} \int_1^{\sigma} \frac{\widehat{K}(\varphi)}{\varphi} d\varphi + \frac{\beta \left(Le_{eff} - 1 \right)}{2 \, (\sigma - 1)} \int_1^{\sigma} ln\left(\frac{\sigma - 1}{\varphi - 1} \right) \frac{\widehat{K}(\varphi)}{\varphi} d\varphi \right] \delta_z \quad (2.35)$$

$\widehat{K}$ is the thermal conductivity normalized by the unburned thermal conductivity. Le_{eff} is the effective Lewis number, which is defined in Eq. (2.36) (Matalon, 2009) in terms of the oxygen and hydrogen Lewis numbers, Le_{O_2} and Le_{H_2} respectively. Le_{H_2} is defined in Eq. (2.37) (Verhelst *et al.*, 2011) as the Lewis number of the deficient reactant in terms of the unburned mixture thermal diffusivity and the diffusion coefficient of the deficient reactant, hydrogen, (D_{H_2}). The same definition is valid for Le_{O_2}.

$$Le_{eff} = \begin{cases} \dfrac{Le_{O_2} + \left(1 - \tilde{\phi}\right) Le_{H_2}}{2 - \tilde{\phi}} & Lean \\ \dfrac{Le_{H_2} + \left(1 + \tilde{\phi}\right) Le_{O_2}}{2 + \tilde{\phi}} & rich \end{cases} \quad (2.36)$$

$$\tilde{\phi} \sim \beta(\phi - 1)$$

$$Le_{H_2} = \frac{\chi_u}{D_{H_2}} = \frac{K_u}{\rho_u \; Cp_u \; D_{H_2}} \quad (2.37)$$

The sign of the Markstein length changes from positive to negative based on the value of $\left(Le_{eff} - 1\right)$. Lean hydrogen-air mixture, which is shown in Fig. 2.5 (Bauwens, Bergthorson and Dorofeev, 2017) has a negative Markstein length. Therefore, positive stretch increases the propagation velocity. Rich hydrogen-air mixture has positive Markstein length and the positive stretch decreases the propagation velocity. The extrapolation of the weakly stretched regime in Fig. 2.5 (Bauwens, Bergthorson and Dorofeev, 2017) to the line of zero stretch rate provides an experimental value of the unstretched propagation velocity, which is related to the unstretched laminar burning velocity. The difficulty to measure the unstretched laminar burning velocity with the increase in the pressure, is due to the diminishing of the linear regime with the pressure rise.

2.6 Propagation of unstable and cellular flame

The second unstable and cellular regime in Fig. 2.5 (Bauwens, Bergthorson and Dorofeev, 2017) is due to the effect of flame instabilities, which increase flame area and propagation velocity. There are two main mechanisms to generate the instabilities, which are the hydrodynamic instability and the thermo-diffusive instability.

2.6.1 Hydrodynamic (Darrieus-Landau) instability (DL)

Hydrodynamic instability is a natural instability introduces due to the difference between the unburned and burned densities along the flame surface. It was first discussed by Darrieus and Landau separately (Ciccarelli and Dorofeev, 2008). It is noted that the terms: hydrodynamic instability and Darrieus-Landau instability are used equivalently in the current presentation. A schematic of the hydrodynamic instability is shown in Fig. 2.6 (Ciccarelli and Dorofeev, 2008). For a convex flame segment toward the unburned gas, the streamlines of initially perturbed flame front at time t_1 are diverged in the unburned gas side and are converged in the burned gas side. As a result, the unburned gas velocity is decreased, and the burned gas velocity is increased. Therefore, laminar burning velocity is increased with respect to the planar laminar burning velocity and flame segment curvature is increased in the next time t_2.

For the concave flame segment toward the unburned gas, the streamlines are converged in the unburned gas side and are diverged in the burned gas side. As a result, the unburned gas velocity is increased, and the burned gas velocity is decreased. The overall effect is to decrease the laminar burning velocity with respect to the planar laminar burning velocity and to increase the flame segment curvature in the next time t_2.

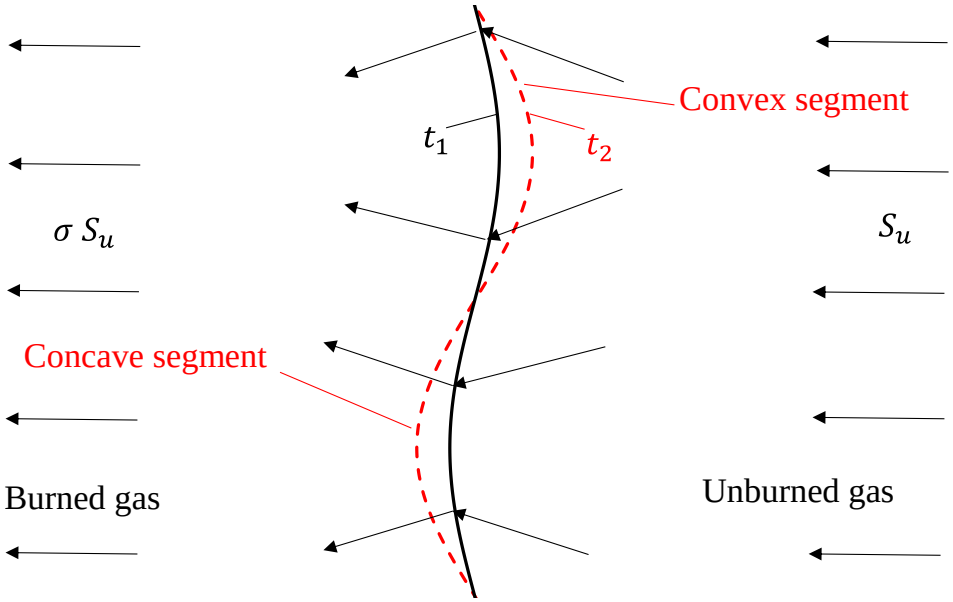

Figure 2.6: Hydrodynamic instability at two proceeding times t_1 and t_2 (Ciccarelli and Dorofeev, 2008).

According to Darrieus and Landau studies, for any perturbation wavelengths the instability is grown, and the planar laminar flame is unconditionally unstable, which is not true. Hydrodynamic instability could be stabilized. The small scale perturbation could be stabilized by thermo-diffusive stabilizing effect (Ciccarelli and Dorofeev, 2008), for $Le > 1$, and the large scale perturbation could be stabilized due to the difference in the nonlinear evolution of the convex and concave parts of the flame (Ciccarelli and Dorofeev, 2008). The competing between the hydrodynamic instability, thermo-diffusive stabilizing effect, and flame curvature under the applied pressure determines the growth or decay of the instability (Gerke *et al.*, 2010).

2.6.2 Thermo-diffusive instability (TD)

Thermo-diffusive instability is the result of the imbalance between diffusion of the deficient reactant, hydrogen in lean mixture, to the flame front and diffusion of the heat from the flame front i.e. it is directly related to the Lewis number. The criterion for the onset of the thermo-diffusive instability is $Le < 1 - 2/\beta$ (Ciccarelli and Dorofeev, 2008), which is equivalent to $Le < 1$ for mixtures with large activation energy.

A schematic of the thermo-diffusive instability is shown in Fig. 2.7 (Ciccarelli and Dorofeev, 2008). For an initially perturbed flame front with $Le < 1$ at time t_1 the

diffusion of the reactants to the convex segment with respect to the unburned gas is higher than the diffusion of the heat from the convex segment. It leads to an increase in the adiabatic flame temperature and the laminar burning velocity with respect to the planar flame (Ciccarelli and Dorofeev, 2008; Giacomazzi, Picchia and Arcidiacono, 2008). Therefore, in the next time t_2 the flame surface curvature is increased. For the concave segment with respect to the unburned gas and $Le < 1$, the diffusion of the reactants is toward larger area than in planar flame. It leads to a decrease in the adiabatic flame temperature and the laminar burning velocity with respect to the planar flame (Ciccarelli and Dorofeev, 2008; Giacomazzi, Picchia and Arcidiacono, 2008). Therefore, in the next time t_2 the flame surface curvature is increased. As a conclusion, for $Le < 1$ thermo-diffusive instability increases flame surface curvature and flame surface area. Therefore, it acts as a destabilizing mechanism.

For $Le > 1$ on the convex flame segment with respect to the unburned gas, diffusion of heat is toward larger area than the in the planar flame. It leads to a decrease in the adiabatic flame temperature and the laminar burning velocity with respect to the planar flame. Therefore, in the next time t_2 the flame surface curvature is decreased. For the concave flame segment with respect to the unburned gas and $Le > 1$, diffusion of heat is toward smaller area than the in the planar flame. It leads to an increase in the adiabatic flame temperature and the laminar burning velocity with respect to the planar flame. Therefore, in the next time t_2 the flame surface curvature is decreased. As a conclusion, for $Le > 1$ thermo-diffusive instability decreases flame surface curvature and flame surface area. Therefore, it acts as a stabilizing mechanism.

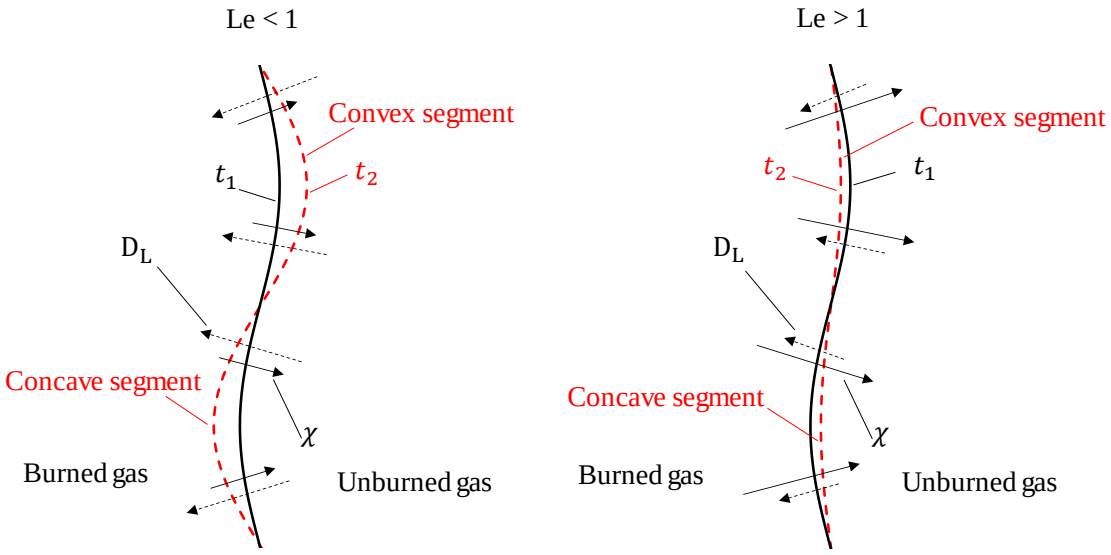

Figure 2.7: Thermo-diffusive instability at two proceeding times t_1 and t_2 (Ciccarelli and Dorofeev, 2008).

D_L is the diffusivity of the limiting component.

2.6.3 Cellular structure of the flame

The combined effect of the hydrodynamic and thermo-diffusive instabilities is manifested in the form of cracks that appear on the flame surface with propagation, which is developed to wrinkling and cellular structure. Different parameters could affect the competing between the stabilizing and the destabilizing mechanisms, which are thermal expansion coefficient, the Lewis number, flame thickness, and the pressure. Larger thermal expansion coefficient, larger pressure, and smaller flame thickness prompt hydrodynamic instability. Smaller Lewis number prompts thermo-diffusive instability. The combined effects would allow the initialization of cellular structure at different propagation radius, which is called the critical radius (R_0). R_0 is provided from experiments as shown in Fig. 2.8 for the hydrogen-air mixture. The experimental data from (Sun *et al.*, 2012; Bauwens, Bergthorson and Dorofeev, 2017) have chosen due to the consistency of their measurements. Bauwens et al. experiments were carried out under the atmospheric pressure, initial temperatures ranged from 297 to 307 K, and relative humidity ranged from 35% to 72%. Sun et al. measurements were carried out under the atmospheric pressure and 300 K. R_0 increases with the increase in the hydrogen mole fraction, as expected due to the change in the mechanism of the thermo-diffusive stability from destabilization to stabilization with the increase in hydrogen concentration.

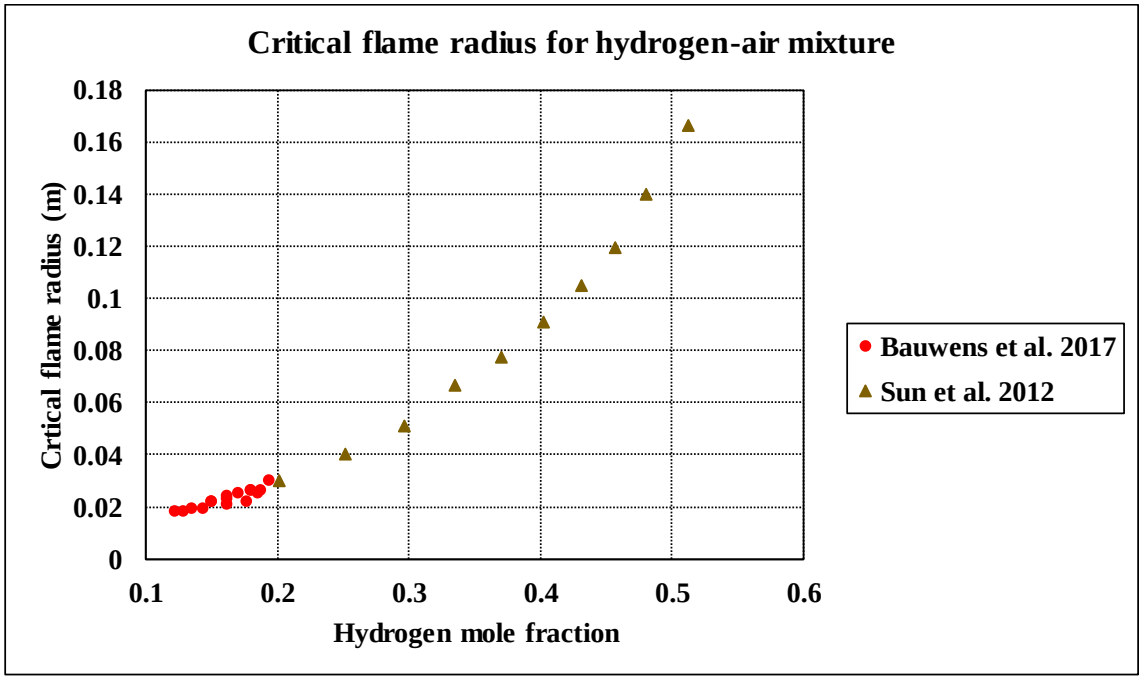

Figure 2.8: Critical flame radius for hydrogen-air mixture under the atmospheric pressure and temperature close to 300 K (Sun *et al.*, 2012; Bauwens, Bergthorson and Dorofeev, 2017).

Cellular structure of the flame follows a self-similar behaviour. Therefore, the fractal theory could be used to determine the effect of the instabilities on the unstretched laminar burning velocity. Fractal theory would require determining the smallest and largest wrinkled flame wavelengths. The analysis of planar and spherical flames using linear stability could provide the required wrinkled wavelengths.

2.6.4 Planar flame analysis

Hydrodynamic analysis of planar flames provides a dispersion relation, which describes the growth rate of the combined instabilities (ω) in relation to the perturbation wave number (f) as shown in Eq. (2.38) (Matalon, 2009). The first term in the right-hand side represents the hydrodynamic instability, which acts as a destabilizing term. The second term in the right-hand side combines the effects of thermal diffusion, molecular diffusion, and viscosity diffusion. Thermal and viscous diffusion terms have a stabilizing effect. Molecular diffusion term acts as stabilizing or destabilizing mechanism depending on the value of the effective Lewis number.

$$\omega = \omega_{DL}\ S_u\ f - \delta_z\ \left[B_1 + \beta\left(Le_{eff} - 1\right) B_2 + Pr\, B_3\right] S_u\, f^2 \qquad (1/s) \qquad (2.38)$$

ω_{DL} is defined in Eq. (2.39) (Matalon, 2009) in terms of the thermal expansion coefficient.

$$\omega_{DL} = \frac{-\sigma + \sqrt{\sigma^3 + \sigma^2 - \sigma}}{\sigma + 1} \qquad (2.39)$$

Pr is the Prandtl number defined in Eq. (2.40) (Giannakopoulos *et al.*, 2019), based on the unburned properties. B_1, B_2, and B_3 are coefficients defined in Eqs. (2.41)–(2.43) (Altantzis *et al.*, 2012).

$$Pr = \frac{Cp_u\ \mu_u}{K_u} \qquad (2.40)$$

μ_u is the unburned viscosity.

$$B_1 = \frac{\sigma}{2}\left[\frac{\sigma\,(2\ \omega_{DL} + \sigma + 1)}{(\sigma - 1)\,[\sigma + (\sigma + 1)\ \omega_{DL}]} \int_1^{\sigma} \frac{\widehat{K}(\varphi)}{\varphi} d\varphi + \frac{1}{\sigma + (\sigma + 1)\,\omega_{DL}} \int_1^{\sigma} \widehat{K}(\varphi)\, d\varphi\right] \qquad (2.41)$$

$$B_2 = \frac{\sigma}{2}\left[\frac{(1 + \omega_{DL})\ (\sigma + \omega_{DL})}{(\sigma - 1)\ [\sigma + (\sigma + 1)\ \omega_{DL}]} \int_1^{\sigma} ln\left(\frac{\sigma - 1}{\varphi - 1}\right) \frac{\widehat{K}(\varphi)}{\varphi} d\varphi\right] \qquad (2.42)$$

$$B_3 = \frac{\sigma}{2}\left[\frac{2\ (\sigma - 1)}{\sigma + (\sigma + 1)\ \omega_{DL}}\, \widehat{K}(\sigma) - \frac{2}{\sigma + (\sigma + 1)\ \omega_{DL}} \int_1^{\sigma} \widehat{K}(\varphi)\, d\varphi\right] \qquad (2.43)$$

$\widehat{K}(\sigma)$ is the normalized thermal conductivity of the burned gas.

The root of the dispersion relation (f_{max}) represents the largest wave number. The smallest wavelength i.e. the inner cut-off length scale of the wrinkling due to the instabilities (λ_{min}) is calculated from f_{max} as shown in Eq. (2.44) (Chaudhuri, Akkerman and Law, 2011; Keppeler and Pfitzner, 2015).

$$\lambda_{min} = \frac{2\,\pi}{f_{max}} \tag{2.44}$$

2.6.5 Spherical flame analysis

Hydrodynamic analysis of spherical flames provides dispersion relation, which describes the growth rate of the combined instabilities (ω_1) in relation to the perturbation wave number as shown in Eq. (2.45) (Addabbo, Bechtold and Matalon, 2002). ϖ and Ω are coefficients defined in Eqs. (2.46) and (2.51) (Addabbo, Bechtold and Matalon, 2002) respectively.

$$\omega_1 \;=\; \frac{\dot{R}}{R}\left(\varpi \;-\; \frac{\delta_z}{R}\;\Omega\right) \qquad (1/s) \tag{2.45}$$

$\dot{R}$ is the normal propagation velocity defined as the time derivative of the flame radius.

$$\varpi \;=\; \frac{-\;(g_2 \;-\; g_1) \;+\; \sqrt{(g_2 \;-\; g_1)^2 \;-\; 4\;g_1\;g_3}}{2\;\;g_1} \tag{2.46}$$

g_1, g_2, and g_3 are coefficients defined in Eqs. (2.47)–(2.49) (Addabbo, Bechtold and Matalon, 2002) respectively.

$$g_1 \;=\; (\sigma_1 \;+\; 1)\;f \;+\; 1 \tag{2.47}$$

$$g_2 = 2\,f^2 + (4 + 5\,\sigma_1)\,f + 4 \tag{2.48}$$

$$g_3 = -\frac{\sigma_1 - 1}{\sigma_1}\,f^3 + 2\,f^2 + \left[3\,(\sigma_1 + 1) - \frac{1}{\sigma_1}\right]f + 2 \tag{2.49}$$

σ_1 is the thermal expansion coefficient defined as the ratio of the burned temperature to the unburned temperature as shown in Eq. (2.50) (Addabbo, Bechtold and Matalon, 2002).

$$\sigma_1 = \frac{T_b}{T_u} \tag{2.50}$$

$$\Omega = \frac{Q_1 + \frac{\beta\left(Le_{eff} - 1\right)}{\sigma_1 - 1}\, Q_2 + Pr\;\; Q_3}{\varpi} \tag{2.51}$$

The coefficients Q_1, Q_2, and Q_3 are defined in Eqs. (2.52)–(2.54) (Addabbo, Bechtold and Matalon, 2002) respectively.

$$\begin{aligned} Q_1 = \frac{\frac{\sigma_1}{\sigma_1 - 1}\int_1^{\sigma_1} \frac{\widehat{K}(\varphi)}{\varphi} d\varphi}{\sigma_1\ \underline{\underline{\Delta}}} \quad & [f^4(\sigma_1 + 1) + \sigma_1 f^3(2\varpi + 5) \\ & + f^2(\varpi\ \sigma_1 - 2\ \sigma_1^2 + \sigma_1 - 1) + f\ \sigma_1(\ \sigma_1 - 7 - 3\varpi - \sigma_1\ \varpi) \\ & - 2\ \sigma_1\ (1 + \varpi)] \\ & + \ \frac{\int_1^{\sigma_1} \widehat{K}(\varphi)\ d\varphi}{\sigma_1\ (\sigma_1 - 1)\ \underline{\underline{\Delta}}}\ [f\ (f^2 - 1)\ (f + 2)\ (\sigma_1 - 1)] \end{aligned} \tag{2.52}$$

$$\begin{aligned} Q_2 = \frac{\int_1^{\sigma_1} \frac{\widehat{K}(\varphi)}{\varphi}\ ln\left(\frac{\sigma_1 - 1}{\varphi - 1}\right) d\varphi}{2\ \underline{\underline{\Delta}}} & \{2\ f^4 + f^3(2\ \varpi\ \sigma_1 + 2\ \varpi + 10\ \sigma_1 - 3) \\ & + f^2[2\ \sigma_1\ \varpi^2 + (5\ \sigma_1 - 1)\varpi + 3\ \sigma_1 - 2\ \sigma_1^2 - 2] \\ & + f\ [\sigma_1\ \varpi^2(1 - 4\ \sigma_1) - (14\ \sigma_1^2 + 1)\ \varpi + 3 - 9\ \sigma_1 - 8\ \sigma_1^2] \\ & - 2\ \sigma_1(\varpi^2 + 4\varpi + 3)\} \end{aligned} \tag{2.53}$$

$$\begin{aligned} Q_3 = \left[\frac{2\ f\ (f^2 - 1)\ (\sigma_1 - 1)}{\sigma_1\ \underline{\underline{\Delta}}}\right] \Bigg[& (f + 2)\left(\widehat{K}(\sigma_1) - \frac{\int_1^{\sigma_1} \widehat{K}(\varphi)\ d\varphi}{\sigma_1 - 1}\right) \\ & - 3\ \left(\widehat{K}(\sigma_1) - 1\right)\Bigg] \end{aligned} \tag{2.54}$$

$\underline{\underline{\Delta}}$ is defined in Eq. (2.55) (Addabbo, Bechtold and Matalon, 2002).

$$\underline{\underline{\Delta}} = 2\ g_1\ \varpi + g_2 - 2\ g_1 \tag{2.55}$$

The range of unstable wave lengths in terms of the Peclet number (Pe) is determined by setting ω_1 to zero in the disperion relation in Eq. (2.45). The Peclet number is defined as the ratio between the flame radius to the flame thickness as shown in Eq. (2.56) (Addabbo, Bechtold and Matalon, 2002). The domain of instability is shown in Fig. 2.9 (Matalon, 2009), it is known as the Bradely peninsula. The instability starts at the nose of the domain, following that, the unstable domain increases with propagation. The instability domain stabilizes at the lower boundary by stretching, which represents the largest unstable wavelength (λ_{max}). λ_{max} approaches an asymptotic value proportional to R with the increase in the Peclet number as shown in Eq. (2.57) (Addabbo, Bechtold and Matalon, 2002). On the upper boundary the instability domain is stabilized by diffusion, where the smallest unstable wavelength is proportional to the flame thickness. λ_{min} is calculated from Eq. (2.58) (Addabbo, Bechtold and Matalon, 2002).

$$Pe = \frac{R}{\delta_z} \tag{2.56}$$

$$\lambda_{max} = \frac{2\,\pi\,R}{f_{min}} \tag{2.57}$$

f_{min} is the minimum spherical wave number, it has a value of 7 (Addabbo, Bechtold and Matalon, 2002).

$$\lambda_{min} = 2\,\pi\,\delta_z \left[\frac{C_1 + \beta\,\left(Le_{eff} - 1\right)\,C_2 + Pr\,C_3}{C_4}\right] \tag{2.58}$$

C_1 to C_4 are defined in Eqs. (2.59)–(2.62) (Addabbo, Bechtold and Matalon, 2002) respectively.

$$C_1 = \left(\frac{\sigma_1 + 1}{\sigma_1}\right)\left(\frac{\sigma_1}{\sigma_1 - 1}\int_1^{\sigma_1}\frac{\widehat{K}(\varphi)}{\varphi}d\varphi\right) + 2\,\sigma_1\,\omega_{DL1} + \frac{\sigma_1 - 1}{\sigma_1}\left(\frac{1}{\sigma_1 - 1}\int_1^{\sigma_1}\widehat{K}(\varphi)\,d\varphi\right) \tag{2.59}$$

$$C_2 = \left(\frac{1}{\sigma_1 - 1}\int_1^{\sigma_1} ln\left(\frac{\sigma_1 - 1}{\varphi - 1}\right)\frac{\widehat{K}(\varphi)}{\varphi}d\varphi\right)(1 + \omega_{DL1})(1 + \sigma_1\ \omega_{DL1}) \quad (2.60)$$

$$C_3 = 2\left(\frac{\sigma_1 - 1}{\sigma_1}\right)\left(\widehat{K}(\sigma_1) - \frac{1}{\sigma_1 - 1}\int_1^{\sigma_1}\widehat{K}(\varphi)\,d\varphi\right) \quad (2.61)$$

$$C_4 = 2\,\omega_{DL1}\,[(\sigma_1 + 1)\ \omega_{DL1} + 1] \quad (2.62)$$

ω_{DL1} is defined in Eq. (2.63) (Addabbo, Bechtold and Matalon, 2002).

$$\omega_{DL1} = \frac{-\sigma_1 + \sqrt{\sigma_1^3 + \sigma_1^2 - \sigma_1}}{\sigma_1 + 1} \quad (2.63)$$

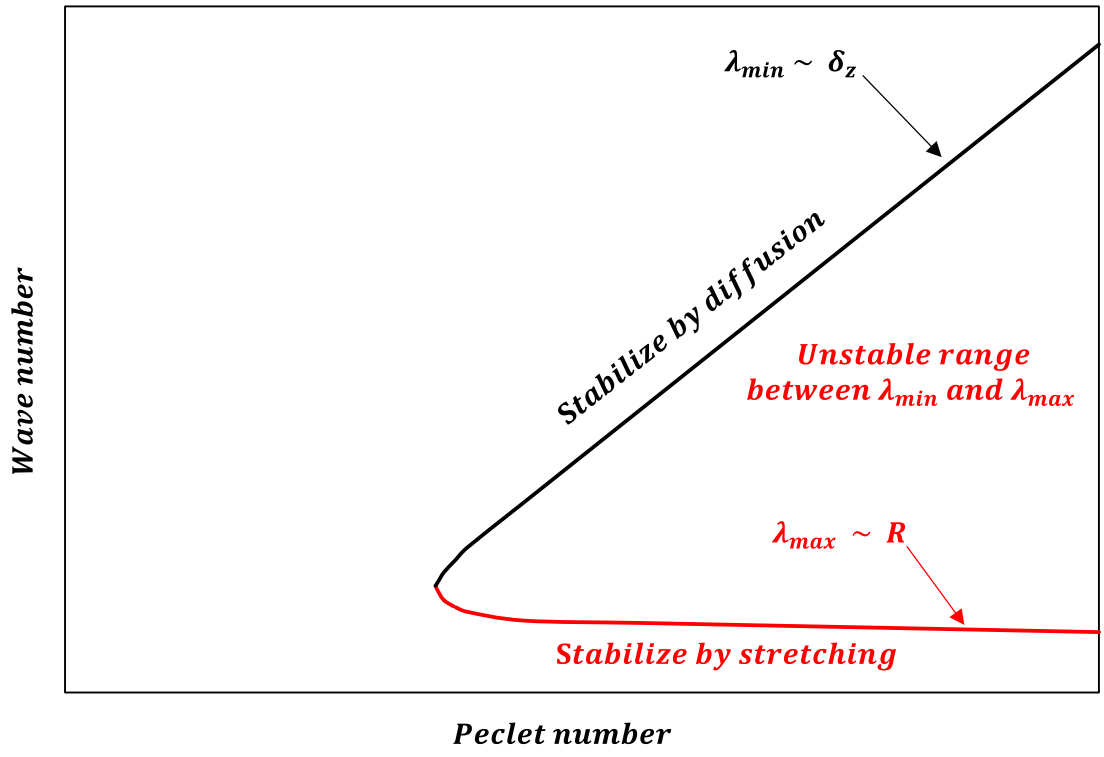

Figure 2.9: Schematic of the instability domain for a spherical expanding flame (Matalon, 2009).

2.7 Propagation of turbulent flame

Flame has different characteristics when it propagates in turbulent flow. The interaction between the flame and the turbulence increases the flame surface area and the propagation speed. The nature of the interaction between the turbulence and the flame is classified in terms of the ratio between the characteristic scales of the turbulence and the flame. Therefore, the following scales and the non-dimensional numbers are important to study turbulence-flame interaction.

2.7.1 Turbulent scales and non-dimensional numbers

Figure 2.10 (McDonough, 2007) shows the logarithmic magnitude of the energy in a turbulent flow with respect to size of the eddies. Turbulent energy is generated at the large-scale eddies then it cascades to the smaller eddies until it dissipates as heat. Two important characteristic length scales at the cascade diagram: the integral length scale and the Kolmogorov length scale.

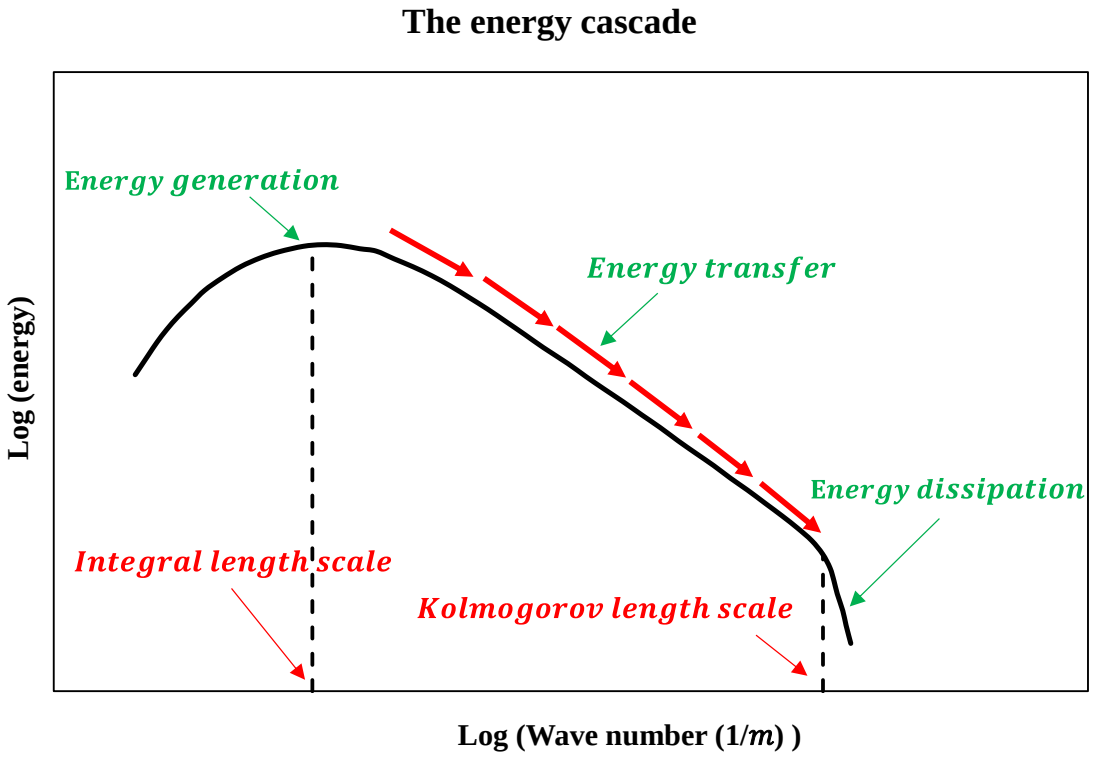

Figure 2.10: The energy cascade (McDonough, 2007).

1- Integral length scale (l)

The integral length scale is the size of the eddies in the energy cascade that contains the largest energy (CFD Online, 2012). In the LES formulation, the filter width, or the grid size (Δ) should be chosen such that it is smaller than l. Therefore, in the LES modelling l is approximated as Δ.

2- Kolmogorov length scale (L_{KO})

The Kolmogorov length scale is the size of the smallest eddies in the energy cascade. It is characterized by a universal structure at high Reynolds number flow (Bakker, 2012), which dissipates turbulent kinetic energy into heat by viscosity. L_{KO} could be estimated for non-reactive LES under the assumption of homogeneous isotropic turbulence as shown in Eq. (2.64) (Giacomazzi, Bruno and Favini, 1999). It is based on the energy balance between turbulent generation at the filter width or the grid size and turbulent dissipation at the Kolmogorov size.

$$L_{KO} = \frac{\Delta}{\left(\frac{\rho_u \, u_\Delta \, \Delta}{\mu_u}\right)^{\frac{3}{4}}} \tag{2.64}$$

u_Δ is the sub-grid scale (SGS) turbulent velocity at the scale Δ. It is calculated from the SGS turbulent kinetic energy (k_Δ), as shown in Eq. (2.65). k_Δ could be evaluated from transport equation.

$$u_\Delta = \sqrt{\frac{2}{3} \, k_\Delta} \tag{2.65}$$

3- Gibson length scale (L_{GI})

The Gibson length scale is the size of the eddy in the Kolmogorov energy spectrum that interacts locally with the flame front. In another words, it is the size of the burned gas that moves into the unburned gas with velocity equal to laminar burning velocity (Peters, 1997). Therefore, there is a kinematic equilibrium mechanism, which penetrates the flame front and leads to its advancement. In the LES formulation, the Gibson length scale is calculated from Eq. (2.66) (Charlette, Meneveau and Veynante, 2002).

$$L_{GI} = \Delta \left(\frac{S_u}{u_\Delta}\right)^3 \tag{2.66}$$

4- Coherent fine scale eddy diameter (L_{Cf})

Direct numerical simulation (DNS) has revealed that there is universal structure of the fine scale eddies of turbulence. The size of this universal structure is called the coherent fine scale eddy diameter. It is estimated in reacting flow as shown in Eq. (2.67) (Shim *et al.*, 2011).

$$L_{Cf} = 8\, L_{KO} \tag{2.67}$$

5- Kolmogorov velocity scale (u_{KO})

The Kolmogorov velocity is the velocity associated with the eddies that have a size equal to the Kolmogorov scale. In LES, u_{KO} could be estimated for non-reactive and homogeneous isotropic turbulence as shown in Eq. (2.68) (Giacomazzi, Bruno and Favini, 1999).

$$u_{KO} = \frac{u_\Delta}{\left(\frac{\rho_u\, u_\Delta\, \Delta}{\mu_u}\right)^{\frac{1}{4}}} \tag{2.68}$$

6- Turbulent time scale (t_{tur})

The turbulent time scale is the time associated with the eddies that have a size equal to the integral length scale. In LES, it is approximated as shown in Eq. (2.69) (Charlette, Meneveau and Veynante, 2002).

$$t_{tur} = \frac{\Delta}{u_\Delta} \tag{2.69}$$

7- Kolmogorov time scale (t_{KO})

The Kolmogorov time scale is the time associated with the eddies that have a size equal to the Kolmogorov scale. In LES, t_{KO} could be estimated for non-reactive and

homogeneous isotropic turbulence as shown in as shown in Eq. (2.70) (Giacomazzi, Bruno and Favini, 1999).

$$t_{KO} = \frac{t_{tur}}{\left(\frac{\rho_u \, u_\Delta \, \Delta}{\mu_u}\right)^{\frac{1}{2}}} \tag{2.70}$$

8- Flame time scale (t_f)

The flame time scale is the time associated with the diffusion of heat or species across the laminar flame thickness, as shown in Eq. (2.71) (PETERS, 1999).

$$t_f = \frac{\delta_z}{S_u} \tag{2.71}$$

9- Turbulent Reynolds number (Re_Δ)

The turbulent Reynolds number is the defined in the LES formulation using the filter or the grid characteristic length and the corresponding velocity scale as shown in Eq. (2.72) (Giacomazzi, Bruno and Favini, 1999) under the assumption of homogeneous isotropic turbulence.

$$Re_\Delta = \frac{\rho_u \, u_\Delta \, \Delta}{\mu_u} \tag{2.72}$$

Re_Δ could be defined, for the purpose of scaling (PETERS, 1999), using flame characteristics as shown in Eq. (2.73) (PITSCH, 2005) by equating the thermal diffusivity to the kinematic viscosity.

$$Re_\Delta = \left(\frac{u_\Delta}{S_u}\right)\left(\frac{\Delta}{\delta_z}\right) \tag{2.73}$$

10- Karlovitz number (Ka_Δ)

The Karlovitz number is defined as the ratio between the flame time scale to the Kolmogorov time scale as shown in Eq. (2.74) (PITSCH, 2005) using the LES

formulation. To derive the Ka_Δ formula, the thermal diffusivity is equated to the kinematic viscosity for the purpose of scaling (PETERS, 1999).

$$Ka_\Delta = \frac{t_f}{t_{KO}} = \left(\frac{\delta_z}{L_{KO}}\right)^2 = \left(\frac{u_\Delta}{S_u}\right)^{3/2} \left(\frac{\delta_z}{\Delta}\right)^{1/2} \quad (2.74)$$

11- Karlovitz number based on the inner flame thickness (Ka_δ)

Ka_δ is defined based on the inner flame thickness. The ratio between the preheated zone to the inner flame thickness is in the order of 10 to 1. Therefore, Ka_δ is related to Ka_Δ as shown in Eq. (2.75) (PETERS, 1999).

$$Ka_\delta = 100\ Ka_\Delta \quad (2.75)$$

2.7.2 Turbulent combustion regimes diagram (Borghi diagram)

The Borghi diagram is used to classify the turbulence-flame interaction. It is constructed using the characteristic scales and the non-dimensional numbers related to turbulence and combustion as shown in Fig. 2.11 (PETERS, 1999; Ciccarelli and Dorofeev, 2008). The axes of the Borghi diagram are the non-dimensional variables l/δ_z and u_Δ/S_u. The lines $u_\Delta = S_u$, $Ka_\Delta = 1$, and $Ka_\delta = 1$ represent the boundaries between different combustion regimes. Inside the diagram, Re_Δ increases parallel to the line $Re_\Delta = 1$ towards the top right corner and Ka_Δ increases parallel to the line $Ka_\Delta = 1$ towards the top left corner.

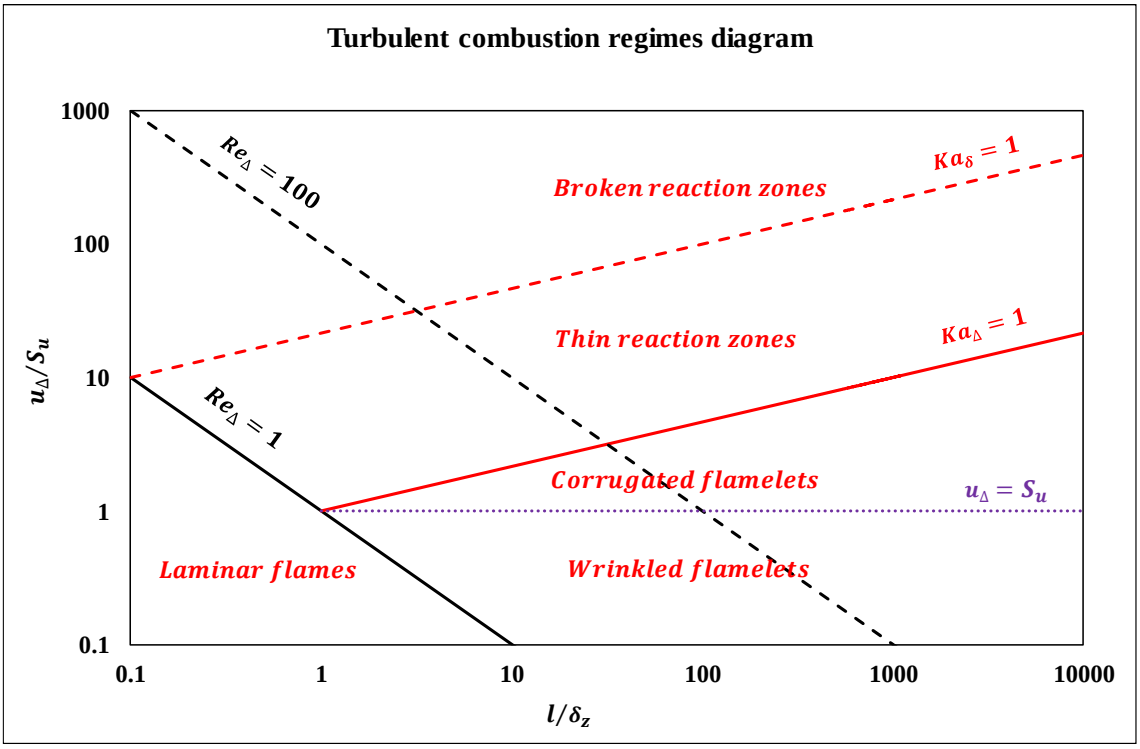

Figure 2.11: Turbulent combustion regimes diagram (Borghi diagram) (PETERS, 1999; Ciccarelli and Dorofeev, 2008).

The diagram includes five main regimes:

1- Laminar flames: it represents fast combustion with a planar flame structure. That is characterized by small flame time scale to the turbulent time scale.

2- Wrinkled flamelets regime: it is a fast combustion regime with $Ka_\Delta < 1$ and $u_\Delta < S_u$. Therefore, turbulence does not produce sufficient corrugation and flame propagation is like laminar.

3- Corrugated flamelets regime: it is a fast combustion that is bounded by the lines $u_\Delta = S_u$ and $Ka_\Delta = 1$. In this regime, all turbulent eddies are larger than the preheated flame thickness and the flame is stretched and curved by the eddies. Therefore, turbulence effect is limited to increase the flame surface.

4- Thin reaction zones regime: it is bounded by the lines $Ka_\Delta = 1$ and $Ka_\delta = 1$. In this regime, small turbulent eddies penetrate the flame preheated thickness but do not penetrate the flame inner layer thickness. That would change mixing properties and the flame structure.

5- Broken reaction zones regime: it is characterized by $Ka_\delta > 1$. In this regime, small turbulent eddies penetrate the inner flame thickness. Therefore, a distributed or broken reaction occurs due to the loss of chemical species and the regime is classified as a slow chemistry.

The classification of the combustion regimes is based on simple refinement of the Kolmogorov theory, while turbulence in real application is not homogenous and there is statistical distribution of the dissipation of the turbulent kinetic energy. Therefore, in real experiments there could be an intermittency, which is the appearance of more than one regime at the same time (Peters, 1997).

2.7.3 Turbulent burning velocity (S_{tur})

Turbulence corrugates the flame at different levels of scales. Therefore, increases flame surface area and could increase the mixing based on the turbulence level. Therefore, flame burning velocity differs from the laminar burning velocity. A statistically stationary planar turbulent burning velocity could be defined for the corrugated flame, using an analogy similar to the stationary planar laminar flame, as shown in Fig. 2.12 (Robin, Mura and Champion, 2011). The velocity of the incoming unburned gas is called the turbulent burning velocity (S_{tur}) and the velocity of the burned gas is $\sigma\, S_{tur}$. Therefore, the propagation velocity of the turbulent flame relative to the burned gas is $\sigma\, S_{tur}$. Modelling S_{tur} is extensively studied theoretically, experimentally, and numerically.

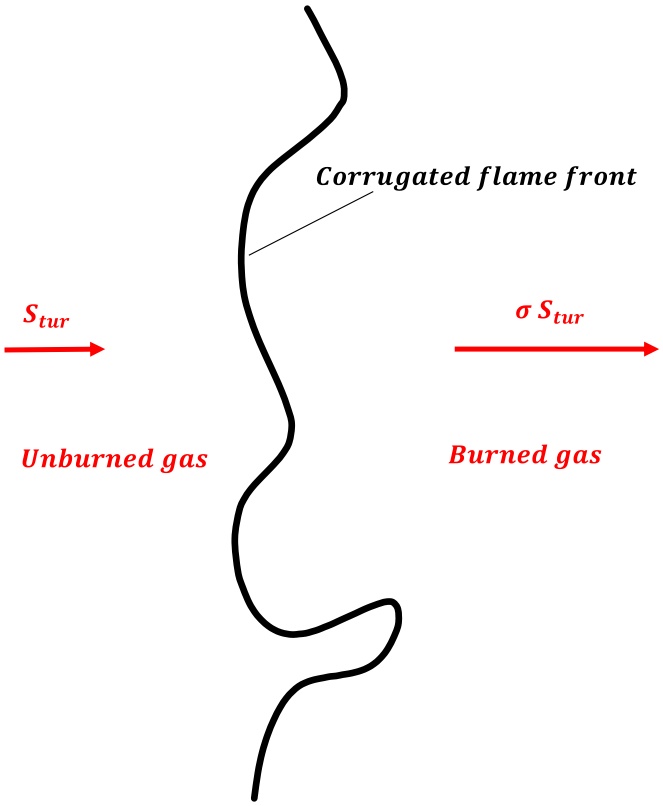

Figure 2.12: Schematic of a statistically stationary planar turbulent flame (Robin, Mura and Champion, 2011).

2.7.4 Turbulent wrinkling factor

A flame wrinkling factor is the ratio between the corrugated flame surface area and the area of the projection of the corrugated flame in the propagation direction. The turbulent wrinkling factor or the closely related flame surface density concept, which is defined as the flame surface area per unit volume, were extensively studied. Different models were developed either for corrugated flame or thin reaction zones flame or both. A brief review of these models is as follows:

1- Fureby (Fureby, 2005) provided a wrinkling factor model (Ξ_{FU}) in the LES fractal-based modelling for corrugated flames, as shown in Eq. (2.76) (Katragadda, Chakraborty and Cant, 2012). The outer cut-off length scale was modelled as the filter width. The inner cut-off length scale (η_{FU}) was estimated as the inverse of the surface average of the flame curvature, as shown in Eq. (2.77) (Fureby, 2005). The fractal dimension (FD_{NO}) was modelled using the parameterization of North & Santavicca, as shown in Eq. (2.79) (Katragadda, Chakraborty and Cant, 2012).

$$\Xi_{FU} = \left(\frac{\Delta}{\eta_{FU}}\right)^{FD_{NO}-2} = \left(\Gamma \frac{u_\Delta}{S_u}\right)^{FD_{NO}-2} \quad (2.76)$$

$$\eta_{FU} = \frac{\Delta\, S_u}{\Gamma\, u_\Delta} \quad (2.77)$$

Γ is an efficiency function, as show in Eq. (2.78) (Katragadda, Chakraborty and Cant, 2012).

$$\Gamma = \Gamma\left(\frac{u_\Delta}{S_u}, \frac{\Delta}{\delta_z}\right) = 0.75 \; e^{\left[-1.2\left(\frac{u_\Delta}{S_u}\right)^{-0.3}\right]} \left(\frac{\Delta}{\delta_z}\right)^{\frac{2}{3}} \quad (2.78)$$

$$FD_{NO} = \frac{2.05}{\frac{u_\Delta}{S_u}+1} + \frac{2.35}{\frac{S_u}{u_\Delta}+1} \quad (2.79)$$

2- Hawkes et al. provided a wrinkling factor model (Ξ_{HA}) in the LES fractal-based modelling for corrugated and thin reaction zones flames, as shown in Eq. (2.80) (Hawkes *et al.*, 2012). The outer cut-off length scale was modelled as the filter width and the inner cut-off length scale (η_{HA}) was modelled as a smooth combination between two limits, as shown in Eq. (2.81) (Hawkes *et al.*, 2012). The first limit is related to the Gibson length scale in the corregated regime, which is known as the Damköhler's large scale limit, as modelled in Eq. (2.82) (Hawkes *et al.*, 2012). The second limit is related to the Obukhov–Corrsin length scale in the thin reaction zones regime, which is known as the Damköhler's small scale limit, as modelled in Eq. (2.83) (Hawkes *et al.*, 2012). The constants in the first and second limits were obtained by only matching a single DNS case from their work. Two fractal dimension models (FD_{HA}), static and dynamic, were provided. The static form was modelled as a function of the two limits length scales, as shown in Eq. (2.84) (Hawkes *et al.*, 2012).

$$\Xi_{HA} = \left(1 + \frac{\Delta}{\eta_{HA}}\right)^{FD_{HA}-2} \quad (2.80)$$

$$\eta_{HA} = \left(L_G^4 + L_{OC}^4\right)^{\frac{1}{4}} \quad (2.81)$$

$$L_G = 0.2 \left(\frac{S_u}{u_\Delta}\right)^3 \quad (2.82)$$

$$L_{OC} = 5.5 \left(\frac{\Delta D_c^3}{u_\Delta^3} \right)^{\frac{1}{4}} \quad (2.83)$$

D_c is the diffusivity of the progress variable.

$$FD_{HA} = \frac{7}{3} + \frac{1}{3} \frac{L_{OC}^4}{L_G^4 + L_{OC}^4} \quad (2.84)$$

3- Chakraborty et. al. provided a wrinkling factor model (Ξ_{CK}) from DNS analysis. It was developed in the LES fractal-based modelling for corrugated and thin reaction zones regimes, where it included a bridging function in terms of the outer and inner cut-off length scales, as shown in Eq. (2.85) (Chakraborty and Klein, 2008). The outer cut-off length scale was modelled as the filter width and the inner cut-off length (η_{CK}) was found to scale with the Gibson length scale in the corrugated regime and with the Kolmogorov length scale in the thin reaction zones regime. Therefore, η_{CK} and the fractal dimension (FD_{CK}) were modelled as a relation with Karlovitz number, as shown in Eqs. (2.86) and (2.87) (Chakraborty and Klein, 2008) respectively. The unburned gas properties are used to define the Karlovitz number in the current presentation.

$$\Xi_{CK} = e^{\left(\frac{-2.5\,\Delta}{\eta_{CK}}\right)} + \left[1 - 0.26\, e^{\left(\frac{-2.5\,\Delta}{\eta_{CK}}\right)}\right] \left(\frac{\Delta}{\eta_{CK}}\right)^{FD_{CK}-2} \quad (2.85)$$

$$\eta_{CK} = \left[0.345\, Ka_\Delta^{-2}\, e^{(-Ka_\Delta)} + \frac{6.41}{\sqrt{Ka_\Delta}} \left[1 - e^{(-Ka_\Delta)}\right]\right] \delta_z \quad (2.86)$$

$$FD_{CK} = 2 + \frac{1}{3}\, erf(2.0\, Ka_\Delta) \quad (2.87)$$

The error function (erf) is defined as shown in Eq. (2.88) (Wolfram MathWorld, 2018).

$$erf(\text{þ}) = \frac{2}{\sqrt{\pi}} \int_0^{\text{þ}} e^{-\text{ę}^2}\, d\text{ę} \quad (2.88)$$

4- Charlette et al. (Charlette, Meneveau and Veynante, 2002) provided a wrinkling factor model (Ξ_{CH}) in the LES fractal-based modelling, as shown in Eq. (2.89) (Katragadda, Chakraborty and Cant, 2012). The outer cut-off length scale was modelled as the filter width. The inner cut-off length scale (η_{CH}) was derived based on the

assumption that there was an equilibrium between flame production and destruction. The derived inner cut-off length scale was compared to the flame thickness, then the largest length was chosen, as shown in Eq. (2.90) (Charlette, Meneveau and Veynante, 2002). A constant value of 0.5 was used for the fractal dimension, while a dynamic procedure was proposed in a different study.

$$\Xi_{CH} = \left(1 + min\left(\frac{\Delta}{\delta_z}, \Gamma\ \frac{u_\Delta}{S_u}\right)\right)^{\frac{1}{2}} \tag{2.89}$$

$$\eta_{CH} = max\left(\frac{\Delta\ S_u}{\Gamma\ u_\Delta}, \delta_z\right) \tag{2.90}$$

Γ is an efficiency function, as shown in Eq. (2.91) (Katragadda, Chakraborty and Cant, 2012).

$$\Gamma = \Gamma\left(\frac{u_\Delta}{S_u}, \frac{\Delta}{\delta_z}, Re_\Delta\right) = \left[\left(\left(f_u^{-a_1} + f_\Delta^{-a_1}\right)^{\frac{-1}{a_1}}\right)^{-b_1} + f_{Re}^{-b_1}\right]^{\frac{-1}{b_1}} \tag{2.91}$$

The coefficients a_1, f_u, f_Δ, f_{Re} are defined in Eqs. (2.92)–(2.95) (Katragadda, Chakraborty and Cant, 2012) respectively. The constant b_1 was set to 1.4 (Katragadda, Chakraborty and Cant, 2012).

$$a_1 = 0.6 + 0.2\ e^{\left[-0.1\ \frac{u_\Delta}{S_u}\right]} - 0.2\ e^{\left[-0.01\ \frac{\Delta}{\delta_z}\right]} \tag{2.92}$$

$$f_u = 4\ \left(\frac{27}{110}\ C_{k1}\right)^{\frac{1}{2}} \left(\frac{18}{55}\ C_{k1}\right) \left(\frac{u_\Delta}{S_u}\right)^2 \tag{2.93}$$

$$f_\Delta = \left(\left(\frac{27}{110}\ C_{k1}\ \pi^{\frac{4}{3}}\right)\left[\left(\frac{\Delta}{\delta_z}\right)^{\frac{4}{3}} - 1\right]\right)^{\frac{1}{2}} \tag{2.94}$$

$$f_{Re} = \left(\frac{9}{55}\ e^{\left(-1.5\ C_{k1}\ \pi^{\frac{4}{3}}\ Re_\Delta^{-1}\right)}\right)^{\frac{1}{2}}\ Re_\Delta^{\frac{1}{2}} \tag{2.95}$$

The constant C_{k1} had a value of 1.5 (Katragadda, Chakraborty and Cant, 2012).

5- Muppala at al. provided an algebraic wrinkling factor model in the RANS formulation (Ξ_{MU}) as shown in Eq. (2.96) (Dinkelacker, Manickam and Muppala, 2011), presented using the LES notations. The model was parameterized against 100 experiments of lean methane-air, propane-air, and ethylene-air mixtures under a pressure that was ranged from 1 bar to 10 bar. Ξ_{MU} includes the effects of the deficient Lewis number, turbulent fluctuation, Reynolds number, and the pressure. The unburned molecular properties are used in the Reynolds number presentation as in (Hasslberger, Boeck and Sattelmayer, 2015). It was applied in a different study in the LES framework under the atmospheric pressure to flames in the boundary between wrinkled and corrugated regimes, in the thin reaction zones regimes, and close to the boundary between thin reaction zones and broken reaction zones regimes.

$$\Xi_{MU} = 1 + \frac{0.46}{Le}\ Re_{\Delta}^{0.25}\ \left(\frac{u_{\Delta}}{S_u}\right)^{0.3}\ \left(\frac{p}{p_0}\right)^{0.2} \tag{2.96}$$

6- Angelberger et al. provided a wrinkling factor model (Ξ_{AN}) in the LES framework for the corrugated flames, as shown in Eq. (2.97) (Katragadda, Chakraborty and Cant, 2012).

$$\Xi_{AN} = 1 + \text{r}\ \frac{u_{\Delta}}{S_u} \tag{2.97}$$

r was an efficiency function, as shown in Eq. (2.78).

7- Weller et al. provided a model for the flame wrinkling factor (Ξ_{WE}) in the LES framework for the corrugated flames, which was recast to the form shown in Eq. (2.98) (Katragadda, Chakraborty and Cant, 2012), the unburned properties are used in the current presentation.

$$\Xi_{WE} = 1 + 2\ \tilde{Y}_b \left(0.62\ \sqrt{\frac{u_{\Delta}}{S_u}}\ \ \frac{\rho_u\ u_{\Delta}\ L_{KO}}{\mu_u}\right) \tag{2.98}$$

8- Colin et al. provided a wrinkling factor model (Ξ_{CO}) in the LES framework for the corrugated flames, as shown in Eq. (2.99) (Katragadda, Chakraborty and Cant, 2012).

$$\Xi_{CO} = 1 + \frac{2\ ln(2)}{0.84\left(\sqrt{\frac{\rho_u\ u_\Delta\ \Delta}{\mu_u}} - 1\right)}\ \Gamma\ \frac{u_\Delta}{S_u} \tag{2.99}$$

Γ was an efficiency function, as shown in Eq. (2.78). The unburned properties and the filter width are used in the current presentation.

9- Pitsch and Lageneste (Pitsch and Duchamp de Lageneste, 2002) provided a model for the turbulent burning velocity in the LES framework for the corrugated flamelets and the thin reaction zones regimes, which was recast into a wrinkling factor model (Ξ_{PI}) in (Chakraborty and Klein, 2008), as shown in Eq. (2.100). The unburned properties are used in the current presentation.

$$\Xi_{PI} = 1 + \frac{u_\Delta}{S_u}\sqrt{\frac{2\left(\frac{u_\Delta}{S_u}\right)^2/Ka_\Delta^2}{1 + 0.5\left(\frac{u_\Delta}{S_u}\right)^2/Ka_\Delta^2}} \tag{2.100}$$

10- Katragadda et al. provided a wrinkling factor model (Ξ_{KA}) for the thin reaction zones flames in the LES fractal-based framework in addition to a bridging function, as shown in Eq. (2.101) (Katragadda, Chakraborty and Cant, 2012). The outer cut-off length scale was modelled as the filter width. The inner cut-off length scale was modelled as the thermal flame thickness. The bridging function included the ratio between the filter width and the inner cut-off length scale. The fractal dimension (FD_{KA}) was modelled using parameterization of the DNS data, which included effects of Karlovitz number, Reynolds number, and Lewis number of the deficient reactant, as shown in Eq. (2.102) (Katragadda, Chakraborty and Cant, 2012). The definitions that were used for Karlovitz number and Reynolds number contain constants to match the DNS data, as shown in Eqs. (2.103) and (2.104) (Katragadda, Chakraborty and Cant, 2012) respectively. FD_{KA} is turned to 2 in the laminar regime.

$$\Xi_{KA} = \left(1 - \frac{1}{1+e^{-60\left(\frac{\Delta}{\delta_{th}} - 1\right)}}\right) + \frac{1}{1+e^{-60\left(\frac{\Delta}{\delta_{th}} - 1\right)}}\left(\frac{\Delta}{\delta_{th}}\right)^{FD_{KA}-2} \tag{2.101}$$

$$FD_{KA} = 2 + \frac{1}{3}\, erf(3.0\, Ka_{\Delta 1}) \left[1 - exp\left(-0.1\left(\frac{Re_{\Delta 1}}{7.5}\right)^{1.6}\right)\right] Le^{-0.45} \qquad (2.102)$$

$$Ka_{\Delta 1} = 6.6 \left(\frac{\sqrt{k_\Delta}}{S_u}\right)^{3/2} \left(\frac{\delta_z}{\Delta}\right)^{1/2} \qquad (2.103)$$

$$Re_{\Delta 1} = 4.0\, \frac{\rho_u\, u_\Delta\, \Delta}{\mu_u} \qquad (2.104)$$

2.8 Turbulence–hydrodynamic & thermo-diffusive instabilities interaction

Propagation of laminar unstable flames at turbulent regime is subjected to two independent corrugations at different scales. Therefore, there would be a competition and an interaction between the two corrugations. The effect of turbulence on the hydrodynamic instability was studied theoretically in (Chaudhuri, Akkerman and Law, 2011) for a unity Lewis number. Two characteristic time scales were used to examine the interaction between the turbulence and the instability, which were the turbulence time scale and the instability time scale, defined as the inverse of the instability growth rate. Based on this study, the instability was developed in the vicinity of turbulence if the instability time scale was smaller than the turbulence time scale. The effect of turbulence on the instability for a self-similar flame, where corrugated surface is represented by a fractal, was only isolated in the form of moderating and suppressing the instability by introducing the so-called turbulence-induced effective DL inner cut-off. In another words, turbulence would change the fractal inner cut-off length scale of the instability. The increase of turbulence would increase the effective inner cut-off length scale until it reaches the outer cut-off length scale. Hence, the wrinkling due to the instability is supressed. The turbulent combustion regimes diagram was modified to include a boundary, which represents the regime, where the instability would be active in vicinity of turbulence, as shown in Fig. 2.13 (Chaudhuri, Akkerman and Law, 2011). According to that, the instablity could be active in the vicinity of turbulence in the wrinkled and corrugated regimes below the line of the instability limit.

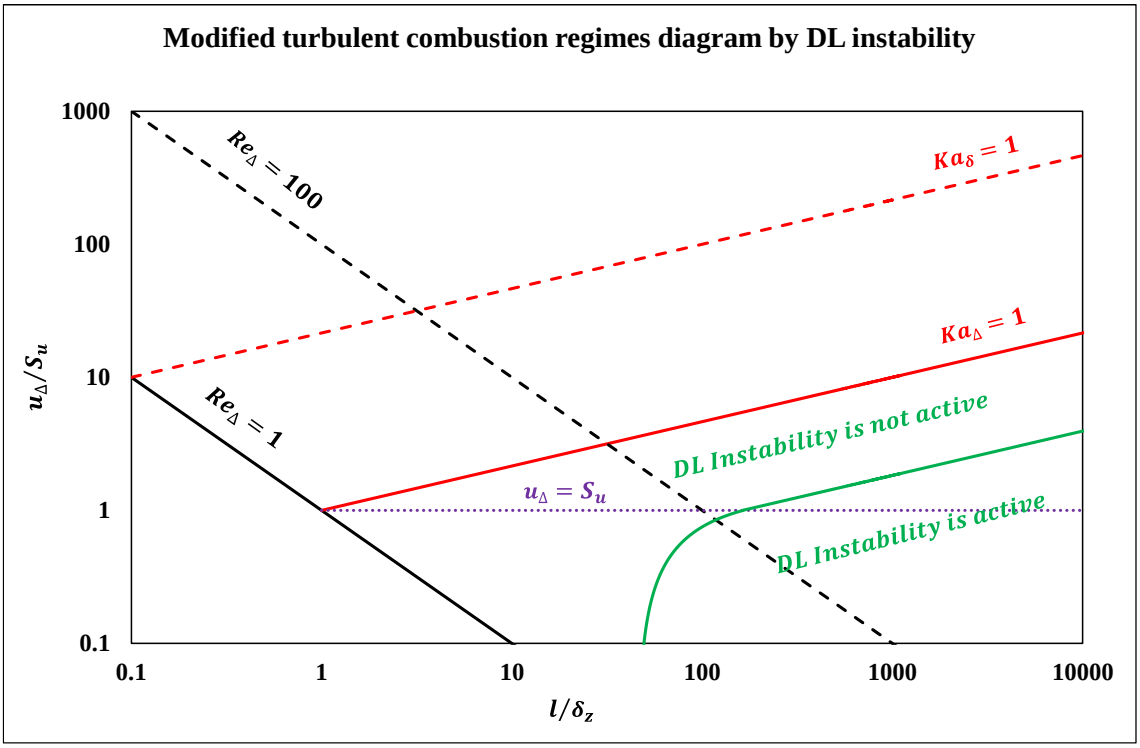

Figure 2.13: Modified turbulent combustion regimes diagram by DL instability (Chaudhuri, Akkerman and Law, 2011), the SGS notations are used in the current pressentation.

2.9 Propagation of detonation wave

Detonation wave is characterized by an increase in the pressure and density of the burned gas relative the unburned gas. That would require a shock wave combined with the chemical reaction.

2.9.1 Initialization of detonation wave

Detonation wave could be initialized by direct ignition, which would require to apply large explosive energy over a small volume. On the other hand, detonation wave could be initialized from DDT. DDT could occur by different mechanisms, two of them are as follows:

DDT could occur if the unburned mixture has a gradient in the reactivity i.e. a gradient in the chemical induction time (t_{ign}) (Oran and Gamezo, 2007; Ciccarelli and Dorofeev, 2008). t_{ign} is inversely proportional to the temperature. Therefore, the

unburned mixture could ignite starting from the location of the smallest t_{ign} and proceeds toward the locations of higher t_{ign}. Hence, a spontaneous reaction wave propagates with a velocity (u_{sp}), which is equal to the inverse of the spatial gradient of t_{ign}, as shown in Eq. (2.105) (Oran and Gamezo, 2007; Ciccarelli and Dorofeev, 2008).

$$u_{sp} = \frac{1}{\frac{dt_{ign}}{dx}} \tag{2.105}$$

If u_{sp} is approximately lying between the speed of sound and u_{CJ}, the spontaneous reaction wave could be coupled with the compression wave, which is produced due to the combustion and expansion of gases, and develops to a self-sustained detonation wave (Oran and Gamezo, 2007).

In a second mechanism, DDT could occur for a wrinkled flame while it accelerates behind a shock wave, if the wrinkling increases above a critical limit (Clavin, 2015).

2.9.2 Planar detonation wave (ZND structure)

The planar structure (ZND structure) of the detonation wave was suggested independently by Zel'dovich, Von Neumann, and Döring. ZND structure is a one-dimensional model, as shown in Fig. 2.14 (Matalon, 2017). ZND detonation is a propagated shock combined with chemical rection after an induction length. It contains three thermodynamic states: state 1 the pre-shock, state *N* is the post-shock, which is an inner state (Neumann state), and state (3) after the completion of the chemical reaction. The half reaction length is measured from the shock to the progress variable that has a value of 0.5 inside the reaction zone.

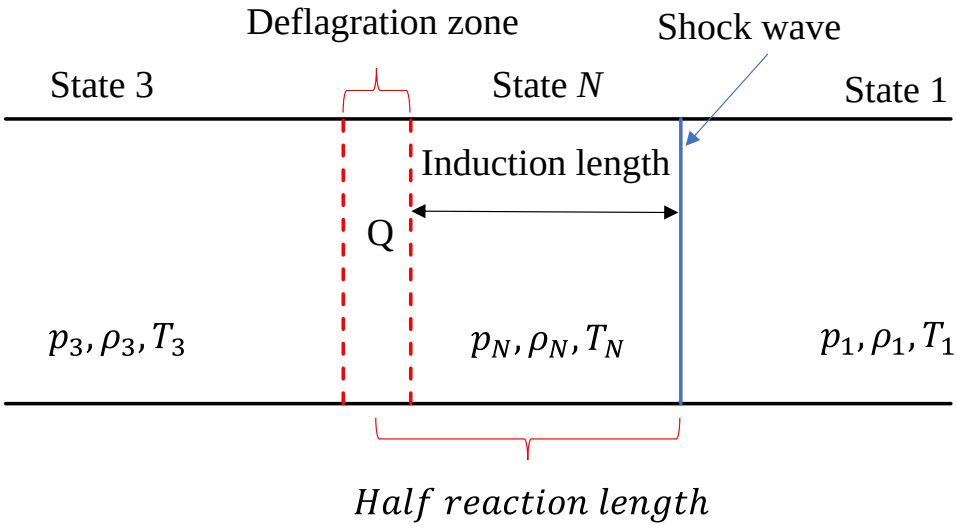

Figure 2.14: Schematic of the ZND detonation structure (Matalon, 2017).

The positions of the three states of the ZND detonation structure are shown in Fig. 2.15 (Matalon, 2017) with respect to the Rayleigh line and the Hugoniot curve. State (N) is located on the inert Hugoniot curve, which is obtained by setting the energy release to zero in the Hugoniot curve. State (3) is located on the Hugoniot curve as an overdriven detonation at point (S). The ZND model explains overdriven detonations up to the CJ detonation at point (J). CJ detonation is a self-driven detonation. Therefore, it does not affect by the downstream boundary condition, while the overdriven detonation requires a pushing mechanism to the gas, like a piston from behind.

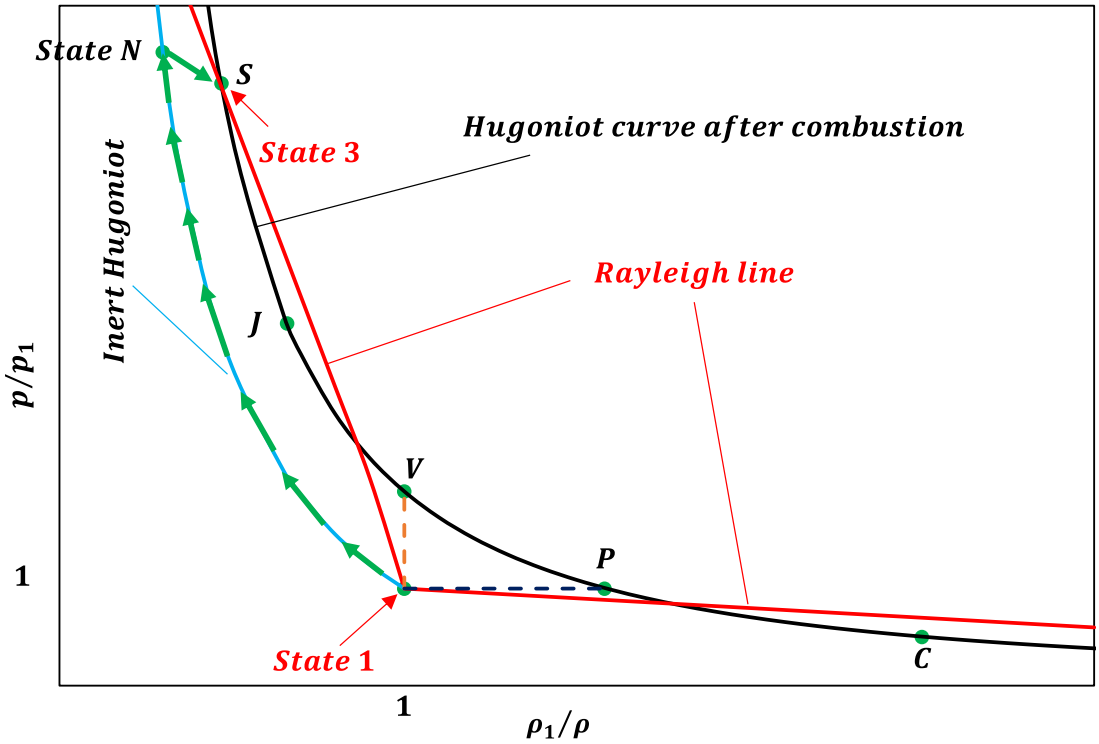

Figure 2.15: Positions of the ZND detonation states with respect to the Rayleigh line and the Hugoniot curve (Matalon, 2017).

2.9.3 Cellular detonation wave

Experiment and numerical simulation have shown that detonation wave is not planar. Detonation wave is unsteady, cellular, and three-dimensional. The detonation front is constructed from cells either of a Mach stem or an incident wave that are surrounded by other cells of opposite type i.e. an incident wave or a Mach stem, respectively. The incident wave and the Mach stem are interested in a point that is called the triple point and are formed a transverse wave and a shear layer. A schematic of a regular cellular detonation structure at two proceeding times, t_1 and t_2 with propagation is shown in Fig. 2.16 (Mahmoudi, Mazaheri and Parvar, 2013).

A Mach stem is propagated from point (A) at t_1, then it is replaced by an incident wave at t_2. This transition is due to the interaction between the triple points at point (B) and point (C) with the triple points from the surrounding cells. The interaction process is repeated at point (D) and a new Mach stem is generated. The interaction formed the detonation diamond cell.

The Mach stem is stronger than the incident wave hence, according to the ZND structure the temperature in the Neumann state after the Mach stem is higher than after the incident shock. Therefore, the detonation thickness after the Mach stem is smaller than after the incident wave. Hence, the detonation thickness increases along the diamond cell. The detonation velocity after the formation of the Mach stem is highest, then it decreases along the diamond cell. Therefore, both the detonation thickness and detonation velocity are pulsed with every diamond cell (Ramamurthi, 2014).

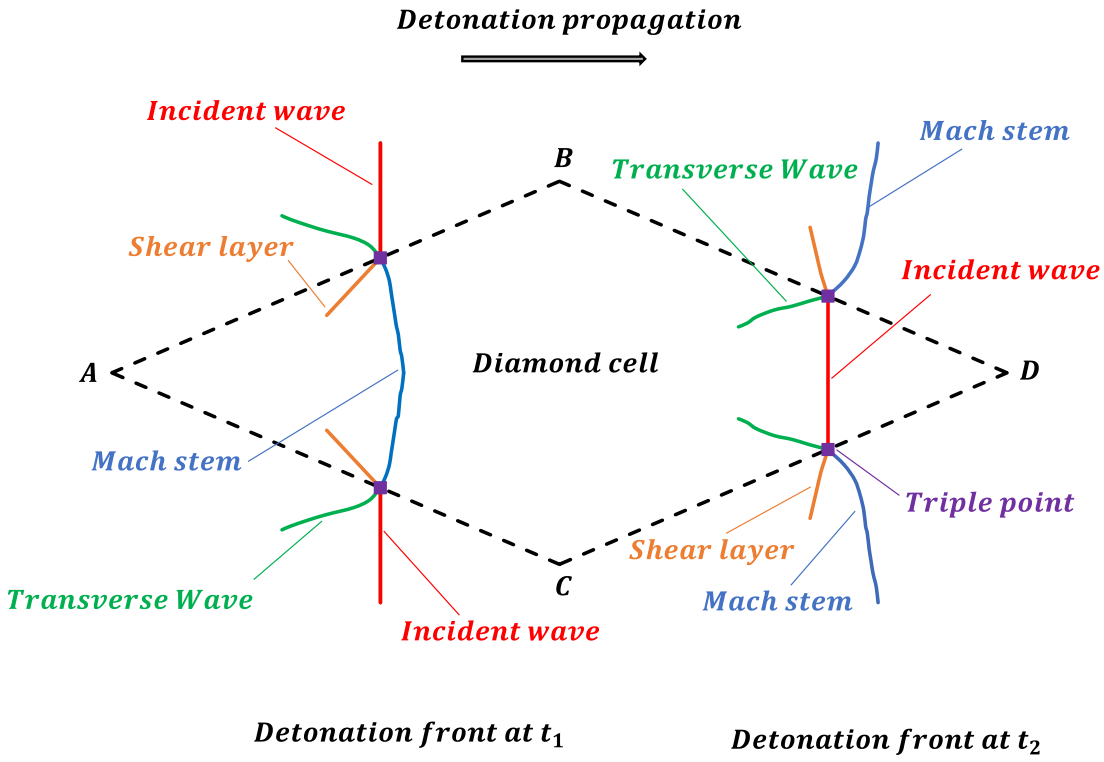

Figure 2.16: Schematic of a regular cellular detonation with propagation at two proceeding times t_1 and t_2 (Mahmoudi, Mazaheri and Parvar, 2013).

2.10 Flame-generated turbulence

Flame-generated turbulence is another aspect of the interaction between flame and turbulence. Different efforts attempted to characterize and model the effect of flame on turbulence, a brief review of these studies is as follows: Nishiki et al. (Nishiki *et al.*, 2002) performed DNS with turbulent intensity close to the laminar burning velocity and a unity Lewis number. They provided models for the pressure and dissipation terms in the turbulent kinetic energy equation in the context of RANS modelling. Chakrabory et al. (Chakraborty, Katragadda and Cant, 2011) performed DNS with a single step chemistry

under a wide range of Lewis numbers from 0.34 to 1.2 and a moderate Reynolds number. They have shown that flame-generated turbulence increases with the decrease of Lewis number inside the flame brush. They provided, in the context of RANS formulation, models for the terms in the turbulent kinetic energy equation in the thin reaction zones regime. Wang and Abraham (Wang and Abraham, 2017) used DNS to provide scaling of the terms of the turbulent kinetic energy for lean methane-air flames under high pressure and temperature in the thin reaction zones regime in the context of RANS modelling.

Robin et al. (Robin, Mura and Champion, 2011) applied the velocity splitting procedure to the DNS of Nishiki et al. (Nishiki *et al.*, 2002) to study flame-generated turbulence in the flamelet regime. They were argued that if small scale of turbulence eddies does not produce large effect of the internal structure of the flame. Their results could be used beyond the flamelet regime. Based on this analysis two algebraic models were derived in two succeeding studies (Champion, Robin and Mura, 2012; Robin, Mura and Champion, 2012) for flame-generated turbulence (K_{fg}) (kg/ms^2) in the context of RANS formulation. The advantage of the algebraic models is that: pressure and dissipation terms of the turbulent kinetic energy equation are similar to the non-reactive flow (Robin, Mura and Champion, 2012). Therefore, the same turbulent kinetic energy equation of non-reactive flow could be used and the effect of combustion on turbulence is only considered through K_{fg}. K_{fg} enters the reactive flow system of equations as a source term in the momentum equation in a differential form $\left(-\nabla \cdot K_{fg}\right)$.

2.11 Conclusions

A brief review of the SOTA in modelling deflagration and detonation is presented. Based on the resolution of the DDT simulations, which are shown in Table 2.2, the closure of the chemical reaction rate using flame wrinkling models are considered to be more suitable for large industrial scales. The necessary physics to understand deflagration and detonation propagations are presented at the rest of the chapter. Based on the presented elements, a flame wrinkling model which is suitable for both deflagration and detonation will be developed in the next chapter. A brief review of the modelling of flame-generated turbulence is presented. Hence, the algebraic closure is more suitable for practical modelling, since it would use the same turbulent kinetic energy equation of non-reactive flow.

CHAPTER 3. PHYSICAL AND MATHEMATICAL MODELLING OF FLAME DEFLAGRATION AND DEFLAGRATION-TO-DETONATION TRANSITION

3.1 Introduction

This chapter presents conservation equations for reactive flow in the LES framework and a procedure for modelling the unclosed terms. A proposed model for the chemical reaction rate is provided based on flame wrinkling concept, which includes wrinkling due to instabilities and wrinkling due to turbulence. A stretching factor for partially or full flame quenching is presented and incorporated in the chemical reaction rate model. An algebraic model for flame-generated turbulence is presented and incorporated in the momentum equation. The developed model is for deflagration and detonation of the hydrogen-air mixtures. However, it could be used for other fuels by changing the corresponding physical properties.

3.2 Conservation equations for reacting flow

Reactive flow is treated as a continuum flow that is described by conservation equations for mass, momentum, energy, and species mass fraction. Different physical phenomena are involved in the reactive flow including convection, diffusion, chemical kinetics, and turbulence generation and dissipation. These phenomena are spread over large spatial and time scales. The range of the spatial scale is from the geometrical scale, for turbulence generation, which could be in the order of meters, to the flame front thickness, which is in the order of 1 to 0.1 mm for typical hydrogen-air mixtures at the atmospheric pressure and temperature. The technique of solving all the spatial and time scales is called DNS. At current computing power, it is only performed for tiny geometries in the order of mm to study physical phenomena. A second technique is called RANS that is based on solving statistical average of the governing equations and modelling the total turbulent spectrum. It is heavily used in industrial applications. A third technique lying between the above two techniques is called LES. It is based on solving spatial filtering of the governing equations and modelling the small spectrum of turbulence.

The filtering process divides the variable (q) into resolved term ($\tilde{q}$) and sub-grid scale term (q_Δ), as shown in Eq. (3.1) (McDonough, 2007). Two spatial filtering

operations could be used in LES for a variable (q): LES filtering per unit volume ($\bar{q}$) and Favre filtering per unit mass ($\tilde{q}$) (Cecere *et al.*, 2011), defined in Eq. (3.2) (Katragadda, Chakraborty and Cant, 2012).

$$q = \tilde{q} + q_{\Delta} \tag{3.1}$$

$$\tilde{q} = \frac{\overline{\rho q}}{\bar{\rho}} \tag{3.2}$$

q is a general variable. The LES formulation of the conservation equations are given based on (Veynante and Poinsot, 1997; Génin and Menon, 2010; Kessler, Gamezo and Oran, 2010; Molkov, 2012; ANSYS-Fluent, 2015; NASA-GRC, 2015) in Eqs. (3.3)–(3.6) for the mass, momentum, energy, and species mass fraction equations, respectively.

$$\frac{\partial \bar{\rho}}{\partial t} + \frac{\partial \bar{\rho}\, \tilde{u}_j}{\partial x_j} = 0 \tag{3.3}$$

$$\frac{\partial \bar{\rho}\, \tilde{u}_i}{\partial t} + \frac{\partial \bar{\rho}\, \tilde{u}_i\, \tilde{u}_j}{\partial x_j} = -\frac{\partial \bar{p}}{\partial x_i} + \frac{\partial}{\partial x_j}\left(\tilde{\tau}_{ij}\right) - \frac{\partial}{\partial x_j}\tau_{ij}\Big|_{sgs} + \bar{\rho}\, g_j - \frac{\partial K_{fg}}{\partial x_i} \tag{3.4}$$

$$\begin{aligned}\frac{\partial \bar{\rho}\, \tilde{E}}{\partial t} + \frac{\partial\left(\bar{\rho}\, \tilde{E}\tilde{u}_j + \tilde{u}_j \bar{p}\right)}{\partial x_j} \\ = \frac{\partial}{\partial x_j}\left(K|_{eff}\frac{\partial \tilde{T}}{\partial x_j} - \sum_{s\,=\,1:\,N} h_s \vec{J}_s + \tau_{ij}\Big|_{eff}\tilde{u}_j\right) + \bar{\rho} g_j \tilde{u}_j + S_E\end{aligned} \tag{3.5}$$

$$\frac{\partial \bar{\rho}\, \tilde{Y}_s}{\partial t} + \frac{\partial \bar{\rho}\, \tilde{Y}_s\, \tilde{u}_j}{\partial x_j} = -\frac{\partial \vec{J}_s}{\partial x_j} + S_{Y_s} \tag{3.6}$$

u, T, E, Y, τ, h, $\vec{J}$, S_E (Kg/ms^3), S_{Y_s} ($Kg/m^3 s$), g, and x are velocity, temperature, total energy, species mass fraction, shear stress, sensible enthalpy, diffusion flux, heat of chemical reaction (source term of the energy equation), chemical reaction rate (source term of the species mass fraction equations), gravitation acceleration, and spatial coordinate respectively. i and j are indices that have values from 1 to 3. s is a specie index that has a value from 1 to the total number of species (N). In the current study, chemical reaction is described by one step reaction and the total number of species

is 3 (air, hydrogen, and burned gas). Molecular shear stresses are defined in Eq. (3.7) (Génin and Menon, 2010).

$$\tilde{\tau}_{ij} = \mu \left(\frac{\partial \tilde{u}_i}{\partial x_j} + \frac{\partial \tilde{u}_j}{\partial x_i} - \frac{2}{3} \frac{\partial \tilde{u}_j}{\partial x_j} I_{ij} \right) \tag{3.7}$$

μ is the molecular viscosity and I_{ij} is a Kronecker delta tensor.

$\tau_{ij}\big|_{sgs}$, $\tau_{ij}\big|_{eff}$, and $K|_{eff}$ are SGS terms due to filtering the conservation equations, which are the SGS stress tensor, effective shear stresses, and effective thermal conductivity respectively. The SGS stresses are closed based on an eddy viscosity concept, as shown in Eq. (3.8) (ANSYS-Fluent, 2015).

$$\tau_{ij}\big|_{sgs} = \frac{\partial}{\partial x_j} \left(\overline{\rho u_i u_j} - \bar{\rho}\, \tilde{u}_i\, \tilde{u}_j \right) = -\mu_{tur} \left(\frac{\partial \tilde{u}_i}{\partial x_j} + \frac{\partial \tilde{u}_j}{\partial x_i} \right) + \frac{2}{3} \bar{\rho}\, k_\Delta\, I_{ij} \tag{3.8}$$

μ_{tur} is the turbulent viscosity, which is defined in terms of the SGS characteristic velocity $\sqrt{k_\Delta}$ and the SGS characteristic length Δ, as shown in Eq. (3.9) (Génin and Menon, 2010; ANSYS-Fluent, 2015). Δ is defined as the filter length, which is equal to the cubic root of the computational grid cell volume in ANSYS-Fluent implementation (ANSYS-Fluent, 2015).

$$\mu_{tur} = C_k\, \bar{\rho} \sqrt{k_\Delta}\, \Delta \tag{3.9}$$

A transport equation is resolved for the SGS turbulent kinetic energy (i.e. for the SGS characteristic velocity), as shown in Eq. (3.10) (ANSYS-Fluent, 2015). The transport equation does not include the assumption of the balance between turbulence generation and turbulent dissipation rate. Therefore, it is expected to be more accurate than the SGS turbulent algebraic models (ANSYS-Fluent, 2015).

$$\bar{\rho} \frac{\partial k_\Delta}{\partial t} + \bar{\rho} \frac{\partial \tilde{u}_j\, k_\Delta}{\partial x_j} = -\tau_{ij}\big|_{sgs} \frac{\partial \tilde{u}_i}{\partial x_j} - C_\varepsilon\, \bar{\rho}\, \frac{k_\Delta^{\frac{3}{2}}}{\Delta} + \frac{\partial}{\partial x_j} \left(\frac{\mu_{tur}}{\sigma_k} \frac{\partial k_\Delta}{\partial x_j} \right) \tag{3.10}$$

C_k and C_ε are constants, which are calculated using a dynamic procedure during running the calculations and σ_k is a constant equal to 1.0 (ANSYS-Fluent, 2015). The

idea of the dynamic procedure is based on using a second filter for the governing equations, which is called the test filter and is usually larger than the grid filter width. The model constants are calculated from the information provided from the difference between the two resolutions of the governing equations using the two filters.

The effective shear stress ($\tau_{ij}\big|_{eff}$) is the sum of the molecular and turbulent stresses, as shown in Eq. (3.11).

$$\begin{aligned}\tau_{ij}\big|_{eff} &= \tilde{\tau}_{ij} - \tau_{ij}\big|_{sgs} \\ &= (\mu + \mu_{tur})\left(\frac{\partial \tilde{u}_i}{\partial x_j} + \frac{\partial \tilde{u}_j}{\partial x_i}\right) - \frac{2}{3}\,\mu\,\frac{\partial \tilde{u}_j}{\partial x_j}\,I_{ij} - \frac{2}{3}\bar{\rho}\,k_\Delta\,I_{ij}\end{aligned} \tag{3.11}$$

The total energy (E) includes the effects of the sensible enthalpy, pressure work, and kinetic energy, as shown in Eq. (3.12) (ANSYS-Fluent, 2015).

$$\tilde{E} = \tilde{h} - \frac{\bar{p}}{\bar{\rho}} + \frac{\tilde{u}_j^2}{2} \tag{3.12}$$

The mixture sensible enthalpy is modelled using the mass fraction mixing law of the constituent species, as shown in Eq. (3.13) (ANSYS-Fluent, 2015). The sensible enthalpy of every species is calculated, as shown in Eq. (3.14) (ANSYS-Fluent, 2015) using the specific heat of the species.

$$\tilde{h} = \sum_{s\,=\,1:\,N} \tilde{h}_s\,\tilde{Y}_s \tag{3.13}$$

$$\tilde{h}_s = \int_{\tilde{T}_{ref}=0}^{\tilde{T}} Cp_s\,d\tilde{T} \tag{3.14}$$

Density of the mixture is calculated from the ideal gas law. The specific heat of the mixture is calculated from the mass fraction mixing law of the constituent species, as shown in Eq. (3.15) (ANSYS-Fluent, 2015).

$$Cp = \sum_{s=\,1:\,N} Cp_s\,\tilde{Y}_s \tag{3.15}$$

The molecular viscosity and thermal conductivity of the mixture are calculated from the ideal gas mixing law from the constituent species according to the kinetic theory, as shown in Eqs. (3.16) and (3.17) (ANSYS-Fluent, 2015) respectively.

$$\mu = \sum_{s=1:N} \frac{\mu_s \tilde{X}_s}{\sum_{n=1:N} \tilde{X}_n \phi_{sn}} \tag{3.16}$$

$$K = \sum_{s=1:N} \frac{K_s \tilde{X}_s}{\sum_{n=1:N} \tilde{X}_n \phi_{sn}} \tag{3.17}$$

ϕ_{sn} is defined in Eq. (3.18) (ANSYS-Fluent, 2015).

$$\phi_{sn} = \frac{\left[1 + \left(\frac{\mu_s}{\mu_n}\right)^{\frac{1}{2}} \left(\frac{Mw_n}{Mw_s}\right)^{\frac{1}{4}}\right]^2}{\left[8\left(1 + \frac{Mw_s}{Mw_n}\right)\right]^{\frac{1}{2}}} \tag{3.18}$$

X_s is the mole fraction of species s and Mw is the molecular weight.

The diffusion of energy is contributed by the conduction, species diffusion, and viscous dissipation (Molkov, 2012; ANSYS-Fluent, 2015). The diffusion flux ($\vec{J}$) of the species is defined using the Fick's law approximation in terms of laminar and turbulent ingredients, as shown in Eq. (3.19) (ANSYS-Fluent, 2015). The molecular, laminar, mass diffusion coefficient (D) is defined in Eq. (3.20) (Molkov, 2012) in terms of the mixture molecular viscosity and a constant value of 0.7 for the molecular, laminar, Schmidt number (Sc). The turbulent mass diffusion coefficient (D_{tur}) is defined in terms of the turbulent viscosity and turbulent Schmidt number (Sc_{tur}), as shown in Eq. (3.21) (ANSYS-Fluent, 2015). Sc_{tur} is calculated dynamically during running the calculation, based on the test filter procedure. The final form of $\vec{J}$ is shown in Eq. (3.22) (Molkov, 2012; ANSYS-Fluent, 2015).

$$\vec{J}_s = -\bar{\rho}\,(D_s + D_{tur})\,\frac{\partial \tilde{Y}_s}{\partial x_n} \tag{3.19}$$

$$\bar{\rho}\, D_s \;=\; \frac{\mu}{Sc} \;=\; \frac{\mu}{0.7} \tag{3.20}$$

$$\bar{\rho}\;\; D_{tur} \;=\; \frac{\mu_{tur}}{Sc_{tur}} \tag{3.21}$$

$$\vec{J}_s \;=\; -\;\left(\frac{\mu}{0.7} + \frac{\mu_{tur}}{Sc_{tur}}\right)\frac{\partial\, \tilde{Y}_s}{\partial x_n} \tag{3.22}$$

The effective thermal conduction coefficient ($K|_{eff}$) is defined as the sum of the molecular thermal conduction coefficient and turbulent conduction coefficient, as shown in Eq. (3.23) (ANSYS-Fluent, 2015). The molecular, laminar, thermal conduction coefficient (K) is defined in Eq. (3.24) (Molkov, 2012) in terms of the mixture molecular viscosity and a constant value of 0.7 for the molecular, laminar, Prandtl number (Pr). The turbulent conduction coefficient is defined using the turbulent viscosity and turbulent Prandtl number (Pr_{tur}), as shown in Eq. (3.25) (ANSYS-Fluent, 2015). Pr_{tur} is calculated dynamically during running the calculation, based on the test filter procedure. The final form of $K|_{eff}$ is shown in Eq. (3.26) (ANSYS-Fluent, 2015).

$$K|_{eff} \;=\; K \;+\; K_{tur} \tag{3.23}$$

$$K = \;\frac{\mu\;\; Cp}{Pr} \;=\; \frac{\mu\;\; Cp}{0.7} \tag{3.24}$$

$$K_{tur} \;=\; \frac{\mu_{tur}\;\; Cp}{Pr_{tur}} \tag{3.25}$$

$$K|_{eff} \;=\; \frac{\mu\;\; Cp}{0.7} \;+\; \frac{\mu_{tur}\, Cp}{Pr_{tur}} \tag{3.26}$$

So far, all the terms in the governing equations are closed except the chemical reaction rates, heat of chemical reaction, and flame-generated turbulence.

3.3 Chemical reaction rate

In the current study, computational grid sizes are larger than the flame thickness. Hence, the inner flame structure is not resolved at the computational grid and it is assumed that, at any moment the concentration of the burned gas is at the chemical equilibrium condition. Since, the Mass fraction of the burned gas ($\tilde{Y}_b$) represents the progress variable. The progress variable equation is used to model the combustion. The chemical reaction rate of the burned gas (S_{Y_b}) (Kg/m^3S), source term of the progress variable equation, is modelled according to the turbulent burning velocity concept incorporating the stretch, quenching, factor (G), as shown in Eq. (3.27) (Ettner, Vollmer and Sattelmayer, 2014), presented in the LES notations.

$$S_{Y_b} = \rho_u \, S_{tur} \, G \, \left|\nabla \, \tilde{Y}_b\right| \tag{3.27}$$

Subscripts u and b refer to unburned and burned gas, respectively. A model for the turbulent burning velocity requires the value of the laminar burning velocity and flame wrinkling. Flame wrinkling includes the net effect of the instabilities and the turbulence.

3.3.1 Modelling laminar burning velocity at the reference condition (S_{u0})

Laminar burning velocity at the standard initial atmospheric pressure and temperature of 298 K (S_{u0}), which is provided by Alekseev (Alekseev, Christensen and Konnov, 2015) is chosen in the current study. It is approximated by the polynomials shown in Eq. (3.28). The Alekseev burning velocity predicts smaller values compared with the experiments for the leaner limit, as shown in Fig. 2.4 (Alekseev, Christensen and Konnov, 2015). Therefore, S_{u0} is limited in the current study at the value corresponds to hydrogen concentration of 12.7% for concentrations less than this limit.

$$S_{u0} = 232.8\, X_{H_2}^4 - 493.55\, X_{H_2}^3 + 261.01\, X_{H_2}^2 - 38.331\, X_{H_2} + 1.7122$$

$$0.127 < X_{H_2} < 0.301$$

$$S_{u0} = -4046.1\, X_{H_2}^4 + 5622.3\, X_{H_2}^3 - 2963.2\, X_{H_2}^2 + 708.22\, X_{H_2} - 62.542$$

$$0.301 \leq X_{H_2} \leq 0.4$$

$$S_{u0} = 1440.1\, X_{H_2}^4 - 2578.5\, X_{H_2}^3 + 1694.2\, X_{H_2}^2 - 485.92\, X_{H_2} + 54.334 \quad (3.28)$$

$$0.4 < X_{H_2} \leq 0.506$$

$$S_{u0} = 32.209\, X_{H_2}^3 - 68.602\, X_{H_2}^2 + 39.076\, X_{H_2} - 3.7917$$

$$0.506 < X_{H_2} \leq 0.75$$

3.3.2 Modelling the effect of the pressure and temperature of the unburned gas on the laminar burning velocity (S_u)

The literature review provides different correlations for the effects of the temperature and pressure of the unburned gas on the laminar burning velocity. Therefore, to determine the capabilities of the prediction of these correlations, laminar burning velocity of the stoichiometric hydrogen-air mixture is calculated using different correlations, as shown in Fig. 3.1. The calculations start from the initial reference condition of the atmospheric pressure and temperature of 298 *K* and go under an adiabatic change of the temperature and pressure of the unburned gas.

Table 3.1 summarizes the parameters used to calculate the correlations in Fig. 3.1. The calculation of the laminar burning velocity based on the data in (Ettner, Vollmer and Sattelmayer, 2014) and the extrapolation based on the data in (Jordan, 2007; Molkov, 2012) are done under the full pressure range.

Table 3.1: Summary of the parameters for calculating the correlations of the laminar burning velocity.

Correlations	S_u	S_{u0}	T_0	p_0	β_1	β_2
Hu 2009	Eq. (2.12)	2.406 m/s	303 K	0.1 MPa	E. (2.13)	Eq. (2.14)
Gerke 2010 Chemical kinetics	Eq. (2.27)	Eq. (2.28)	500 K	20 bar	Eq. (2.29)	Eq. (2.30)
Ravi 2012	Eq. (2.16)	Eq. (2.17)	500 K	10 atm	Eq. (2.18)	Eq. (2.19)
Verhelst 2011	Eq. (2.20)	Eq. (2.21)	300 K	N/A	Eq. (2.22)	N/A
Ettner 2014	Eq. (2.7)	Eq. (3.28), $X_{H_2} = 0.295$	298 K	1 atm	1.75	-0.2
Extrapolation of Jordan 2007	Eq. (2.7)	Eq. (3.28), $X_{H_2} = 0.295$	298 K	1 atm	1.7	0.09
Gerke 2010 Experiment	Eq. (2.23)	Eq. (2.24)	600 K	20 bar	Eq. (2.25)	Eq. (2.26)
Milton 1984	Eq. (2.15)	217 cm/s	298 K	1 atm	1.26	0.26
Dahoe 2005	Eq. (2.7)	2.139 m/s at 291 K	291 K	1 bar	1.4	0.194
Jordan 2007	Eq. (2.7)	Eq. (3.28), $X_{H_2} = 0.295$	298 K	1 atm	1.7	0.09

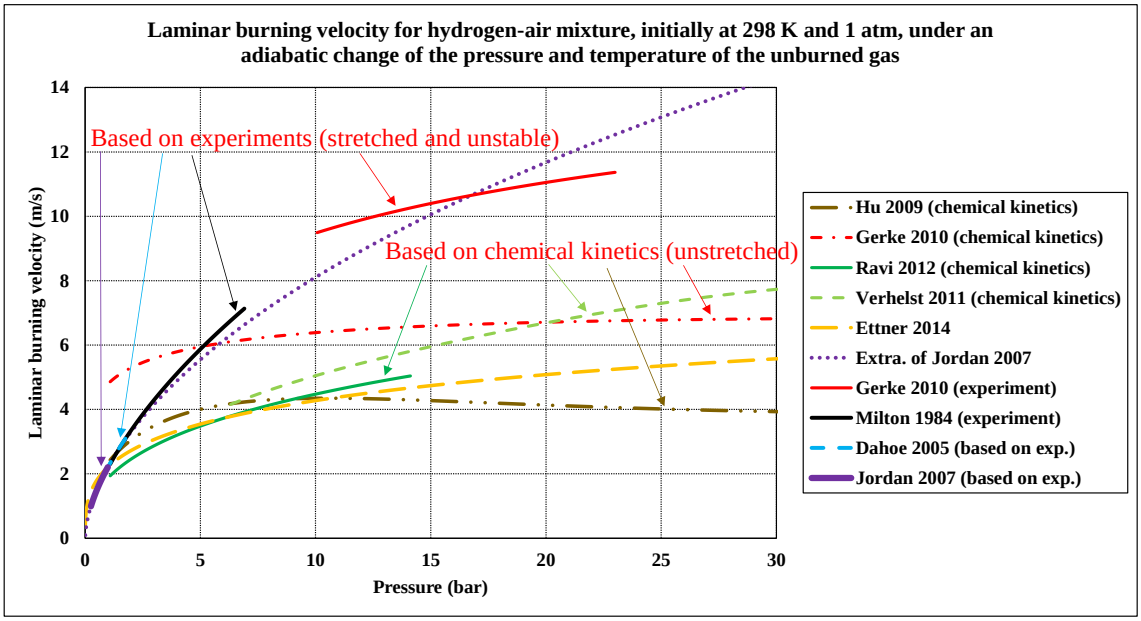

Figure 3.1: Laminar burning velocity for a stoichiometric hydrogen-air mixture, initially at the atmospheric pressure and temperature of 298 K, under an adiabatic change of the temperature and pressure of the unburned gas.

There is difference in the values of S_u in Fig. 3.1. The predicted values of S_u from the experimental correlations are larger than the predicted values from the chemical kinetics correlations. It is expected, as the burning velocities of the experiments, from which the experimental correlations were developed, included the effects of flame instabilities and stretch (Gerke *et al.*, 2010; Verhelst *et al.*, 2011), while S_u from the chemical kinetics represents the stable and unstretched laminar burning velocity.

There is a close matching between the experimental correlations of Dahoe and Milton, at low pressure, while the trend of the experimental correlation of Gerke could match the trend of Milton and determines the locus of the experimental laminar burning velocity. The values of the laminar burning velocity from the correlations based on the chemical kinetics are different. There is no experiment for a stable and unstretched laminar burning velocity at high pressure, in the order of 20 bar and above. Therefore, there is a large uncertainty in S_u at high pressure. A similar conclusion was derived for the methane-air mixture in (Poinsot, 2016), where the discrepancy in the prediction of different chemical schemes was related to the less of knowledge about chemistry in the condition of high pressure. Another source of the discrepancy between the correlations

based on the chemical kinetics in Fig. 3.1, could be related to the relative error in constructing the correlations from the original chemical kinetics data.

The exponents β_1 and β_2, provided in Table 2.3, provide values for the pressure exponent $\in$ that are in the same order of the values recommended by (Babkin, 2003) in pressure close to the atmospheric pressure. Despite the range of the calculation of the laminar burning velocity in Fig. 3.1 based on the data presented in (Jordan, 2007; Molkov, 2012) is below the atmospheric pressure, the extrapolation under the full pressure range based on using the same data from (Jordan, 2007; Molkov, 2012) in Fig. 3.1, provides prediction close to the experimental correlations of Dahoe, Milton, and Gerke. In addition to, the data presented in (Jordan, 2007; Molkov, 2012) covers the range of the hydrogen model fraction from 0.15 to 0.7. Therefore, the effect of the pressure and temperature of the unburned gas on the laminar burning velocity is calculated in the current study based on the exponents β_1 and β_2, provided in Table 2.3.

β_1 and β_2 are approximated in Eqs. (3.29) and (3.30) respectively. Values of β_1 and β_2 corresponding to hydrogen mole fraction of less than 0.15 or larger than 0.7, are calculated at the hydrogen mole fraction of 0.15 and 0.7, respectively.

$$\beta_1 = 13.053\, X_{H_2}^2 - 11.766\, X_{H_2} + 4.0443 \qquad 0.15 \le X_{H_2} \le 0.7 \tag{3.29}$$

$$\beta_2 = 34.039\, X_{H_2}^3 - 24.423\, X_{H_2}^2 + 6.5996\, X_{H_2} - 0.6053 \qquad 0.15 \le X_{H_2} < 0.295$$

$$\beta_2 = 0.1818\, X_{H_2} + 0.0364 \qquad 0.295 \le X_{H_2} < 0.35$$

$$\beta_2 = 0.1 \quad , \quad 0.35 \le X_{H_2} \le 0.5 \tag{3.30}$$

$$\beta_2 = 133.33\, X_{H_2}^4 - 320\, X_{H_2}^3 + 285.67\, X_{H_2}^2 - 112.9\, X_{H_2} + 16.8 \qquad 0.5 < X_{H_2} \le 0.7$$

The temperature of the unburned gas is assumed to be under an adiabatic change for all the cases in the present work. Therefore, the laminar burning velocity is calculated in the current study, as shown in Eq. (2.11).

Figure 3.2 shows the thermodynamic process diagram for flame propagation under an adiabatic compression of the temperature and pressure of the unburned gas. Equation (2.11) provides a correction to the laminar burning velocity if the initial temperature $T_{initial}$ is different from the reference value T_0.

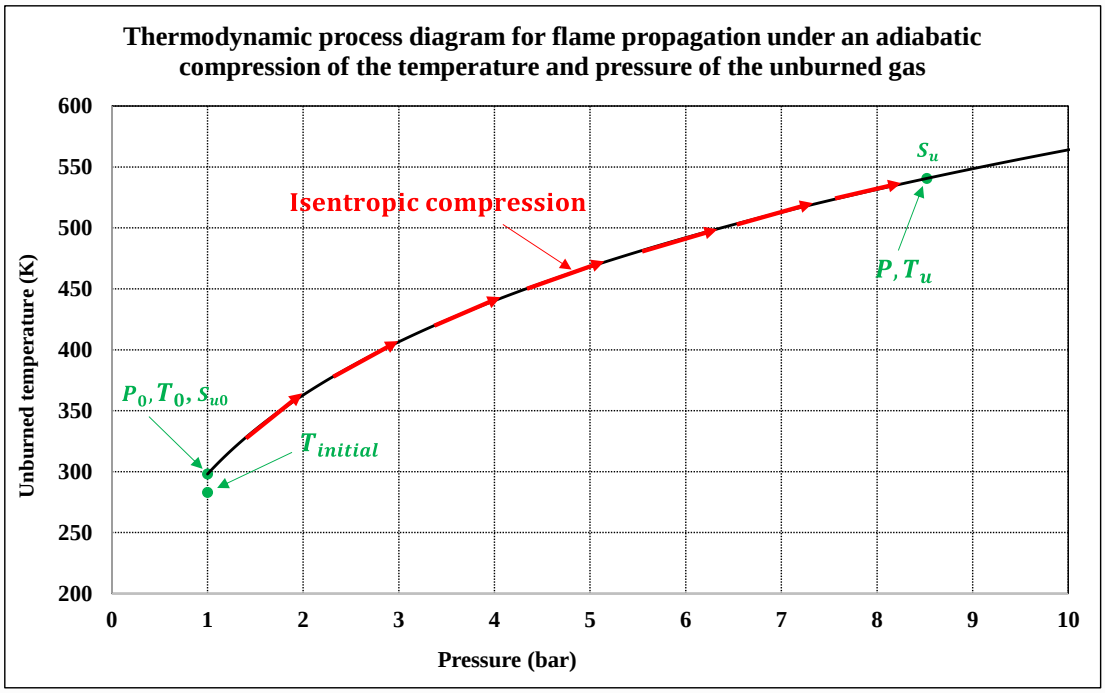

Figure 3.2: Thermodynamic process diagram for flame propagation under an adiabatic compression of the pressure and temperature of the unburned gas.

3.3.3 Modelling hydrodynamic & thermo-diffusive instabilities wrinkling factor (Ξ_{ins})

Hydrodynamic & thermo-diffusive instabilities increase the flame surface area through the formation of cellular structure. Therefore, the burning velocity increases following a power law (Kim *et al.*, 2015; Bauwens, Bergthorson and Dorofeev, 2017). The effect of these instabilities is treated in the current study through a multiplier term to the laminar burning velocity, which is called the instabilities wrinkling factor (Ξ_{ins}). The instabilities wrinkling factor is applied after the flame passes R_0. The effect of the weakly

stretched before R_0 on the flame is neglected in the current study. R_0 is modelled using Eq. (3.31), which approximates the experimental data in Fig. 2.8.

$$R_0 = 7.7818\, X_{H_2}^4 - 7.9147\, X_{H_2}^3 + 3.4196\, X_{H_2}^2 - 0.467\, X_{H_2} + 0.0368 \qquad (3.31)$$

Ξ_{ins} is modelled using the fractal description based on (Bychkov and Liberman, 2000; Addabbo, Bechtold and Matalon, 2002; Chaudhuri, Akkerman and Law, 2011). Fractal modelling requires defining the outer cut-off length scale (λ_{max}), inner cut-off length scale (λ_{min}), and fractal dimension (FD_{ins}). λ_{max} is calculated from Eq. (2.57), which is related to R. R should be limited by the geometric constrains (Gouldin, 1987; Im, 2018). Therefore, when the flame is propagated inside a bounded enclosure, it is proposed in the current study that R does not increase more than half of the shortest length of the enclosure in the direction perpendicular to the flame propagation. λ_{min} is calculated from the flame dispersion relations weather the planar or spherical i.e. from Eqs. (2.44) or (2.58) respectively. The fractal dimension due to instabilities (FD_{ins}) could have values from 2.2 to 2.25 (Kwon, Rozenchan and Law, 2002). In the current study, a fixed value of 2.2 is used for the three simulated cases. The proposed model in the current study for the instabilities wrinkling factor is shown in Eq. (3.32).

$$\begin{aligned} \Xi_{ins} &= \left(\frac{\lambda_{max}}{\lambda_{min}}\right)^{FD_{ins}-2} \times erf\left(20.0 \times \left(\frac{R}{R_0} - 0.9\right)\right) \\ &= \left(\frac{2\,\pi\,R}{f_{min}\,\lambda_{min}}\right)^{FD_{ins}-2} \times erf\left(20.0 \times \left(\frac{R}{R_0} - 0.9\right)\right) \end{aligned} \qquad (3.32)$$

The instabilities wrinkling factor is applied smoothly starting from 90% of R_0 using the error function.

3.3.4 Modelling turbulence-hydrodynamic & thermo-diffusive instabilities interaction

The effect of turbulence on the hydrodynamic & thermo-diffusive instabilities is treated similar to (Chaudhuri, Akkerman and Law, 2011) adopting the concept of turbulence-induced effective DL inner cut-off. Chaudhuri et al. considered only Darrieus-Landau instability. The main consequence was to use a unity Lewis number in calculating the Darrieus-Landau inner cut-off length scale. In the current study, it is argued that

calculating the inner cut-off length scale of the instability with non-unity Lewis number would include the effect of both the hydrodynamic & thermo-diffusive instabilities. Therefore, the inner cut-off length scale (λ_{min}) that is calculated either from Eq. (2.44) for planar flames or from Eq. (2.58) for spherical flames would include the effects of both the hydrodynamic & thermo-diffusive instabilities. λ_{min} from the spherical relation covers hydrogen mole fraction approximately from 0.13 to 0.74, while from the planar relation covers hydrogen mole fraction approximately from 0.15 to 0.74, under the atmospheric pressure and temperature of 293 K, as shown in Fig. 3.3. The range of the covered concentrations changes with the initial condition. In the current study, the value of λ_{min} at the smallest possible calculated concentration, like approximately 0.13 at the atmospheric pressure and temperature of 293 K from the spherical flame relation in Fig. 3.3, is used for hydrogen concentrations from 0.13 to 0.04.

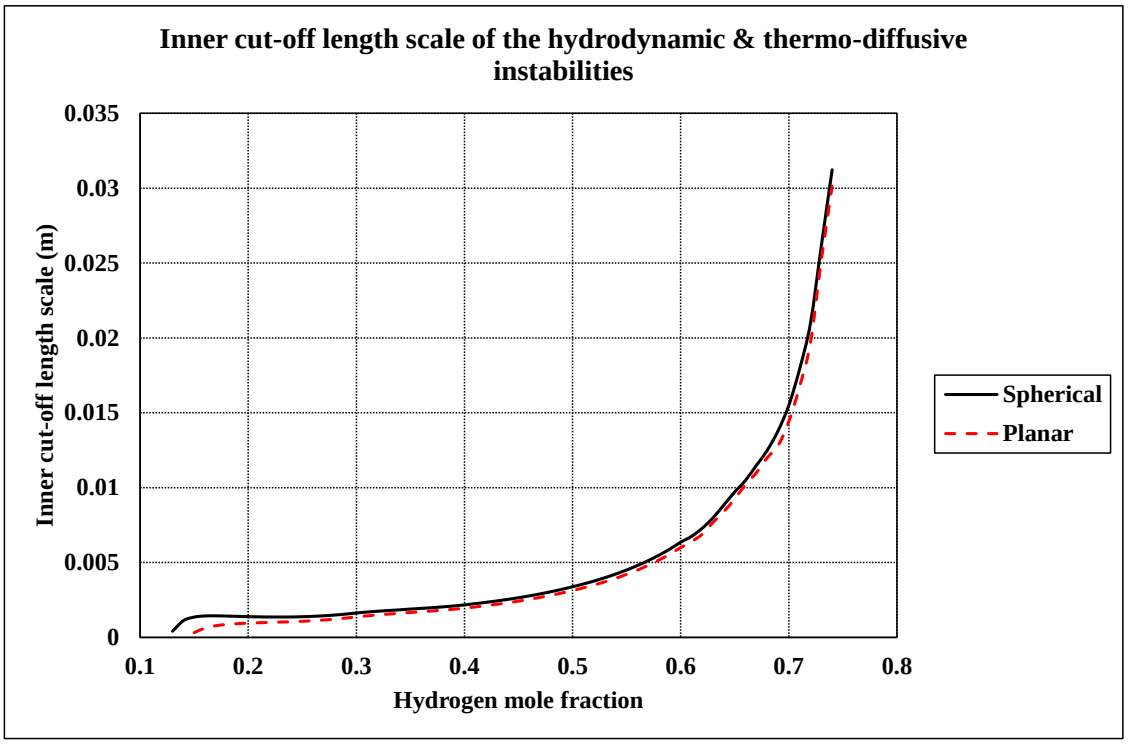

Figure 3.3: Inner cut-off length scale of the hydrodynamic & thermo-diffusive instabilities for spherical and planar flames under the atmospheric pressure and temperature of 293 K.

The turbulence-induced effective instabilities inner cut-off length scale (λ_{eff}) is calculated in the current study in the LES framework from Eq. (3.33) (Chaudhuri, Akkerman and Law, 2011), where the SGS notation is used.

$$\lambda_{eff} = \lambda_{min}\left[1 - \frac{3}{4}\frac{u_\Delta}{U_{tr}}\right]^{-1} \quad , \quad u_\Delta \leq U_{tr}$$
$$\lambda_{eff} = 4\,\lambda_{min}\left[\frac{u_\Delta}{U_{tr}}\right]^{3} \quad , \quad u_\Delta > U_{tr} \tag{3.33}$$

U_{tr} is the Transition turbulent intensity defined, as shown in Eq. (3.34) (Chaudhuri, Akkerman and Law, 2011).

$$U_{tr} = \frac{3}{4} S_u \frac{-\sigma + \sqrt{\sigma^3 + \sigma^2 - \sigma}}{\sigma + 1} \tag{3.34}$$

The proposed model in the current study for the instabilities wrinkling factor under the existence of turbulence is shown in Eq. (3.35).

$$\Xi_{ins} = \left(\frac{\lambda_{max}}{\lambda_{eff}}\right)^{FD_{ins}-2} \times erf\left(20.0 \times \left(\frac{R}{R_0} - 0.9\right)\right)$$
$$= \left(\frac{2\,\pi\,R}{f_{min}\;\lambda_{eff}}\right)^{FD_{ins}-2} \times erf\left(20.0 \times \left(\frac{R}{R_0} - 0.9\right)\right) \tag{3.35}$$

In comparison with Chaudhuri's modelling, they have used the integral length scale as the fractal outer cut-off, while the maximum instability length scale (λ_{max}) from Eq. (2.57) is used in the current implementation. The current implementation provides instabilities wrinkling for the case, where λ_{eff} is larger than the integral length scale but still smaller than λ_{max}. This would extend the effect of the instability above the instability limit in Fig. 2.13 (Chaudhuri, Akkerman and Law, 2011) under strong turbulence. The recent findings in (Yang *et al.*, 2018) have shown that there could be instability above the Chaudhuri's limit. Despite of that the current modification does not mean to correct the instability limit.

3.3.5 Modelling turbulent wrinkling factor (Ξ_{tur})

It is widely proven experimentally and numerically that corrugated flames follow a self-similar regime as in the DNS of (Shim *et al.*, 2011; Katragadda, Chakraborty and Cant, 2012). Therefore, in the current study turbulent wrinkling factor is modelled using

the fractal theory. The outer cut-off length scale is chosen as the filter size. The inner cut-off length scale (η_{tur}) is developed such that the wrinkling model is applicable to the corrugated and the thin reaction zones regimes. η_{tur} is modelled as a combination of two scale: the first scale is the inner cut-off length scale provided by Shim et al. (η_{SH}) in terms of the Kolmogorov length scale and the ratio between the flame thickness to the coherent fine scale eddy diameter, as shown in Eq. (3.36) (Shim *et al.*, 2011). The second scale is the Kolmogorov length scale. η_{tur} is designed such that η_{SH} is dominant in the corrugated regime and L_{KO} is dominant in the thin reaction zones regime. A smooth transition between the two scales is achieved using an error function in Karlovitz number, based on its definition in Eq. (2.103).

$$\eta_{SH} \;=\; 8\; L_{KO}\; e^{\left(\frac{6\,\delta_z}{L_{cf}}\right)} \tag{3.36}$$

It is not expected that, flame could be corrugated with a scale smaller than its thickness. Therefore, the Zel'dovich flame thickness is used as a limiting condition for the inner cut-off length scale. The inner cut-off length scale was limited by the flame thickness in (Charlette, Meneveau and Veynante, 2002) as well. The proposed model in the current study for the turbulent inner cut-off length scale is shown in Eq. (3.37).

$$\begin{aligned}\eta_{tur} = Max\big[\,&\delta_z\,,\\ &\eta_{SH}\;\times\;\big(1\;-\;erf(3\;\times\;Ka_{\Delta 1})\big)\;+\;L_{KO}\;\times\;erf(3\;\times\;Ka_{\Delta 1})\big]\\ &= Max\Bigg[\delta_z\,,8\;L_{KO}\;e^{\left(\frac{6\,\delta_z}{8\,L_{KO}}\right)}\;\times\;\big(1\;-\;erf(3\;\times\;Ka_{\Delta 1})\big)\\ &+\;L_{KO}\;\times\;erf(3\;\times\;Ka_{\Delta 1})\Bigg]\end{aligned} \tag{3.37}$$

The fractal dimension is chosen as the parameterized formula of Katragadda et al., which is shown in Eq. (2.102). In the current study, it is assumed that the wrinkling due to turbulence becomes effective when flame enters the corrugated regime i.e. when the SGS turbulent intensity is equal to the laminar burning velocity. A smooth transition error function is used to apply the turbulent wrinkling factor if the SGS turbulent intensity exceed 90% of the laminar burning velocity. The proposed model in the current study for the turbulent wrinkling factor is shown in Eq. (3.38).

$$\Xi_{tur} = \left(\frac{\Delta}{\eta_{tur}}\right)^{FD_{KA}-2} \times erf\left(20.0 \times \left(\frac{u_\Delta}{S_u} - 0.9\right)\right) \quad (3.38)$$

3.3.6 Modelling turbulent burning velocity

Turbulent burning velocity is calculated by taking into account the effect of wrinkling due to the flame instabilities and turbulence as what was done in (Chaudhuri, Akkerman and Law, 2011; Keppeler and Pfitzner, 2015). The proposed model in the current study for the turbulent burning velocity in shown in Eq. (3.39).

$$S_{tur} = S_u \, \Xi_{ins} \, \Xi_{tur} =$$
$$S_u \times \left(\frac{2\,\pi\,R}{f_{min}\;\lambda_{eff}}\right)^{FD_{ins}-2} \times erf\left(20.0 \times \left(\frac{R}{R_0} - 0.9\right)\right) \times \quad (3.39)$$
$$\left(\frac{\Delta}{\eta_{tur}}\right)^{FD_{KA}-2} \times erf\left(20.0 \times \left(\frac{u_\Delta}{S_u} - 0.9\right)\right)$$

3.3.7 Modelling flame quenching under excessive stretching

The possibility of partially or fully quenching the flame under excessive stretching is modelled using the stretch (quenching) factor (G), which was applied in RANS in (Zimont and Lipatnikov, 1995; Zimont *et al.*, 1998; Hasslberger, Boeck and Sattelmayer, 2015) and in LES in (Flohr and Pitsch, 2000). In the current study, the model constants from RANS are used.

G represents the probability of unquenched flamelet with values between 1 for unquenched flamelet and 0 for fully quenched flamelet. It could present the bending behaviour of the turbulent burning velocity with increasing flow turbulence. It is defined in Eq. (3.40) (Zimont and Lipatnikov, 1995; Zimont *et al.*, 1998), which was obtained by integrating the log-normal distribution of the dissipation rate (ε) (m^2/s^3) of the turbulent kinetic energy.

$$G = \frac{1}{2}\, erfc\left[-\frac{1}{\sqrt{2}\,\varsigma}\left(\ln\left(\frac{\varepsilon_{cr}}{\tilde{\varepsilon}}\right) + \frac{\varsigma}{2}\right)\right] \quad (3.40)$$

$erfc$ is the complementary error function, which is defined in Eq. (3.41) (Ettner, 2013).

$$erfc(\text{þ}) = 1 - \frac{2}{\sqrt{\pi}} \int_0^{\text{þ}} e^{-\text{ę}^2}\, d\text{ę} \tag{3.41}$$

ś is the standard deviation of the log-normal distribution of ε. It was modelled using the integral length scale and the Kolmogorov scale in RANS and the filter width and the Kolmogorov scale in LES. In the current study, ś is modelled as shown in Eq. (3.42) (Zimont and Lipatnikov, 1995; Zimont *et al.*, 1998; Flohr and Pitsch, 2000), which is implemented using LES formulations. It was not clear if the unburned properties of the density and viscosity or the local properties, affected by the temperature rise inside the flame brush, should be used. In the current study, the local properties are used, which could be consider under the uncertainty of the model.

$$\text{ś} = 0.26\ ln\left(\frac{\Delta}{L_{KO}}\right) = 0.26\ ln\left(\left(\frac{\rho\ u_\Delta\ \Delta}{\mu}\right)^{\frac{3}{4}}\right) \tag{3.42}$$

$\tilde{\varepsilon}$ is estimated in LES as shown in Eq. (3.43) (Battista, Troiani and Picano, 2015).

$$\tilde{\varepsilon} = \frac{u_\Delta^3}{\Delta} \tag{3.43}$$

ε_{cr} (m^2/s^3) is the critical dissipation rate, which is defined in Eq. (3.44) (Zimont *et al.*, 1998; Hasslberger, Boeck and Sattelmayer, 2015). Again, the local properties of ρ and μ are used for the same reason.

$$\varepsilon_{cr} = 15\ \frac{\mu\ g_{cr}^2}{\rho} \tag{3.44}$$

g_{cr} $(1/s)$ is the critical flow velocity gradient, which could quench the flame. There is large uncertainty in modelling g_{cr}. In the current study, it is modelled as shown in Eq. (3.45) (Hasslberger, Boeck and Sattelmayer, 2015), which depends on the unburned thermal diffusivity.

$$g_{cr} = \frac{S_u^2}{\chi(T_u)} \tag{3.45}$$

If the dissipation rate $\tilde{\varepsilon}$ is much smaller than the critical dissipation rate ε_{cr} flame does not quench and the opposite is true. There are sources of uncertainties on deriving the quenching model based on G as the unsteady effects was neglected and the full turbulent energy spectrum was cosidered (Flohr and Pitsch, 2000). The DNS in (Meneveau and Poinsot, 1991) has shown that small length scale of turbulence has small effect on flame stretching.

3.3.8 Modelling chemical reaction rates and heat of chemical reaction

The proposed model in the current study for chemical reaction rate of the burned gas (S_{Y_b}), source term of the progress variable equation, is shown in Eq. (3.46).

$$S_{Y_b} = \rho_u S_u \Xi_{ins} \Xi_{tur} G \left|\nabla \tilde{Y}_b\right| \tag{3.46}$$

The proposed model in the current study for chemical reaction rate of the hydrogen mass fraction, source term of the hydrogen mass fraction equation, is shown in Eq. (3.47), based on the previous implementation at Ulster University's deflagration UDF in terms of S_{Y_b}.

$$S_{Y_{H_2}} = \frac{-\tilde{Y}_{H_2}}{\tilde{Y}_{H_2} + \tilde{Y}_{air}} S_{Y_b} = \frac{-\tilde{Y}_{H_2}}{\tilde{Y}_{H_2} + \tilde{Y}_{air}} \rho_u S_u \Xi_{ins} \Xi_{tur} G \left|\nabla \tilde{Y}_b\right| \tag{3.47}$$

The proposed model in the current study for heat of chemical reaction, source term of the energy equation, is shown in Eq. (3.48), based on (Molkov, 2012) in terms of S_{Y_b}.

$$S_E = Hc\ S_{Y_b} = Hc\ \rho_u S_u \Xi_{ins} \Xi_{tur} G \left|\nabla \tilde{Y}_b\right| \tag{3.48}$$

$Hc\ (J/Kg\ of\ burned\ gas)$ is the heat of chemical reaction.

3.4 Modelling flame-generated turbulence

Flame-generated turbulence is modelled adopting the algebraic model $\left(-\nabla \cdot K_{fg}\right)$ as a source term in the momentum equations. K_{fg} is defined in Eq. (3.49) (Champion, Robin and Mura, 2012). There is a typo in the multiplication by the density in Eq. (3.49) that is corrected here. The model was derived initially for RANS under a unity Lewis number, it is adopted in the current study in the LES based on the common practice that

different RANS models are adopted in the LES. The validation of this usage is beyond the scope of the current study. k_Δ from Eq. (3.10) is used in the current study in Eq. (3.49). $\left(-\nabla \cdot K_{fg}\right)$ is activated after the ignition time inside the flame brush, the turbulent intensity would be far from the model driven condition. Therefore, the validity of this usage is beyond the scope of the current study. Examining K_{fg} in the current study shows that, it could have negative values with the increase in the turbulent kinetic energy. Therefore, a limiting condition is used to prevent negative K_{fg}. In a private conversation, V. Robin suggested that the model could not be applicable for the compressible flow and an extension of the model might be needed.

$$
\begin{aligned}
K_{fg} = \frac{1}{3}\left((\sigma-1)\,S_u\right)^2 \Bigg[& \overline{\rho\, Y_b''^2} + \bar{\rho}\,\tilde{Y}_b^2(1-\mathbb{F}^2) \\
& - \frac{\bar{\rho}\tilde{Y}_b\left(1-\tilde{Y}_b\right)}{\left(\mathfrak{c}_2\,\tilde{Y}_b^{\mathfrak{m}}\right)^{-1}-\tilde{Y}_b}(1-\mathbb{F})\left(\frac{\tilde{Y}_b\left(1-\tilde{Y}_b\right)}{\left(\mathfrak{c}_2\,\tilde{Y}_b^{\mathfrak{m}}\right)^{-1}-\tilde{Y}_b}(1-\mathbb{F})\right. \\
& \left. + 2\,\tilde{Y}_b\,\mathbb{F}\right)\Bigg] \\
& + \frac{2}{3}(\sigma-1)\,S_u\,\mathbb{F}\left(-\tilde{Y}_b\left(1-\tilde{Y}_b\right)\,\bar{\rho}\sqrt{k_\Delta}\right. \\
& \left. + C_{ae}\,(\sigma-1)\;S_u\,\tilde{Y}_b\;\overline{\rho\, Y_b''^2}\right)
\end{aligned}
\tag{3.49}
$$

$\overline{\rho\, Y_b''^2}$ is the variance of the progress variable, it is modelled in Eq. (3.50) (Robin, Mura and Champion, 2012).

$$
\overline{\rho\, Y_b''^2} = \bar{\rho}\,\tilde{Y}_b\left(1-\tilde{Y}_b\right)S \tag{3.50}
$$

S is the segregation factor which was modelled as a constant value of 0.98 in (Robin, Mura and Champion, 2012) and is adopted here. $\mathfrak{c}_2$, $\mathfrak{m}$ are constants with the values of 0.95 and 0.4 respectively (Champion, Robin and Mura, 2012). C_{ae} is a model constant with the value of 0.45, but it is not precise for the low thermal expansion coefficient (Robin, Mura and Champion, 2011). $\mathbb{F}$ is an orientation parameter, which is defined in Eq. (3.51) (Champion, Robin and Mura, 2012).

$$\mathbb{F} = \left(1 - \frac{\tilde{Y}_b\left(1-\tilde{Y}_b\right) - \tilde{Y}_b\left(1-\tilde{Y}_b\right)S}{I_1 - I_2}\right)\left[\frac{1}{1+\frac{k_\Delta}{\tilde{u}\cdot\tilde{u}}}\right] + \left(\tilde{Y}_b - \frac{\tilde{Y}_b\left(1-\tilde{Y}_b\right) - \tilde{Y}_b\left(1-\tilde{Y}_b\right)S}{I_1 - I_2}\ I_1\right)\left(1 - \left[\frac{1}{1+\frac{k_\Delta}{\tilde{u}\cdot\tilde{u}}}\right]\right)\ \mathfrak{c}_2\ \tilde{Y}_b^{\mathfrak{m}} + \frac{\tilde{Y}_b\left(1-\tilde{Y}_b\right) - \tilde{Y}_b\left(1-\tilde{Y}_b\right)S}{I_1 - I_2}\ \frac{1}{\Xi_{tur}} \tag{3.51}$$

I_1 and I_2 are constants with the values of 0.43 and 0.28 respectively (Champion, Robin and Mura, 2012). $\tilde{u}$ is the flow velocity. Turbulent intensity related to flame-generated turbulence (U_{fg}) is defined based on K_{fg}, as shown in Eq. (3.52) (Robin, Mura and Champion, 2011).

$$U_{fg} = \sqrt{\frac{2}{3}\ \frac{K_{fg}}{\bar{\rho}}} \tag{3.52}$$

3.5 Conclusions

The system of equations governs reactive flow in the LES formulation is presented. Turbulent SGS terms are closed using turbulent kinetic energy equation. A developed closure model for the chemical reaction rate is presented for deflagration and detonation. The model incorporates the effects of wrinkling due to hydrodynamic & thermo-diffusive flame instabilities, wrinkling due to turbulence, and quenching due to excessive stretching.

The instabilities and the turbulent wrinkling factors are presented in two separated fractal models. The outer cut-off length scale of the instabilities is set in proportionality with flame radius. The inner cut-off length scale of the instabilities is calculated from the dispersion relation of either spherical or planar flames. The fractal dimension of the instabilities is set to a constant value of 2.2. The outer cut-off length scale of the turbulent wrinkling factor is set to the filter width. The inner cut-off length scale of the turbulent wrinkling factor is developed and designed such that it is a combination of two length

scales: the inner cut-off length scale of Shim, to be dominated in corrugated flamelets regimes, and the Kolmogorov length scale in the unburned gas, to be dominated in the thin reaction zones regime. The inner cut-off length scale of the turbulent factor is limited by the Zel'dovich flame thickness. The fractal dimension of the turbulent factor is set to the parameterized formula of Katragadda in terms of Karlovitz number, Reynolds number, and Lewis number.

An algebraic model for flame-generated turbulence is incorporated, which is linked to the momentum equation. A schematic for data transfer between the sub-models and the reactive system of equations is shown in Fig. 3.4. The chemical reaction rate is coupled to the species mass fraction equations through a source term. The heat of chemical reaction is coupled to the energy equation through a source term. Flame-generated turbulence is coupled to the momentum equation through a source term.

In the next chapters, the proposed model for the chemical reaction rate is applied to different experiments. Every experiment allows to show the important of different wrinkling sub-model.

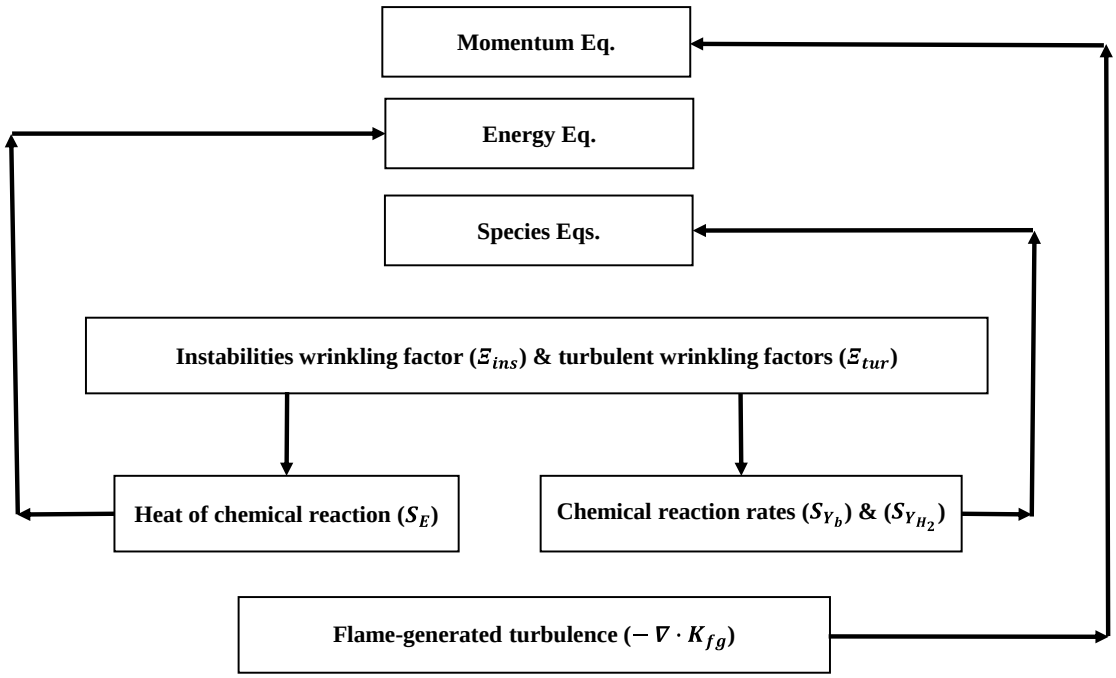

Figure 3.4: Schematic of data transfer between sub-models and the governing equations.

CHAPTER 4. NUMERICAL SIMULATION OF DEFLAGRATION-TO-DETONATION TRANSITION EXPERIMENT

4.1 Introduction

The purpose of the present chapter is to numerically test the proposed chemical reaction rate model against lab scale DDT experiment. The ability of the model to predict the transition to detonation, detonation velocity, and the experiment overpressure is investigated.

A rectangular channel with a baffled part followed by another smooth part is chosen as a validation test case. The baffles generate turbulence, which increases the burning velocity and would promote the transition to detonation. Therefore, the ability of the proposed chemical reaction rate model to produce the required wrinkling for DDT is manifested in this simulation. If the flame is detonated as an overdriven detonation inside the baffled part, it would require a support to propagate with the overdriven velocity, like a piston driven which is not existing. Therefore, it will relax to the CJ velocity. If this relaxation happens inside the baffled part, the propagation velocity would decrease lower than the CJ velocity due to collide with the succeeding baffles. In the smooth part of the channel, the detonation velocity is expected to propagate with the CJ velocity. Predicting all these regimes of velocities would indicate a good capability of the model.

Different studies have been conducted for the chosen configuration. A summary of the grid resolutions and combustion models of the SOTA is shown in Table 4.1. The SOTA have used different combustion models based on single step chemistry, multistep chemistry, and wrinkling factor. Wang did not provide details about the turbulence modelling and the simulation domain 2D or 3D. The other two cases performed 2D simulations. All the cases have used fine grid sizes, with a minimum grid size close to 10 μm. Therefore, testing the performance of the model based on a coarse grid against the fine resolution would declare the capability of the model.

It should be mentioned that the current study is based on 3D, which would add an advantage in the prediction against the SOTA at this point.

Table 4.1: Numerical resolution and combustion models of the SOTA of the DDT (Azadboni *et al.*, 2017; C.J. Wang and Wen, 2017; Khodadadi Azadboni *et al.*, 2019).

Model	Grid resolution	Combustion model
Wang and Wen 2017	AMR: Entire domain: Coarse grid Regions with high temperature gradients: fine grid, that had the smallest grid size close to 1/32 of the hrl, if the hrl is considered to be 0.3 mm (Khodadadi Azadboni *et al.*, 2017) then the smallest grid size was approximately 9.375 μm.	Compressible Navier-Stokes – density-based solver – single step chemistry based on Arrhenius model 30% hydrogen-air mixture
Azadboni at al. 2017	2D mesh – AMR The minimum grid size is 10 μm, which is corresponds to 30 points per hrl close to the flame and the shock.	Compressible Navier-Stokes – density-based solver – LES and one eddy equation – flame wrinkling combustion based on Weller's formulation. 30% hydrogen-air mixture
Azadboni at al. 2019	2D mesh – AMR The minimum grid size is 10 μm, which is corresponds to 30 points per hrl.	Compressible Navier-Stokes – density-based solver – monotone integrated LES – multistep chemistry model. 30% hydrogen-air mixture

4.2 Experiment description

The Gravent DDT experiments database is selected for testing the developed model. The database is an online open access, which represents results of explosion experiments conducted at the Institute of Thermodynamics at Technical University of Munich. A summary of the chosen experiment from (Boeck *et al.*, 2016) is as follows: The Gravent experimental is a closed channel with rectangular cross-section. Its length is

5.4 m, its width is 0.3 m, and its height is 0.06 m. Horizontal obstacles were used with a spacing of 0.3 m. The obstacles had a thickness of 12 mm and a blockage ratio (BR) of 60%. BR was defined as $\frac{2 \times \text{obstacle height}}{\text{channel total height}}$ (Boeck *et al.*, 2016). Figure 4.1 (Boeck *et al.*, 2016) shows the configuration of the channel and a cross-section view. The mixture was ignited using spark plug at the center of one of the channel plates. The channel contains baffled region followed by smooth region. The first obstacle is located at 0.25 m from the ignition source and the last obstacle is located at 2.05 m from the ignition source. It was not clear during performing the simulations from where these distances were measured with respect to the baffles. In the current study, they are measured from the end of the baffles but the sketch in (Dounia *et al.*, 2019) shows that they were measured from the middle of the baffles. The channel was filled with homogeneous hydrogen-air mixture with a stoichiometric concentration of 29.9%. The mixture was initially at the atmosphere pressure and temperature of 293 K.

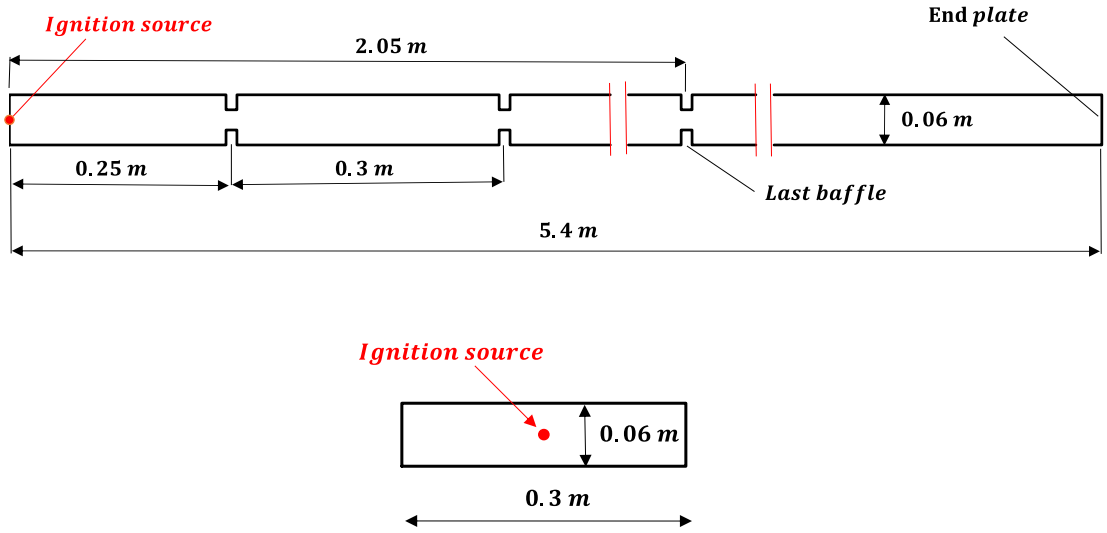

Figure 4.1: Schematic of the baffled channel (top – not to scale) and the channel cross-section at the ignition plane (bottom) (Boeck et al., 2016).

Experiments data were collected using piezoelectric pressure transducer mounted at the middle of the top plate of the channel. Pressure transducers were installed at (0.4 m, 1.4 m, 2.3 m, 3.2 m, 4.1 m and 5.0 m) from the ignition plate. Another pressure transducer was installed at the center of the plate opposite to the ignition plate i.e. at 5.4 m from the ignition source. Pressure signals were filtered using 45 kHz low pass filter,

which allowed over prediction of the pressure to not increase more than 110% of the real value. The pressure transducer measured range was from 0 to 250 bar. Pressure signals were collected simultaneously on 8 channels with sample rate of 250,000 per s. Flame front was traced along channel axis using photodiodes, optical high-speed shadowgraph, and 20 kHz OH-PLIF.

4.3 Simulations description

3D numerical simulation is performed for the full geometry of the channel. The channel is filled with a homogeneous hydrogen-air mixture with stoichiometric concentration of 29.9%. ANSYS-Fluent software is used as the framework for numerical simulation. The developed model is implemented in UDF, which was initially developed at Ulster University. Different sub-modules of the UDF are refined in the current study, which includes the laminar burning velocity at the standard pressure and temperature and turbulent wrinkling factor. New Flame-generated turbulence modelling strategy is used and replaces the previous technique in the UDF. The developed hydrodynamic & thermo-diffusive instabilities wrinkling factor sub-model and flame stretching factor sub-model are included in the current work. The turbulent kinetic energy LES-SGS closure model replaces the RNG LES-SGS model. The leading point sub-module is removed. The total changes could be in the order of 50% of the original UDF. The simulations are performed on high performance computing with 4×12 cores, which have 2.2 GHz and a memory of 64 GB. However, the total numbers of cores are not used in a single simulation due to the limitation of the shared ANSYS-Fluent license.

4.3.1 Mesh setup

Three hexahedral (hexa) meshes: coarse, medium, and fine, with no refinement close to the walls, are used to investigate the dependence of the solution on the grid. The coarse mesh has an average grid size of 7.5 mm and the baffles have grid size in the longitudinal direction of 6 mm, as shown in Fig. 4.2. The total coarse mesh size is 230 k cells. The medium mesh has a uniform grid with a grid size of 6 mm and a total mesh size of 446 k cells. The fine mesh has an average grid size of 4.5 mm and a total mesh size of 1.1 M cells. Using more finer grid sizes is not possible during the time of the current study due to the limitation of the shared license of ANSYS-Fluent software. It is

required to have a matching interface at the baffles to have different grid sizes. The effect of the interface is tested for the medium mesh. A summary of the meshes is shown in Table 4.2. It is expected that, these meshes will not resolve the boundary layer and the microstructure of the flow. Therefore, the capability to predict flame propagation and DDT relies on the SGS combustion modelling.

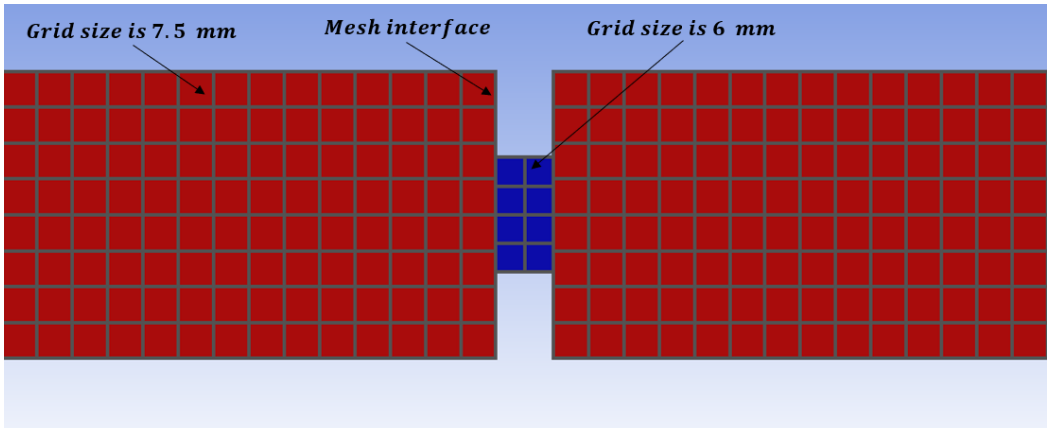

Figure 4.2: Front section from the coarse mesh.

Table 4.2: Summary of the DDT meshes.

Mesh	Average grid size	Total mesh size
Coarse	7.5 mm	230 k cells
Medium	6 mm	446 k cells
Fine	4.5 mm	1.1 M cells

4.3.2 Simulation setup

Navier-Stokes equations are solved using the density based explicit solver. A second order upwind based on AUSM+ scheme is used to discretize the convective terms. The gradients are calculated using Green-Gauss node based. An explicit time discretization is used based on 4-stages Runge-Kutta. Different CFL numbers of 0.8, 0.6, 0.1, and 0.07 are tested to investigate the solution dependence on CFL number. The default CFL number with the density based explicit solver is 1.0. Turbulence is treated using LES technique with the turbulent kinetic energy SGS closure.

λ_{min} is calculated from the planar flame relation in Eq. (2.44), since the ratio of the channel height to its length is 0.01 and the ratio of the channel width to its length is 0.056. The proposed chemical reaction rate model is linked to the governing equations as source terms to the mass fraction equations of the burned gas, mass fraction equation of hydrogen, and the energy equation, as shown in Eqs. (3.46)–(3.48). Flame-generated turbulence is modelled using source terms in the momentum equations based on derivative of the algebraic model in Eq. (3.49). A limiting condition is included to prevent negative K_{fg} at high k_{Δ}.

Thermodynamics and combustion properties are calculated in an initial step using the Ó Conaire chemical reaction mechanism in the framework of Cantera. The Ó Conaire input mechanism is extracted from (Ettner, 2014). Specific heat, sensible enthalpy, molecular viscosity, and thermal conductivity dependence on temperature for the air, hydrogen, and the burned gas are approximated in polynomials with temperature variable up to 5000 K. The effect of pressure on the unburned mixture properties, combustion, and flame properties is considered under the isentropic change. A constant value of 0.89 is considered for the Lewis number of the deficient reactant.

Heat transfer is neglected in the current setup, it was also neglected in the DDT study in (Hasslberger, Boeck and Sattelmayer, 2015). channel plates and the baffles are treated as solid adiabatic walls. Simple gradient diffusion law is used to model transport terms in the governing equations.

The simulation is ignited by increasing linearly the progress variable from 0 to 1.0 and the temperature from the unburned temperature to the adiabatic flame temperature in a cell close to the ignition source position during the ignition time ($t_{ign,initial}$). The ignition time is calculated as the time needed to propagate laminar flame under the initial pressure and temperature through half of the ignition cell length (Δ), as shown in Eq. (4.1) (Molkov, 2012). Δ is calculated as cubic root of the ignition cell volume.

$$t_{ign,initial} = \frac{1}{2}\frac{\Delta}{\sigma\, S_u} \tag{4.1}$$

The behavior of the model is compared against overpressure signals and flame propagation velocity from the experiment and the SOTA.

4.3.3 Mesh independence study

The solution dependence on the mesh resolution is investigated using the three meshes with CFL number of 0.6. Table 4.3 summarizes the simulations run time. The quality of the LES resolution is investigated used the Pope criterion (Pc). It is defined as the ratio of the resolved turbulent kinetic energy (k_{res}) to the total turbulent kinetic energy, as shown in Eq. (4.2) (Balaji, De and De, 2016). The total turbulent kinetic energy is defined as the sum of the resolved turbulent kinetic energy and the SGS turbulent kinetic energy. A Pope criterion value of larger than 0.8 would be an indication for good LES resolution. Since a model for flame-generated turbulence is used in the current study, which represents SGS turbulence effect of the flame. It could be included in calculating the total turbulent kinetic energy for the Pope criterion, as shown in Eq. (4.3).

Table 4.3: Running time of the mesh independence study for the DDT.

Mesh	CFL number	Processors	Approximate CPU time
Coarse	0.6	8	0.8 day
Medium	0.6	16	0.95 day
Fine	0.6	8	5.9 days

$$Pc = \frac{k_{res}}{k_{res} + k_{\Delta}} \tag{4.2}$$

$$Pc = \frac{k_{res}}{k_{res} + k_{\Delta} + K_{fg}/\bar{\rho}} \tag{4.3}$$

Figure 4.3 shows the average of Pope criterions using Eqs. (4.2) and (4.3), applied for two parts of the channel. The first part is measured from the ignition source until the fourth baffle, which represents deflagration. The second part is measured from the fourth baffle to the end of the channel, which represents detonation. The transition to detonation at the fourth baffle is determined later. The Pope criterion (2) in the figure is calculated using Eq. (4.3). The effect of flame-generated turbulence on calculating the average of Pope criterion for the two parts of the channel is small and could be neglected. The Pope criterion changes with the simulation time. The three meshes satisfy a good resolution,

according to the pope criterion, only in the deflagration parts at the early time of the propagation, close to (I) in the figure. Refining the mesh provides higher values of the Pope criterion, as shown for the fine mesh close to (II) in the figure.

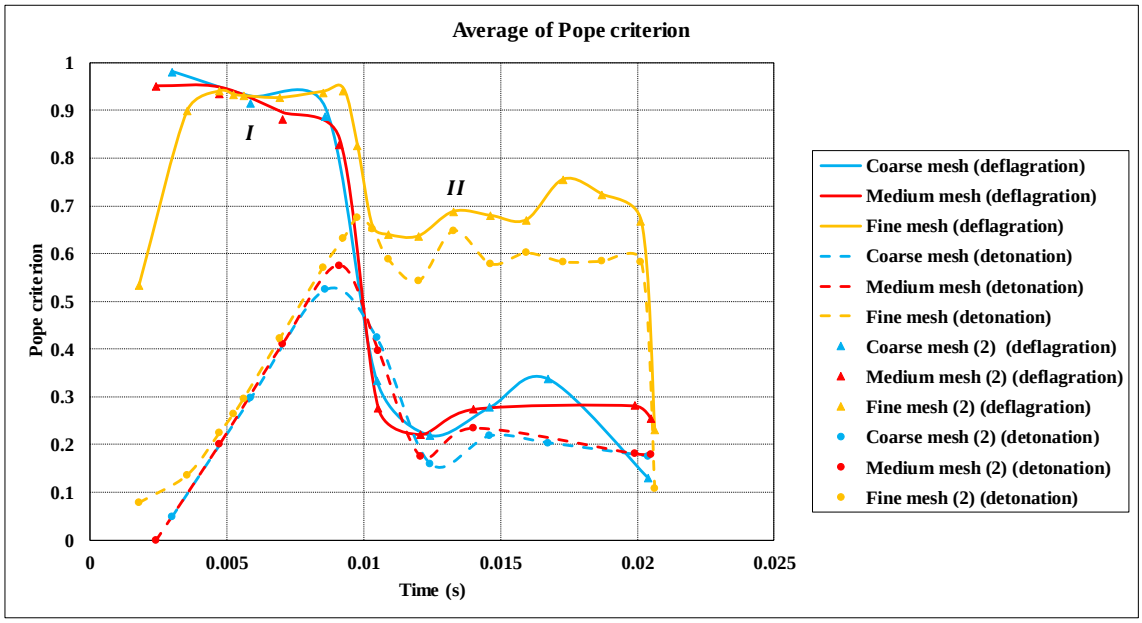

Figure 4.3: Average of the Pope criterions for the three meshes. The lines are calculated from Eq. (4.2) and the symbols are calculated from Eq. (4.3).

Figure 4.4 shows shock propagation velocities predicted by the three meshes compared with the CJ velocity and the experiment shock and flame propagation velocities. The shock propagation velocities are calculated by taking the time derivatives of the shock position with respect to a fixed observer. CJ velocity is calculated using the initial atmospheric pressure and temperature of 293 K. There is convergence at the shock propagation velocities predicted by the three meshes in the smooth part of the channel, after a distance from the last baffles. Considering the difference in the computational times of the meshes and the close detonation results, the medium mesh is used to present the results and complete the analysis in the next sections.

The experiment predicted large increase in the flame propagation velocity at the beginning of the smooth part of the channel. This increase is not physical, as it was mentioned in the experiment description that the accuracy of the photodiodes is only guaranteed below a flame propagation velocity of 1000 m/s. Above this limit, unphysical high oscillations could occur. Therefore, they suggested to predict the propagation velocity from the overpressure signals in that case. By calculating the shock propagation

velocity of the experiment from the overpressure signals, as shown in Fig. 4.4, the non-physical increase of the flame propagation velocity in the beginning of the smooth part of the channel is confirmed.

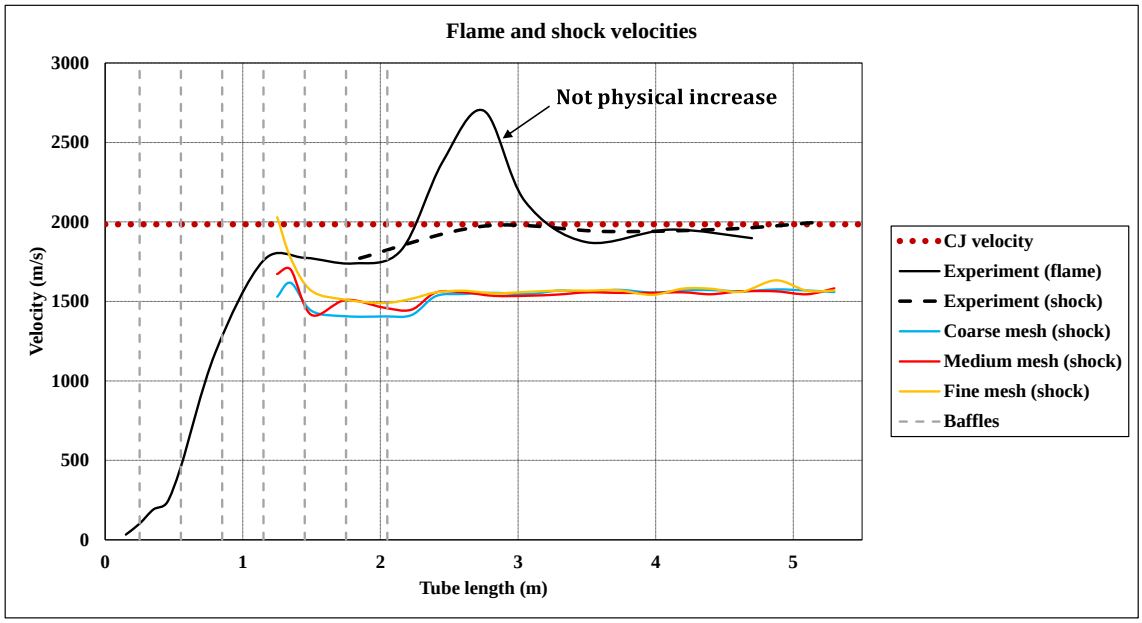

Figure 4.4: Shock propagation velocities, predicted by the three meshes, compared with the shock and flame propagation velocities of the experiment (Boeck et al., 2016).

The effect of using interfaces in the mesh, as shown in Fig. 4.2, is investigated using the medium mesh compared to another typical mesh with the same grid size of 6 mm but without interfaces. Figure 4.5 shows shock propagation velocities predicted by the medium mesh with and without interfaces. There are closely matching, especially in the smooth part of the channel. However, for the mesh with interfaces there is temperature divergence to 5000 K for some cells over a period. The medium mesh without interfaces is used in the next sections.

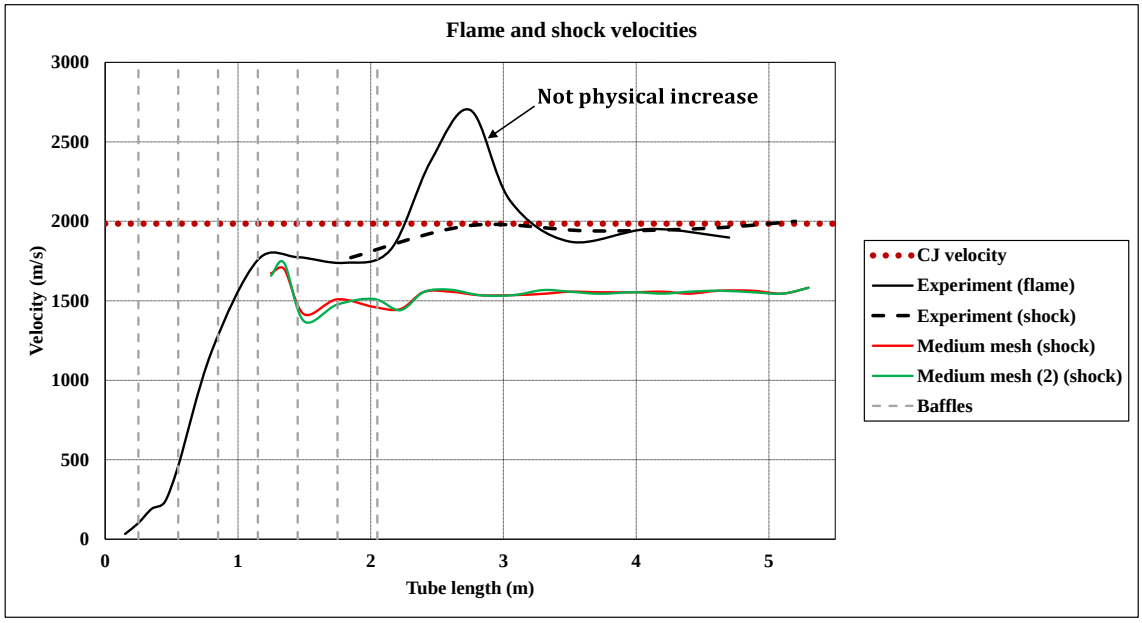

Figure 4.5: Shock propagation velocities predicted by the medium mesh, with and without interfaces, compared with the experiment shock and flame propagation velocities (Boeck et al., 2016).

4.3.4 Time-step independence study

The medium mesh (2), without interfaces, is used to investigate the time-step independence study. four CFL numbers are investigated: 0.8, 0.6, 0.1, and 0.07. Table 4.4 summarizes the simulations run time. Figure 4.6 shows the average of Pope criterions calculated using Eq. (4.2) for the medium mesh (2) at the deflagration and detonation parts of the channel, declared in the previous section, using the different CFL numbers. There is convergence for the CFL numbers at the early time of the simulations. The Pope criterion is below 0.8 at the late time. It is difficult to conclude solid conclusion. Therefore, the flame propagation velocities is examined to determine the effect of the CFL numbers.

Table 4.4: Running time of the time-step independence study for the DDT.

Mesh	CFL number	Processors	Approximate CPU time
Medium (2)	0.8	6	1.8 days
Medium (2)	0.6	16	0.98 day
Medium (2)	0.1	16	5.8 days
Medium (2)	0.07	16	7.9 days

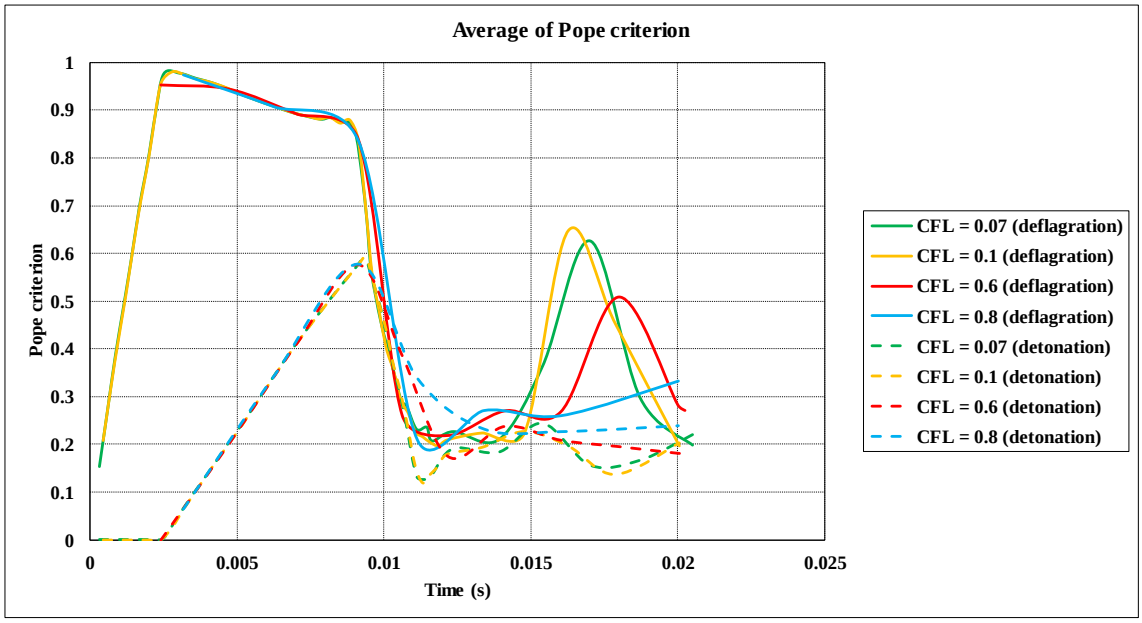

Figure 4.6: Average of the Pope criterions for the medium mesh (2) using different CFL numbers.

Figure 4.7 shows flame and shock propagation velocities predicted by the simulations, for the investigated CFL numbers, compared with the experiment. Flame propagation velocities are calculated in the current simulations by taking the time derivative of the tip flame positions with respect to a fixed observer. Flame positions were recorded every 200 time-steps during the simulations. Hence, it is not clear if there is an effect on the post processing of the flame propagation velocities in the baffled part of the channel, especially for large CFL numbers. For all the CFL numbers, shock and flame are propagated with close velocities in the smooth part of the channel, after a distance from the seventh baffle. Propagation velocity increases with the decrease in the CFL number.

Propagation velocities for CFL numbers of 0.8 and 0.6 are smaller than the experiment and the CJ velocity. Flame and shock propagation velocities for CFL numbers of 0.1 and 0.07 are close to each other, as an indication to the beginning of convergence in the time resolution. The initiation velocities of detonation for CFL numbers of 0.1 and 0.07 are larger than the CJ velocity, as an indication of overdriven detonation. Flame propagation velocities of the simulations converge to values close to the CJ velocity and the shock propagation velocity of the experiment in the smooth part of the channel.

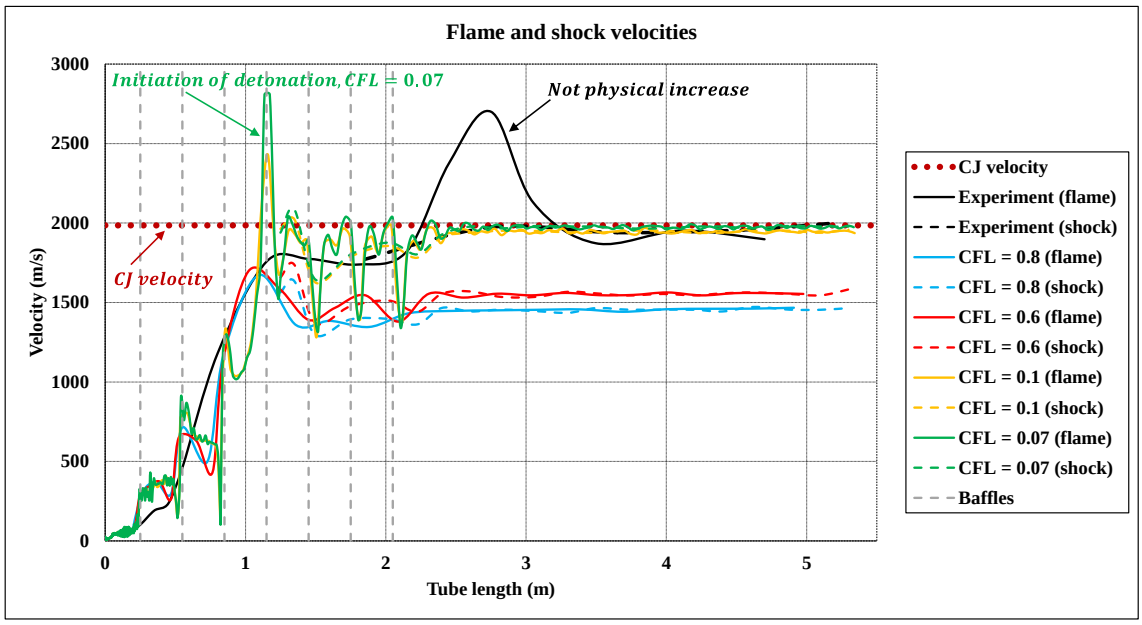

Figure 4.7: Flame and shock propagation velocities predicted by the simulation for different CFL numbers compared with the experiment (Boeck et al., 2016).

4.4 Simulation results and discussion

4.4.1 Performance of the proposed model against the SOTA

Figure 4.8 shows flame tip position for CFL numbers of 0.1 and 0.07 from the medium mesh (2), on a nodal progress variable of 0.5, compared with the experiment and the SOTA (C.J. Wang and Wen, 2017). The current simulations flame tip is measured within 0.01 m around the channel center. The experimental data is extracted from (C.J. Wang and Wen, 2017), which seems to be shifted in time by comparing the overpressure time in Figs. 4.10–4.16. The current simulations are shifted in time by 3.3 ms. The simulations predict qualitatively good match with the experiment and the SOTA, which is much closer to the experiment than the SOTA.

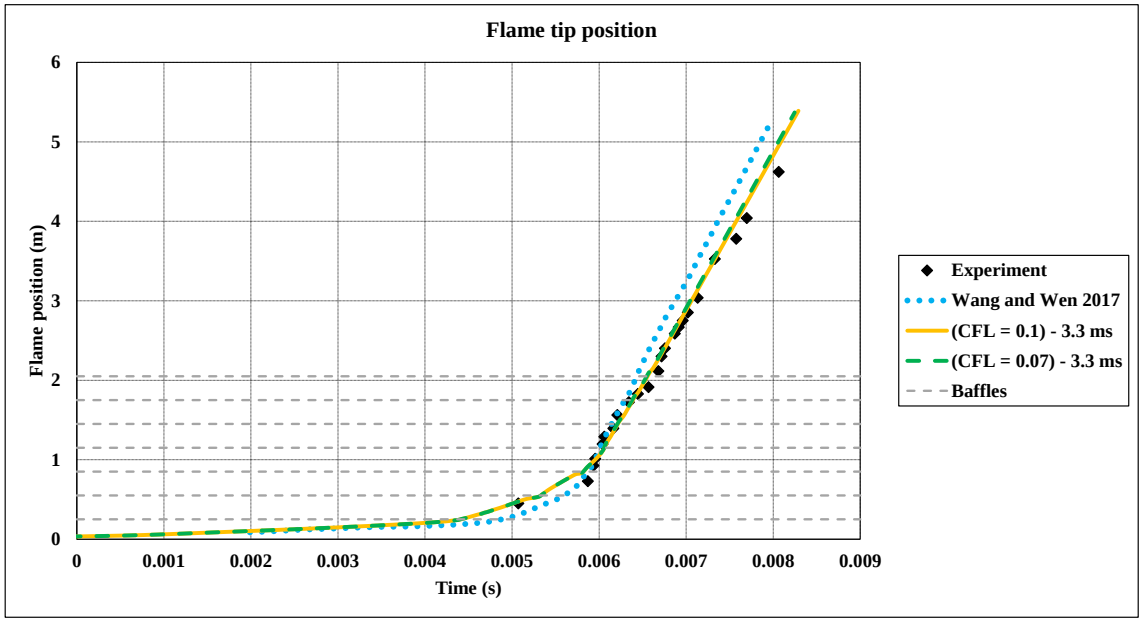

Figure 4.8: Flame tip position of the current simulations for CFL numbers of 0.1 and 0.07, on a nodal progress variable of 0.5, compared with the SOTA and the experiment (C.J. Wang and Wen, 2017).

Figure 4.9 shows the simulations flame tip velocities for CFL numbers of 0.1 and 0.07 from the medium mesh (2), on a nodal progress variable of 0.5, compared with the experiment and the SOTA. The current simulations predict good match with the experiment. The baffles accelerate the flame until initiation of detonation occurs at the fourth baffle with as overdriven detonation. Following the detonation initialization, the flame propagation velocity decreases, and the average of flame propagation velocity with propagation is smaller than the CJ velocity in the baffled part of the channel. That is due to the succeeding decrease in the flame propagation velocity due to crossing the baffles, as shown in the figure. After the baffles in the smooth part of the channel, flame propagates with a velocity close to the shock propagation velocity of the experiment and the CJ velocity.

Wang predicted an initiation of detonation close to the third baffle and their flame propagation velocity is larger than the shock propagation velocity of the experiment and the prediction of the current study. (Azadboni *et al.*, 2017) predicted an initiation to detonation between the third and fourth baffles, which is close to the current study prediction. Before DDT, propagation velocities of (Azadboni *et al.*, 2017) is close to the current study and after the detonation, it is a little bit higher than the current study and is much closer to the Wang simulation at the end of the channel. (Khodadadi Azadboni *et*

al., 2019) predicted DDT at 1.3 m and their propagation velocity has oscillation. As a conclusion, the overall propagation velocities of the simulations are close to each other and to the experiment shock propagation velocity. Considering the corase resolution of the current study, 6 mm using 3D, compare to the fine resolutions of the SOTA, 10 μm for the smallest grid using 2D, in addition to the good quality of the current prediction, the current model would be would be more superior than the SOTA for predicting the flame detonation velocity.

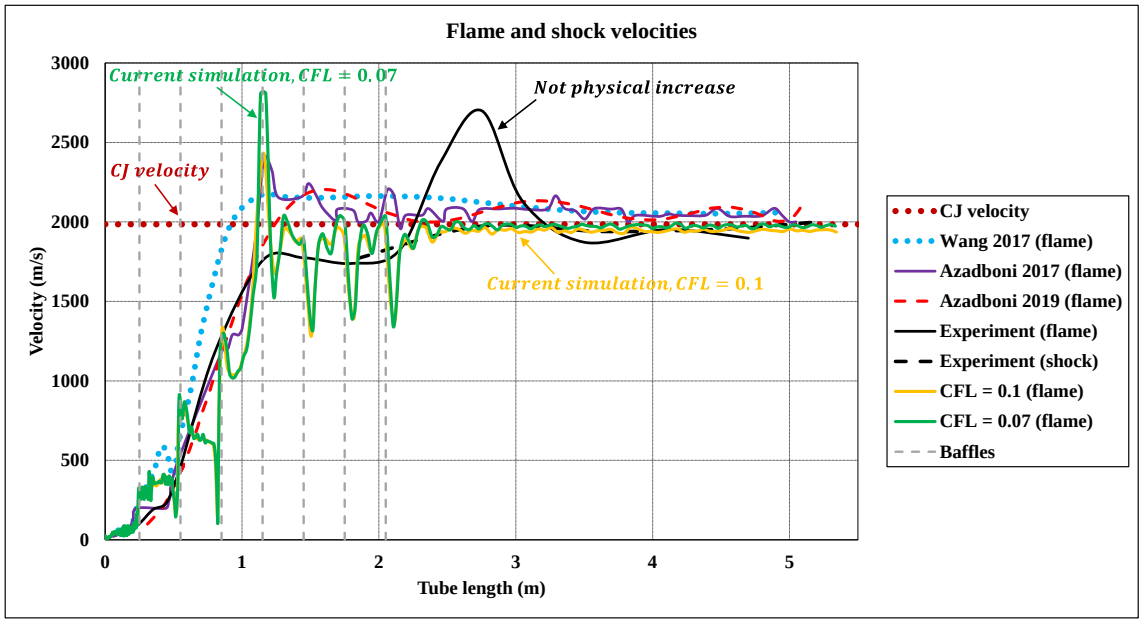

Figure 4.9: Flame tip velocity predicted by the current simulations, on a nodal progress variable of 0.5, compared with the experiment (Boeck et al., 2016) and the SOTA (Azadboni *et al.*, 2017; C.J. Wang and Wen, 2017; Khodadadi Azadboni *et al.*, 2019).

Figures 4.10–4.16 show sequence of the overpressures at different sensors from the experiment and the current simulation using CFL number of 0.1. The simulation data is shifted by 2.62 ms. Azadboni et al. (Khodadadi Azadboni *et al.*, 2019) presented the overpressure at only one sensor while the other SOTA did not present a prediction of the overpressure. There is a qualitatively good matching with the experiment. The first pressure sensor is in the deflagration regime, which is characterized by graduate overpressure rise. The rest of the sensors are in the detonation regime, which are characterized by sharp shock rise. The detonation wave from the simulation, after a shifting by 2.62 ms, is nearly coincidence with the experiment starting from the second

sensor at points p_1–p_6, as shown in Figs. 4.11–4.16 respectively. It is an indication of the correct prediction of the detonation propagation velocity.

The overpressure of (Khodadadi Azadboni *et al.*, 2019) is shifted by 0.235 ms, it is close to the experiment and the current simulation, while their overpressure peak at point (p_1) is much closer to the experiment.

The reflected shock (1) is formed due to reflection of the detonation wave from the end wall of the channel. It propagates toward the ignition wall. The second reflected shock (2) is formed due to reflection of the first reflected shock by the seventh baffle. It propagates in the opposite direction toward the channel end wall. The reflected shocks from the simulation is faster than the experiment and the magnitude of the decay of the overpressure signals from the simulation is higher than the experiment, as shown in the figures. The experiment description mentioned that pressure transducers might subjected to thermal shock, which could have the effect of underpredicting the overpressure with the long run. This phenomenon provides a logical explanation of the discrepancies between decay of the simulation and the experiment overpressures. Another explanation could be related to not including heat transfer modelling in the current study. Therefore, there is an accumulation of energy in the channel with the running time, which is reflected to high values of overpressures in the simulation. In addition to, the two effects could be combined.

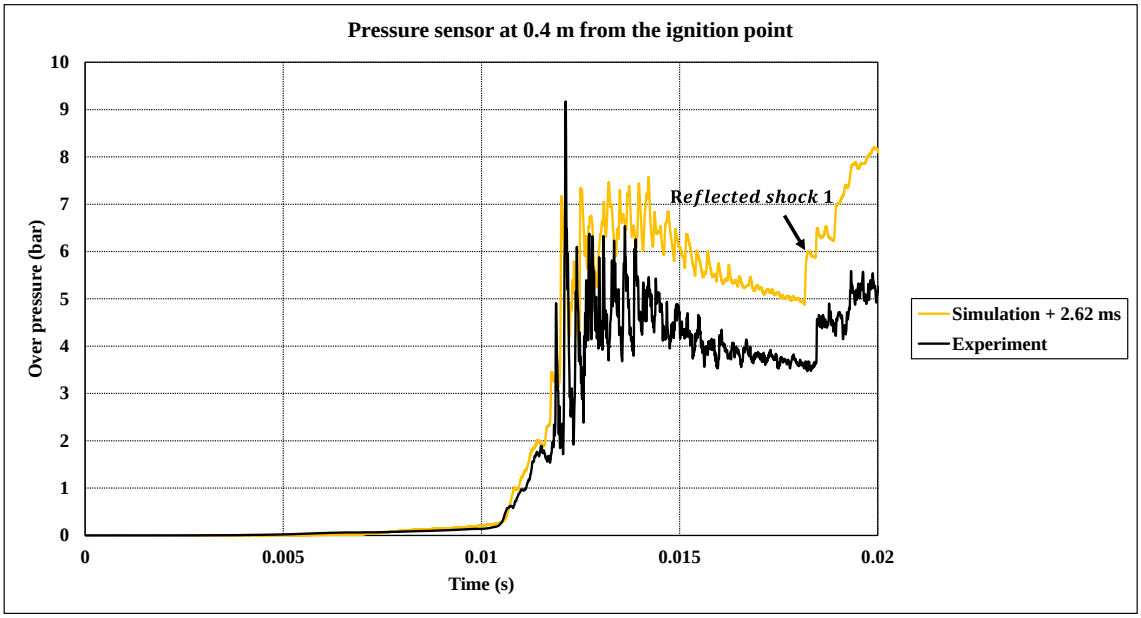

Figure 4.10: Overpressure of the simulation and the experiment (Boeck et al., 2016) at 0.4 m.

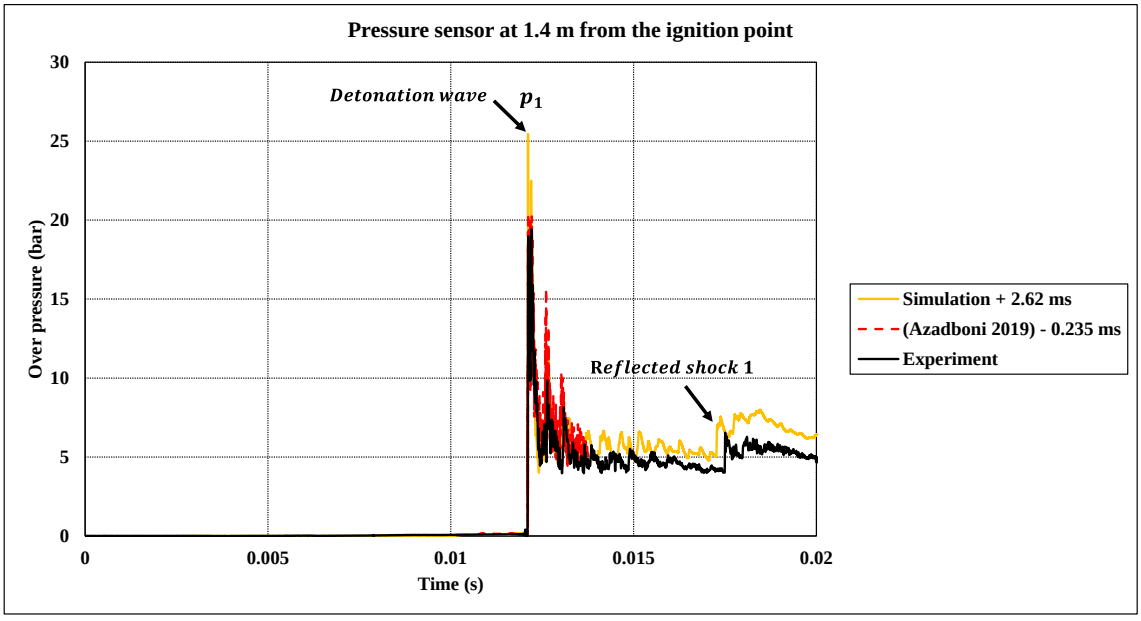

Figure 4.11: Overpressure of the simulation and the experiment (Boeck et al., 2016) at 1.4 m.

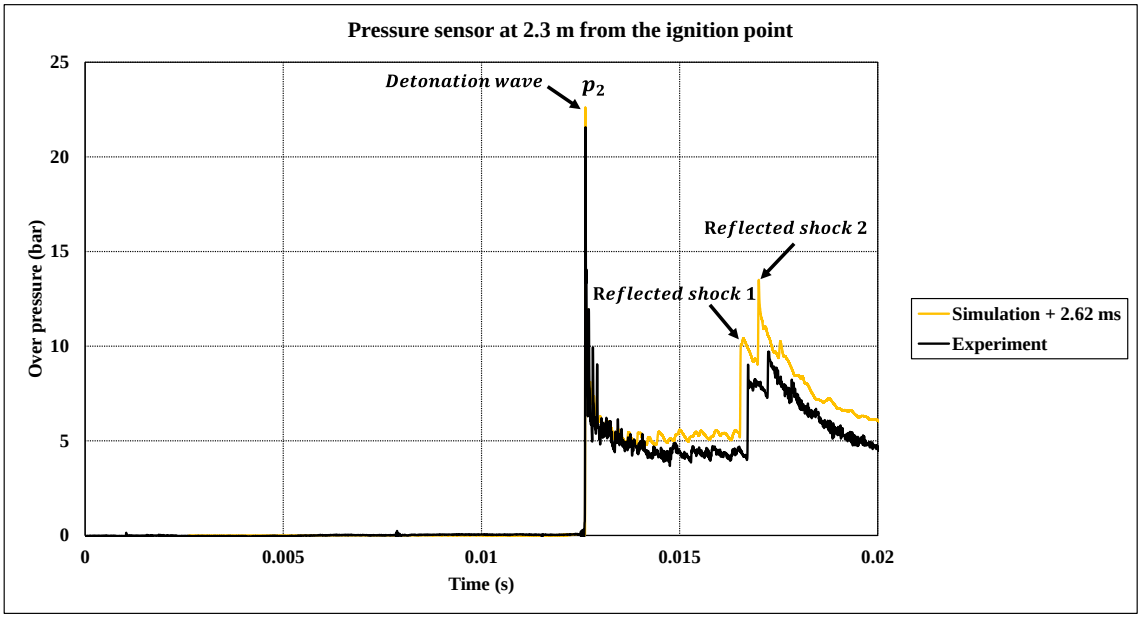

Figure 4.12: Overpressure of the simulation and the experiment (Boeck et al., 2016) at 2.3 m.

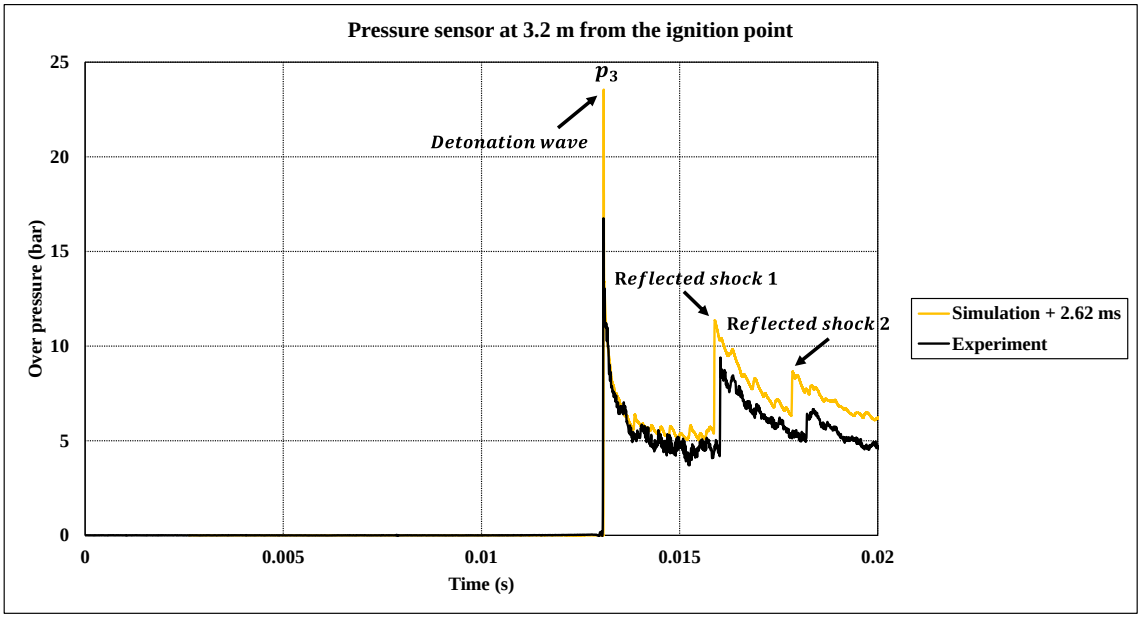

Figure 4.13: Overpressure of the simulation and the experiment (Boeck et al., 2016) at 3.2 m.

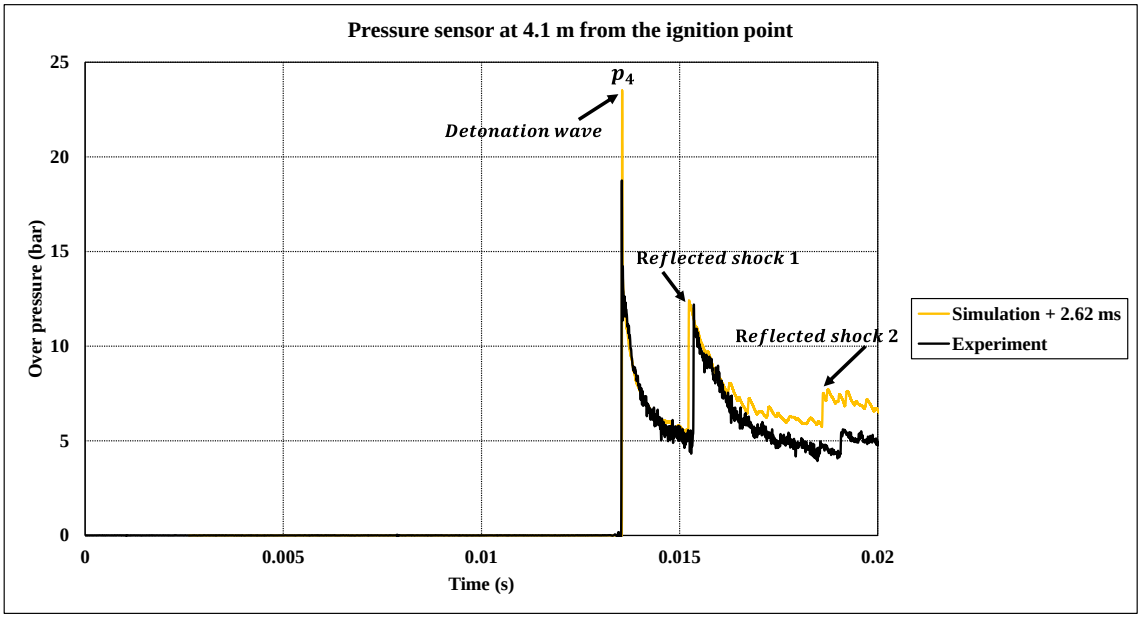

Figure 4.14: Overpressure of the simulation and the experiment (Boeck et al., 2016) at 4.1 m.

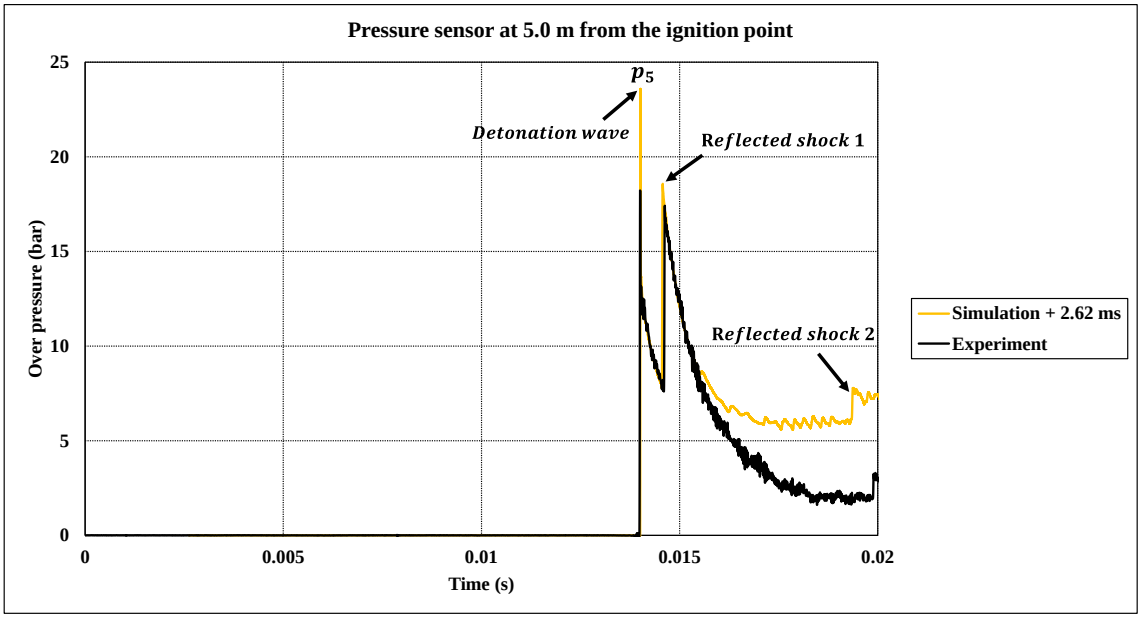

Figure 4.15: Overpressure of the simulation and the experiment (Boeck et al., 2016) at 5.0 m.

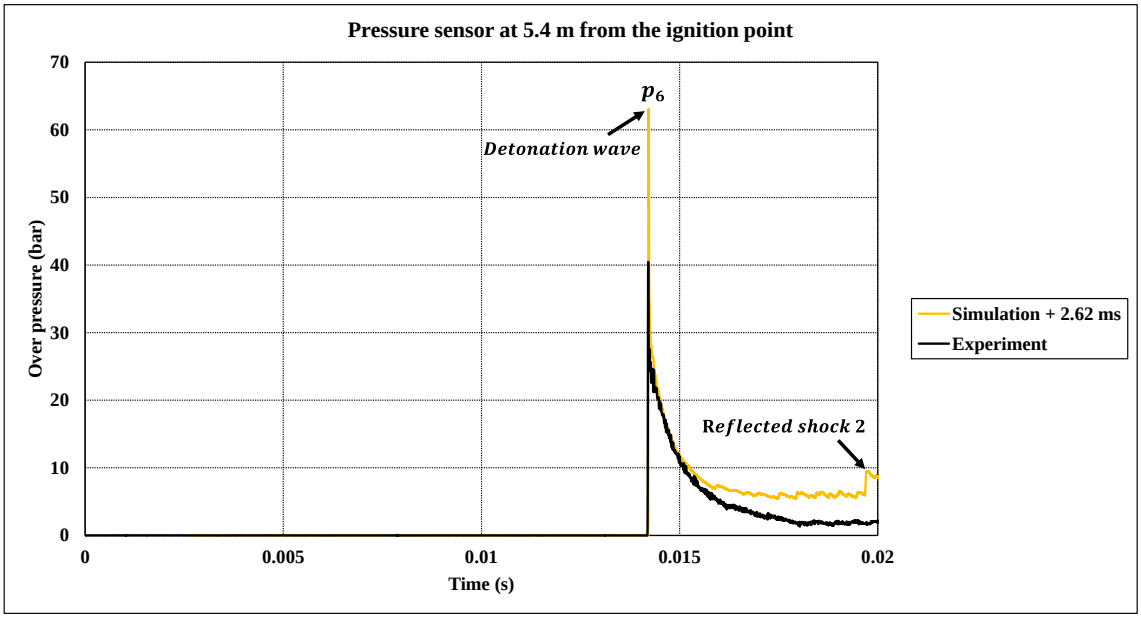

Figure 4.16: Overpressure of the simulation and the experiment (Boeck et al., 2016) at 5.4 m.

4.4.2 Performance of the instabilities and the turbulent wrinkling factors

Figure 4.17 shows the average of instabilities wrinkling factor on a nodal progress variable of 0.5 with flame propagation. Instabilities wrikling factor is generated from the early phase of propagation after the critical radius. Its average contribution in the turbulent burning velocity is relativily small, except before the second baffle. The contribution decreases with the increase in the SGS turbulent intensity and it is neglected in the smooth part of the channel.

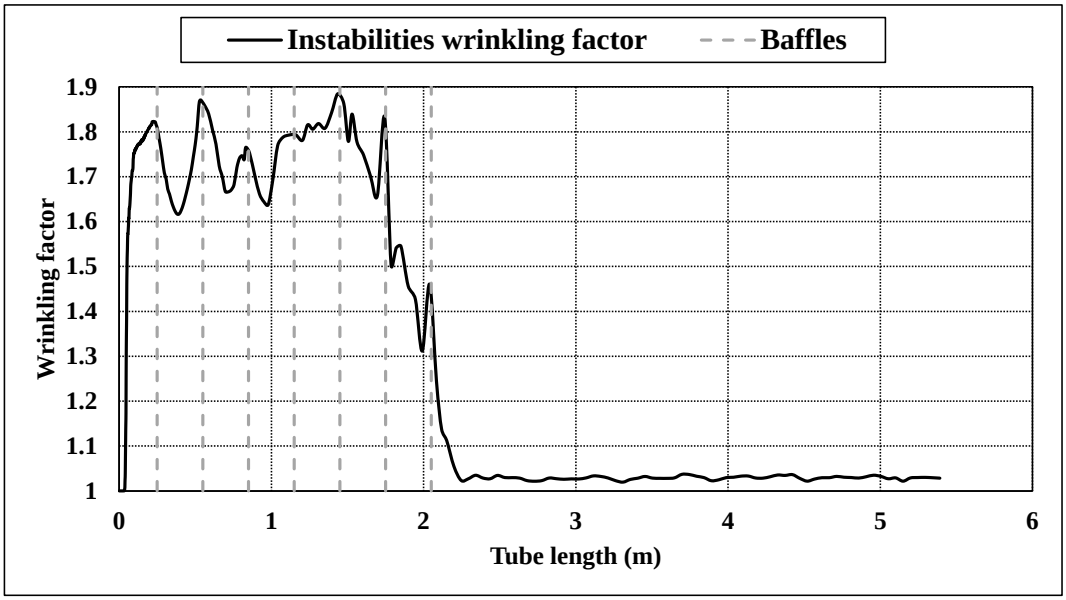

Figure 4.17: Average of the instabilities wrinkling factor with flame propagation on a nodal progress variable of 0.5.

Figure 4.18 shows the average of turbulent wrinkling factor with flame propagation on a nodal progress variable of 0.5. There is no turbulence contibution in the beginning of the propagation until the flame passes the first baffle of the channel. Turbulence contribution increases and reaches its maximum in the smooth part of the channel, then it becomes the largest contributor in the turbulent burning velocity.

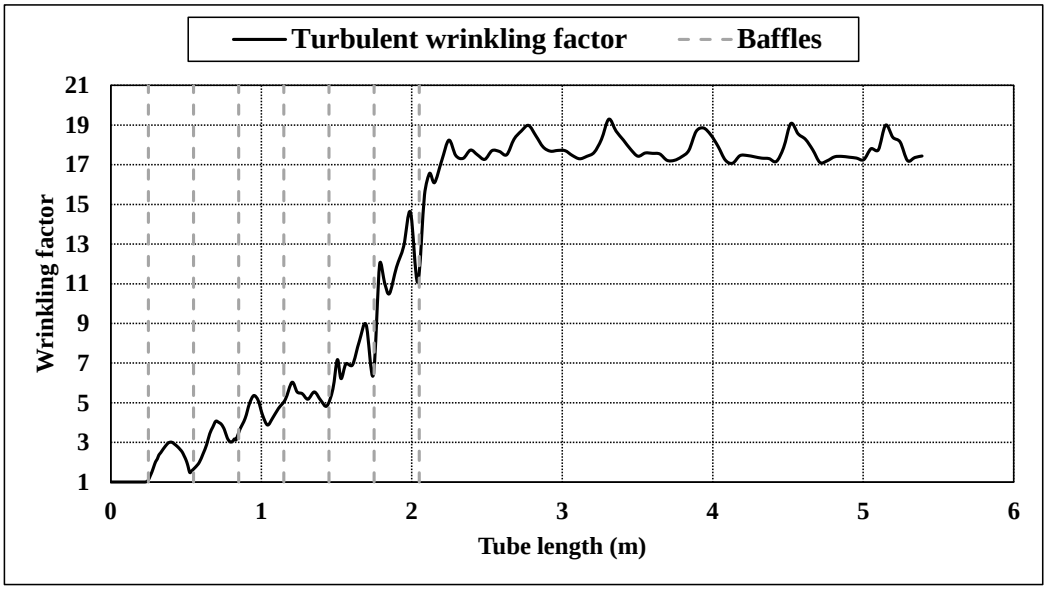

Figure 4.18: Average of the turbulent wrinkling factor with flame propagation on a nodal progress variable of 0.5.

4.4.3 Performance of flame-generated turbulence model

Figure 4.19 shows the average of flame-generated turbulence with flame propagation on a nodal progress variable of 0.5. Flame-generated turbulence is increased with propagation, then it decreases with the increase in turbulent kinetic energy and it could become negative in the smooth part of the channel. Therefore, a limiting condition is used in the current implementation to prevent negative K_{fg}. The original model was developed for flames with laminar burning velocity close to the turbulent intensity. Therefore, there is uncertainty in the usage of this model when turbulence intensity is far from the laminar burning velocity.

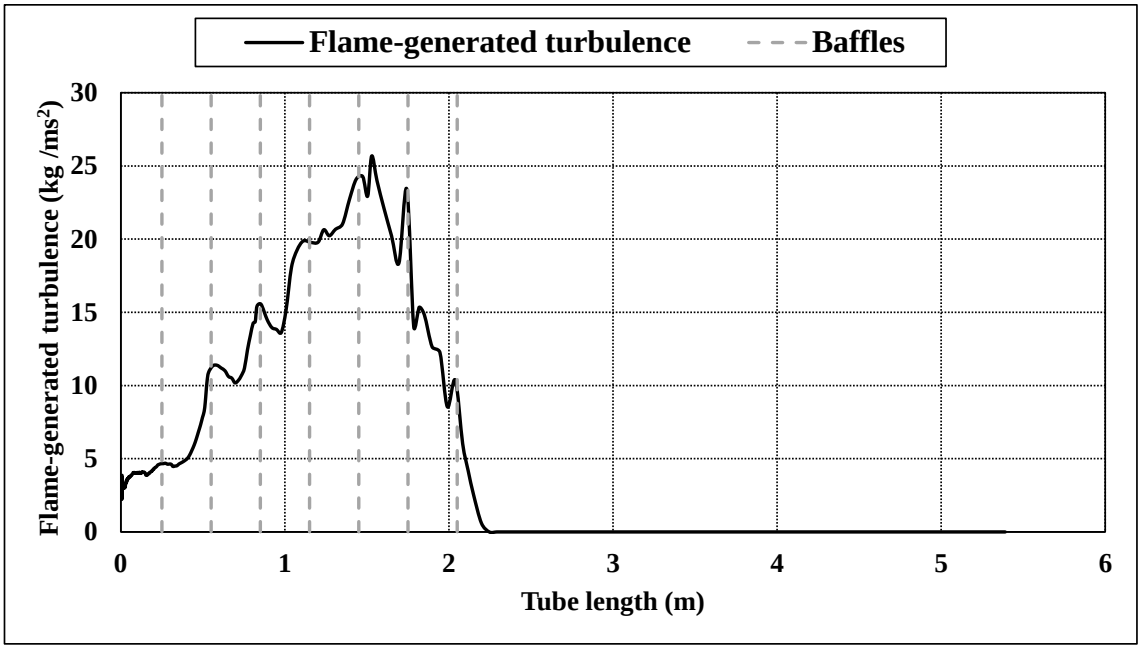

Figure 4.19: Average of flame-generated turbulence with flame propagation on a nodal progress variable of 0.5.

4.4.4 Sources of discrepancies between the proposed model and the experiment

The discrepancies between the prediction of the current model and the experiment could be originated from different sources. The following list contains different possible reasons:

1- There could be temperature divergence for some cells over a period, as temperature goes for high values close to 5000 K and to low values close to 37 K for some simulations.

2- There could be an effect due to the non-clearance of the position of the baffles during performing the simulations. It might affect the time of the arrival of the detonation wave.

3- There could an effect due to not modelling the weakly stretched propagation.

4- There might be an effect due to not modelling heat transfer. That could be the reason for the difference in the time and values of the reflected shocks between the experiment and the simulation.

5- There might be an effect due to the inaccuracy in the measurements of the photodiodes above a flame propagation velocity of more than 1000 m/s. That is the reason for the high velocity of the flame experiment in the beginning of the smooth part of the channel compared to the experiment shock velocity.

6- There might be an effect due to the thermal shock of the pressure transducers. That could be the reason for the difference in the time and values of the reflected shocks between the experiment and the simulation.

4.5 Conclusions

The proposed model is tested against DDT experiment in a channel. Different grid sizes and CFL numbers are tested, as summarized in Table 4.5. Detonation velocity is less sensitive to the grid sizes, while it is very sensitive to the CFL numbers. CFL numbers of 0.1 and 0.07 predict the correct detonation velocity using a mesh with a grid size of 6.0 mm and a total number of 446 k cells. This simulation predicts good detonation velocity compared with the shock propagation velocity of the experiment, the Chapman–Jouget velocity, and the SOTA. The simulation predicts more than detonation regime, staring with an overdriven detonation at 1.15 m from the ignition, inside the baffled part. That is followed by an oscillation in the flame propagation velocity below the CJ velocity due to the succeeded baffles. In the smooth part of the channel, flame propagation velocity relaxes to a value close to the shock propagation velocity of the experiment and the CJ velocity. Considering the relative coarse grid of the simulation using 3D and the fine grids of the SOTA, order of 10 μm for the smallest grid size using 2D, in addition to the good quality of the prediction. The current model would be more superior than the SOTA for predicting the flame detonation velocity.

The reflected shocks are faster than the experiment and the decay of the overpressures are higher than the experiment. It is possible to be either due to the thermal shock of the pressure transducers or due to not including heat transfer modelling or due to both. Wrinkling due to flame instabilities is generated in the beginning of the propagation, after the critical radius, while wrinkling due to turbulence is generated after the first baffle of the channel and overwhelms the instabilities with propagation. At the end, the turbulent wrinkling factor becomes the largest contribution in the chemical reaction rate. Finally, the proposed model for the chemical reaction rate is succeeded to qualitatively predict DDT in terms of initiation, detonation velocity, and overpressure signals.

Table 4.5: Summary of the performed simulations using different grid sizes and CFL numbers for the DDT experiment.

Mesh	Average grid size	Total mesh size	CFL number	Processors	Approximate CPU time
Coarse	7.5 mm	230 k cells	0.6	8	0.8 day
Medium	6 mm	446 k cells	0.6	16	0.95 day
Fine	4.5 mm	1.1 M cells	0.6	8	5.9 days
Medium (2)	6 mm	446 k cells	0.8	6	1.8 days
Medium (2)	6 mm	446 k cells	0.6	16	0.98 day
Medium (2)	6 mm	446 k cells	0.1	16	5.8 days
Medium (2)	6 mm	446 k cells	0.07	16	7.9 days

CHAPTER 5. NUMERICAL SIMULATION OF OPEN ATMOSPHERE DEFLAGRATION EXPERIMENT

5.1 Introduction

The purpose of the present chapter is to numerically test the proposed chemical reaction rate model against large-scale hydrogen-air deflagration experiment in the open atmosphere. The open atmosphere experiment was used as a numerical benchmark for developing computational fluid dynamics (CFD) codes for a safety purpose. This scenario could be like the release of hydrogen in refueling station if the dispersion of the gas is neglected. There is no initial turbulence at the early phase of propagation. Therefore, it is expected that the main physical acceleration mechanism in the early propagation at this experiment is the hydrodynamic & thermo-diffusive instabilities and their related formation of cellular structure through continuous surface splitting. The capability of the new developed wrinkling model due to hydrodynamic & thermo-diffusive instabilities is manifested in this simulation.

Different teams have simulated the open atmosphere experiment in (Gallego *et al.*, 2005; García *et al.*, 2010). They have used different combustion, and turbulence modelling. A summary of their turbulence and combustion models are given in Table 5.1 (García *et al.*, 2010). The model used in the UU simulation is an early version of the Ulster deflagration model. Different domain sizes, mesh topology, and grid sizes are used and summarized in Table 5.2 (García *et al.*, 2010). Most of the SOTA have used RANS in their simulations except one case, which has used LES.

Table 5.1: Turbulence and combustion models of the SOTA of the open atmosphere (García *et al.*, 2010).

Team	Turbulence model	Combustion model
CEA	None	CREBCOM Combustion model
FzK	RANS standard $(k-\varepsilon)$	CREBCOM model with flame tracking
Gexon	RANS standard $(k-\varepsilon)$	Beta flame model
NH	RANS standard $(k-\varepsilon)$	Beta flame model

Continuation of Table 5.1.

JRC	RANS standard $(k-\varepsilon)$	Modified Eddy Dissipation Concept
TNO	RANS standard $(k-\varepsilon)$	
UU	RNG-LES	Gradient method

Table 5.2: Setup of the SOTA of the open atmosphere (García *et al.*, 2010).

Team	Grid type	Grid size	CFL	Domain size
CEA	1D domain	0.1 m	0.5	1D spherical domain
FzK	3D Arbitrary equidistant and orthogonal grid	0.3 m for combustion. 0.59 m for pressure propagation. Total cells: 912000	0.96	Parallelepipedic with $24\,m \times 24\,m \times 24\,m$ for combustion. $29.5\ m \times 29.5\ m \times 94\ m$ for pressure propagation.
Gexon	3D cartesian grid	0.5 m		
NH	3D cartesian grid			
JRC	3D unstructured tetrahedral grid with AMR	0.27 m inside the combustion. Initial cells: 1789911. Maximum cells: 3336095	$<$ 1.0	Hemisphere with a radius of 300 m.
TNO	3D cartesian grid	Total cells: 27000	0.9	

Continuation of Table 5.2.

UU	3D unstructured tetrahedral grid	(a): 0.2-0.6 m for hydrogen mixture & 0.8-0.9 for pure air Total cells: 677729 (b): 0.4-1.0 m for hydrogen mixture & 1.2-1.4 m for pure air – Total cells: 258671	0.8	Hemisphere with a radius of 30 m. Extended in single side to 100 m for pressure propagation

5.2 Experiment description

Large-scale deflagration experiment in open atmosphere was conducted by Fraunhofer Institute for Chemical Technology (FhG-ICT) in 1983, a summary of the experiment from (Jordan, 2006) is as follows: The experiment consisted of a polyethylene hemispherical balloon with a diameter of 20 m and a volume of 2094 m^3. It is filled with stoichiometric hydrogen-air mixture and is fixed to the ground, as shown in Fig. 5.1 (Jordan, 2006). To overcome the buoyancy force, an inside weight was used, where the balloon shell faced the ground in addition to a wire net of rhombus-shape was placed above the balloon that was fixed to the ground at 16 positions.

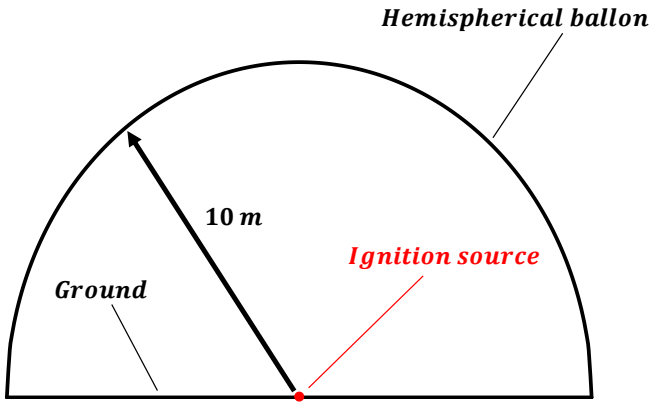

Figure 5.1: Schematic of the open atmosphere experiment setup (Jordan, 2006).

The balloon was filled with a special care to the hydrogen concentration and the mixture homogeneity. Air was drawn from the atmosphere using a fan and enters the balloon through a tube that was controlled by a flutter valve. Hydrogen was provided in parallel using several bottles, where the quantity of hydrogen was controlled by the supplied bottles volumes and their pressure. Hydrogen and air were mixed using air fans. Samples of the mixture from different heights were collected and analyzed using gas chromatography. The mixing produced homogeneous concentration of 29.7% by volume at the initial temperature and pressure of 283 K and 98.9 kPa respectively. The mixture ignited at the balloon center using 150 J ignition pills and flame was propagated nearly in a hemispherical shape. Flame propagation stretched the balloon shell that was blasted along its longitudinal welding parts and along the balloon perimeter which faced the ground. The balloon shell blasting happened nearly at flame propagation radius of 5 m. Overpressure was recorded using pressure transducers, which were located at the ground along radial direction with distances of 2.0 m, 5.0 m, 8.0 m, 18.0 m, 35.0 m, and 80.0 m from the balloon center. High speed cameras were used to track flame front propagation, they were installed along the pressure transducer axis and along its normal axis. Flame front section between 45^0 and 135^0 from the ignition source was used for evaluating an average values of the flame front radius and the flame front velocity. The errors due to blurriness at flame front and fluctuation of the picture frequency was estimated to be $\pm 5\%$ without taking any farther effects like flame asymmetry at flame propagation. Flame front propagation radius is obtained after averaging the data from the different cameras.

5.3 Simulation description

Numerical simulation of the experiment is performed using 3D Navier-Stokes equations with TKE-LES turbulence closure and the same setting of the DDT simulation.

5.3.1 Mesh setup

3D domain with length, width, and height of 200 m, 200 m, and 100 m respectively is used to simulate the experiment. The mesh design is close to the mesh that was used by Ulster University in previous study. The domain is discretized using tetrahedral (tetra) and hexahedral grid elements. Tetrahedral elements are constructed inside a hemispherical shape with a radius of 21 m starting from domain center. It is followed by another coarse tetrahedral elements, which extends until 25 m from the

ignition point in all directions. The rest of the domain is constructed using hexahedral elements with the size of 5.0 m, where an intermediate layer of hexahedral elements with the size of 2.5 m is used for transition. Three meshes: coarse, medium, and fine for the tetrahedral elements are used to investigate the dependence of the solution on the grid size. The coarse mesh has tetrahedral elements of the size of 1.25 m and 1.5625 m and a total mesh size of 235 k cells. The medium mesh has tetrahedral elements of the size of 0.8 m and 1.5625 m and a total mesh size of 474 k cells. The fine mesh has tetrahedral elements of the size of 0.63 m and 1.25 m and a total mesh size of 1.0 M cells. A summary of the meshes is shown in Table 5.3. Using more finer grid sizes is not possible during the time of the current study due to limitation of the shared license of ANSYS-Fluent.

Table 5.3: Summary of the Open atmosphere meshes.

Mesh	Average grid size	Total mesh size
Coarse	Tetra (1.25 m & 1.5625 m) – hexa (2.5 m & 5 m)	235 k cells
Medium	Tetra (0.8 m & 1.5625 m) – hexa (2.5 m & 5 m)	474 k cells
Fine	Tetra (0.63 m & 1.25 m) – hexa (2.5 m & 5 m)	1 M cells

Figure 5.2 shows front section from the medium mesh and Fig. 5.3 shows a zoom to the tetrahedral part at the front section. Mesh interface is used between hexahedral elements and tetrahedral elements. Another two mesh interfaces are used inside the tetrahedral region. The first is to separate between the finer and coarser grid and the second is to separate between pure air and hydrogen-air mixture.

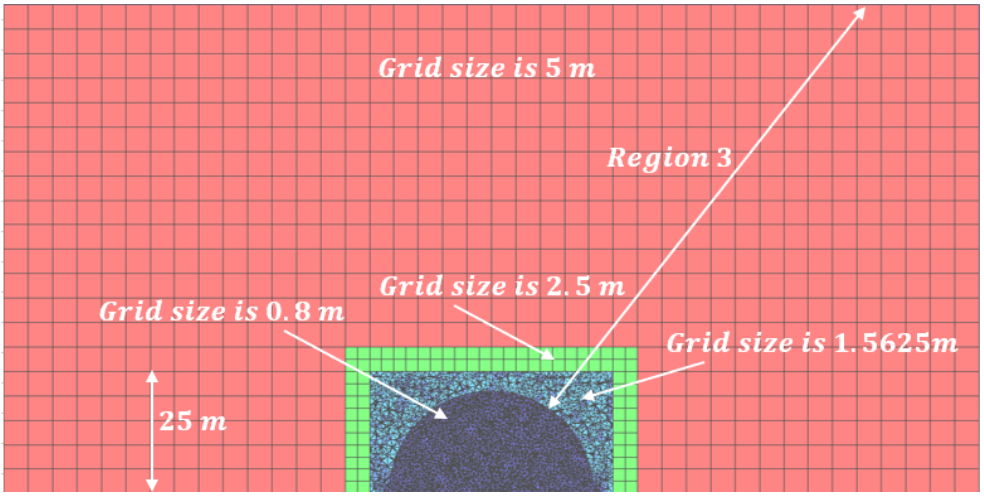

Figure 5.2: Front section from the medium mesh.

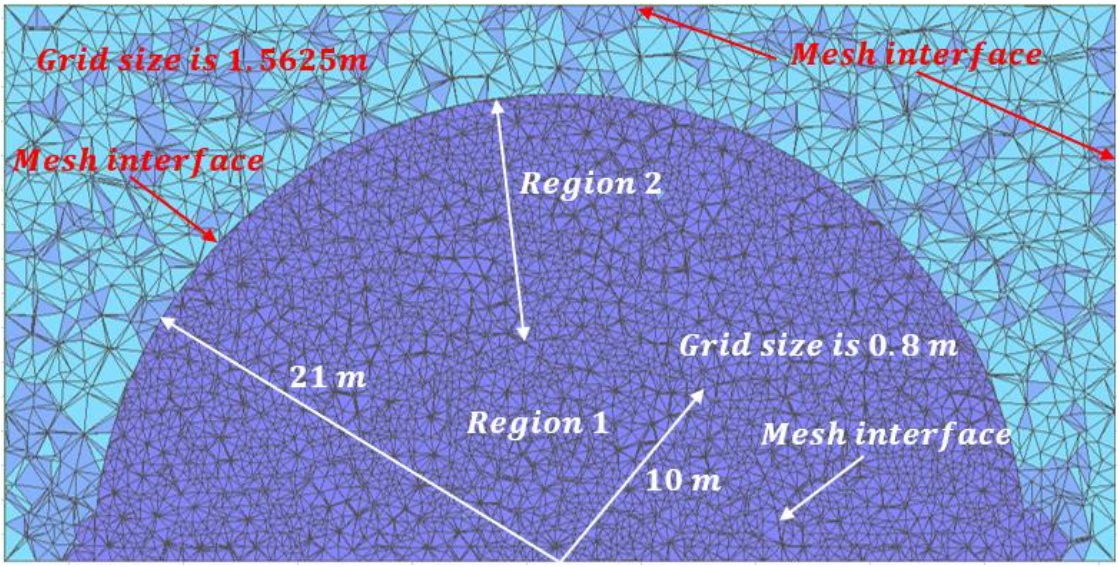

Figure 5.3: Zoom to the front section from the medium mesh.

Figure 5.4 shows the tetrahedral region with respect to the domain from the bottom view of the medium mesh.

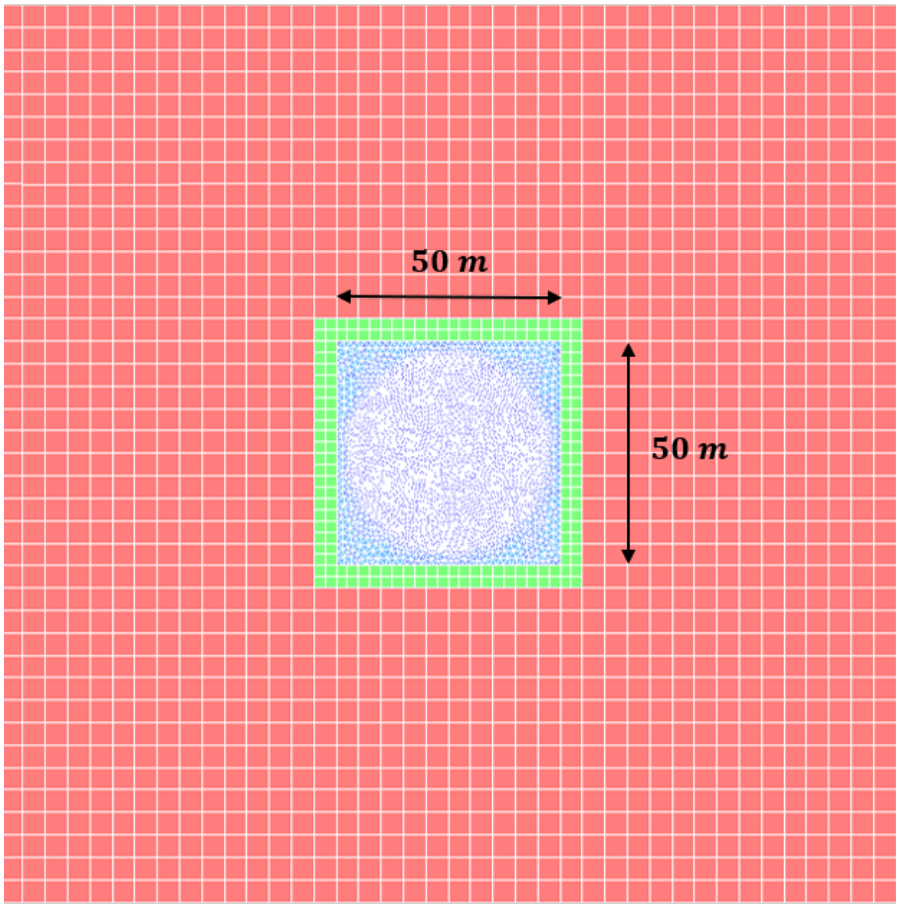

Figure 5.4: Bottom view of the medium mesh.

5.3.2 Simulation setup

The governing equations are solved using density-based explicit solver with TKE-LES turbulence closure. The convective terms are discretized using second order upwind based on AUSM+ scheme. The gradients are calculated using Green-Gauss node-based method. Simple gradient diffusion law is used to model transport terms in the governing equations. Time derivatives are discretized using an explicit 4-stages Runge-Kutta scheme. Solution dependence on time-step is investigated using CFL numbers of 1.0, 0.8, and 0.6 based on the medium mesh.

The outer cut-off length scale of the instability in Eq. (2.57) is not limited. λ_{min} is calculated from the spherical flame relation in Eq. (2.58). The source terms of the governing equations are calculated like the DDT simulation, as shown in Eqs. (3.46)–(3.48) based on the proposed chemical reaction model. Flame-generated turbulence is modelled in the source terms of the momentum equations based on derivative of the algebraic model in Eq. (3.49). It is applied inside the flame brush after the ignition time. A limiting condition is used to prevent negative K_{fg} at high k_{Δ}.

Thermodynamics and combustion properties are calculated in an initial step using the Ó Conaire chemical reaction mechanism in the framework of Cantera. Specific heat, sensible enthalpy, molecular viscosity, and thermal conductivity dependence on temperature for the air and hydrogen are approximated in polynomials with temperature variable up to 3000 K. Specific heat, sensible enthalpy, molecular viscosity, thermal conductivity for the burned gas are changed with the unburned mixture concentration, as show for example in Fig. 5.5 for the specific heat under pressure and temperature of 101.325 kPa and 283 K respectively. Therefore, their dependence on temperature is approximated using three polynomials up to 3000 K, which are calculated for the unburned mixture with hydrogen concentrations of 0.04, 0.297, and 0.75. A linear interpolation is used for different values of the hydrogen concentration. For temperature above 3000 K, the corresponding values of the specific heat, sensible enthalpy, molecular viscosity, and thermal conductivity at 3000 K are used.

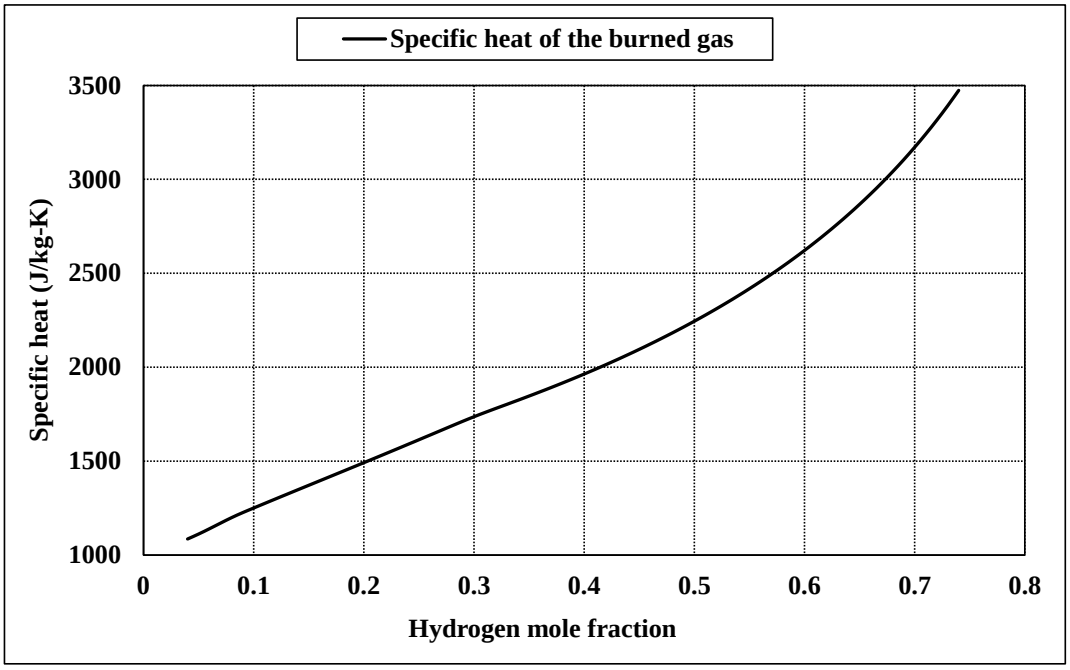

Figure 5.5: Change of specific heat with hydrogen concentration under pressure and temperature of 101.325 kPa and 283 K respectively.

The effect of pressure on the unburned mixture density is considered using an isentropic relation. Expansion coefficient, adiabatic flame temperature, and inner cut-off length scale of the instabilities are changed with the unburned mixture concentration and the isentropic change of the initial pressure, as shown for example in Fig. 5.6 for the expansion coefficient under an isentropic change of the pressure. The heat of chemical reaction and the Lewis number of the deficient reactant are changed with the unburned mixture concentration.

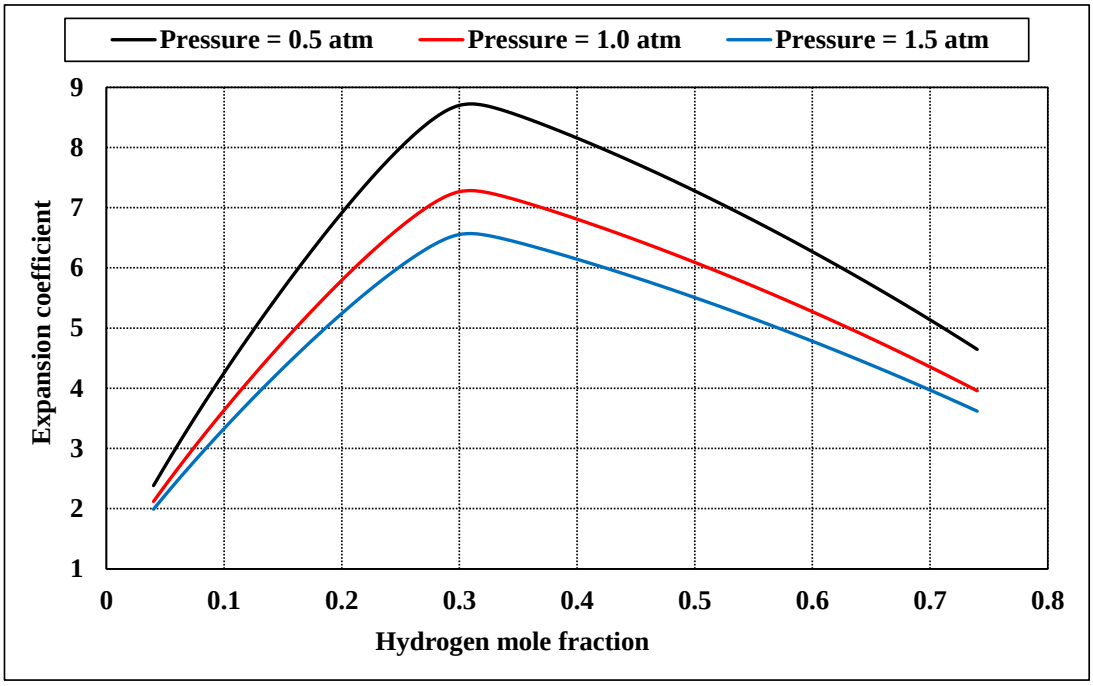

Figure 5.6: Change of expansion coefficient with concentration and pressure.

The effects of the unburned mixture concentration and the isentropic change of the pressure on the expansion coefficient, adiabatic flame temperature, inner cut-off length scale of the instabilities, heat of chemical reaction, and the Lewis number of the deficient reactant are considered by constructing three polynomials in hydrogen concentration. The first is at initial pressure and temperature of 101.325 kPa and 283 K respectively. The second is at pressure of 50.6625 kPa and temperature corresponds to isentropic expansion from the initial value. The third is at pressure of 151.9875 kPa and temperature corresponds to isentropic compression from the initial value. The pressure values of 151.9875 kPa and 50.6625 kPa are chosen to represent upper and lower boundaries of the expected pressure by inspecting the experiment data. A linear interpolation is used for pressure in between. If the pressure is higher or lower than the boundary pressure, the boundary pressure is used. It should be noted that, there is no effect of the isentropic change of the pressure, under the current specified range, on the heat of chemical reaction and the Lewis number of the deficient reactant.

The effect of the isentropic change of the pressure on the unburned mixture molecular viscosity, thermal conductivity, and specific heat is considered for the pressure between 50.6625 kPa and 151.9875 kPa. Outside this range, the corresponding boundary values are used.

The hemisphere of radius 10 m from the domain center is filled with stoichiometric hydrogen-air mixture, which has volumetric concentration of 29.7%, while the rest of the domain is filled with pure air. The domain ground boundary condition is modelled as an adiabatic wall with no slip. The top and side boundaries of the domain are set to pressure far field, which does not allow reflection of acoustic waves. The mesh interfaces are set to matching interfaces. The simulation initial temperature is set to 283 K and initial pressure is set to 98.9 kPa. Heat transfer either between the flow in the computational domain and the external far field or between the burned gas and the unburned gas inside the computational domain is not treated in the current study.

The mixture is ignited by varying linearly the progress variable from 0 to 1 and the cell temperature from the initial temperature to the adiabatic flame temperature during the ignition time inside the ignition cell. The ignition cell is chosen close to the domain center. The equivalent length of the ignition cell (Δ_Δ) is defined based on its volume, as what was done in Ulster University UDF for tetrahedral cell, as shown in Eq. (5.1).

$$\Delta_\Delta = \sqrt[3]{6\sqrt{2}\,V_c} \tag{5.1}$$

V_c is the volume of the ignition cell.

Ignition time is defined as the time to propagate a laminar flame under the initial temperature and pressure along half of the equivalent length of the ignition cell as shown in Eq. (5.2) (Molkov, 2012).

$$t_{ign,initial} = \frac{1}{2}\,\frac{\Delta_\Delta}{\sigma\, S_u} \tag{5.2}$$

The ignition time was multiplied by a mistake by the factor 1.0022, which is expected to not produce substantial effects on the results. The effect of the difference between the initial pressure 98.9 kPa and the reference pressure 101.325 kPa on the laminar burning velocity and the thermodynamic properties is neglected.

5.3.3 Mesh independence study

The solution dependence on the mesh resolution is investigated using the three meshes with CFL number of 1.0. Table 5.4 summarizes the running time of the simulations. Figure 5.7 shows the average of Pope criterion calculated using Eq. (4.2) for three geometrical regions. The first region is a hemisphere with a radius 10 m i.e. the original hydrogen-air mixture region, as shown in Fig. 5.3. The second region is between two hemispheres of radiuses 21 m and 10 m, as shown in Fig. 5.3. The third region is the rest of the domain i.e. outside the hemisphere of radius 21 m, as shown in Fig. 5.2. The coarse and medium meshes are close to each other, especially in the second and third regions with a Pope criterion above 0.8. The fine mesh has a contradicted behavior as the Pope criterion decreases. The flow could be different from the shear stress flow (Menon, 2015b). Therefore, the Pope criterion might be less constructive. Hence, mesh convergence could be examining from the predicted flame propagation and the overpressure.

Table 5.4: Running time of the mesh independence study for the open atmosphere.

Mesh	CFL number	Processors	Approximate CPU time
Coarse	1.0	16	0.28 day
Medium	1.0	16	1 day
Fine	1.0	8	5.7 days

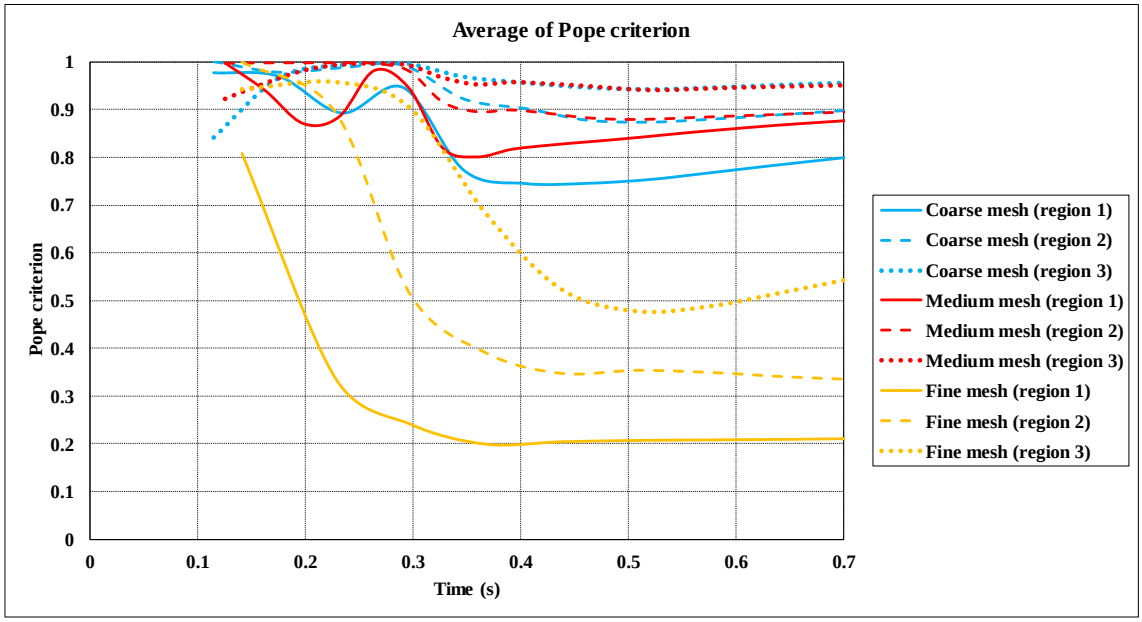

Figure 5.7: Average of the pope criterion for the coarse, medium, and fine meshes.

Figures 5.8–5.10 show flame tip propagation radius and the overpressures at 5 m and 35 m respectively of the three meshes compared with the experiment (Gallego *et al.*, 2005). The tip flame radius is measured between 45^0 and 135^0 along the vertical axis, on a nodal progress variable of 0.5. The pressure sensor at 35 m is inside the hexahedral grid, which is not refined. In general, refining the mesh produces higher propagation velocity and higher overpressure. The solution is going to converge toward the fine mesh. It is expected that using much higher refining will not substantially change the results. The medium and fine meshes can qualitatively be used for farther analysis in the next sections.

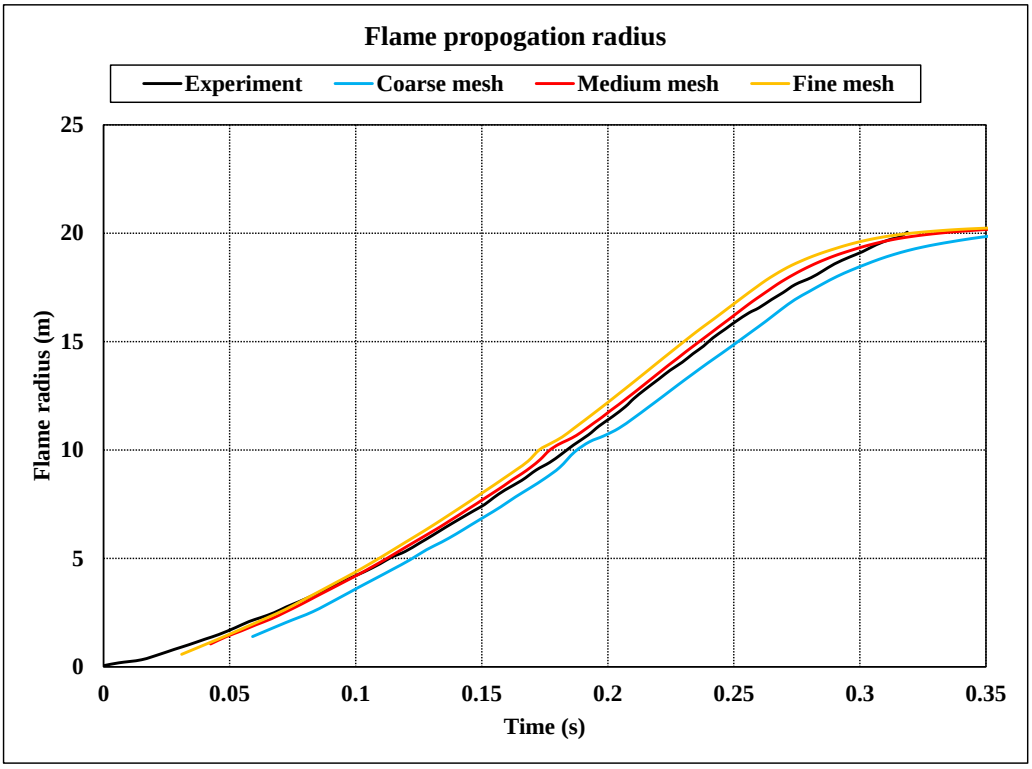

Figure 5.8: Flame tip radius predicted by the three meshes on a nodal progress variable of 0.5 compared with the experiment (Gallego *et al.*, 2005).

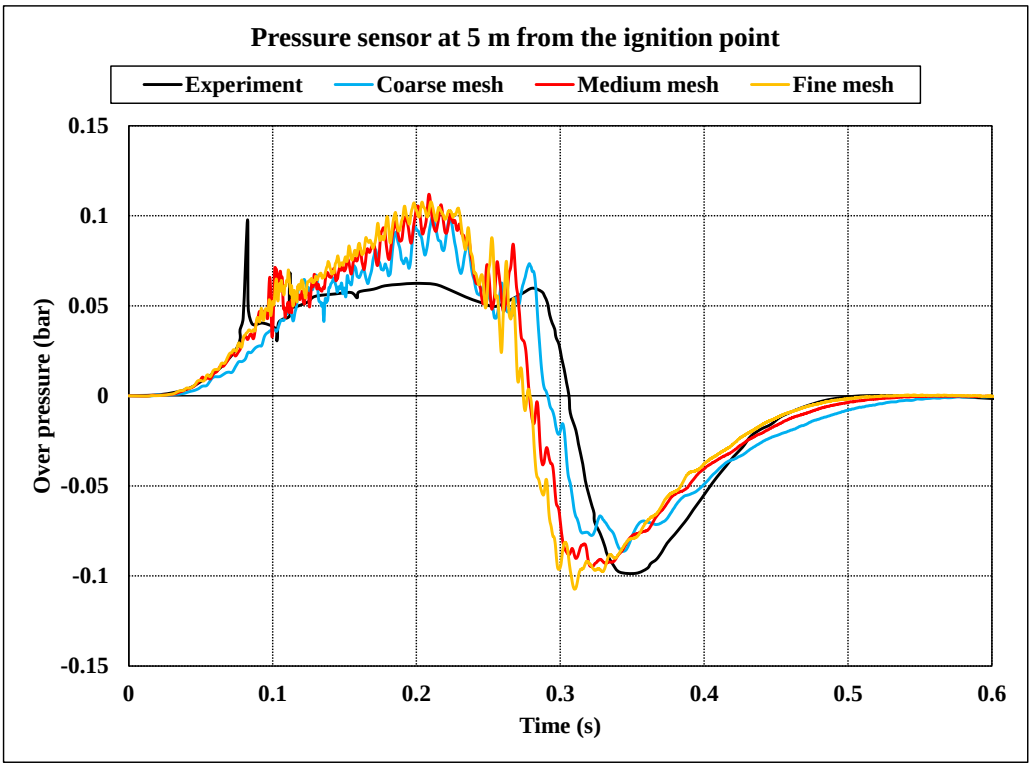

Figure 5.9: Overpressure at 5 *m* predicted by the three meshes compared with the experiment (Gallego *et al.*, 2005).

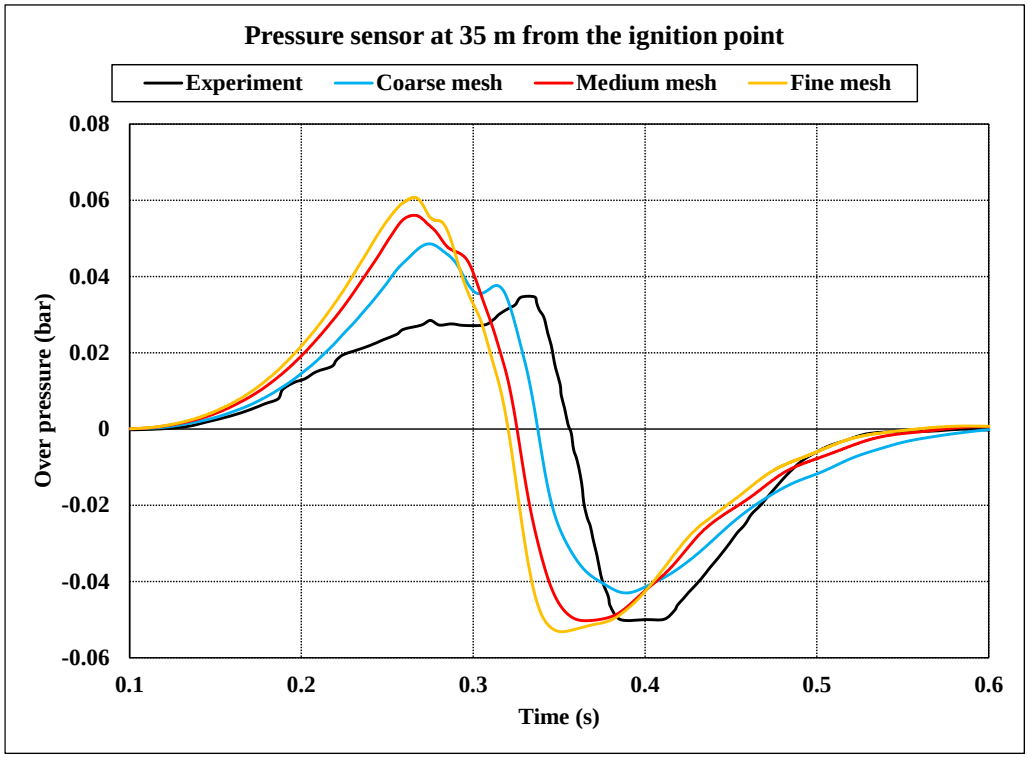

Figure 5.10: Overpressure at 35 m predicted by the three meshes compared with the experiment (Gallego *et al.*, 2005).

5.3.4 Time-step independence study

The medium mesh is used to investigate the time-step independence study. Three CFL numbers are tested: 1.0, 0.8, and 0.6. Table 5.5 summarizes the running time of the simulations. Figure 5.11 shows the average of Pope criterion using Eq. (4.2) for the three CFL numbers in the same geometrical regions, which are declared in the previous section. There is convergence between the three cases for most of the running time and the Pope criterion is above the value of 0.8 except at the late time for CFL number of 0.8.

Table 5.5: Running time of the time-step independence study for the open atmosphere.

Mesh	CFL number	Processors	Approximate CPU time
Medium	1.0	16	1 day
Medium	0.8	16	1.23 days
Medium	0.6	8	2.95 days

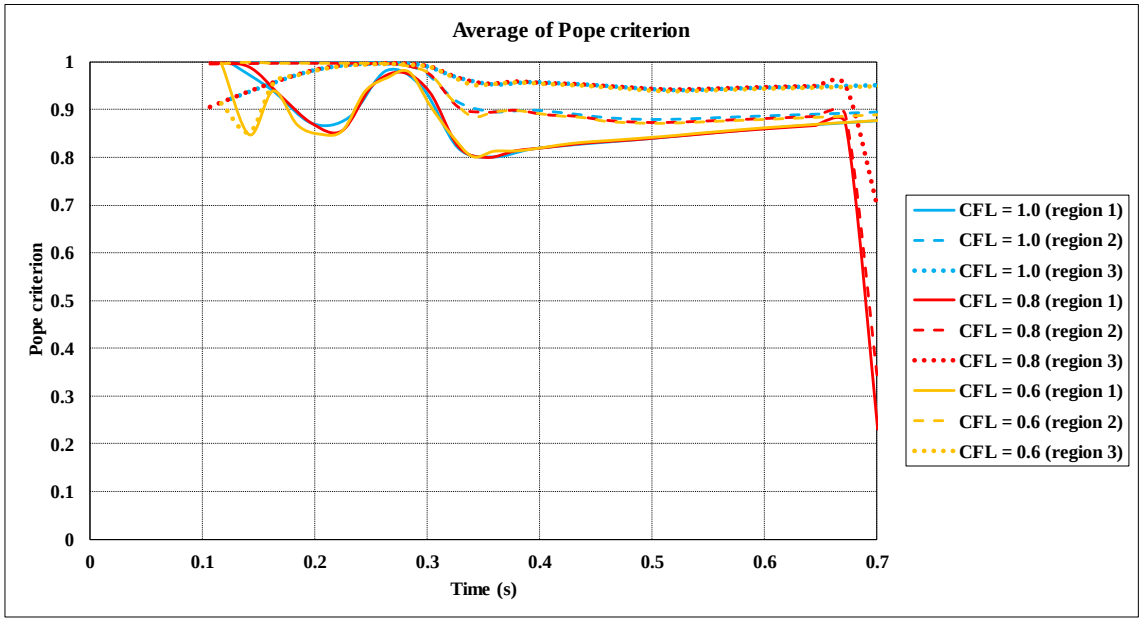

Figure 5.11: Average of the Pope criterion for CFL numbers of 1.0, 0.8, and 0.6 using the medium mesh.

Figure 5.12 shows the predicted overpressure at 5 m using CFL numbers of 1.0, 0.8, and 0.6 compared with the experiment (Gallego *et al.*, 2005). There is convergence using the three CFL numbers. Hence, the solution is less dependent on the time-step discretization.

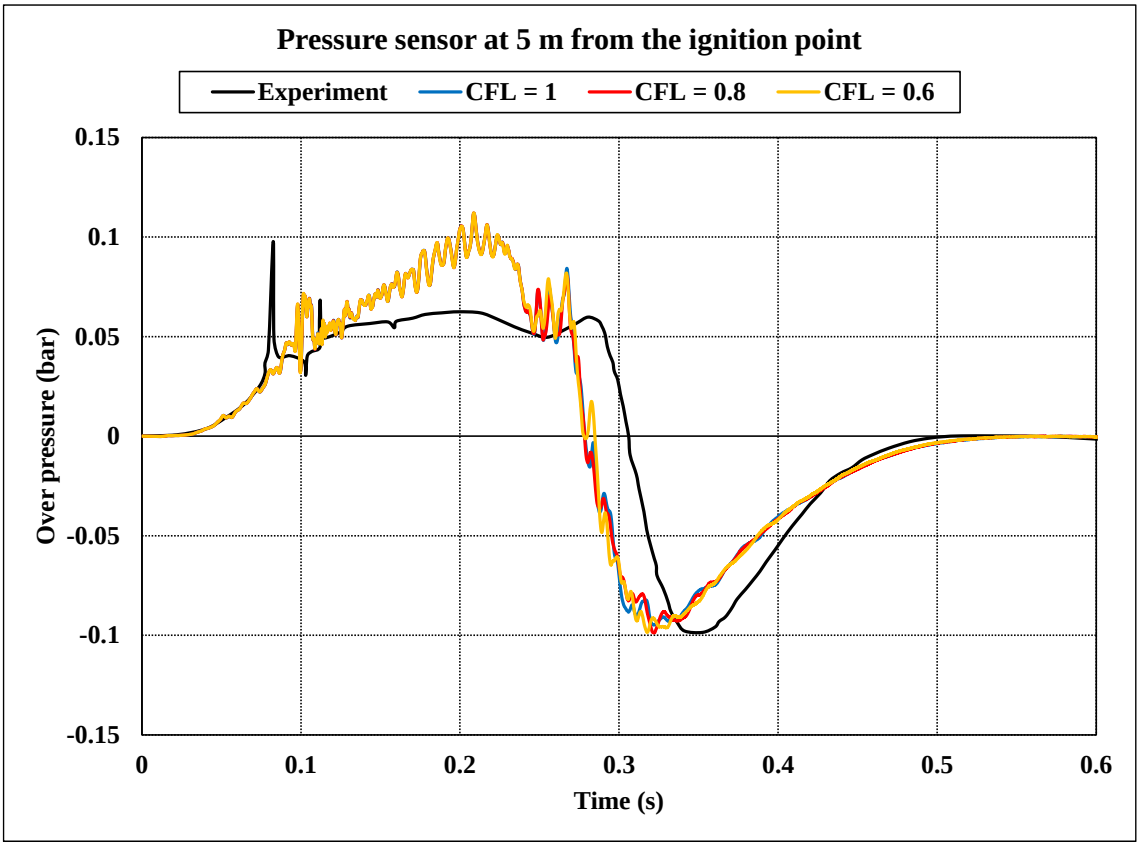

Figure 5.12: Overpressure at 5 m using CFL numbers of 1.0, 0.8 and 0.6 compared with the experiment (Gallego *et al.*, 2005).

5.4 Simulation results and discussion

5.4.1 Performance of the proposed model against the SOTA

Figure 5.13 shows flame tip propagation radius of the current study using the fine and medium meshes, on a nodal progress variable of 0.5, compared with the experiment and the SOTA. CFL number of 1.0 is used in the fine and medium meshes. Flame radius from the current proposed model is qualitatively compared well with the experiment, but there is a cumulative increase to the flame radius with propagation. Some of the SOTA predicted flame propagation radius close to the experiment while the others predicted slow propagation. The slow propagation was explained in (Gallego *et al.*, 2005) for the TNO's simulations as due to the use of inappropriate boundary condition.

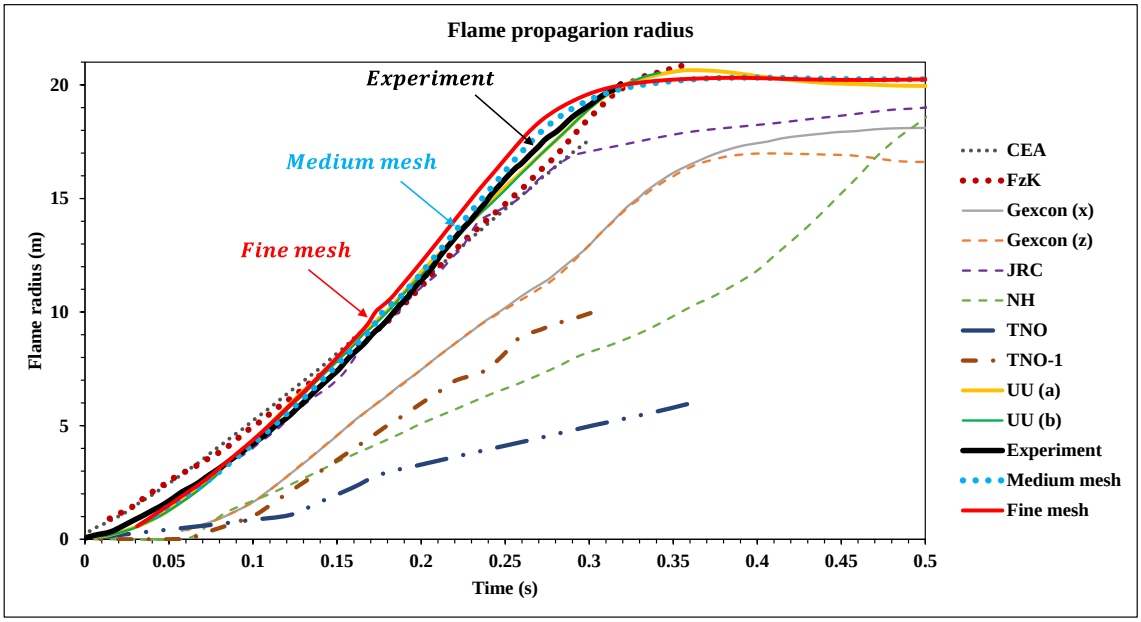

Figure 5.13: Flame tip propagation radius for the fine and medium meshes on a nodal progress variable of 0.5 compared with the experiment and the SOTA (Gallego *et al.*, 2005).

Figures 5.14–5.19 show the overpressure at different transducers from the fine and medium meshes compared with the experiment and the SOTA. CFL number of 1.0 is used in the fine and medium meshes. Some of the overpressure data from the SOTA have high oscillations, which are not considered in the current presentation. Overpressure signals of the experiment are in general smooth, when extracting the experiment data some of the oscillations are removed.

Pressure transducers inside the flame region were affected by the heat of combustion during the experiment, therefore they did not return to the ambient pressure as shown in Figs. 5.14, 5.16, and 5.17. The pressure transducer at 5 m returned to the ambient pressure, because it was thermally protected. The measured overpressure at 2 m is lower than the measured overpressures at 5 m, 8 m, and 18 m. It is also lower than most of the prediction of the SOTA. Therefore, it was assumed that this sensor did not measure the correct overpressure (García *et al.*, 2010). Hence, the comparison with the experiment's overpressures is considered qualitatively, especially for most of the sensors inside the combustion region.

Pressure dynamics were explained in (Gallego *et al.*, 2005) as follows: overpressures inside the balloon in the unburned mixture in front of the flame were

increased due to the compression by the thermal expansion and the closure of the balloon. This was followed by a sudden decrease due to the burst of the balloon close to 0.1 s and at the flame radius close to 5 m. After that, the overpressures were kept constant until the arrival of the expansion wave, which decreased the overpressures to the negative values, as shown in Figs. 5.14–5.16. The expansion wave was generated due to flame quenching. Outside the balloon, the overpressures were increased linearly due to compression wave derived by the thermal expansion. This was followed by a decrease to the negative values due to the expansion wave, as shown in Figs. 5.17–5.19.

There are discrepancies between the SOTA and experiment. The present simulations qualitatively predict overpressures in the same order of magnitude as the experiment and the SOTA, for both the compression and expansion phases.

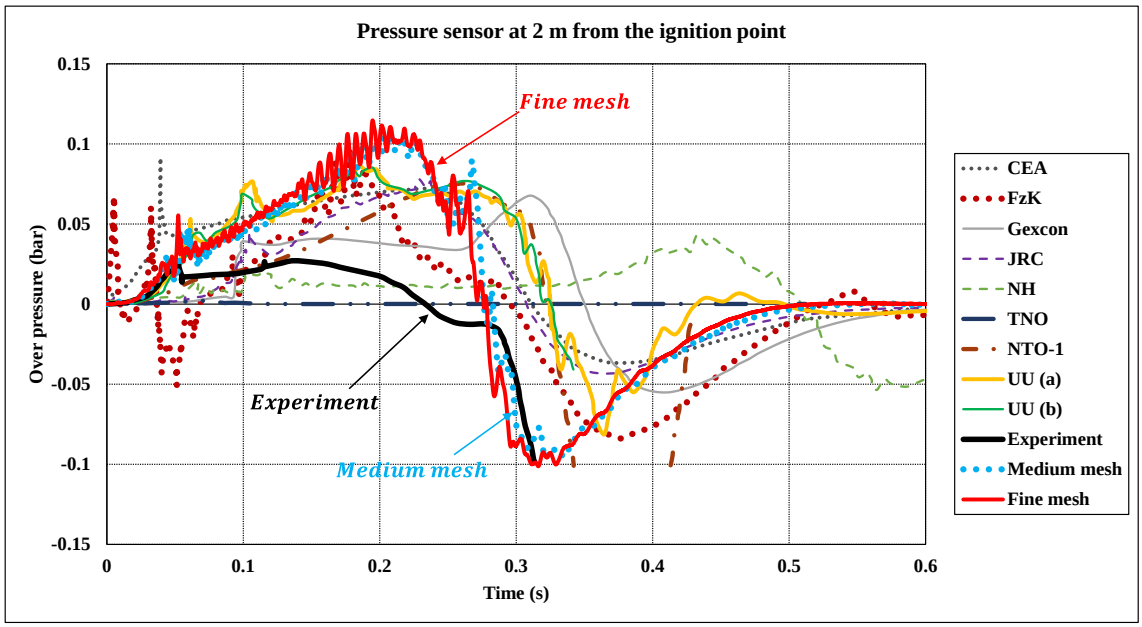

Figure 5.14: Overpressure dynamics at 2 m compared with the experiment and the SOTA (Gallego *et al.*, 2005).

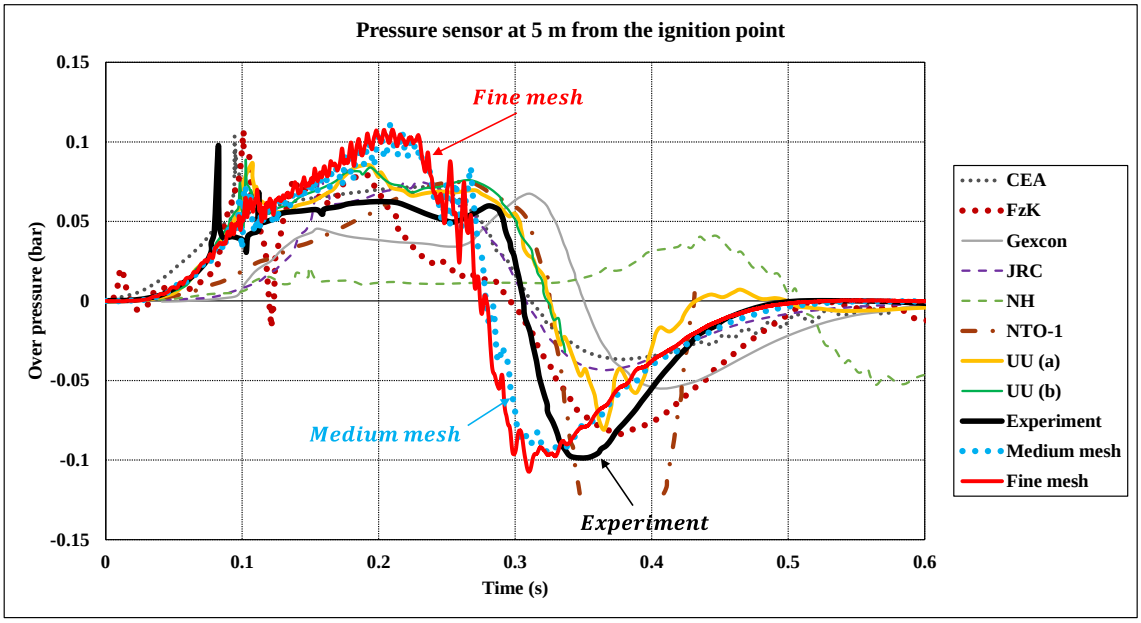

Figure 5.15: Overpressure dynamics at 5 m compared with the experiment and the SOTA (Gallego *et al.*, 2005).

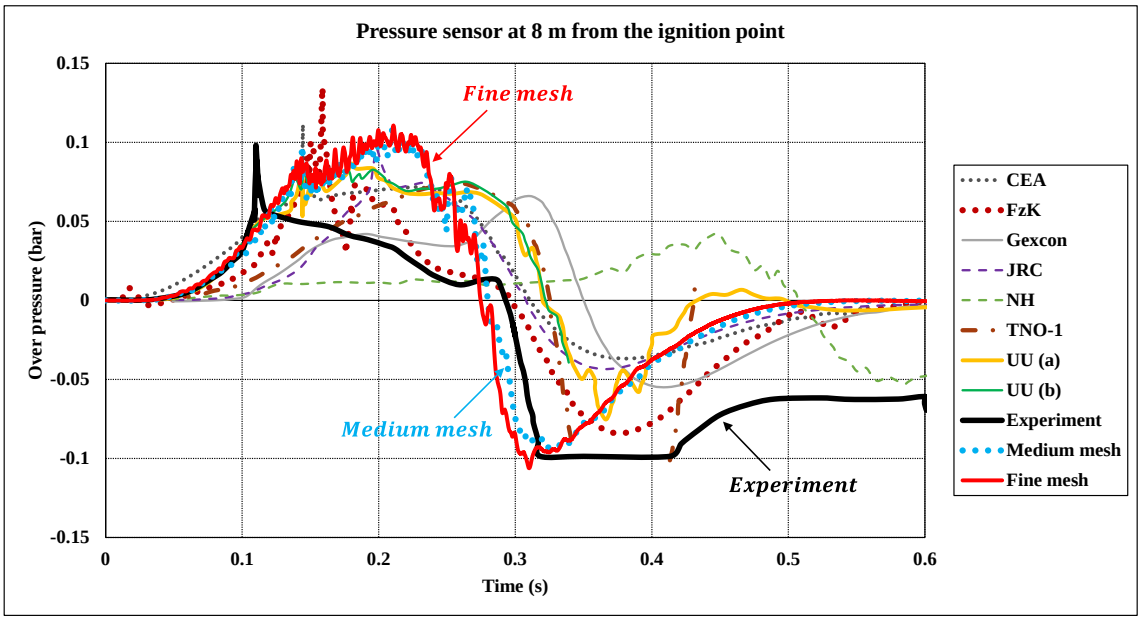

Figure 5.16: Overpressure dynamics at 8 m compared with the experiment and the SOTA (Gallego *et al.*, 2005).

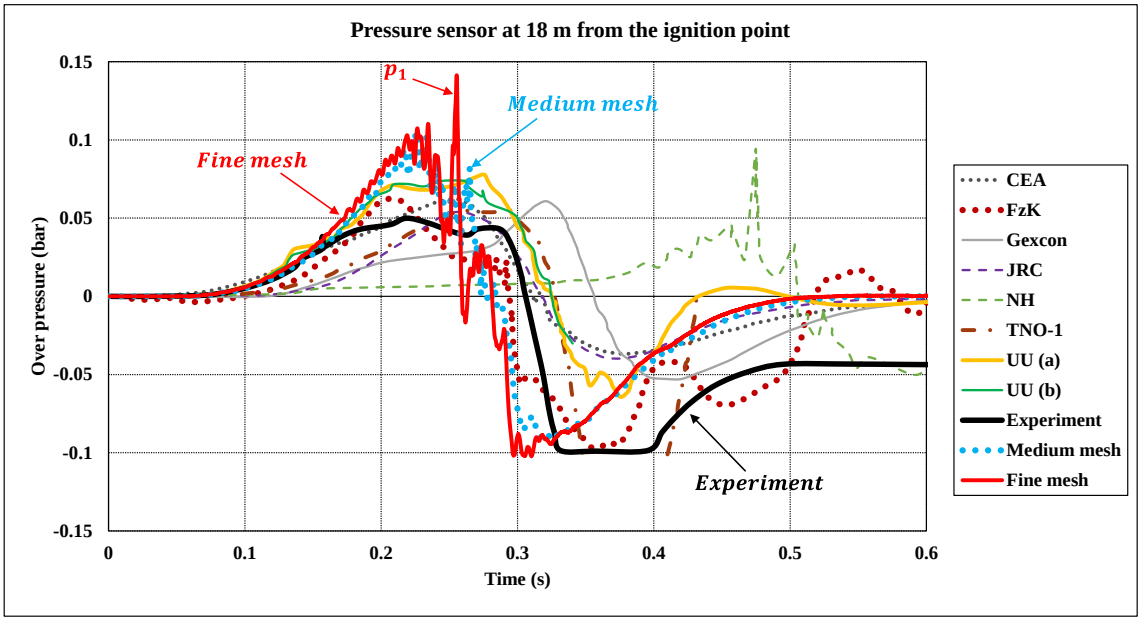

Figure 5.17: Overpressure dynamics at 18 m compared with the experiment and the SOTA (Gallego *et al.*, 2005).

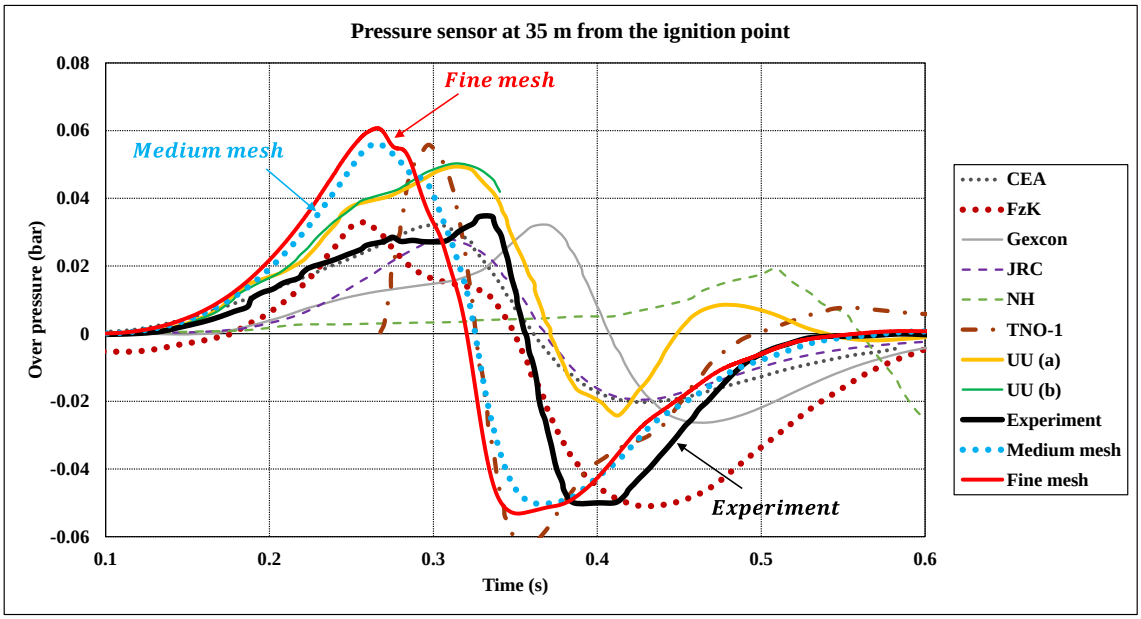

Figure 5.18: Overpressure dynamics at 35 m compared with the experiment and the SOTA (Gallego *et al.*, 2005).

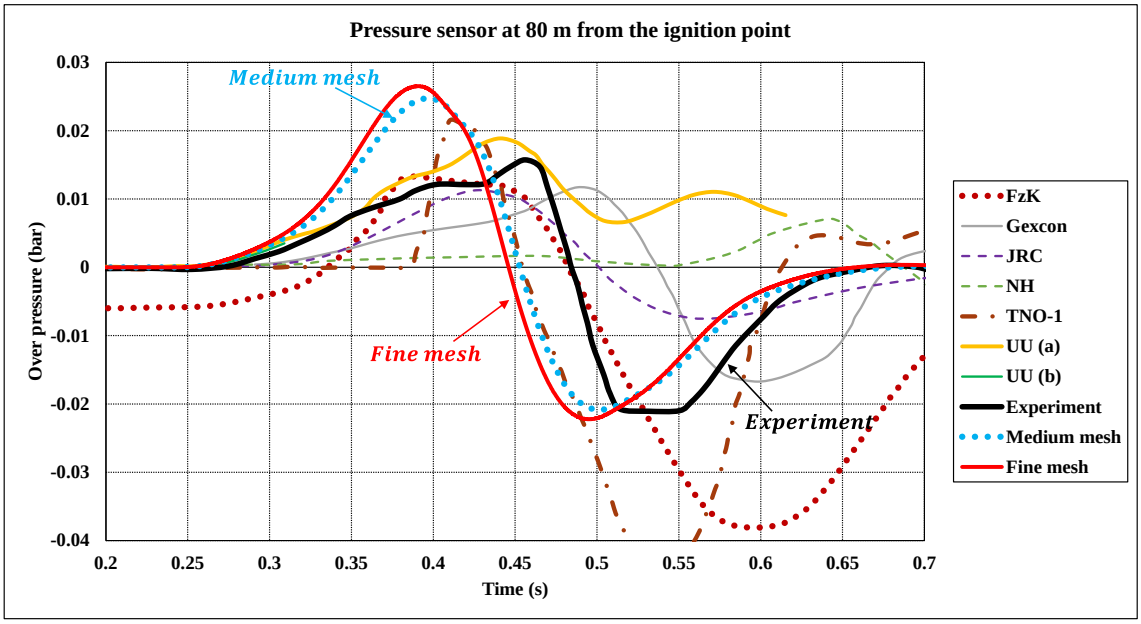

Figure 5.19: Overpressure dynamics at 80 m compared with the experiment and the SOTA (Gallego *et al.*, 2005).

5.4.2 Performance of the instabilities and the turbulent wrinkling factors

Figure 5.20 shows the average of instabilities wrinkling factor on a nodal progress variable of 0.5. Instabilities wrikling factor increases linearly with flame propagation, then it decreases due to the decrease in the mixture concentration, which occurs due to mixing of the hydrogen-air mixture with the surrounding air.

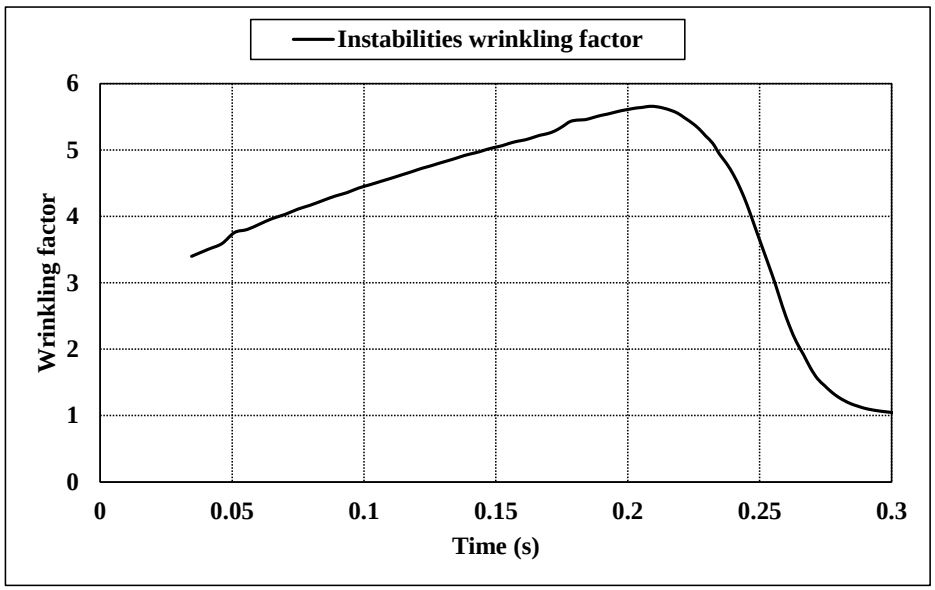

Figure 5.20: Average of the instabilities wrinkling factor on a nodal progress variable of 0.5.

Figure 5.21 shows the average of turbulent wrinkling factor with flame propagation on a nodal progress variable of 0.5. There is no contibution of the turbulence in the beginning of the propagation. Turbulent wrinkling factor increases due to the decrease in the hydrogen concentration.

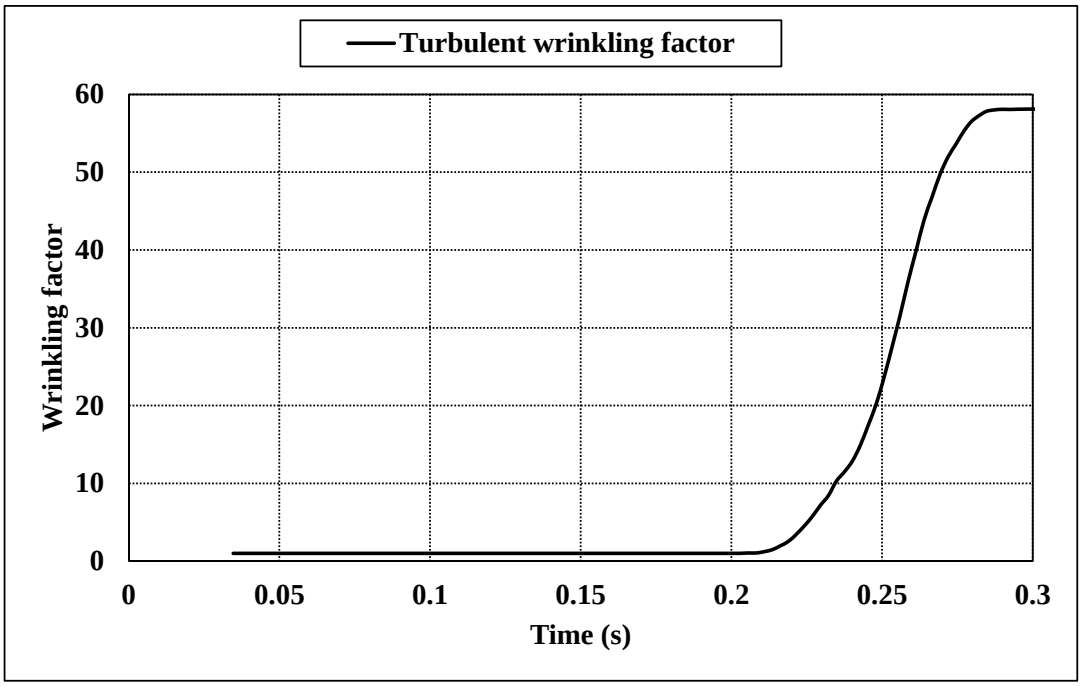

Figure 5.21: Average of the turbulent wrinkling factor on a nodal progress variable of 0.5.

5.4.3 Sources of discrepancies between the proposed model and the experiment

The discrepancies between the prediction of the current model and the experiment could be originated from different sources. The following list contains different possible reasons:

1- There is temperature divergence for some cells over a period, as temperature goes to high values of 5000 K. That is possible to be due to mesh construction and using interfaces.

2- Applying the turbulent wrinkling factor after the concentration decreases provides higher chemical reaction rate, which could be the reason for the peak overpressure at point p_1 in Fig 5.17. This could be treated by modifying the fractal dimension of the turbulent wrinkling factor to another model.

3- The value of the fractal dimension of the instabilities affects flame propagation velocity and the overpressure magnitude. It might be tuned for better fitting with the experiment. However, a fixed value of 2.2 is used for the three simulated cases.

4- There might be an effect due to not modelling heat transfer.

5- There is uncertainty in the experiment overpressures especially for most of the sensors inside the balloon (Gallego *et al.*, 2005).

5.5 Conclusions

The proposed model is tested against the large-scale deflagration experiment in an open atmosphere. Different grid sizes and CFL numbers are tested, as summarized in Table 5.6. The overpressure and flame propagation from the current study are less sensitive to the CFL numbers, while they are sensitive to the grid sizes. The predicted flame propagation and overpressures based on the medium and fine meshes, are qualitatively comparable with the experiment and SOTA.

The instabilities wrinkling factor is the dominant contributor to the chemical reaction rate before the decrease in the mixture concentration. Turbulent wrinkling factor has no contribution in the beginning of the propagation. Its contribution starts with the decrease in the mixture concentration due to mixing with the surrounding air. Finally, the proposed model for the chemical reaction rate is succeeded to qualitatively predict large scale deflagration.

Table 5.6: Summary of the performed simulations using different grid sizes and CFL numbers for the open-atmosphere experiment.

Mesh	Average grid size	Total mesh size	CFL number	Processors	Approximate CPU time
Coarse	Tetra (1.25 m & 1.5625 m) – hexa (2.5 m & 5 m)	235 k cells	1.0	16	0.28 day
Medium	Tetra (0.8 m & 1.5625 m) – hexa (2.5 m & 5 m)	474 k cells	1.0	16	1 day
Fine	Tetra (0.63 m & 1.25 m) – hexa (2.5 m & 5 m)	1 M cells	1.0	8	5.7 days
Medium	Tetra (0.8 m & 1.5625 m) – hexa (2.5 m & 5 m)	474 k cells	0.8	16	1.23 days
Medium	Tetra (0.8 m & 1.5625 m) – hexa (2.5 m & 5 m)	474 k cells	0.6	8	2.95 days

CHAPTER 6. NUMERICAL SIMULATION OF VENTED EXPLOSION EXPERIMENT

6.1 Introduction

The purpose of the present chapter is to numerically test the proposed chemical reaction rate model against vented explosion experiment. The vented chamber is a safety technique that is used to protect buildings by releasing gas through a vent if there is a release of a gas inside the building. The explosion of the released gas in front of the vent could lead to an internal explosion. The released gas concentration, chamber size, vented area, ignition location, and the existing of obstacles in front of the released gas affect the internal explosion (Bauwens, Chaffee and Dorofeev, 2011). The vented explosion problem has been studied experimentally and numerically.

One of vented explosion experiments is chosen as a test case for developing the proposed turbulent burning velocity model. There is no initial turbulence at the early phase of propagation inside the chamber. Therefore, it is expected that the main physical acceleration mechanism in the early propagation is the hydrodynamic & thermo-diffusive instabilities and their related formation of cellular structure through continuous surface splitting. The vented gas from the chamber would expect to generate turbulence outside the chamber. Hence, the turbulent wrinkling factor is expected to contribute to the external explosion. The contribution of the instability and turbulent wrinkling factors is demonstrated in this simulation.

Five teams have simulated the vent explosion experiment. They have used different combustion and turbulence modelling. A summary of their models is shown in Table 6.1 (Vyazmina *et al.*, 2019). Different domain sizes, mesh topology, and grid sizes are used and summarized in Table 6.2 (Vyazmina *et al.*, 2019). Air Liquide and ODZ teams have performed mesh independence study for their simulations.

Table 6.1: Turbulence and combustion models of the SOTA of the vented explosion (Vyazmina *et al.*, 2019).

Team	Turbulence model	Combustion model
Air Liquide	RANS $(k-\varepsilon)$	Thickened flame model and Bray correlation for turbulent burning velocity
APSYS	LES k equation eddy viscosity model	Flame surface wrinkling model
CEA	Euler equations with algebraic expressions	Reactive discrete equation and closure for the turbulent burning velocity
Fluidyn	RANS $(k-Omega)$ SST	Modified BML
ODZ	RANS $(k-\varepsilon)$	Bray correlation for turbulent burning velocity

Table 6.2: Setup of the SOTA of the vented explosion (Vyazmina *et al.*, 2019).

Team	CFD domain	Grid size of the mesh	Total Mesh size
Air Liquide	Length: 10 m Width: 5.5 m Height: 5.5 m	Combustion region and pressure sensors region: 2.5 cm Outside: stretch by a factor of 1.1	6 M
APSYS	Length: 7.5 m Width: 7.0 m Height: 3.5 m	Close to the walls: 1.5 cm. Inside the chamber and outside the chamber close to the vent: 3.125 cm Outside: 6.25 cm	1.2 M
CEA	Length: 7.5 m Width: 2.5 m Height: 3.0 m	Uniform 5.0 cm	1.0 M

Continuation of Table 6.2.

Fluidyn	Length: 7.5 m Width: 8.5 m Height: 4.5 m	Inside the chamber: structured 3.0 cm Outside the chamber: stretched up to 23.0 cm	750 k
ODZ	Length: 8.0 m Width: 7.5 m Height: 3.0 m	Uniform 3.0 cm	6.2 M

6.2 Experiment description

The vented explosion experiment conducted by Daubech et al. is chosen as the test case, a summary of the experiment from (Daubech *et al.*, 2013) is as follows: The enclosure is a rectangular chamber with a volume of 4 m^3. It is two meters height, two meters width, and one-meter depth. It has a vent with an area of 0.5 m^2 at the center of one of its sides as shown in Fig. 6.1 (Daubech *et al.*, 2013). The chamber has three transparent walls on: the front side, the vent side, and the top side. The transparent walls have a thickness of 2 cm. The remaining walls are made from steel with a thickness of 5 mm. The chamber can resist overpressure up to three bar due to the use of I and T steel beams. The chamber was filled with hydrogen using 1 mm orifice at its lower part. Hydrogen was suppled directly from bottles with pressure of 200 bar. The mixture was controlled using six oxygen analyzers and a homogeneous mixture with a concentration of 16.5% by volume was achieved using a fan. Samples from the mixture were collected every 35 cm along a vertical axis. Micro particles of ammonium chloride were seeded into the mixture to monitor flame propagation inside and outside the chamber, which do not affect flame propagation. The vent was closed using a thin plastic sheet. An electric spark with an energy of 10 mJ was located on the middle of the wall that was opposite to the vent. The initial pressure and temperature of the experiment was 101.325 kPa and 293 K respectively.

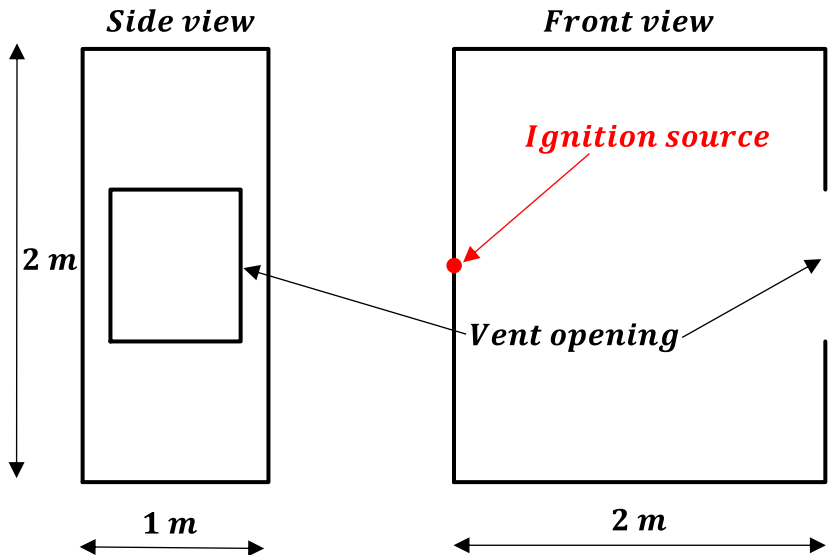

Figure 6.1: Vented explosion chamber (Daubech *et al.*, 2013).

The overpressure was measured inside the chamber at two positions using KISTLER piezoresistive gauge, which measures gauge pressure from zero to 10 bar. Its accuracy is $\pm$ 0.1%. The first gauge pressure is located on the wall containing the ignition source and opposite to the vent. The second pressure gauge was located at the center of the large wall opposite to the transparent front side. The overpressure outside the chamber was measured at three different locations using KISTLER piezoresistive gauge, which measures gauge pressure from zero to two bar. Its accuracy is $\pm$ 0.1 %. The first pressure gauge was located on the vent axis at two meters far from the chamber. The second pressure gauge was located on the vent axis at five meters far from the chamber. The third pressure gauge was located on the chamber exit plane at five meters far from the vent center on the direction perpendicular to the chamber front transparent side. A PHOTRON Fastcam high speed camera was used to record the internal and external explosion.

6.3 Simulation description

6.3.1 Mesh setup

3D rectangular domain with length, width, and height of 8.5 m, 2.5 m, and 3.0 m respectively is used to simulate the experiment. The chamber is located at the center of one of the domain sides, above the lower boundary of the domain by 0.5 m, as shown in Fig. 6.2. The domain is discretized using hexahedral grid elements without refinement

close to the chamber walls. Three meshes: coarse, medium, and fine are used to investigate the dependence of the solution on the grid. The domain of the mesh is divided into 34 blocks to have hexahedral cells for any grid size with close lengths. A cut view shows part of the mesh blocks is in Fig. 6.3, where the color is used to differentiate between the individual blocks.

The coarse mesh has an average grid size of 6.4 cm and a total mesh size of 248 k cells. The medium mesh has a grid size of 5 cm and a total mesh size of 510 k cells. The fine mesh has an average grid size close to 4.0 cm and a total mesh size of 1.0 M cells. Using more finer grid sizes is not possible during the time of the current study due to the limitation of the shared license of ANSYS-Fluent. A summary of the meshes is shown in Table 6.3. Figure 6.2 shows a cut view of the coarse mesh, where the color is used to differentiate between the individual boundaries.

Table 6.3: Summary of the vented explosion meshes.

Mesh	Average grid size	Total mesh size
Coarse	6.4 cm	248 k cells
Medium	5.0 cm	510 k cells
Fine	4.0 cm	1.0 M cells

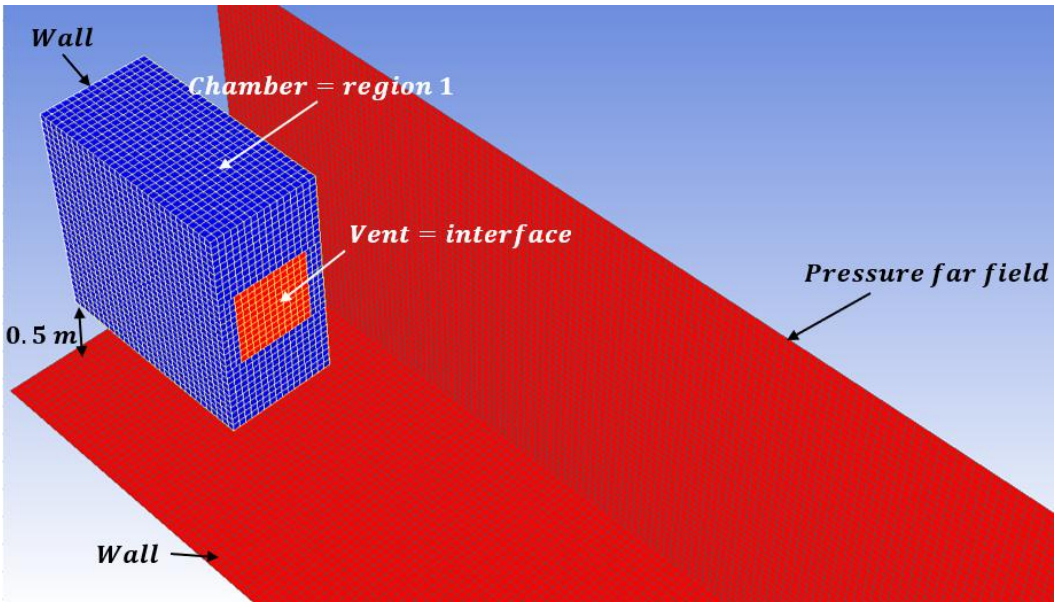

Figure 6.2: A cut view of the coarse mesh, the color is used to differentiate between the individual boundaries.

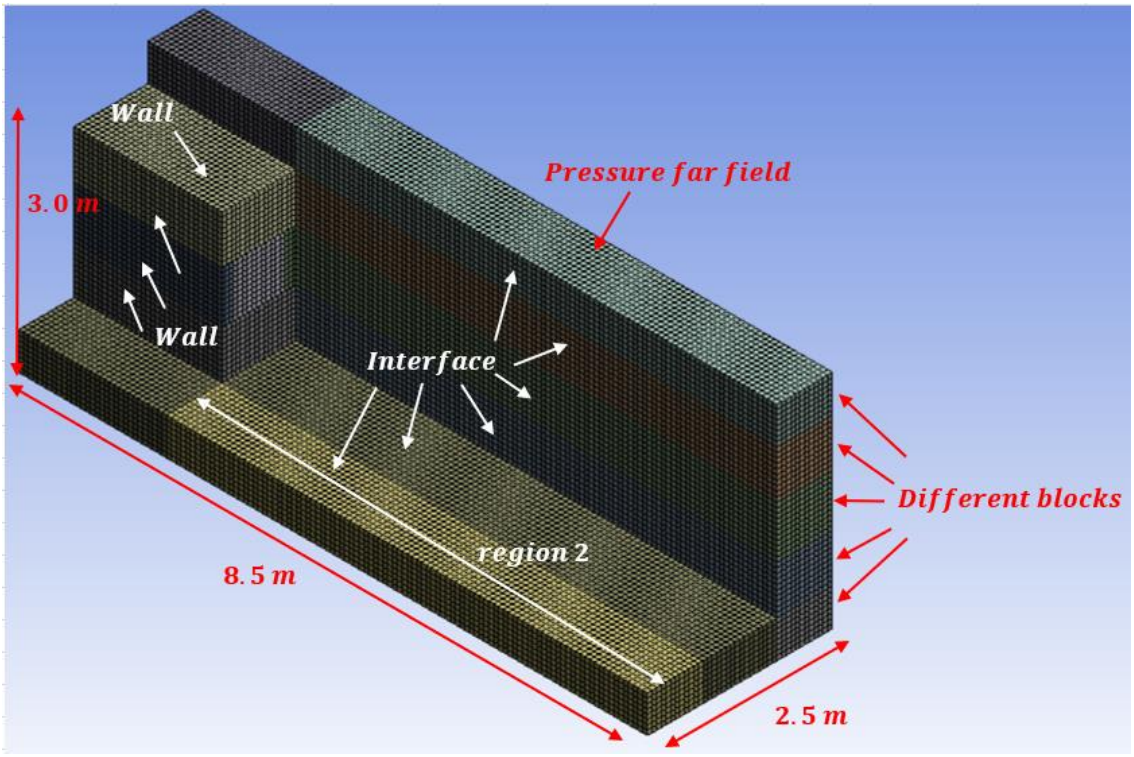

Figure 6.3: A cut view shows part of the mesh blocks, the color is used to differentiate between the individual blocks.

6.3.2 Simulation setup

The same numerical setting of the open atmosphere simulation is used. The outer cut-off length scale of the instability in Eq. (2.57) is limited inside the chamber to half of the shortest length, i.e. 0.5 m. Outside the chamber, it increases with flame propagation radius that is measured from the vent center. λ_{min} is calculated from the spherical flame relation in Eq. (2.58). Flame-generated turbulence is modelled as a source term in the momentum equation, which is based on the derivative of the algebraic model in Eq. (3.49). It is applied inside the flame brush after the ignition time. A limiting condition is used to prevent negative K_{fg} at high k_{Δ}.

Thermodynamics and combustion properties are calculated in an initial step using the Ó Conaire chemical reaction mechanism in the framework of Cantera. Specific heat, sensible enthalpy, molecular viscosity, and thermal conductivity dependence on temperature for the air and hydrogen are approximated in polynomials with temperature variable up to 3000 K. Specific heat, sensible enthalpy, molecular viscosity, and thermal conductivity for the burned gas are approximated in polynomials up to 3000 K, which are calculated for the unburned mixture with hydrogen concentrations of 0.04, 0.165, 0.297,

and 0.75. A linear interpolation is used for different values of the hydrogen concentration. For temperature above 3000 K, the corresponding values of the specific heat, sensible enthalpy, molecular viscosity, and thermal conductivity at 3000 K are used.

The effect of the pressure on the unburned mixture density is considered using an isentropic relation. Expansion coefficient, adiabatic flame temperature, and inner cut-off length scale of the instabilities are changed with the unburned mixture concentration and the isentropic change of the initial pressure. The heat of chemical reaction and the Lewis number of the deficient reactant are changed with the unburned mixture concentration. The effects of the unburned mixture concentration and the isentropic change of the pressure on the expansion coefficient, adiabatic flame temperature, inner cut-off length scale of the instabilities, heat of chemical reaction, and the Lewis number of the deficient reactant are considered by constructing three polynomials in hydrogen concentration. The first is at initial pressure and temperature of 101.325 kPa and 293 K respectively. The second is at pressure of 50.6625 kPa and temperature corresponds to isentropic expansion from the initial value. The third is at pressure of 151.9875 kPa and temperature corresponds to isentropic compression from the initial value. The pressure values of 151.9875 kPa and 50.6625 kPa are chosen to represent upper and lower boundaries of the expected pressure by inspecting the experiment data. A linear interpolation is used for pressure in between. If the pressure is higher or lower than the boundary pressure, the boundary pressure is used. It should be noted that, there is no effect of the isentropic change of the pressure, under the current specified range, on the heat of chemical reaction and the Lewis number of the deficient reactant.

The effect of the isentropic change of the pressure on the unburned mixture molecular viscosity, thermal conductivity, and specific heat is considered for the pressure between 50.6625 kPa and 151.9875 kPa. Outside this range, the corresponding boundary values are used.

The chamber is filled with hydrogen-air mixture, which has volumetric concentration of 16.5%, while the rest of the domain is filled with pure air. The domain ground boundary condition is modelled as an adiabatic wall with no slip, as shown in Fig. 6.2. The sides and top boundaries of the domain are set to pressure far field, which does not allow reflection of acoustic waves, as shown in Figs. 6.2 and 6.3. The chamber walls are modelled as an adiabatic wall with no slip, as shown in Figs. 6.2 and 6.3. A matching

interface boundary condition is used between the neighboring blocks inside the mesh, as shown in Figs. 6.2 and 6.3. The simulation initial temperature and pressure are set to 293 K and 101.325 kPa respectively. Heat transfer either between the flow in the computational domain and the external far field or between the burned gas and the unburned gas inside the computational domain is not treated in the current study.

The mixture is ignited by varying linearly the progress variable from 0 to 1 and the cell temperature from the initial temperature to the adiabatic flame temperature during the ignition time inside the ignition cell. The ignition cell is chosen close to the domain center with a length (Δ), which is defined as the cubic root of the cell volume. Ignition time is defined as the time to propagate a laminar flame under the initial temperature and pressure along half of the ignition cell length, as shown in Eq. (6.1) (Molkov, 2012).

$$t_{ign,initial} = \frac{1}{2}\frac{\Delta}{\sigma S_u} \tag{6.1}$$

6.3.3 Mesh independence study

The solution dependence on the mesh resolution is investigated using the three meshes with CFL number of 1.0. Table 6.4 summarizes the running time of the simulations. Figure 6.4 shows the average of Pope criterion using Eq. (4.2) for the three meshes for two regions. Region 1 represents the chamber and region 2 represents the domain in front of the chamber, as shown in Figs. 6.2 and 6.3 respectively. The three meshes satisfy the pope criterion of larger than 0.8 for most of the running time and for a period the Pope criterion is close to one. Here again, the Pope criterion could be less constructive. Therefore, examining the predicted overpressure could be used to check the convergence.

Table 6.4: Running time of the mesh independence study for the vented explosion.

Mesh	CFL number	Processors	Approximate CPU time
Coarse	1.0	16	0.47 day
Medium	1.0	8	2.1 days
Fine	1.0	8	6.31 days

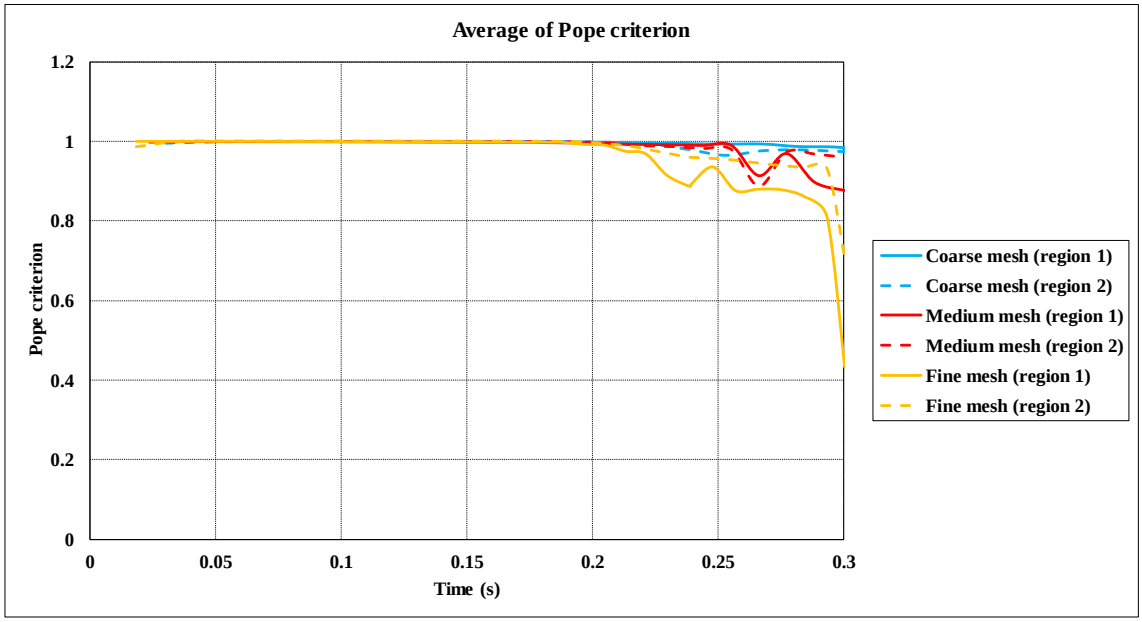

Figure 6.4: Average of the Pope criterion for the coarse, medium, and fine meshes.

Figure 6.5 shows the internal and external overpressures predicted by the three meshes compared with the experiment. The simulations are shifted in time. The overpressure of the current simulations, all over the chapter, is taken at a neighboring cell close to the location of the corresponding pressure sensor, where this cell has the maximum overpressure compared to the other neighboring cells.

The internal and the external overpressures are increased with refining the mesh. The medium and the coarse meshes are qualitatively comparable to each other, however there is a large difference considering the fine mesh. Comparing the external explosion moment with the maximum of the internal overpressure for the experiment and the simulations shows: the external explosion for the experiment feeds the overpressure inside the chamber. Point p_1 shows the experiment external explosion leads the maximum of the internal overpressure. The fine mesh is the only case which predicts this coupling, as shown at point p_2. The external explosion of the medium and coarse meshes occurs after the internal overpressure reaches its maximum, as shown at point p_3. Hence, it is assumed that the fine mesh correctly predicts the pressure coupling. It is difficult to conclude that there is convergence. Therefore, the results are qualitatively compared with the experiment and the SOTA.

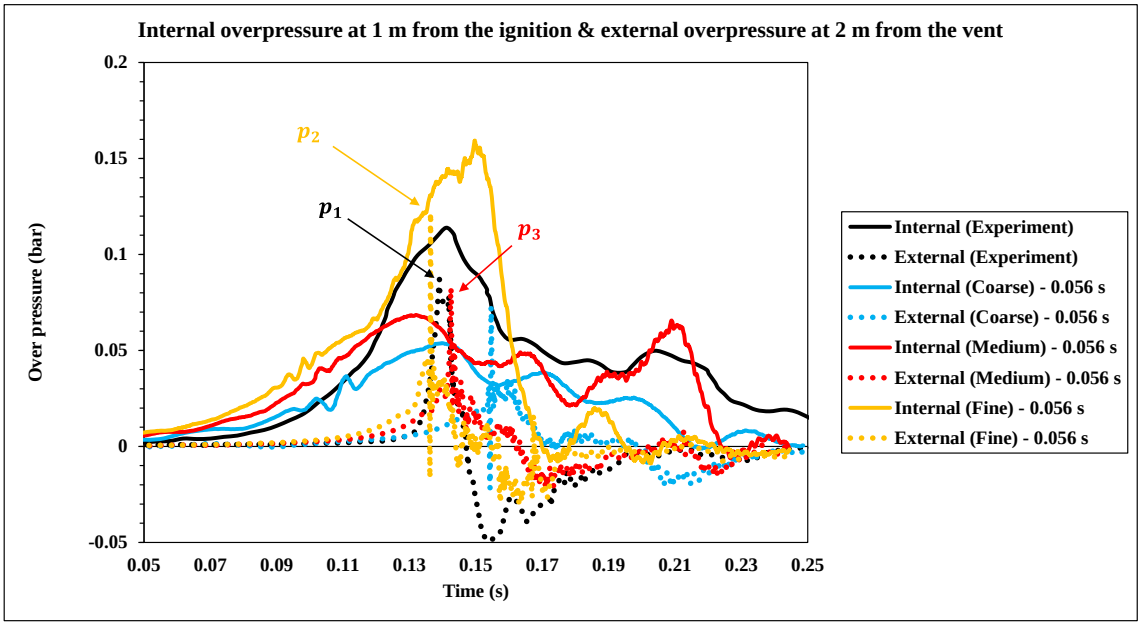

Figure 6.5: Internal and external overpressures predicted by the three meshes compared with the experiment (Daubech *et al.*, 2013; Vyazmina *et al.*, 2019).

Figure 6.6 shows the internal and external overpressures of two medium meshes, shifted in time, using CFL number of 1.0, and with the same grid size. The difference between the two meshes is in the number of the blocks used to construct the meshes. The first mesh is constructed from 34 blocks and the second medium mesh (2) is constructed from two blocks: the first block is for the chamber and the second block is for the rest of the computational domain. It seems like using 34 blocks leads to temperature divergence to 5000 K for some cells over a period, which might lead to the difference in the internal and external overpressures, but this difference could be qualitatively acceptable. The mesh based on the two blocks is used for the time-step independence study in the next section.

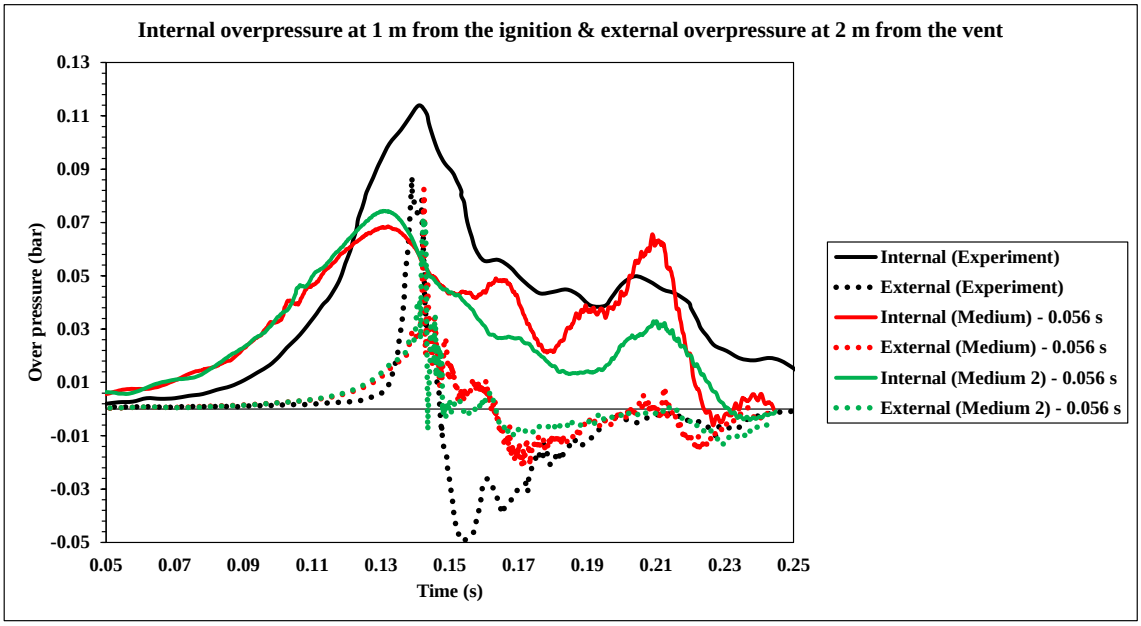

Figure 6.6: Internal and external overpressures predicted by two medium meshes, with difference in the construction, compared with the experiment (Daubech *et al.*, 2013; Vyazmina *et al.*, 2019).

6.3.4 Time-step independence study

The medium mesh (2), based on using two blocks, is used to investigate the time-step independence study. Three CFL numbers are investigated: 1.0, 0.8, and 0.6. Table 6.5 summarizes the simulations running time. Figure 6.7 shows the average of Pope criterion using Eq. (4.2) for the three CFL numbers in the geometrical regions described in the previous section. The three CFL numbers satisfy the pope criterion of larger than 0.8 for most of the running time, with a value close to one. Therefore, examining the predicted overpressure could be used to check the convergence.

Table 6.5: Running time of the time-step independence study for the vented explosion.

Mesh	CFL number	Processors	Approximate CPU time
Medium 2	1.0	16	0.92 day
Medium 2	0.8	16	1.14 days
Medium 2	0.6	16	1.51 days

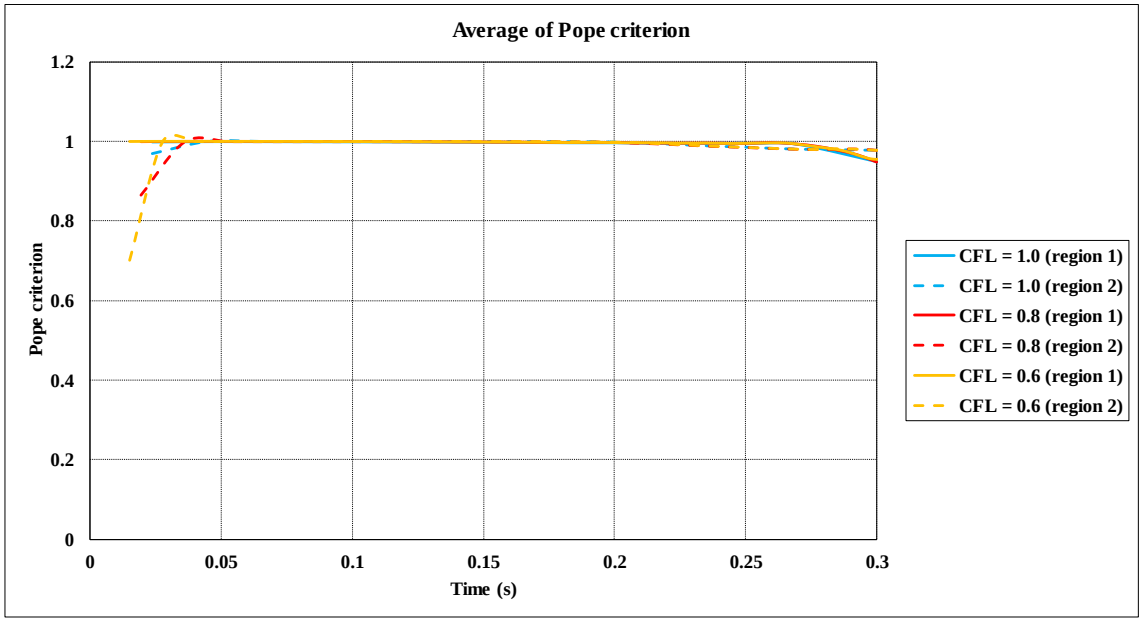

Figure 6.7: Average of the Pope criterion for CFL numbers of 1.0, 0.8, and 0.6 using the medium mesh (2).

Figure 6.8 shows the internal and external overpressures using the medium mesh (2) compared with the experiment. There is good convergence for all the tested CFL numbers. Hence, the simulation is less sensitive to CFL number.

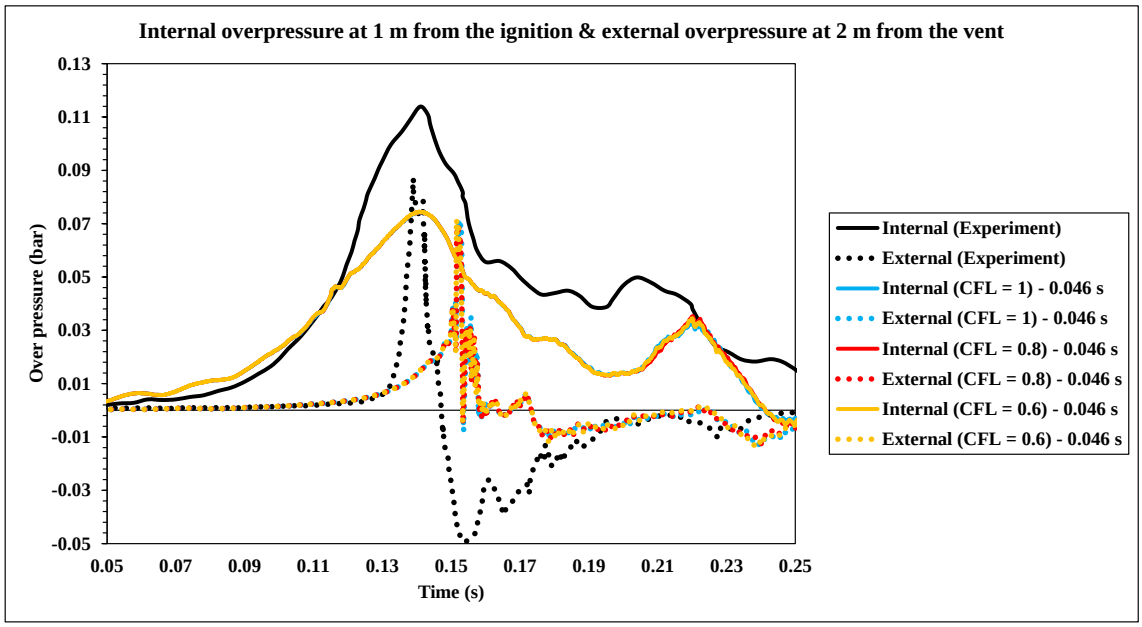

Figure 6.8: Internal and external overpressures for CFL numbers of 1.0, 0.8, and 0.6 compared with the experiment (Daubech *et al.*, 2013; Vyazmina *et al.*, 2019).

6.4 Simulation results and discussion

6.4.1 Performance of the proposed model against the SOTA

Results from the fine and medium meshes, using CFL number of 1.0, are compared with the experiment and the SOTA in the next discussion. Figure 6.9 shows flame tip position on a nodal progress variable of 0.5. Flame tip is measured between 45^0 and -45^0 along the vent axis. The current simulations and the SOTA are shifted in time. The current simulation predicts the three phases of propagation: the slow propagation inside the chamber up to 2 m, the fast propagation outside the chamber up to approximately 4 m, and the decrease in the propagation speed after the decrease in the concentration due to mixing with the surrounding air. Flame propagation from the current simulations are qualitatively matching the experiment and the SOTA, especially before the mixing with the surrounding air.

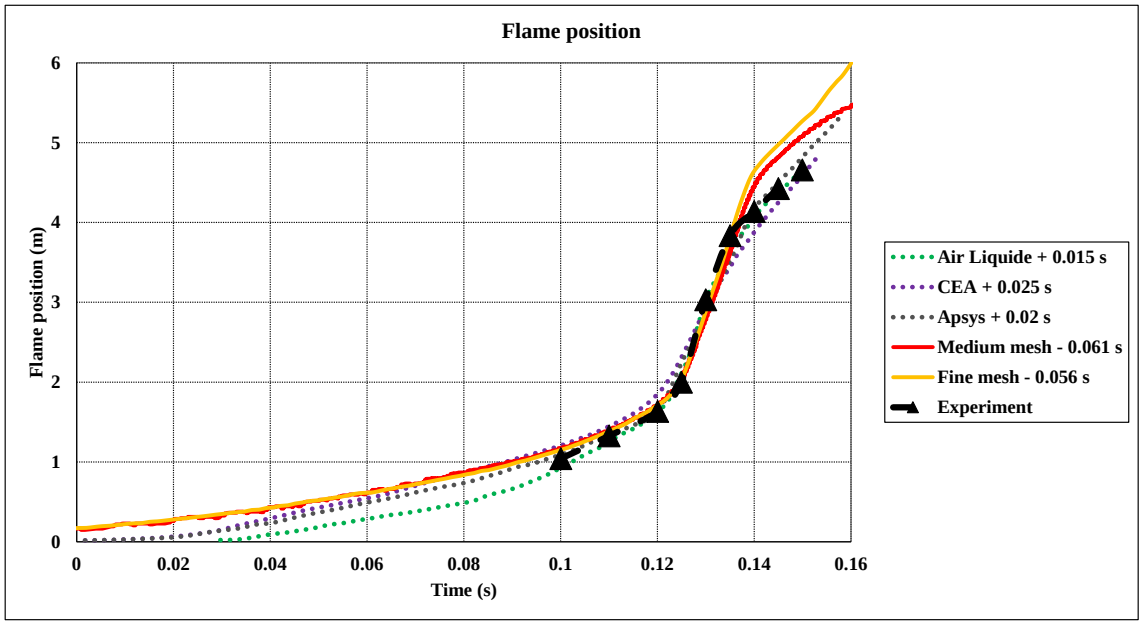

Figure 6.9: Flame tip propagation, on a nodal progress variable of 0.5, compared with the experiment and the SOTA (Vyazmina *et al.*, 2019).

Figure 6.10 shows the overpressures of the current simulations at one meter from the ignition, inside the chamber, compared with the filtered overpressure of the experiment and the SOTA. The results are qualitatively in the order the experiment and the SOTA.

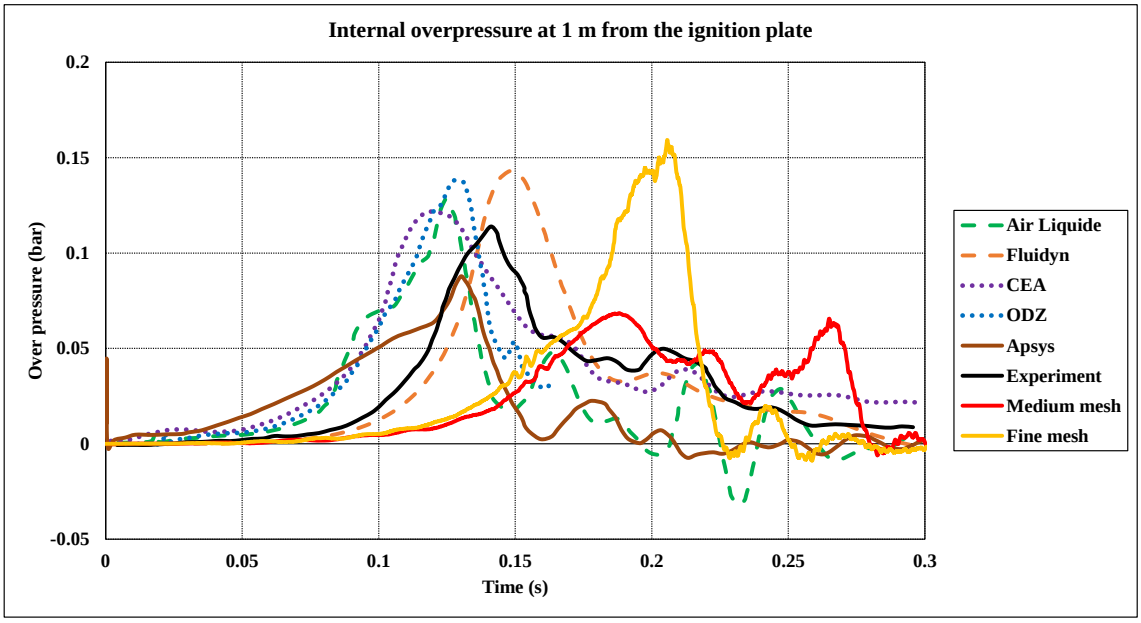

Figure 6.10: Overpressures dynamics inside the chamber at 1 m from the ignition compared with the experiment and the SOTA (Vyazmina *et al.*, 2019).

Figure 6.11 shows the external overpressures of the current simulations at 2 m from the vent compared with the experiment and the SOTA. The fine mesh predicts a sharp shock, which overestimates the experiment, but it is still in the prediction order of one of the SOTA.

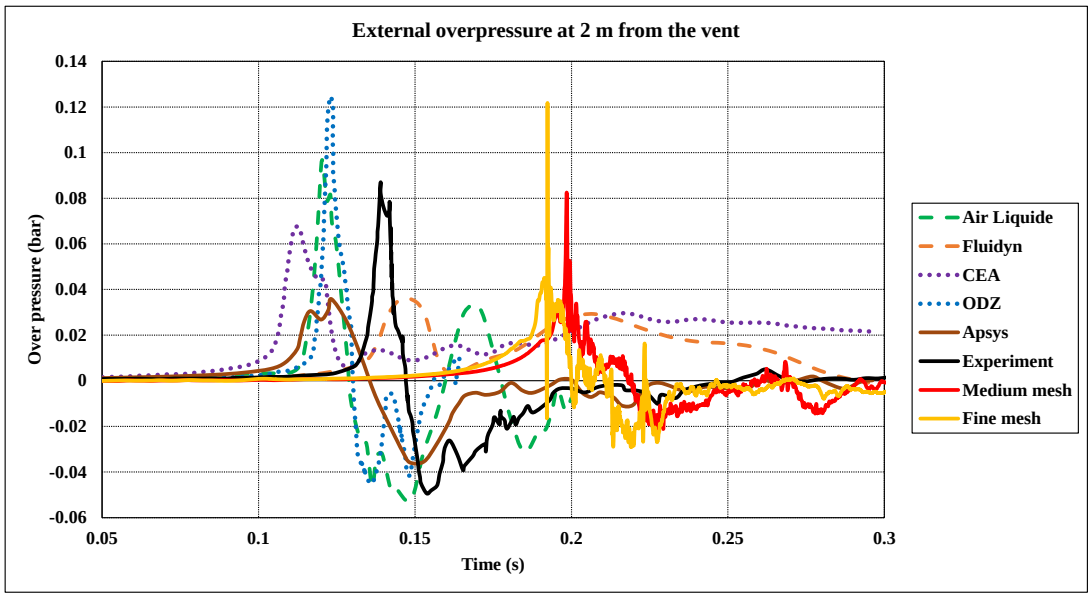

Figure 6.11: Overpressures dynamics outside the chamber at 2 m from the vent compared with the experiment (Daubech *et al.*, 2013) and the SOTA (Vyazmina *et al.*, 2019).

Figure 6.12 shows the external overpressures of the current simulations at 5 m from the vent compared with the experiment and the SOTA. The current simulations underestimate the experiment. The shape of the predicted overpressures signal is different from the experiment. It was mentioned in (Vyazmina *et al.*, 2019) that the experiment was surrounded by two walls: the first was in the vent direction at 50 cm after the last pressure sensor and the second was in one of the lateral directions at 50 cm away from the chamber, which was not known during performing the simulations. One of the SOTA tested the effect of the external confinement, they found that there is an increase to the overpressures, especially for the sensor at 5 m from the vent. Hence, changing the simulation boundary condition to wall in the direction downstream of the vent might fix the shape of the overpressure signal at the last sensor.

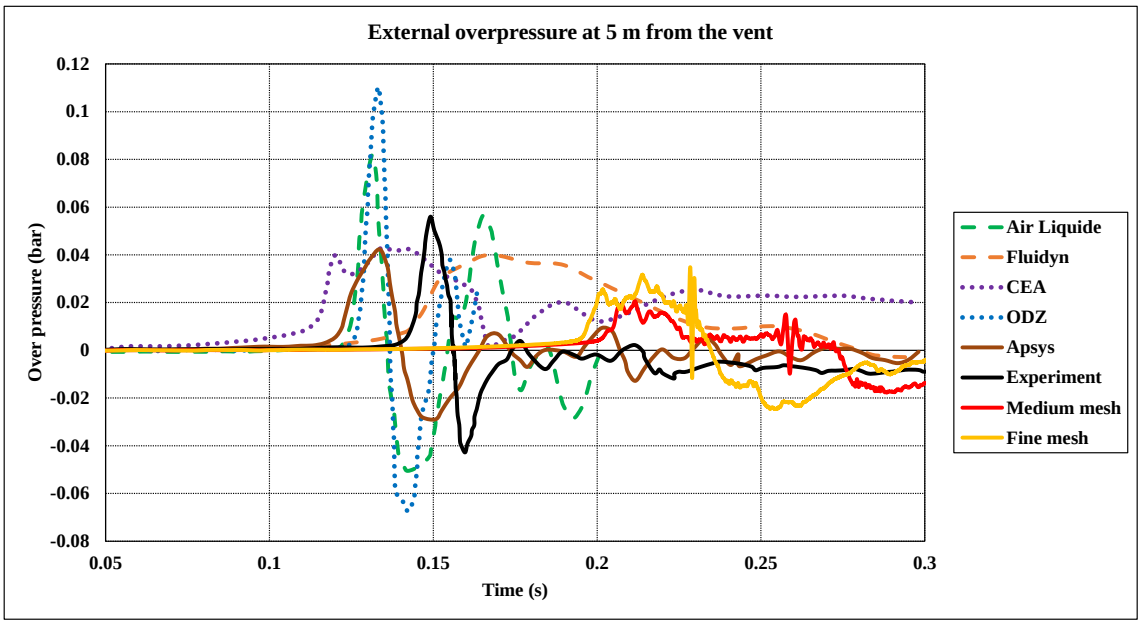

Figure 6.12: Overpressures dynamics outside the chamber at 5 m from the vent compared with the experiment (Daubech *et al.*, 2013) and the SOTA (Vyazmina *et al.*, 2019).

6.4.2 Performance of the instabilities and the turbulent wrinkling factors

Figure 6.13 shows the average of instabilities and turbulent wrinkling factors with flame propagation for the medium mesh (2) using for CFL number of 0.8 on a nodal progress variable of 0.5. Instabilities wrinkling factor is the main contributor to the chemical reaction rate inside the chamber. Outside the chamber, after a certain distance from the vent, turbulent wrinkling increases and dominates the chemical reaction rate.

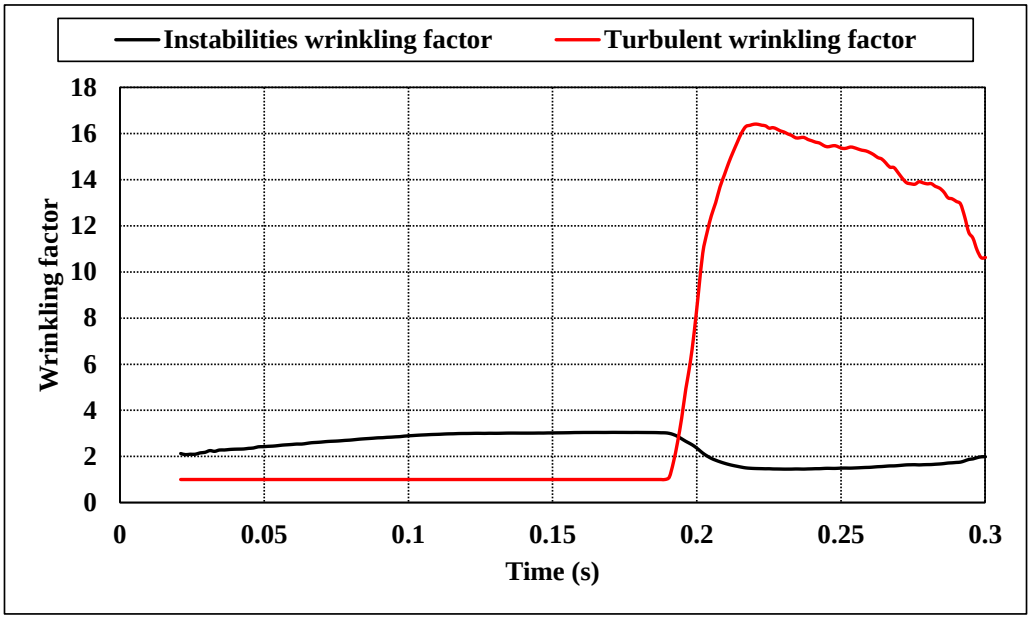

Figure 6.13: Average of the instabilities and turbulent wrinkling factors with flame propagation on a nodal progress variable of 0.5.

6.4.3 Performance of the stretching factor

Figure 6.14 shows the average of stretching factor with flame propagation on a nodal progress variable of 0.5. The flame is partially quenched outside the chamber, after a certain distance from the vent, affected by the change in the Karlovitz number, where a maximum average of 20% of partial quenching occurs.

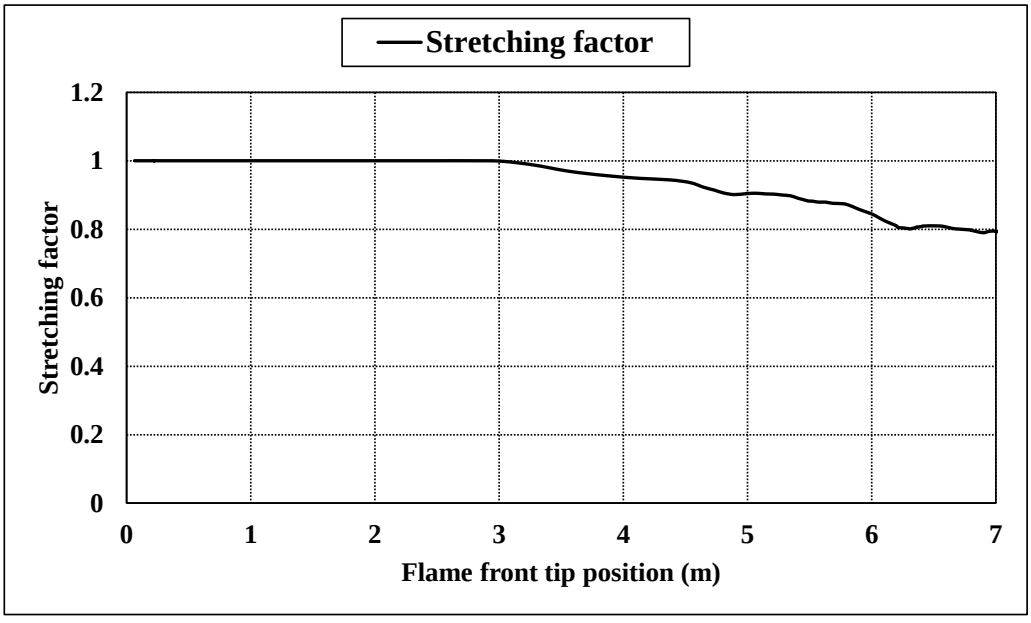

Figure 6.14: Average of the stretching factor with flame propagation on a nodal progress variable of 0.5.

6.4.4 Sources of discrepancies between the proposed model and the experiment

The discrepancies between the prediction of the current model and the experiment could be originated from different sources. The following list contains different possible reasons:

1- There is temperature divergence for some cells over a period, as temperature goes to 5000 K. That is possible to be due to mesh construction and using interfaces.

2- The unburned mixture and flame properties are calculated under isentropic change of pressure between 50.6625 kPa and 151.9875 kPa. However, pressure crosses this limit for some cells over a period to high values of 202.65 kPa and low values of 20.265 kPa.

3- There could an effect due to not modelling the weakly stretched propagation. That might affect the time of flame propagation.

4- There might be an effect due to not modelling heat transfer.

5- There could be an effect due to the external confinement. Hence, a wall boundary condition downstream of the vent might increase the overpressure signal, especially at the last sensor.

6- There could be an effect related to the computational domain size.

7- There is an effect due to non-convergence of the results based on the tested grid size.

6.5 Conclusions

The proposed model is tested against the vented explosion experiment. Different grid sizes and CFL numbers are tested, as summarized in Table 6.6. The overpressures from the current study are less sensitive to the CFL numbers, while they are sensitive to the grid sizes. The resolutions of the tested meshes do not provide convergence for the overpressures. Despite of that, flame propagation distance based on the medium and fine meshes has relatively good matching with the experiment and the SOTA, especially before mixing with the surrounding air. The predicted internal and external overpressures are within the order of the SOTA. Therefore, the model succeeds to predict the key features of the vent explosion and its behavior is qualitatively acceptable.

Inside the chamber, instabilities wrinkling factor is the key dominant for accelerating the flame. Outside the chamber, after a certain distance from the vent, turbulent wrinkling factor becomes the key dominant in accelerating the flame. A maximum average of 20% of partial quenching occurs outside the chamber, after a certain distance from the vent. Finally, the proposed model for the chemical reaction rate is succeeded to qualitatively predict vented explosion experiment.

Table 6.6: Summary of the performed simulations using different grid sizes and CFL numbers for the vented explosion experiment.

Mesh	Average grid size	Total mesh size	CFL number	Processors	Approximate CPU time
Coarse	6.4 cm	248 k cells	1.0	16	0.47 day
Medium	5.0 cm	510 k cells	1.0	8	2.1 days
Fine	4.0 cm	1.0 M cells	1.0	8	6.31 days
Medium 2	5.0 cm	510 k cells	1.0	16	0.92 day
Medium 2	5.0 cm	510 k cells	0.8	16	1.14 days
Medium 2	5.0 cm	510 k cells	0.6	16	1.51 days

CHAPTER 7. CONCLUSIONS AND RECOMMENDATIONS FOR FUTURE RESEARCH

7.1 The proposed model

A proposed chemical reaction rate closure for the progress variable equation is developed in the current study for deflagration and detonation propagations. The model is developed for hydrogen-air mixture, but it could be applicable to other reactive mixtures by replacing the corresponding mixture parameters. The model is developed in the framework of the LES. It predicts reasonably global flame parameters, flame propagation velocity and overpressure, using large grid sizes. Hence, it is suitable for studying safety and the possibility of detonation, due to releasing of hydrogen and formation of highly reactive mixture, for large industrial scales with a compromised computational cost. One of the promised applications could be the safety of the nuclear reactors.

The model is based on the flame winkling concept. Different flame wrinkling models from the SOTA do not consider the effect of flame instabilities on the propagation velocity. Flame in explosion could experience different combustion regimes. Therefore, the proposed model considers the wrinkling due to the hydrodynamics & thermo-diffusive instabilities and the winkling due to turbulence. The proposed turbulent wrinkling model is developed such that it is suitable for the corrugated flamelets and the thin reaction zones regimes. This makes the model suitable for studying combustion in engines.

The modelling strategy is based on using separately two flame wrinkling models: the first is for flame instabilities including turbulence interaction and the second is for turbulence. The two-flame wrinkling models are implemented using the fractal approach. The outer cut-off length scale of the instabilities is set in proportionality with flame propagation radius, in an open space. In a bounded domain, a proposed limiting of the flame radius to half of the smallest domain size, in the direction perpendicular to the flame propagation, is used. The inner cut-off length scale of the instabilities is calculated from the dispersion relations of either planar or spherical flames. A proposed value of 2.2 is set to the fractal dimension of the instabilities. The turbulent outer cut-off length scale is set to the filter width. A proposed turbulent inner cut-off length scale is developed, which is

suitable for predicting detonation. It is a combination of two length scales: the inner cut-off length scale of Shim and the Kolmogorov length scale in the unburned gas. The proposed inner cut-off length scale is limited by the Zel'dovich flame thickness. The turbulent fractal dimension is set to the parameterized formula of Katragadda, which includes the effects of Karlovitz number, Reynolds number, and Lewis number.

The interaction between the instabilities and the turbulence is considered using an originally developed model for a unity Lewis number. It was based on examining time scales of the turbulence and Darrieus-Landau instability. Hence, the inner cut-off length scale of the Darrieus-Landau instability is changed in the vicinity of turbulence. In the current study, it is argued that using an inner cut-off length scale, which includes the effects of the hydrodynamic and the thermo-diffusive instabilities, would extend model to non-unity Lewis number. Another change to the model is done by replacing the turbulence integral length scale in the original implementation, at the fractal outer cut-off length scale, with the maximum wavelength of the instabilities. This would allow the existence of instabilities, under excessive turbulence, over the originally proposed diminishing limit. The purpose from this change was not mean to correct the instability limit, but to use an outer cut-off length scale with proportionality to the flame propagation radius.

Finally based on the developed wrinkling models, the turbulent burning velocity is defined. A model for excessive stretching of the flame is implemented, which could represent the effects of partial or full flame quenching. An algebraic flame-generated turbulence model is implemented. These developments achieve the thesis objectives.

The model contains different sources of uncertainties, the most important is the dependence of the laminar burning velocity on the pressure and temperature. The ability to provide the required chemical reaction rate to propagate detonation wave would depend on the chosen dependency. The model of flame-generated turbulence contains an uncertainty, as the adopted model was derived from DNS of statistically planar turbulent flame with turbulent intensity close to the laminar burning velocity under a unity Lewis number. Therefore, the performance of the model far from this condition is uncertain.

7.2 The performed simulations

The model is tested against three experiments: DDT in a rectangular channel, large-scale deflagration in an open atmosphere, and vented explosion.

The DDT channel has a length of 5.4 m, width of 30 cm, and a height of 6 cm. It contains baffled region with a blockage ratio of 60%, for accelerating the flame, followed by a smooth region. A stoichiometric hydrogen-air mixture with a concentration of 29.9% is simulated. Based on the tested grid sizes and CFL numbers, detonation velocity is less sensitive to the grid sizes but very sensitive to the CFL numbers. In the current study, the convergence occurs for CFL number of 0.1 using a grid size of 6.0 mm and a total number of 446 k cells. The simulation predicts good matching for the flame propagation velocity with the shock propagation velocity of the experiment and the CJ velocity. The simulation predicts more than detonation regime, staring with an overdriven detonation at 1.15 m from the ignition, inside the baffled part. That is followed by an oscillation in the flame propagation velocity, below the CJ velocity, due to the succeeded baffles. In the smooth part of the channel, flame propagation velocity relaxes to a value close to the shock propagation velocity of the experiment and the CJ velocity. Considering the relative coarse grid of the simulation using 3D and the fine grids of the SOTA, order of 10 μm for the smallest grid size using 2D, in addition to the good quality of the prediction. The current model would be more superior than the SOTA for predicting the flame detonation velocity.

The reflected shocks are faster than the experiment and the decay of the overpressures are higher than the experiment. It is possible to be, either due to the thermal shock of the pressure transducers or due to not including heat transfer modelling or due to both. Wrinkling due to instabilities is generated after the critical radius, while wrinkling due to turbulence is generated after the first baffle of the channel and overwhelms the instabilities with propagation. At the detonation phase, turbulent wrinkling has the largest contribution in the chemical reaction rate. Finally, the proposed model for the chemical reaction rate is succeeded to qualitatively predict DDT in terms of initiation, detonation velocity, and overpressure signals.

The second simulation is for deflagration of a stoichiometric hydrogen-air mixture, with a concentration of 29.7%, inside a hemispheric balloon with a radius of 10 m in the open atmosphere. Based on the tested grid sizes and CFL numbers, the

simulations are less sensitive to the CFL numbers, while they are sensitive to the grid sizes. Average grid sizes of 0.8 m and 0.63 m for the medium and the fine meshes are respectively used in the burned region. The total mesh size for the medium and the fine meshes are 474 k and 1.0 M, respectively. The medium and fine meshes are performed using CFL numbers of 0.8 and 1.0, respectively. The predicted flame propagation radius and overpressures are qualitatively comparable with the experiment and the SOTA. The main acceleration mechanism during flame propagation before the decrease in the concentration is the instabilities wrinkling factor. The concentration is decreased due to mixing with the surrounding air. The effect of the turbulent wrinkling factor is introduced after the decrease in the hydrogen concentration. Finally, the proposed model for the chemical reaction rate is succeeded to qualitatively predict large scale deflagration.

The third simulation is vented explosion, in a chamber with a volume of 4.0 m^3, for a hydrogen-air mixture with a concentration of 16.5%. Based on the tested grid sizes and CFL numbers, the simulations are less sensitive to the CFL numbers, while they are sensitive to the grid sizes. Average grid sizes of 5.0 cm and 4.0 cm for the medium and fine meshes are respectively used. The medium mesh is constructed from 2 blocks, while the fine mesh uses 34 blocks. The total mesh sizes for the medium and fine meshes are 510 k and 1.0 M, respectively. The medium and fine meshes are performed using CFL numbers of 0.8 and 1.0, respectively.

The predicted overpressures are not converged based on the investigated resolutions. Despite of that, flame propagations based on the medium and fine meshes are qualitatively comparable with the experiment and the SOTA, especially before mixing with the surrounding air. The predicted internal and external overpressures are qualitatively in the order of the prediction from the SOTA. Therefore, the model succeeds to predict the key features of the vent explosion and its behavior is qualitatively acceptable. The main acceleration mechanism during flame propagation inside the chamber, is the flame instabilities. Outside the chamber, after a certain distance from the vent, turbulent wrinkling factor increases and dominates the chemical reaction rate. A maximum average of 20% of partial quenching occurs outside the chamber, after a certain distance from the vent. Finally, the proposed model for the chemical reaction rate is succeeded to qualitatively predict vented explosion experiment.

The overall performance of the model is qualitatively acceptable for predicting deflagration and DDT.

7.3 Recommendations for future research

Different unclosed matters should be clarified, I would recommend:

1- To include a heat transfer model so that to determine if there would be substantial effect on the flame propagation and the overpressure.

2- To include a model for the weakly stretched flame before the flame passes the critical radius. The critical radiuses of hydrogen-air mixtures are relatively small, but if for any other fuels, the critical radius is large compared to the propagation domain, a model for the weakly stretched propagation would be useful.

3- The adopted algebraic model for flame-generated turbulence contains uncertainties, especially when turbulence intensity is far from laminar burning velocity. Therefore, applying the model directly after ignition, as what was done in the current study, should be modified. The model itself could be replaced by another suitable model, if it is existing, otherwise it could be removed.

4- The fractal dimension of the instabilities could be modelled such that it includes the effect of the concentration. The fractal dimension of the turbulent wrinkling factor could be modified to another model if it provides better fitting.

5- The role of flame instabilities due to confinement and obstructions should be investigated, namely the Rayleigh-Taylor (RT) and the Richtmyer-Meshkov (RM) instabilities. RT and RM instabilities could increase flame surface area and generate turbulence (Ciccarelli and Dorofeev, 2008).

The Rayleigh-Taylor is a buoyancy-driven instability (Reckinger, 2006), which occurs if the flame is subjected to large acceleration toward the unburned gas. It could occur over an obstacle or through a vent (Ciccarelli and Dorofeev, 2008). Figure 7.1 (Jiang *et al.*, 2016) shows the mushroom shape characterized the RT instability.

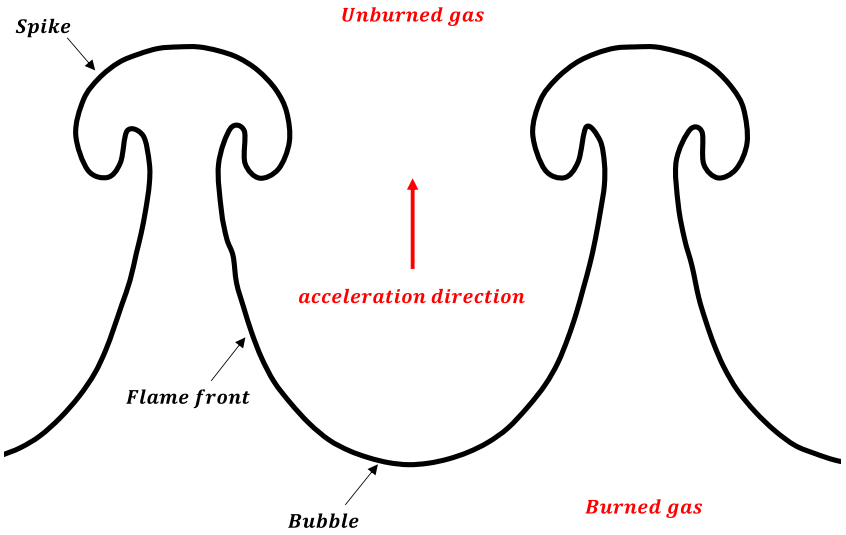

Figure 7.1: Rayleigh-Taylor instability development due to acceleration toward the unburned gas (Jiang *et al.*, 2016).

The Richtmyer-Meshkov instability is introduced due to collision between an incident or a reflected shock and the flame front (Reckinger, 2006). The instability develops for both directions of interaction i.e. whether the shock propagates from the burned gas toward the unburned gas or the opposite. Figure 7.2 (Jiang *et al.*, 2016) shows the development of the RM instability on the flame front after an incident shock collides with the flame.

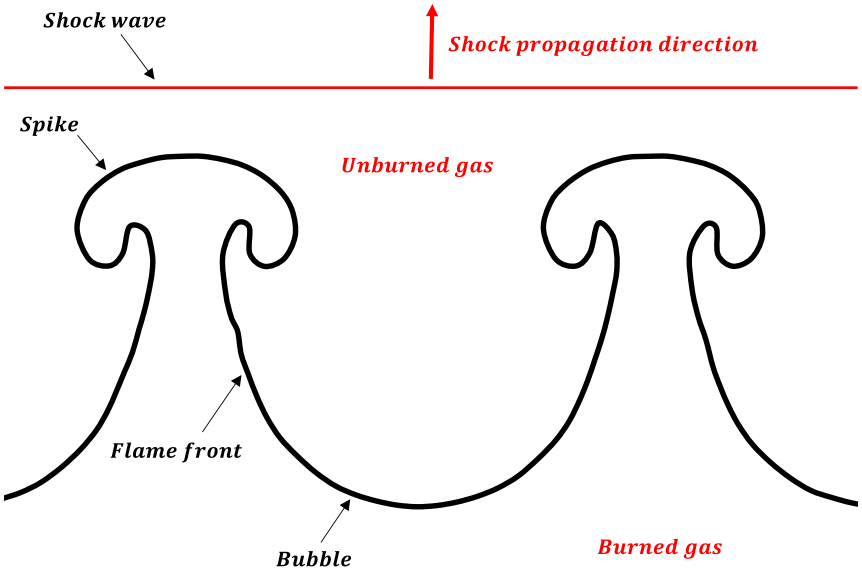

Figure 7.2: Richtmyer-Meshkov instability development after a shock collides with the flame (Jiang *et al.*, 2016).

A model for turbulent burning velocity including the RT instability, was suggested in (Modestov *et al.*, 2008). It was based on combining two limiting cases: the first was under zero acceleration, which was related to the burning velocity governed by the Darrieus-Landau instability. The second was under large acceleration, which was governed by the Rayleigh-Taylor instability.

I would suggest extending this approach, such that the first limit, under zero acceleration, would be replaced by the current developed model for the turbulent burning velocity in Eq. (3.39). In addition to adding a third limit that represents the change in the burning velocity due to collide with shocks, which could be governed by the RM instability. This model will incorporate the main physical mechanisms for flames: Darrieus-Landau & thermo-diffusive instabilities, turbulence, quenching, Rayleigh-Taylor instability, and Richtmyer-Meshkov instability.

REFERENCES

Addabbo, R., Bechtold, J. K. and Matalon, M. (2002) 'Wrinkling of spherically expanding flames', *Proceedings of the Combustion Institute*, 29(2), pp. 1527–1535. doi: http://dx.doi.org/10.1016/S1540-7489(02)80187-0.

Alekseev, V. A., Christensen, M. and Konnov, A. A. (2015) 'The effect of temperature on the adiabatic burning velocities of diluted hydrogen flames: A kinetic study using an updated mechanism', *Combustion and Flame*. The Combustion Institute, 162(5), pp. 1884–1898. doi: 10.1016/j.combustflame.2014.12.009.

Altantzis, C. *et al.* (2012) 'Hydrodynamic and thermodiffusive instability effects on the evolution of laminar planar lean premixed hydrogen flames', *Journal of Fluid Mechanics*, 700, pp. 329–361. doi: 10.1017/jfm.2012.136.

ANSYS-Fluent (2015) 'ANSYS® ANSYS Student Fluent, Release 16.2, Help System, Solver Theory Guide, ANSYS, Inc.'

Aung, K. T., Hassan, M. I. and Faeth, G. M. (1997) 'Flame stretch interactions of laminar premixed hydrogen/air flames at normal temperature and pressure', *Combustion and Flame*, 109(1–2), pp. 1–24. doi: 10.1016/S0010-2180(96)00151-4.

Azadboni, R. K. *et al.* (2017) 'Numerical Study of Deflagration-to-Detonation Transition in Homogenous and Inhomogeneous Hydrogen-Air Mixtures', *26th ICDERS*.

Babkin, V. S. (2003) *Private commutation between V. Molkov and V.S. Babkin.*

Bakker, A. (2012) *The Colorful Fluid Mixing Gallery*. Available at: http://www.bakker.org/cfm.

Balaji, V. S., De, A. and De, S. (2016) 'Numerical Investigation of Swirling Hydrogen Flames: Effect of Swirl and Fuel Jet in Coherent Structures', *Journal of Energy and Environmental Sustainability*.

Battista, F., Troiani, G. and Picano, F. (2015) 'Fractal scaling of turbulent premixed flame fronts: Application to LES', *International Journal of Heat and Fluid Flow*. Elsevier Inc., 51, pp. 78–87. doi: 10.1016/j.ijheatfluidflow.2014.08.006.

Bauwens, C. R., Chaffee, J. and Dorofeev, S. B. (2011) 'Vented explosion overpressures from combustion of hydrogen and hydrocarbon mixtures', *International Journal of Hydrogen Energy*. Elsevier Ltd, 36(3), pp. 2329–2336. doi:

10.1016/j.ijhydene.2010.04.005.

Bauwens, C. R. L., Bergthorson, J. M. and Dorofeev, S. B. (2017) ‘Experimental investigation of spherical-flame acceleration in lean hydrogen-air mixtures’, *International Journal of Hydrogen Energy*. Elsevier Ltd, 42(11), pp. 7691–7697. doi: 10.1016/j.ijhydene.2016.05.028.

Boeck, L. R. *et al.* (2016) ‘The GraVent DDT database’, *Shock Waves*. Springer Berlin Heidelberg, 26(5), pp. 683–685. doi: 10.1007/s00193-016-0629-0.

Bychkov, V. and Liberman, M. a. (2000) ‘Dynamics and stability of premixed flames’, *Physics reports*, 325(4–5), pp. 115–237. doi: 10.1016/S0370-1573(99)00081-2.

Cecere, D. *et al.* (2011) ‘Hydrogen/air supersonic combustion for future hypersonic vehicles’, *International Journal of Hydrogen Energy*. Elsevier Ltd, 36(18), pp. 11969–11984. doi: 10.1016/j.ijhydene.2011.06.051.

CFD Online (2012) *Turbulence length scale*. Available at: http://www.cfd-online.com/Wiki/Turbulence_length_scale.

Chakraborty, N., Katragadda, M. and Cant, R. S. (2011) ‘Effects of Lewis number on turbulent kinetic energy transport in premixed flames’, *Physics of Fluids*, 23(7). doi: 10.1063/1.3609278.

Chakraborty, N. and Klein, M. (2008) ‘A priori direct numerical simulation assessment of algebraic flame surface density models for turbulent premixed flames in the context of large eddy simulation’, *Physics of Fluids*, 20(8), p. 085108. doi: 10.1063/1.2969474.

Champion, M., Robin, V. and Mura, A. (2012) ‘A simple strategy to model the effects of thermal expansion on turbulent transports in premixed flames’, *Comptes Rendus Mécanique*. Elsevier Masson SAS, 340(11–12), pp. 769–776. doi: 10.1016/j.crme.2012.10.025.

Charlette, F., Meneveau, C. and Veynante, D. (2002) ‘A power-law flame wrinkling model for LES of premixed turbulent combustion Part I: non-dynamic formulation and initial tests’, *Combustion and Flame*, 131(1–2), pp. 159–180. doi: 10.1016/S0010-2180(02)00400-5.

Chaudhuri, S., Akkerman, V. and Law, C. K. (2011) ‘Modification of Turbulent Combustion Regime Diagram and Turbulent Flame Speed by Darrieus-Landau Instability’, *7th US Combustion Meeting*.

Ciccarelli, G. and Dorofeev, S. (2008) ‘Flame acceleration and transition to detonation in ducts’, *Progress in Energy and Combustion Science*, 34(4), pp. 499–550. doi: 10.1016/j.pecs.2007.11.002.

Clavin, P. (2015) ‘Dynamics of Gaseous Combustion Waves (from flames to detonations) - Lecture XI Initiation of detonations’, *Combustion Summer School*. Available at: https://www.youtube.com/watch?v=fyhvIxGAg9s&list=PLbInEHTmP9Vb6NJdPXU0hRfUUtYV_LPpn&index=13.

Colin, O. *et al.* (2000) ‘A thickened flame model for large eddy simulations of turbulent premixed combustion’, *Physics of Fluids*, 12(7), pp. 1843–1863. doi: 10.1063/1.870436.

Dahoe, A. E. (2005) ‘Laminar burning velocities of hydrogen–air mixtures from closed vessel gas explosions’, *Journal of Loss Prevention in the Process Industries*, 18(3), pp. 152–166. doi: 10.1016/j.jlp.2005.03.007.

Das, A. K., Kumar, K. and Sung, C. J. (2011) ‘Laminar flame speeds of moist syngas mixtures’, *Combustion and Flame*. The Combustion Institute., 158(2), pp. 345–353. doi: 10.1016/j.combustflame.2010.09.004.

Daubech, J. *et al.* (2013) ‘Hydrogen-Air Vented Explosions : New Experimental Data’, *Proc. 5th ICHS, Brussels*.

Dinkelacker, F., Manickam, B. and Muppala, S. P. R. (2011) ‘Modelling and simulation of lean premixed turbulent methane/hydrogen/air flames with an effective Lewis number approach’, *Combustion and Flame*. The Combustion Institute., 158(9), pp. 1742–1749. doi: 10.1016/j.combustflame.2010.12.003.

Dounia, O. *et al.* (2019) ‘Influence of kinetics on DDT simulations’, *Combustion and Flame*. Elsevier Inc., 200, pp. 1–14. doi: 10.1016/j.combustflame.2018.11.009.

Emami, S. *et al.* (2015) ‘LES of flame acceleration and DDT in hydrogen-air mixture using artificially thickened flame approach and detailed chemical kinetics’, *International Journal of Hydrogen Energy*. Elsevier Ltd, 40(23), pp. 7395–7408. doi: 10.1016/j.ijhydene.2015.03.165.

Ettner, F. (2014) ‘ddtFoam solver for DDT’. Available at: https://sourceforge.net/projects/ddtfoam/.

Ettner, F. A. (2013) ‘Efficient numerical simulation of the deflagration-to-detonation transition, PhD thesis, Technical University of Munich’.

Ettner, F., Vollmer, K. G. and Sattelmayer, T. (2014) 'Numerical Simulation of the Deflagration-to-Detonation Transition in Inhomogeneous Mixtures', *Journal of Combustion*, 2014, pp. 1–15. doi: 10.1155/2014/686347.

Flohr, P. and Pitsch, H. (2000) 'A turbulent flame speed closure model for LES of industrial burner flows', *Proceedings of the Summer Program of the Center for Turbulence Research*.

Fureby, C. (2005) 'A fractal flame-wrinkling large eddy simulation model for premixed turbulent combustion', *Proceedings of the Combustion Institute*, 30(1), pp. 593–600. doi: 10.1016/j.proci.2004.08.068.

Gaathaug, A. V., Vaagsaether, K. and Bjerketvedt, D. (2012) 'Experimental and numerical investigation of DDT in hydrogen-Air behind a single obstacle', *International Journal of Hydrogen Energy*, 37(22), pp. 17606–17615. doi: 10.1016/j.ijhydene.2012.03.168.

Gallego, E. *et al.* (2005) 'An Intercomparison Exercise on the Capabilities of CFD Models to Predict Deflagration of a Large-Scale H2-Air Mixture in Open Atmosphere-Paper', *ICHS*. Available at: https://www.hydrogen.energy.gov/pdfs/safety_biblio/ichs2005/papers/120003.pdf.

Gamezo, V. N., Ogawa, T. and Oran, E. S. (2007) 'Numerical simulations of flame propagation and DDT in obstructed channels filled with hydrogen–air mixture', *Proceedings of the Combustion Institute*, 31(2), pp. 2463–2471. doi: 10.1016/j.proci.2006.07.220.

García, J. *et al.* (2010) 'An intercomparison exercise on the capabilities of CFD models to reproduce a large-scale hydrogen deflagration in open atmosphere', *International Journal of Hydrogen Energy*, 35(9), pp. 4435–4444. doi: 10.1016/j.ijhydene.2010.02.011.

Génin, F. and Menon, S. (2010) 'Studies of shock/turbulent shear layer interaction using Large-Eddy Simulation', *Computers and Fluids*. Elsevier Ltd, 39(5), pp. 800–819. doi: 10.1016/j.compfluid.2009.12.008.

Gerke, U. *et al.* (2010) 'Derivation of burning velocities of premixed hydrogen/air flames at engine-relevant conditions using a single-cylinder compression machine with optical access', *International Journal of Hydrogen Energy*. Elsevier Ltd, 35(6), pp. 2566–2577.

doi: 10.1016/j.ijhydene.2009.12.064.

Giacomazzi, E., Bruno, C. and Favini, B. (1999) 'Fractal modelling of turbulent mixing', *Combustion Theory and Modelling*, 3(4), pp. 637–655. doi: 10.1088/1364-7830/3/4/303.

Giacomazzi, E., Picchia, F. R. and Arcidiacono, N. (2008) 'A review of chemical diffusion: Criticism and limits of simplified methods for diffusion coefficient calculation', *Combustion Theory and Modelling*, 12(1), pp. 135–158. doi: 10.1080/13647830701550370.

Giannakopoulos, G. K. *et al.* (2015) 'Consistent definitions of "Flame Displacement Speed" and "Markstein Length" for premixed flame propagation', *Combustion and Flame*, 162(4), pp. 1249–1264. doi: 10.1016/j.combustflame.2014.10.015.

Giannakopoulos, G. K. *et al.* (2019) 'Consumption and displacement speeds of stretched premixed flames - Theory and simulations', *Combustion and Flame*. Elsevier Inc., 208, pp. 164–181. doi: 10.1016/j.combustflame.2019.06.027.

Gouldin, F. C. (1987) 'An application of fractals to modeling premixed turbulent flames', *Combustion and Flame*, 68(3), pp. 249–266. doi: 10.1016/0010-2180(87)90003-4.

Gubba, S. R. *et al.* (2009) 'An assessment of large eddy simulations of premixed flames propagating past repeated obstacles', *Combustion Theory and Modelling*, 13(3), pp. 513–540. doi: 10.1080/13647830902928532.

Hasslberger, J., Boeck, L. R. and Sattelmayer, T. (2015) 'Numerical simulation of deflagration-to-detonation transition in large confined volumes', *Journal of Loss Prevention in the Process Industries*, 36, pp. 371–379. doi: 10.1016/j.jlp.2014.11.018.

Hawkes, E. R. *et al.* (2012) 'A petascale direct numerical simulation study of the modelling of flame wrinkling for large-eddy simulations in intense turbulence', *Combustion and Flame*, 159(8), pp. 2690–2703. doi: 10.1016/j.combustflame.2011.11.020.

Hu, E. *et al.* (2009) 'Experimental and numerical study on laminar burning velocities and flame instabilities of hydrogen-air mixtures at elevated pressures and temperatures', *International Journal of Hydrogen Energy*. Elsevier Ltd, 34(20), pp. 8741–8755. doi: 10.1016/j.ijhydene.2009.08.044.

Im, H. G. (2018) *Theory of basic flame properties (laminar and turbulent) - Numerical simulation of laminar and turbulent flame properties*, *Combustion summer school* ,

KAUST. Available at: https://www.youtube.com/watch?v=Z33-UAKadhc & https://ciss.kaust.edu.sa/Documents/Flame Fundamentals II Part 2 Hong Im.pdf.

Jiang, H. *et al.* (2016) 'Numerical simulations of the process of multiple shock–flame interactions', *Acta Mechanica Sinica*. The Chinese Society of Theoretical and Applied Mechanics; Institute of Mechanics, Chinese Academy of Sciences, 32(4), pp. 659–669. doi: 10.1007/s10409-015-0552-0.

Jordan, T. (2006) *HySafe project: SBEP-V2: Fh-ICT Balloon Test Deflagration of large-scale stoichiometric hydrogen-air mixture in open atmosphere 20-m diameter hemisphere http://www.hysafe.org/download/768/SBEPV2_Spec.pdf*.

Jordan, T. (2007) *HySafe project Wiki: BRHS: Combustion of Hydrogen www.hysafe.org/download/1205/BRHS_Chap3_Combustion_V1p1.pdf*.

Karanam, A., Sharma, P. K. and Ganju, S. (2018) 'Numerical simulation and validation of flame acceleration and DDT in hydrogen air mixtures', *International Journal of Hydrogen Energy*. Elsevier Ltd, 43(36), pp. 17492–17504. doi: 10.1016/j.ijhydene.2018.07.108.

Katragadda, M., Chakraborty, N. and Cant, R. S. (2012) 'A Priori Assessment of Algebraic Flame Surface Density Models in the Context of Large Eddy Simulation for Nonunity Lewis Number Flames in the Thin Reaction Zones Regime', *Journal of Combustion*, 2012, pp. 1–17. doi: 10.1155/2012/794671.

Keppeler, R. and Pfitzner, M. (2015) 'Modelling of Landau–Darrieus and thermo-diffusive instability effects for CFD simulations of laminar and turbulent premixed combustion', *Combustion Theory and Modelling*, 19(1), pp. 1–28. doi: 10.1080/13647830.2014.975747.

Kessler, D. A., Gamezo, V. N. and Oran, E. S. (2010) 'Simulations of flame acceleration and deflagration-to-detonation transitions in methane-air systems', *Combustion and Flame*. The Combustion Institute., 157(11), pp. 2063–2077. doi: 10.1016/j.combustflame.2010.04.011.

Khodadadi Azadboni, R. *et al.* (2017) 'Numerical modeling of deflagration to detonation transition in inhomogeneous hydrogen/air mixtures', *Journal of Loss Prevention in the Process Industries*. Elsevier Ltd, 49, pp. 722–730. doi: 10.1016/j.jlp.2017.04.024.

Khodadadi Azadboni, R. *et al.* (2019) 'The effect of concentration gradients on

deflagration-to-detonation transition in a rectangular channel with and without obstructions – A numerical study', *International Journal of Hydrogen Energy*. Elsevier Ltd, 44(13), pp. 7032–7040. doi: 10.1016/j.ijhydene.2019.01.157.

Khodadadi Azadboni, R., Heidari, A. and Wen, J. X. (2018) 'A Computational Fluid Dynamic Investigation of Inhomogeneous Hydrogen Flame Acceleration and Transition to Detonation', *Flow, Turbulence and Combustion*, 101(4), pp. 1009–1021. doi: 10.1007/s10494-018-9977-4.

Kim, W. K. *et al.* (2015) 'Self-similar propagation of expanding spherical flames in large scale gas explosions', *Proceedings of the Combustion Institute*. The Combustion Institute, 35(2), pp. 2051–2058. doi: 10.1016/j.proci.2014.08.023.

Konnov, A. A. (2008) 'Remaining uncertainties in the kinetic mechanism of hydrogen combustion', *Combustion and Flame*, 152(4), pp. 507–528. doi: 10.1016/j.combustflame.2007.10.024.

Kwon, O. C. and Faeth, G. M. (2001) 'Flame/stretch interactions of premixed hydrogen-fueled flames: Measurements and predictions', *Combustion and Flame*, 124(4), pp. 590–610. doi: 10.1016/S0010-2180(00)00229-7.

Kwon, O. C., Rozenchan, G. and Law, C. K. (2002) 'Cellular instabilities and self-acceleration of outwardly propagating spherical flames', *Proceedings of the Combustion Institute*, 29(2), pp. 1775–1783. doi: http://dx.doi.org/10.1016/S1540-7489(02)80215-2.

Lamoureux, N., Djebaïli-Chaumeix, N. and Paillard, C. E. (2003) 'Laminar flame velocity determination for H2-air-He-CO2mixtures using the spherical bomb method', *Experimental Thermal and Fluid Science*, 27(4), pp. 385–393. doi: 10.1016/S0894-1777(02)00243-1.

Mahmoudi, Y., Mazaheri, K. and Parvar, S. (2013) 'Hydrodynamic instabilities and transverse waves in propagation mechanism of gaseous detonations', *Acta Astronautica*. Elsevier, 91, pp. 263–282. doi: 10.1016/j.actaastro.2013.06.009.

Malik, K. *et al.* (2016) 'NUMERICAL AND EXPERIMENTAL INVESTIGATION OF METHANE-OXYGEN DETONATION IN A 9 M LONG TUBE', *Journal of KONES. Powertrain and Transport*, 23(4), pp. 311–318. doi: 10.5604/12314005.1217241.

Matalon, M. (2009) 'Flame dynamics', *Proceedings of the Combustion Institute*. The Combustion Institute, 32 I(1), pp. 57–82. doi: 10.1016/j.proci.2008.08.002.

Matalon, M. (2017) ‘Combustion Theory’, *Combustion Summer School*. Available at: https://cefrc.princeton.edu/sites/cefrc/files/combustion-summer-school/lecture-notes/2017_Matalon_All_combined.pdf.

Maxwell, B. *et al.* (2015) ‘Reaction Rate Closure for Turbulent Detonation Propagation through CLEM-LES’, *25th ICDERS*. Available at: http://www.icders.org/ICDERS2015/abstracts/ICDERS2015-225.pdf.

McDonough, J. M. (2007) *INTRODUCTORY LECTURES on TURBULENCE: Physics, Mathematics and Modeling*. Available at: http://web.engr.uky.edu/~acfd/lctr-notes634.pdf.

Meneveau, C. and Poinsot, T. (1991) ‘Stretching and quenching of flamelets in premixed turbulent combustion’, *Combustion and Flame*, 86(4), pp. 311–332. doi: 10.1016/0010-2180(91)90126-V.

Menon, S. (2015a) ‘Winter school - computational combustion - Lecture 3’. Available at: https://www.youtube.com/watch?v=zhH-87E0MOU.

Menon, S. (2015b) ‘Winter school - computational combustion - Lecture 5’. Available at: https://www.youtube.com/watch?v=s9QwQuc3x-I.

Milton, B. E. and Keck, J. C. (1984) ‘Laminar burning velocities in stoichiometric hydrogen and hydrogen-hydrocarbon gas mixtures’, *Combustion and Flame*, 58(1), pp. 13–22. doi: 10.1016/0010-2180(84)90074-9.

Modestov, M. *et al.* (2008) ‘Bubble velocity in the nonlinear Rayleigh-Taylor instability at a deflagration front’, *Physics of Plasmas*, 15(4), p. 042703. doi: 10.1063/1.2901191.

Molkov, V. (2012) *Fundamentals of Hydrogen Safety Engineering II, Comprehensive Renewable Energy*. doi: 10.1016/B978-0-08-087872-0.00418-2.

NASA-GRC (2015) *Navier-Stokes equations*. Available at: https://www.grc.nasa.gov/WWW/k-12/airplane/nseqs.html.

Nishiki, S. *et al.* (2002) ‘Modeling of flame-generated turbulence based on direct numerical simulation databases’, *Proceedings of the Combustion Institute*, 29(2), pp. 2017–2022. doi: http://dx.doi.org/10.1016/S1540-7489(02)80246-2.

Oran, E. S. and Gamezo, V. N. (2007) ‘Origins of the deflagration-to-detonation transition in gas-phase combustion’, *Combustion and Flame*, 148(1–2), pp. 4–47. doi:

10.1016/j.combustflame.2006.07.010.

Peters, N. (1997) ‘Four Lectures on Turbulent Combustion’, *ERCOFTAC Summer School*.

PETERS, N. (1999) ‘The turbulent burning velocity for large-scale and small-scale turbulence’, *Journal of Fluid Mechanics*. University of Ulster Library, 384(1999), pp. 107–132. doi: 10.1017/S0022112098004212.

PITSCH, H. (2005) ‘A consistent level set formulation for large-eddy simulation of premixed turbulent combustion’, *Combustion and Flame*, 143(4), pp. 587–598. doi: 10.1016/j.combustflame.2005.08.031.

Pitsch, H. and Duchamp de Lageneste, L. (2002) ‘Large-eddy simulation of premixed turbulent combustion using a level-set approach’, *Proceedings of the Combustion Institute*, 29, pp. 2001–2008. doi: 10.1016/S1540-7489(02)80244-9.

Poinsot, T. (2016) ‘Prediction and Control of Combustion Instabilities in Real Engines’, *36th international symposium in combustion*. Available at: https://www.youtube.com/watch?v=6U3iKhU3dYI.

Ramamurthi, K. (2014) *Introduction to Explosions and Explosion Safety - Lecture 24*. Available at: http://www.infocobuild.com/education/audio-video-courses/mechanical-engineering/IntroductionToExplosions-IIT-Madras/lecture-24.html.

Ravi, S. and Petersen, E. L. (2012) ‘Laminar flame speed correlations for pure-hydrogen and high-hydrogen content syngas blends with various diluents’, *International Journal of Hydrogen Energy*. Elsevier Ltd, 37(24), pp. 19177–19189. doi: 10.1016/j.ijhydene.2012.09.086.

Reckinger, S. (2006) ‘Development and Applications of Important Interfacial Instabilities : Rayleigh-Taylor, Richtmyer-Meshkov, and Kelvin-Helmholtz’, *Fluid Dynamics Term Paper*.

Robin, V., Mura, A. and Champion, M. (2011) ‘Direct and indirect thermal expansion effects in turbulent premixed flames’, *Journal of Fluid Mechanics*, 689, pp. 149–182. doi: 10.1017/jfm.2011.409.

Robin, V., Mura, A. and Champion, M. (2012) ‘Algebraic Models for Turbulent Transports in Premixed Flames’, *Combustion Science and Technology*, 184(10–11), pp. 1718–1742. doi: 10.1080/00102202.2012.690628.

Di Sarli, V., Di Benedetto, A. and Russo, G. (2010) 'Sub-grid scale combustion models for large eddy simulation of unsteady premixed flame propagation around obstacles', *Journal of Hazardous Materials*. Elsevier B.V., 180(1–3), pp. 71–78. doi: 10.1016/j.jhazmat.2010.03.006.

Shim, Y. *et al.* (2011) 'Local structure and fractal characteristics of H2-air turbulent premixed flame', *Proceedings of the Combustion Institute*. Elsevier Inc., 33(1), pp. 1455–1462. doi: 10.1016/j.proci.2010.09.002.

Sun, Z. Y. *et al.* (2012) 'Research on cellular instabilities in outwardly propagating spherical hydrogen-air flames', *International Journal of Hydrogen Energy*. Elsevier Ltd, 37(9), pp. 7889–7899. doi: 10.1016/j.ijhydene.2012.02.011.

Taylor, S. C. (1991) 'BURNING VELOCITY AND THE INFLUENCE OF FLAME STRETCH Simon Crispin Taylor BSc CPhys MInstP Submit', *PhD thesis - University of Leeds*.

Verhelst, S. *et al.* (2011) 'A correlation for the laminar burning velocity for use in hydrogen spark ignition engine simulation', *International Journal of Hydrogen Energy*. Elsevier Ltd, 36(1), pp. 957–974. doi: 10.1016/j.ijhydene.2010.10.020.

Vermorel, O., Quillatre, P. and Poinsot, T. (2017) 'LES of explosions in venting chamber: A test case for premixed turbulent combustion models', *Combustion and Flame*. Elsevier Inc., 183, pp. 207–223. doi: 10.1016/j.combustflame.2017.05.014.

Veynante, D. and Poinsot, T. (1997) 'Effects of pressure gradients on turbulent premixed flames', *Journal of Fluid Mechanics*, 353(1997), pp. 83–114. doi: 10.1017/S0022112097007556.

Vyazmina, E. *et al.* (2019) 'Vented explosion of hydrogen/air mixture: An intercomparison benchmark exercise', *International Journal of Hydrogen Energy*. Elsevier Ltd, 44(17), pp. 8914–8926. doi: 10.1016/j.ijhydene.2018.07.195.

Wang, C. J. and Wen, J. X. (2017) 'Numerical simulation of flame acceleration and deflagration-to-detonation transition in hydrogen-air mixtures with concentration gradients', *International Journal of Hydrogen Energy*. Elsevier Ltd, 42(11), pp. 7657–7663. doi: 10.1016/j.ijhydene.2016.06.107.

Wang, C.J. and Wen, J. X. (2017) 'Numerical simulation of flame acceleration and deflagration-to-detonation transition in hydrogen-air mixtures with concentration

gradients', *International Journal of Hydrogen Energy*, 42(11), pp. 7657–7663. doi: 10.1016/j.ijhydene.2016.06.107.

Wang, Z. and Abraham, J. (2017) 'Effects of Karlovitz number on turbulent kinetic energy transport in turbulent lean premixed methane/air flames', *Physics of Fluids*, 29(8). doi: 10.1063/1.4995303.

Wen, X. *et al.* (2012) 'Large eddy simulation of methane–air deflagration in an obstructed chamber using different combustion models', *Journal of Loss Prevention in the Process Industries*. Elsevier Ltd, 25(4), pp. 730–738. doi: 10.1016/j.jlp.2012.04.008.

Wolfram MathWorld (2018) *Calculus and Analysis, Special Functions, Error function*. Available at: http://mathworld.wolfram.com/Erf.html.

Yang, S. *et al.* (2018) 'Role of Darrieus–Landau instability in propagation of expanding turbulent flames', *Journal of Fluid Mechanics*, 850, pp. 784–802. doi: 10.1017/jfm.2018.426.

Zimont, V. *et al.* (1998) 'An Efficient Computational Model for Premixed Turbulent Combustion at High Reynolds Numbers Based on a Turbulent Flame Speed Closure', *Journal of Engineering for Gas Turbines and Power*, 120(3), pp. 526–532. doi: 10.1115/1.2818178.

Zimont, V. L. and Lipatnikov, A. N. (1995) 'A numerical model of premixed turbulent combustion of gases', *Chem. Phys. Reports*, 14(7), pp. 993–1025.